Exploring many-body effects in doped multiferroic $BiFeO_3$ for possible applications

Anjan Kumar Jena

A Thesis Submitted to

Indian Institute of Technology Hyderabad

In Partial Fulfillment of the Requirements for

The Degree of Doctor of Philosophy

भारतीय प्रौद्योगिकी संस्थान हैदराबाद

Indian Institute of Technology Hyderabad

Department of Physics

January 2020

Declaration

I declare that this written submission represents my ideas in my own words, and where ideas or words of others have been included, I have adequately cited and referenced the original sources. I also declare that I have adhered to all principles of academic honesty and integrity and have not misrepresented or fabricated or falsified any idea/data/fact/source in my submission. I understand that any violation of the above will be a cause for disciplinary action by the Institute and can also evoke penal action from the sources that have thus not been properly cited, or from whom proper permission has not been taken when needed.

(Anjan Kumar Jena)

PH15RESCH11001

Approval Sheet

This thesis entitled "Exploring many-body effects in doped multiferroic $BiFeO_3$ for possible applications" by Anjan Kumar Jena is approved for the degree of Doctor of Philosophy from IIT Hyderabad

---

Associate Professor
Dept. of Physics
IIT Hyderabad
External Examiner

Dr. Jyoti Ranjan Mohanty
Associate Professor
Dept. of Physics
IIT Hyderabad
Adviser

IIT Hyderabad
Examiner

IIT Hyderabad
Chairman

Acknowledgements

This thesis would not have been possible without the support of many people, who helped me directly or indirectly in the preparation and completion of this study. It gives me immense pleasure to convey my gratitude to all of them in my humble acknowledgement.

First and foremost, I would like to express my deepest gratitude to my research advisor Dr. Jyoti Ranjan Mohanty for giving me the opportunity to work under his guidance. His constant scientific, strategic and personal guidance, support and motivation were essential for the success of this thesis.

I am extremely thankful to my doctoral committee (DC) members, Prof. Saket Asthana, Department of Physics, IIT Hyderabad, India and Dr. Kaushik Nayak, Department of Electrical Engineering, IIT Hyderabad, India, for the valuable feedback and support throughout my research period.

I would like to thank Dr. J. Arout Chelvane, AMG, DMRL, Hyderabad, India for providing experimental facility to carry out magnetization measurements. I am grateful to Dr. Srinibas Satapathy, RRCAT, Indore, India for providing experimental facility to carry out SQUID, dielectric and ferroelectric measurements. I would also like to thank Dr. Sriganesh Prabhu, TIFR Mumbai, India, for providing experimental facility to carry out terahertz spectroscopy measurements.

I am grateful to Faculty members and staff of Department of Physics for their kindness and support. I am also grateful to Indian Institute of Technology (IIT) Hyderabad and Council for Scientific and Industrial Research (CSIR), India for providing research facility and financial support, respectively to carry out the present thesis work. I take this opportunity to thank my lab mates, Dr. M. Venkatnarayana, Mr. A. Soundara Raj, Dr. Abhishek Talapatra, Dr. G. Kotnana, Dr. U. M. Kannan, Mr. Dwipak Prasad Sahu, Mr. Apu Kumar Jana, Mr. Bhibuti Bhushan Nayak, Mr. Ajit Kumar Sahoo, Mr. Himadri N. Mohanty, Mr. Syam Prasad for their wonderful company during my Ph.D. work.

I am very grateful for the good friends I have made during my stay at IIT Hyderabad. I thank Miss. Subhasmita Mishra, Miss. Itishree Sethy, Mr. Krishna Banerjee, Mr. Goutham Chileveni, Mr. L. Panoop Patro, Miss. Karuna Kumari, for their help and support during my stay at IITH. I would also like to thank my fellow researchers, seniors for their constant support. Most importantly, none of this would have been possible without the love and support of my family. I would like to express my heart-felt gratitude to my parents and family members for their constant support and encouragement for my higher studies.

Anjan Kumar Jena

Dedication

To all my **Teachers** for their unconditional support
and **Family** and **Friends**

Abstract

Multiferroic (MF) materials have a tremendous interest in the scientific community due to the existence of many order parameters in a single phase. These order parameters bring various novel many-body concepts such as magneto-electric coupling (MEC), piezoelectric (PE) effect, magneto-striction effects, etc., which not only used to understand enrich science but also useful for many potential applications. Room temperature (RT) perovskites (ABO_3) are the most versatile materials in oxide research. Among various oxides, bismuth ferrite ($BiFeO_3$), Yttrium ferrite ($YFeO_3$), $YScO_3$, etc. are promising RT MF materials have studied till date. But $BiFeO_3$ (BFO) is one of the most studied and versatile MF systems possess antiferromagnetic (AFM) and ferroelectric (FE) properties well above RT. But due to the presence of high leakage current and spiral spin modulated structure, it possesses feeble many-body effects. The elementary substitution effect (doping/co-doping), rapid thermal annealing, thin-film, etc. successfully overcome the problems and improve the multiferroicity.

Non-magnetic doping/co-doping is a useful approach to improve multiferroic properties and several coupling effects as a comparison to many magnetic modified systems. The physical properties of BFO can be tuned either by magnetic (Nd-Gd), non-magnetic (Y-Sc/Mn) ions without changing the crystal structure (Rhombohedral: R3c) of the parent. Individual doping with Gd^{3+}, Y^{3+}, Sc^{3+} ions loses the structural stability of BFO at higher concentrations with poor electrical performance. But, one can improve the magnetic properties comprehensively improved from the vicinity of the parent compound. The Nd-Gd co-doping exhibits weak FM order with the appearance of secondary phases. However, Y-Sc co-doping improves many physical properties (FM, FE, MEC, PE) in single-phase material, which promises for future applications in terahertz, memory, solar-cell device applications.

Non-magnetic Y-Sc/Mn co-doping at low concentration exhibits single-phase structure with improved physical properties. The role of magnon in AFM ordering investigated by temperature-dependent terahertz spectroscopy. The change in spin state density in modified ceramics is observed during the investigation. The AFM ceramics promises for potential applications in terahertz sensors and tunable lasers. The tuned compounds exhibit tremendous MF properties with many such interesting observations. The frequency-temperature dependent dielectric study reveals the relaxation peaks shift near to RT during the transition from Y-Mn to Y-Sc co-doping. The bulk system is not useful for device applications to date, which leads to study the properties in thin-film materials.

Like Y-Sc tuned BFO ceramics, sol-gel grown insulating Y and Sc modified BFO films possess excellent multiferroicity ar RT in single phases structure. Piezo-force microscopy reveals maximum domains switched to ferroelastic type [71^0 and 108^0] domains after Y-Sc co-doping. The complete switching of upward and downward FE domains under dc applied bias reveals the symmetry and homogeneous FE polarization and capacitance-voltage. With significant improvement in FE, FM, and PE properties, the non-magnetic modified BFO films are promising candidate for future non-volatile memory applications. The MF based non-volatile resistive random access memory devices are fabricated and investigated by conventional $I - V$ characteristics. The device performance is improved under various perturbations like elementary substitution effect, magnetic field, white light, etc. The RRAM device under the application of magnetic field promises for high-storage data density devices. Several multi-level states are achieved by modulating the pulse-width, pulse-height, and the magnetic field, which is useful for multi-bit data storage devices and neuromorphic applications.

(**Keyword:** *Multiferroic, dielectric, magneto-electric coupling, piezo-electric, RRAM*)

Contents

Declaration . . . ii
Approval Sheet . . . iii
Acknowledgements . . . iv
Abstract . . . vi
Nomenclature . . . ix

List of publications **7**

1 Introduction and Motivation **8**
1.1 Introduction to Multiferroics . . . 8
1.2 Multiferroism in perovskite oxides . . . 9
1.3 Bismuth Ferrite ($BiFeO_3$) Identity . . . 11
1.3.1 Primary ferroic orders in $BiFeO_3$ . . . 12
1.3.2 Secondary ferroic orders in $BiFeO_3$ . . . 15
1.4 Field of Terahertz (THz) Spectroscopy . . . 17
1.4.1 Dynamic Magnetoelectric Coupling . . . 18
1.4.2 Optical properties of solids . . . 19
1.5 Resistive Switching and its applications . . . 21
1.5.1 Non-volatile memory . . . 22
1.5.2 Operation of electric field-induced resistive switching and its classification . . . 22
1.5.3 Microscopic origin of bipolar resistive switching . . . 25
1.5.4 Effects of additional perturbation on resistive switching . . . 26
1.6 Motivation . . . 27

2 Experimental Techniques **28**
2.1 Introduction . . . 28
2.2 Material synthesis . . . 29
2.2.1 Solid-state reaction route . . . 29
2.2.2 Thin-film fabrication using sol-gel spin coating . . . 30
2.3 X-Ray diffraction . . . 31
2.4 Microscopy Techniques . . . 35
2.4.1 Field-emission scanning electron microscope (FESEM) . . . 35
2.4.2 Transmission Electron Microscope (TEM) . . . 35
2.4.3 Atomic Force Microscope . . . 36
2.4.4 Magnetic Force Microscope (MFM) . . . 37

2.4.5 Piezo Force Microscope (PFM) . . . 37
2.5 Spectroscopy techniques . . . 38
2.5.1 Raman spectroscopy . . . 38
2.5.2 Terahertz (THz) spectroscopy . . . 40
2.5.3 X-ray photo-electron spectroscopy (XPS) . . . 40
2.6 Magnetic measurement techniques . . . 42
2.6.1 Vibrating scanning magnetometer (VSM) . . . 42
2.6.2 Superconducting quantum interference device (SQUID) . . . 43
2.7 Electrical measurement techniques . . . 43
2.7.1 Ferrolectric Polarization . . . 43
2.7.2 Dielectric measurement . . . 44
2.8 Magnetically Induced Magneto-Electric Coupling . . . 45
2.9 Summary . . . 46

3 Optimization for stable multifunctional magnetoelectric $BiFeO_3$ ceramics under d-shell ion modification 47
3.1 Experimental Details . . . 47
3.1.1 Sample preparation . . . 47
3.1.2 Material characterization . . . 48
3.2 Partially filled d-shell $Nd^{3+} - Gd^{3+}$ ions tuned $BiFeO_3$ ceramic systems . . . 48
3.3 Unfilled (Y)-Partially filled (Mn) d-shell ions tuned $BiFeO_3$ ceramic systems . . . 52
3.3.1 Unfilled $Y^{3+} - Sc^{3+}$ d-shell ions tuned $BiFeO_3$ ceramic systems . . . 56
3.4 Ferroelectric properties . . . 58
3.5 Magnetoelectric Effect . . . 60
3.6 Summary . . . 61

4 Temperature dependent dielectric and terahertz spectroscopy studies of co-doped $BiFeO_3$ ceramics 63
4.1 Introduction . . . 63
4.2 Experimental Details . . . 64
4.3 Dielectric properties at extremely low frequency region (ELF) . . . 64
4.3.1 Elemental substitution effect on the dipolar polarization of Y-Mn/Sc co-doped BFO ceramic . . . 64
4.3.2 Impedance Spectroscopy Analysis . . . 67
4.3.3 Complex Modulus Analysis . . . 70
4.3.4 Conductivity Studies: . . . 72
4.4 Temperature-dependent continuous-wave terahertz (CW-THz) spectroscopy studies . . . 74
4.5 Summary . . . 78

5 Electrically tuned stable ferroelectric switching in non-magnetic ion modified $BiFeO_3$ films 80
5.1 Introduction . . . 80
5.2 Experimental details . . . 81
5.3 Structural and Microstructural Analysis . . . 82

5.4 Manipulation of ferromagnetic properties in non-magnetic ion modified BFO thin-film 85
5.5 Quantitative ferroelectric polarization switching in non-magnetic modified multiferroic films under voltage response . . . 91
5.6 Summary . . . 94

6 Magneto-electric rectifying multilevel resistive switching in multiferroic based devices 96
6.1 Introduction . . . 96
6.2 Experimental Techniques . . . 97
6.3 Effect of doping (Y) and co-doping (Y-Sc) on the resistive switching properties of multiferroic $BiFeO_3$ . . . 98
6.3.1 Electric field rectifying RS effect in un-doped and modified BFO system . . . 98
6.3.2 Endurance characteristics or retention properties of $Ag/MF/FTO$ RRAM devices . . . 99
6.3.3 Conduction mechanism of resistive switching behavior in multiferroic based devices . . . 101
6.4 Magnetic field modulated multilevel resistive switching behavior in $Ag/BiFeO_3/FTO$ device . . . 105
6.4.1 Effect of the magnetic field to the resistive switching behavior . . . 106
6.4.2 Magnetic field controlled pulse-width (PW) and pulse-height (PH) modulated multilevel resistive switching behavior in $Ag/BFO/FTO$ device . . . 108
6.4.3 Magnetic field influence impedance spectroscopy analysis at HRS and LRS of $Ag/BFO/FTO$ device . . . 110
6.5 Conclusion . . . 111

7 Summary and scope for future work 112
7.1 Summary . . . 112
7.1.1 Temperature-dependent terahertz signal from antiferromagnetic tuned $BiFeO_3$ ceramics . . . 112
7.1.2 Elementary substitution effect on dipolar polarization modulation of multiferroic $BiFeO_3$ ceramics . . . 113
7.1.3 Electrically tuned stable ferroelectric switching in non-magnetic ion modified $BiFeO_3$ films . . . 113
7.1.4 Magneto-electric rectifying multilevel resistive switching in multiferroic based devices . . . 114
7.2 Future outlook . . . 114
7.2.1 Experimental evidence for the dynamic spin-charge ordering mediate through strain in $BiFeO_3$ . . . 114
7.2.2 Tuning of magnetoelectric coupling in multiferroic based novel heterostructure for possible application . . . 115

Nomenclature

List of symbols

k_B	Boltzman's constant
h	Planck's constant
$\hbar$	Reduced Planck's constant (J. s)
V_{eff}	Interaction between the electrons mediated by the electron-phonon coupling
M	Atomic mass of ion
$N(E_F)$	Density of states at Fermi level
E_F	Fermi level
V_{ext}	External nuclear potential
$\widehat{H}$	Hamiltonian
m_i	Electronic mass
Z_I	Nuclear charges
M_I	Nuclear mass
$\widehat{T}_e$	Kinetic energy of the electron
$\widehat{V}_{ee}$	Potential energy of the electron
$\widehat{T}_n$	Kinetic energy of the nucleus
$\widehat{V}_{en}$	Potential energy of the electron and nucleus
$\widehat{V}_{nn}$	Potential energy of the nucleus
$\widehat{\theta}$	Time reversal operator
$\widehat{K}$	Conjugation operator
E_0	Ground state energy
E_{xc}	Exchange-correlation energy
V_{KS}	Kohn-Sham potential
j_l	Spherical Bessel functions
$n(r)$	Electronic density as a function of position
R_{MT}	Muffin-tin radius
K_{Max}	Plane wave cut-off
G_{max}	Charge-density Fourier expansion (a.u.$^{-1}$)
C_{ij}	Elastic constants (GPa)
G_H	Hill's shear modulus (GPa)
G_R	Reuss shear modulus (GPa)
G_v	Voigt shear modulus (GPa)
E	Young's modulus (GPa)
B	Bulk modulus (GPa)
A	Anisotropy factor
v_l	Longitudinal sound velocity (km/s)
v_t	Transverse sound velocity (km/s)
v_m	Mean sound velocity (km/s)
Θ_D	Debye temperature (K)
N_A	Avogadro's number
n_e	Electron concentration
n_h	Hole concentration

Greek Letters

ψ	wave function
σ	Electrical conductivity
τ	Relaxation time
ρ	Density
Ω	Ohm
κ	Thermalconductivity
κ_e	Electronic thermalconductivity
κ_l	Lattice thermalconductivity

Subscripts

i, j	Number of electron index
I, J	Number of nucleus index
e	Electron
n	Nucleus

Abbreviations

NVM	Non-volatile memory
LDA	Local density approximation
GGA	Genelarized gradient approximation
TB-mBJ	Tran Blaha-modified Becke-Johnson
LAPW	Linearized augmented planewave
FP-LAPW	Full-potential linearized augmented planewave
SOC	Spin-orbit coupling
BZ	Brillouin zone
DOS	Density of states
HF	Hartree-Fock
AE	All electron
ps	Pseudo function
ZT	Figure of merit

List of Figures

1.1.1 (a) Origin of various many-body effects during interplay between ferroic orders and (b) possible multiferroic heterostructure design for possible applications. 9
1.1.2 (a) Schematic diagram of type-I and type-II multiferroics in order to their critical transition temperature. 10
1.2.1 (a) Schematic diagram of a perovskite structure and (b) distorted rhombohedral perovskite $BiFeO_3$. 10
1.3.1 (a) Multiferroic bismuth ferrite identity. 11
1.3.2 Comparative analysis of (a) ferroelectric and (b) ferromagnetic properties for some of the well-controlled multiferroic $BiFeO_3$ system. 13
1.3.3 Schematic representation of spiral spin arrangement of spins in multiferroic $BiFeO_3$. 14
1.3.4 Schematic representation of interplay between polarization (P) and magnetization (M) leads to magnetoelectric effects, (b) statistical comparison of few ME effect multiferroic BFO. 16
1.3.5 Schematic representation of interplay between polarization (P) and magnetization (M) leads to magnetoelectric effects. 17
1.4.1 Schematic representation of terahertz gap in the frequency range. 17
1.4.2 Electromagnetic wave propagation through the medium for optical properties. 20
1.5.1 Schematic representation of (a) resistive memory configuration, (b) origin of pristine, low resistance, and high resistance states. 22
1.5.2 Schematic representation of (a) unipolar resistive switching (URS), (b) bipolar-resistive switching (BRS) (F8), (c) bipolar-resistive switching (BRS) (cF8), and (d) threshold resistive switching effect in resistive memory. 24
1.5.3 Oxygen vacancy migrated pristine state, low resistance states (formation of conducting filaments), and high resistance states (rupture of conducting filament). 25

2.1.1 Characterization techniques used to explore the properties of bulk ceramics and thin film materials. 28
2.2.1 Schematic representation of working principle of high-energy ball milling technique. . 29
2.2.2 Flowchart for ceramic sample preparation through high-energy ball milling technique. 30
2.2.3 Processes for thin film fabrication using spin-coating technique. 31
2.2.4 Processes for thin film fabrication using spin-coating technique. 31
2.3.1 (a) XRD, (b) regular incidence XRD, (c) Grazing incidence XRD. 32
2.3.2 (a) Schematic representation for origin crystal planes from various Bragg's angle during X-ray diffraction measurement and (b) Rietveld refinement for $BiFeO_3$ ceramic. 32

2.4.1 Schematic diagram of FESEM technique and the scanned topography images of BFO ceramics at 3X, 5X and 10X. . . . 34
2.4.2 Schematic representation of working principle of TEM technique and the scanned images (TEM, HRTEM,and SAED) of BFO film. . . . 36
2.4.3 (a) Schematic representation of working principle of AFM technique, (b) tapping and non-contact mode in AFM, and (c) scanned AFM images of spin coated BFO film. . . . 37
2.4.4 (a) Schematic representation of working principle of MFM technique in NCM, (b) scanned MFM images of spin coated BFO film. . . . 38
2.4.5 Schematic representation of cantilever movement during (a) in-phase, (b) out-of-phase piezoresponse with respect to driving voltage, and its respective signal (c) in-phase, and (d) out-of-phase. . . . 39
2.5.1 Schematic representation of energy-level diagram of the Raman scattering. . . . 39
2.5.2 Schematic representation of (a) CW-THz spectrometer technique (b) material behavior at various frequency range. . . . 41
2.6.1 Schematic diagram of VSM and magnetization measurement of $Bi_{0.94}Y_{0.06}Fe_{0.95}Mn_{0.05}O_3$ ceramic. . . . 42
2.6.2 Schematic representation of SQUID magnetometer [163]. . . . 43
2.7.1 (a) Schematic representation of P-E measurement set-up and the obtained (b) P-E hysteresis loop for $Bi_{0.97}Y_{0.03}Fe_{0.95}Sc_{0.05}O_3$ ceramics. . . . 44
2.7.2 (a) Schematic representation principle arrangement for dielectric setup and (b) material sandwitched between the electrodes [165]. . . . 45
2.8.1 Schematic representation of magnetically induced magneto-electric coupling experimental set-up. . . . 46

3.2.1 (a) X-ray rietveld refinement, and (b) FESEM micro-graph for un-doped and Gd-Nd co-doped BFO ceramics. . . . 49
3.2.2 (a) Raman spectroscopy, (b) Tauc's plot for un-doped and Gd-Nd co-doped BFO ceramics. . . . 50
3.2.3 (a) M-H hysteresis loops at maximum applied magnetic field 15 kOe and (b) magnetic parameter of BFO at various Gd-concentration label. . . . 51
3.3.1 (a) XRD Reitveld refinement, (b) Lorentzian fitted Raman spectra, and (c) FESEM micrograph images for BFO, Y-Mn co-doped BFO ceramics. . . . 52
3.3.2 (a) Room temperature M-H hysteresis curve, (b) tuning of magnetization with Y-concentration, and (b) BSD images for BFO and BYFMO ceramics. . . . 54
3.3.3 Magnetization-temperature (M-T) and [DSC: inset] plots for (a) BFO, (b) BY3FMO, (c) BY6FMO, and (d) BY12FMO at 1000 Oe 55
3.3.4 (a) Reitveld refinement of XRD spectra and (b) FESEM micrograph for BYFSO ceramics. . . . 56
3.3.5 (a) Raman spectroscopy phonon modes and (b) M-H hysteresis curve obtained from Y-Sc co-doped BFO ceramics. . . . 57
3.4.1 Ferroelectric polarization P-E curve for BFO, BG10N10FO, BYFMO, and BYFSO compounds. . . . 59
3.5.1 Magnetoelectric coupling plots obtained from BFO, BYFMO, and BYFSO compounds at 26 Oe. . . . 60

4.1.1 (a) Polarization mechanism in dielectric materials (b) polarization distribution with respect to the frequency. 64
4.3.1 RT (a) dielectric constant (ϵ_r), (b) loss tangent ($tan\delta$), and their (c) comparative plots for BFO, BYFMO, and BYFSO ceramics. 65
4.3.2 (a) Dielectric constant (ϵ_r), (b) loss tangent ($tan\delta$) at various temperature between $30^0 - 210^0$ C for BFO, BYFMO, and BYFSO ceramics. 66
4.3.3 Frequency modulation (a) real part (Z') and (b) imaginary part (Z'') of complex impedance at various temperature for BFO, BYFMO, and BYFSO ceramics. 68
4.3.4 Nyquist's plots (a) BFO, (b) BYFMO, (c) BYFSO, and (d) equivalent electrical circuit to fit the Nyquist's plots. 69
4.3.5 Frequency modulation (a) real part (M') and (b) imaginary part (M'') of complex electrical modulus at various temperature for BFO, BYFMO, and BYFSO ceramics. 71
4.3.6 Arrhenius plots obtained from $ln\omega$ vs $\frac{1000}{T}$ of BFO, BYFMO, and BYFSO ceramics. 72
4.3.7 (a) Frequency dependent ac conductivity and (b) Arrhenius plots of $ln\sigma_{ac}$ vs $\frac{1000}{T}$ for BFO, BYFS5O, and BYFS10O ceramics. 73
4.4.1 (a) Terahertz time-domain spectra obtained from BFO and BYFSO compounds. . . 74
4.4.2 (a) Transmission spectra obtained from First Fourier Transform (FFT) of time-domain spectra of BFO and BYFSO ceramics. 75
4.4.3 (a) Refractive Index (n) and (b) extinction coefficient (k) of BFO and BYFSO ceramics. 76
4.4.4 Extremely low frequency (a) ϵ', (b) ϵ'' and terahertz frequency (c) ϵ', (d) ϵ'' of BFO and BYFSO ceramics. 77
4.4.5 Frequency variation conductivity of BFO and BYFSO ceramics in THz region [inset: extremely low frequency region]s. 78

5.3.1 (a) X-ray diffraction pattern (b) shifting of primary peaks for un-doped BFO, doped BYFO, and co-doped BYFSO films. 82
5.3.2 (a) Transmission electron microscope (TEM), (b) high resolution transmission electron microscope (HRTEM), (c) SAED patterns for BFO, BYFO, and BYFSO compounds. 83
5.3.3 (a) FESEM micrograph, (b) 2D-AFM, and (c) 3D-AFM images of BFO, BYFO, and BYFSO film on 5×5 μm scanned region. 84
5.3.4 (a) C-AFM topography, (b) current mapping image, and (c) current profile of BFO, BYFO, and BYFSO film on $5 \times 5\mu m$. 86
5.4.1 M-H hysteresis loop of BFO, BYFO, and BYFSO film at maximum applied field of 15 kOe. (b) comparison with various non-magnetic magnetization, and (c) spin-cycloid nature of multiferroic BFO. 86
5.4.2 X-ray photoelectron spectrometer (XPS) spectra of Bi4f (a) BFO, (b) BYFSO; and Fe2p (c) BFO, (d)BYFSO films. 88
5.4.3 Field cooling (FC) and zero field cooling (ZFC) for (a) BYFO [Inset: BFO], and (b) BYFSO film between the temperature range 4-350 K at applied magnetic field of 100 Oe. 89
5.4.4 MFM images of un-doped BFO, Y-doped BYFO, and Y-Sc co-doped BYFSO films. . 89
5.5.1 (a-c) Topography, (d-f) out-of-plane (OP), and (g-i) in-plane (IP) phase PFM images of BFO, BYFO, and BYFSO films. 90

5.5.2 Capacitance-Voltage (C-V) measurements of BFO, BYFO, and BYFSO films. 91
5.5.3 (a) Ferrolectric polarization orientation in BYFSO film and schematic representation of ferroelectric domain switching with opposite bias, (b) in-plane (IP) phase, (c) out-of-plane (OP) phase PFM images with applied bias of +2 V, (d) ferroelectric polarization switching under dc applied bias $\pm 8\ V$, (c) CP-AFM current profile image under various voltage ±10 of BYFSO film. 92
5.5.4 (a) phase vs. voltage, (b) amplitude vs. voltage obtained during PFM measurements, (c) Room temperature P-E hysteresis loop of Y-Sc co-doped BYFSO films, and (d) sketch to demonstrate FE polarization ordering along [111] direction. 93

6.1.1 Multiferroic based $Ag/BFO/FTO$, $Ag/BYFO/FTO$, & $Ag/BYFSO/FTO$ resistive random access memory devices configuration and its effects under additional perturbation which provide extra degree of freedom to achieve multifunction. 97
6.3.1 BRS $I-V$ characteristics for [(a) BFO, (b) BYFO, (c) BYFSO], and $logI-V$ curve for [(d) BFO, (c) BYFO, (c) BYFSO] based RRAM device. 98
6.3.2 fig3 99
6.3.3 Endurance characteristics (a) BFO, (b) BYFO and BYFSO, (c) cumulative probability distribution, and (d) $R_{OFF}/R_{ON} = OFF/ON$ ratio for 50 complete testing cycles of BFO, BYFO, and BYFSO based device. 100
6.3.4 XPS spectroscopy for oxygen O1S core-level spectra of (a) BFO, (b) BYFO and BYFSO films. 101
6.3.5 (a)LRS, (b) HRS Ohmic-SCLC conduction model for Ag/BFO/FTO; (c) LRS Ohmic-SCLC, (d) HRS Schottky barrier emission model for Ag/BYFO/FTO, (e) LRS Ohmic-SCLC, (f) HRS Schottky barrier emission model for Ag/BYFO/FTO. 102
6.3.6 Impedance spectroscopy analysis explaining RS mechanism at HRS (a) BFO, (b) BYFO, and (c) BYFSO, and at LRS (d) BFO, (e) BYFO, and (f) BYFSO multiferroic based RRAM devices. 103
6.3.7 fig6 105
6.4.1 (a) Stability of the Ag/BFO/FTO device over a period of one year, (b) schematic representation of $I-V$ measurements set-up with the application of magnetic field, (c) typical $I-V$ characteristics in linear scale, and (d) shifting of V_t under the influence of various magnetic field. 106
6.4.2 Enhance OFF/ON ratio with varying magnetic field applied externally to the device. 107
6.4.3 (a) The change of resistance state at pulse width 30 μs and 60 μs, (b) resistive switching of Ag/BFO/FTO device with varying pulse voltage and magnetic field. . . 108
6.4.4 (a) The change of resistance state at pulse width 30 μs and 60 μs, (b) resistive switching of Ag/BFO/FTO device with varying pulse voltage and magnetic field. . . 109
6.4.5 (a) Impedance spectroscopy at HRS and LRS, and (b) Nequist plots at HRS and LRS with varying magnetic field. 110

List of Tables

3.1.1 Synthesized Gd-Nd, Y-Mn, and Y-Sc co-doped $BiFeO_3$ bulk samples at various concentration level. . . . 48
3.2.1 Structural and microstructural parameters extracted from the simulation results and FESEM micrograph images of un-doped and Nd-Gd co-doped BFO ceramics. . . . 49
3.2.2 Modulation of phonon modes and energy band-gap (E_g) of magnetic Nd-Gd ion modified BFO ceramics. . . . 50
3.2.3 (a) Room temperature M-H hysteresis curve (b) variation of magnetic parameters at various Gd-concentration of BFO and BGNFO ceramics. . . . 51
3.3.1 (a) Structural parameters of Y-Mn co-doped $Bi_{1-x}Y_xFe_{1-y}Mn_yO_3$ (x=y=0; x=0.03, 0.06, 0.12, y=0.05). . . . 53
3.3.2 Modulation of Raman phonon modes of BFO ceramics after Y-Mn co-doping. . . . 53
3.3.3 Magnetic parameters extracted from the M-H magnetization curve and M-T curve of Y-Mn co-doped BFO ceramics. . . . 55
3.3.4 Structural and microstructural parameters extracted from the simulation results and FESEM images of Y-Sc co-doped ceramics. . . . 57
3.3.5 Modulation of Raman phonon modes of BFO ceramics after Y-Mn co-doping. . . . 58
3.3.6 Magnetic parameters extracted from the M-H magnetization curve of Y-Sc co-doped BFO ceramics. . . . 58
3.4.1 Ferrolectric polarization parameters extracted from P-E hysteresis curve of BFO, BGNFO, BYFMO, and BYFSO ceramics. . . . 60

4.3.1 Dielectric parameters extracted from Cole-Cole relation of BFO, BYFMO, and BYFSO ceramics at 100^0 C. . . . 67
4.3.2 Electrical parameters extracted from equivalent electrical R-C circuitry model of BFO, BYFMO, and BYFSO ceramics. . . . 70
4.3.3 Activation energy extracted from the Arrhenius plots of lnω vs $\frac{1000}{T}$ and $ln\sigma_{ac}$ vs $\frac{1000}{T}$ for BFO, BYFMO, and BYFSO samples. . . . 72

5.3.1 Structural and microstructural parameter obtained from the XRD pattern and various microscopy (FESEM, AFM, and TEM) techniques of BFO, BYFO and BYFSO film. 83
5.4.1 Magnetic parameters extracted from the M-H curve of BFO, BYFO and BYFSO film. 87

6.3.1 Conduction models explaining the resistive switching effect at high resistance state (HRS) and low resistance state (LRS) by sweeping the positive and negative bias voltage for BFO, BYFO, and BYFSO based RRAM devices. . . . 103

6.3.2 The electrical parameters at HRS [grain/bulk resistance (R1), grain boundary resistance (R2), CPE1, and CPE2) and at LRS (contact resistance (R_c), R1, and CPE1) are extracted from the fitting model for BFO, BYFO, and BYFSO based memory device. 104

List of Publications

Under the scope of the thesis

1. **A. K. Jena** and J. Mohanty, Enhancing ferromagnetic properties in bismuth ferrites with non-magnetic Y and Sc co-doping, *J. of Mat. Sci.: Mat. in Elect.* **29** (6), 5150-5156 (2018).

2. **A. K. Jena**, J. Arout Chelvane, and J. Mohanty, Enhanced ferromagnetic properties in Nd and Gd co-doped $BiFeO_3$ ceramics, *AIP Conference Proceedings* **1953**, 120072 (2018).

3. **A. K. Jena**, S. Satapathy, and J. Mohanty, Magnetic and dielectric response in yttrium (Y)-manganese (Mn) substituted multiferroic $Bi_{1x}Y_xFe_{1y}Mn_yO_3(x = y = 0; x = 0.03, 0.06, 0.12, y = 0.05)$ ceramics, *J. of Appl. Phys.***124**, 174103 (2018).

4. **A. K. Jena**, S. Satapathy, and J. Mohanty, Magnetic properties and oxygen migration induced resistive switching effect in Y substituted multiferroic bismuth ferrite, *Phys. Chem. Chem. Phys.* **21**, 15854-15860 (2019).

5. **A. K. Jena**, J. Arout Chelvane, and J. Mohanty, Simultaneous improvement of piezoelectric and magnetic properties in diamagnetic ion modified $BiFeO_3$ film, *J. of Allo. and Comp.* **805**, 1168-1174 (2019).

6. **A. K. Jena**, J. Arout Chelvane, and J. Mohanty, Evidence for dielectric suppression in non-magnetic modified multiferroic bismuth ferrite, *J. of Appl. Phys.* **126**, 184101 (2019).

7. **A. K. Jena**, Ajit Kumar Sahoo, and J. Mohanty, Effects of magnetic field on the resistive switching behavior of $Ag/BiFeO_3/FTO$ RRAM device, *Appl. Phys. Lett.*, (Revision submitted) (2019).

8. **A. K. Jena**, S. Prabhu, and J. Mohanty, Temperature-dependent terahertz signal from anti-ferromagnetic modified $BiFeO_3$ ceramics, *Appl. Phys. Lett.*, (to be communicated) (2020).

9. **A. K. Jena**, S. Satapathy, and J. Mohanty, Stable ferroelectric switching mediated multilevel non-volatile memory application in multiferroic based devices, (Manuscript under preparation) (2020).

Outside the scope of the thesis

1. N. Pradhani, P. K. Mahapatra, R. N. P. Choudhary, **A. K. Jena**, J. Mohanty, Investigation on the effect of Mn substitution on the structural, electrical and ferroelectric characteristics of $Bi_{0.5}Na_{0.5}TiO_3$ ceramic, *Mat. Res. Bull.* **119**, 110566 (2019).

2. **A. K. Jena**, Himadri Nandan Mohanty, Ajit Kumar Sahoo, S. Satapathy, and J. Mohanty, Voltage-controlled ferromagnetic behavior of multi-valence ion manipulated $BiFeO_3$ prepared under thermal quenching condition, (Manuscript under preparation) (2020).

Chapter 1

Introduction and Motivation

1.1 Introduction to Multiferroics

The functional electronic and magnetic materials play a significant role in modern technology. In the current scenario, the development in modern electronic techniques, from the sensing component in smartphone mobiles to next-generation non-volatile memory (NVM) are functioning directly from the intrinsic electronic and magnetic behavior of their constituent compounds. Essentially, the selection of a particular material depends on the approaching problem and its possible practical applications. Led by the continuous hunt for novel multifunctional materials and drift towards miniatured application, the trending research termed *'multiferroics'* has the potential to combine the intrinsic electronic and magnetic properties in a single-phase [1]. It involves the coexistence of two or more *'ferroic'* orders such as *ferroelectric* (change in polarization under applied electric field), *ferromagnetic* (change in magnetization under applied magnetic field), and *ferroelastic* (change in strain under applied mechanical stress), etc. simultaneously in single-phase. The interplay of ferroic orders brings various novel many-body effects (*magnetoelectricity, piezoelectricity, magnetostriction, etc.*), which is useful to understand the novel phenomena involving spin dynamic, charge ordering, phonon interaction, and their correlation. The origin of various many-body effects during interplay between the ferroic orders are represented schematically in Fig. 1.1.1 (a). The study of these ferroic orders and its many-body effects in perovskite compounds are the central focus to track the cutting-edge potential applications. The multiferroic materials exhibit precise macroscopic properties (ferroelectricity, ferromagnetism, and ferroelastic, etc.) below a certain critical temperature, which can be simultaneously switchable and scalable. These properties exist independently, and also can be manipulated under any external perturbations. For example, the ferroelectric polarization P and magnetization M can be simultaneously tuned under the applied electric field (E) or magnetic field (H) or strain (σ).

Due to such unique properties, multiferroics have a broad spectrum of applications in memory technology, solar cell, sensor, actuator, transformer, oscillator, filters, phase shifters, etc. [2, 3]. Essentially, the NVM require strong piezoelectric effect and magnetoelectric effect between the ferroic orders, which helps to achieve the multistate high-storage data density memory device. The possible design of such potential device is illustrated in Fig 1.1.1 (b) [4].

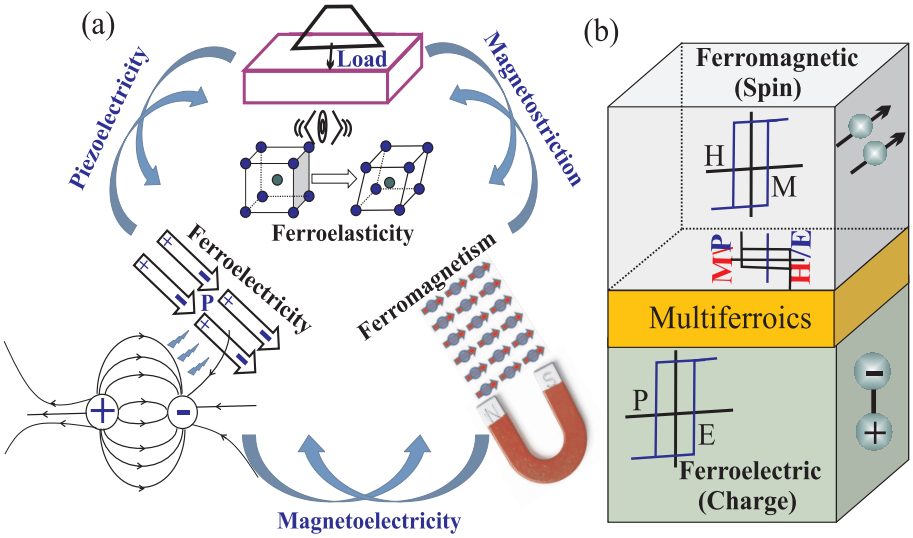

Figure 1.1.1: (a) Origin of various many-body effects during interplay between ferroic orders and (b) possible multiferroic heterostructure design for possible applications.

Classification of Multiferroics

The multiferroics are classified into two categories according to their origin of ferroelectric order, i.e. (i) type-I and (ii) type-II multiferroics. The type-I multiferroics reffers to the material in which the ferroelectric (FE) and ferromagnetic (FM) orders appeared at various critical temperatures. Usually, the ferroelectricity occurs at very high temperature (800-1100 K) due to structural distortion, while the ferromagnetism has appeared at a low transition temperature (40-220 K). In this class, FE and FM orders are not coupled directly, often being elucidated as 'weakly coupled' [5]. Room temperature (RT) $BiFeO_3$ is one of the most prominent stable multiferroic system occurring FE at 1100 K driven by the stereochemically active lone pair of Bi^{3+} ion and FM ordering ocuured near 643 K due to super-exchange interaction [6].

In term type-II, the magnetic ordering breaks the inversion symmetry and immediate causes ferroelectricity i.e., both the orders occur simulataneously at an identical transition temperature. This class of multiferroics is referred to as the improper ferroelectrics, in which the polarization strongly coupled with magnetization. The critical temperature is rather low ($<$ 50 K) due to magnetic frustration arises from the non-centrosymmetric structure [5]. $TbMnO_3$ is a perfect prototypical example, where the non-centrosymmetric magnetization driven the FE order directly at 28 K. They observed the polarization fliped by 90^0 under magnetic influence [7].

The FE and FM ordering according to their critical temperatures (T_c *or* T_N) for type-I and type-II multiferroics is represented schematically in Fig. 1.1.2.

1.2 Multiferroism in perovskite oxides

Multiferroics are much attention in the modern scientific community due to the appearance of many order parameters in single phase, simultaneously. Perovskite type (ABO_3) oxide multiferroics brought significant attention due to their simple structure [Fig. 1.2.1 (a)] and ease of material synthesis. The ferroelectricity in perovskites arises from the transition metal ions with empty d-shell

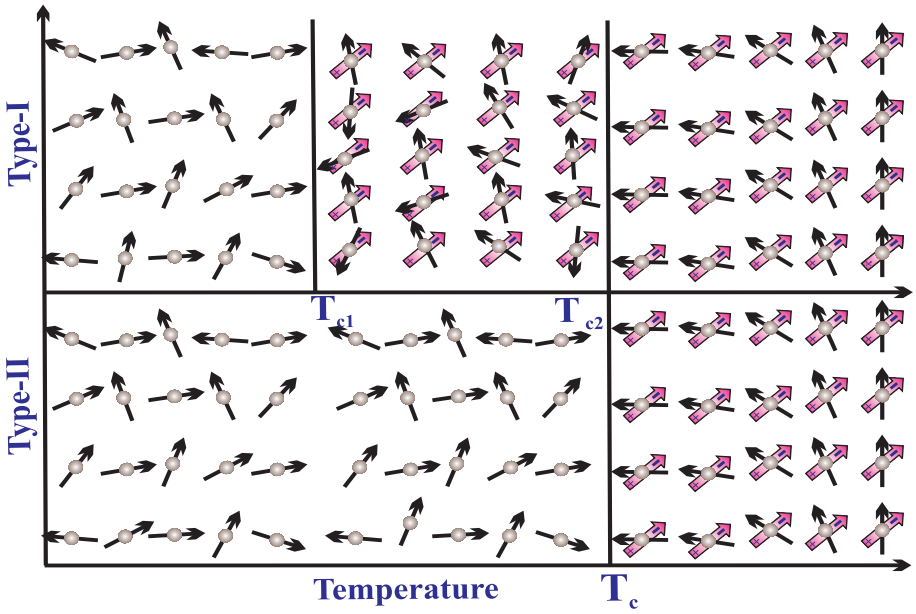

Figure 1.1.2: (a) Schematic diagram of type-I and type-II multiferroics in order to their critical transition temperature.

(d^0), while the partially filled d-shell responsible for the magnetization. The first studied perovskite multiferroic material $(1-x)Pb(Fe_{2/3}W_{1/3})O_{3-x}Pb(Mg_{1/2}W_{1/2})O_3$, where manganese (Mg) and Tungsten (W) driven the ferroelectricity, while d^5 of Fe^{3+} dominates the ferromagnetism [8]. But, the lead (Pb) free research motivates the scientific community to search for new multiferroic materials. The lead free multiferroic materials $BiFeO_3$, $BiMnO_3$, $BiCrO_3$, $TbMnO_3$, $YMnO_3$ plays a significant role to understand the correlation of charge and spin order. The manganites, $BiMnO_3$ and $YMnO_3$ shows effective [FM, FE] and [antiferromagnetic (AFM), FE] ordering, respectively [9, 10, 11]. The chromite based $BiCrO_3$ exhibit considerable multiferroicity [12]. But, the material with good multiferroicity at RT is still challenging and has a lot of grey areas for the researchers.

Under several multiferroic systems, Bismuth ferrite ($BiFeO_3$) is one of the well-controlled RT

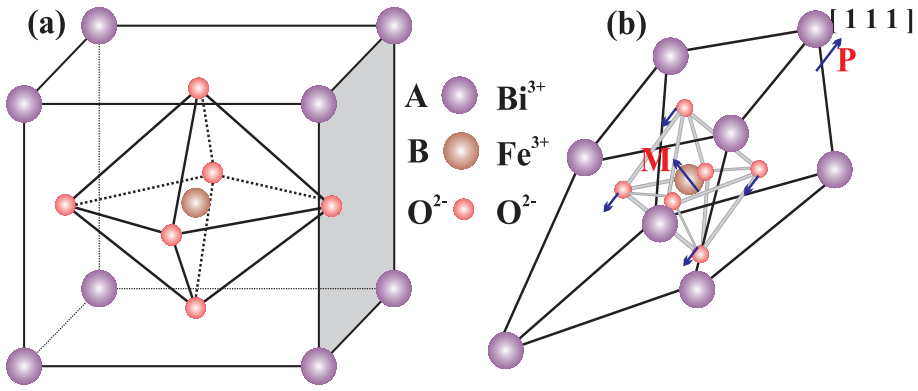

Figure 1.2.1: (a) Schematic diagram of a perovskite structure and (b) distorted rhombohedral perovskite $BiFeO_3$.

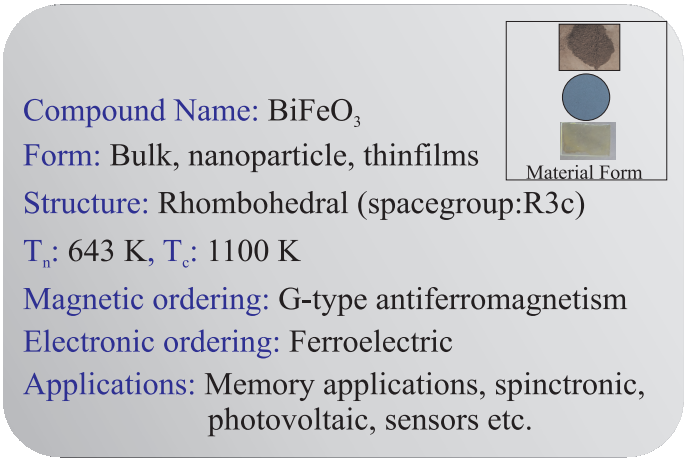

Figure 1.3.1: (a) Multiferroic bismuth ferrite identity.

multiferroic material having distorted perovskite structure, as shown in Fig. 1.2.1 (b). Due to its unique physical properties well above RT, researchers have the primary focus to explore the novel phenomena from the last two decades. In $BiFeO_3$, the FE and FM ordering originated from Bi^{3+} and Fe^{3+}, respectively. As per discussion, the d-shell plays a significant role tuning the electronic and magnetic properties. The present thesis provides the salient features of various d-shell ion modification of multiferroic $BiFeO_3$ helps to achieve the multifunctional materials, which will be briefly explained in *Chapter-3*.

1.3 Bismuth Ferrite ($BiFeO_3$) Identity

Among several multiferroics, Bismuth Ferrite ($BiFeO_3$: BFO) is one of the prototypical multiferroic system that possesses various ferroic orders simultaneously well above RT [6]. The basic information regarding BFO is displayed schematically in Fig. 1.3.1. Due to its unique character, it attracts the researcher for depth understanding, which brought a broad spectrum of potential applications. The presence of many-body effects such as *magnetoelectric (ME) effect, piezoelectric (PE) effect, magnetostriction, ferrotorodoicity, etc.* motivates researchers to urge for developing new concepts. However, due to the presence of high *'leakage current'* and *'spiral spin modulated structure (SSMS)'* of order 62 nm, BFO exhibit poor electric and magnetic properties at RT [13]. Essentially, the oxygen octahedral of rhombohedrally distorted structure plays a crucial role in achieving the various order parameters. In BFO, Bi^{3+} leads to octahedra distortion due to shifting of their cations from the centrosymmetric positions. The oxygen octahedra is a tilted [aaa] system that moves anticlockwise rotation in $[111]_c$ direction [14] at distortion angle $10 - 15^0$ [15].

The existence ferroic orders in multiferroics are already discussed in above section. These ferroic orders are classified into two catagories (i) Primary ferroic orders (individual macroscopic properties) and (ii) Secondary ferroic orders (interplay of two or more macroscopic properties). The primary ferroic orders include ferroelectricity, ferromagnetism, ferroelasticity, etc., while magnetoelectricity, piezoelectricity, magnetostriction, etc. referred as the secondary ferroic orders. The origin of these ferroic orders obtained from the change in Landau free energy [16]:

$$-\triangle F = \triangle P_{(s)i}E_i + \triangle M_{(s)i}H_i + \triangle \epsilon_{(s)ij}\sigma_{ij} + \frac{1}{2}\triangle \epsilon_{ij}E_iE_j + \frac{1}{2}\triangle \mu_{ij}H_iH_j + \frac{1}{2}\triangle s_{ijkl}\sigma_{ij}\sigma_{kl} + \triangle \alpha_{ij}E_iH_j + \triangle d_{ijk}E_i\sigma_{jk} + \triangle Q_{ijk}H_i\sigma_{jk} \quad (1.1)$$

where, ϵ, μ, Q, and d are the magnetic permeability, magnetoelectric, piezomagnetic, piezoelectric coefficient, respectively. *i, j, k, and l* are tensor components. The multiferroic or any ferroic system must have a finite value for any of the term is represented in Equation [1.1]. The prominent ferroic orders observed in BFO are explained as follows.

1.3.1 Primary ferroic orders in $BiFeO_3$

Ferroelectricity

If $\triangle P(s)i$ in Equation [1.1] is finite for at least single pair of orientation states of a crystal, it is said to be ferroelectric (FE). Unlike ferromagnetism, ferroelectricity is very much a 20^{th} century phenomena, was first observed in Rochelle salt by Joseph Valasek in 1920 [17]. Titrate-based $BaTiO_3$ is the most stable FE, which is used for modern transducers and capacitors [18, 19]. In $BaTiO_3$, the FE is driven from the polar distortion of oxygen octahedra $O^{2-} - Ti^{4+}$, which reduces the bond-energy. In recent years, several new FE materials and its mechanisms were investigated. In multiferroics, FE is one of the primary properties, which leads to several scientific phenomena for modern technology.

The ferroelectricity in BFO is considered as RT proper FE (order parameters are proportional to the spontaneous polarization) material. In BFO, the Bi^{3+} ions have a lone pair of electron in their outermost shell. The FE is originated mainly due to the displacement of these lone pair electrons present in stereochemically active Bi^{3+} ion along the [111] direction [Fig. 1.2.1 (b)]. The stereochemical hybridization of lone pair electrons of $6s^2$ orbital with $6p^0$ orbital of Bi^{3+} and $2p^6$ orbitals of O^{2-} ion. The $2p^6$ orbital of O^{2-} ion helps to form BiO covalent bond, which causes the noncentrosymmetric distortion of the electrons cloud and results in FE behavior [20]. The RT ferroelectric ordering of bulk BFO is negligible due to the presence of large leakage current at T_c 1100 K. However, the single crystal system possesses spontaneous polarization (P_s) 6.1 μm^{-2} at very low temperature, which is one order lower than the theoretical prediction [6]. Till now, the BFO based thin-films shows significant P_s of 100 μm^{-2} at RT [21, 22].

The FE properties can be improved by elementary substitution effects [doping (e.g. either at Bi- or Fe-site of BFO) and co-doping (at the both-site of BFO)], fabrication of high-quality thin-film material, etc. Doping with rare-earth Gadolinium (Gd)/Lanthanum (Nd)/Yttrium (Y) at A-site and Manganese (Mn)/Scandium (Sc)/Titanium (Ti) at B-site effectively improved the multiferroic properties of BFO [23, 24, 25, 26, 27]. Also, (Nd-Sc, Y-Sc, Y-Zr, Y-Mn) co-doped BFO system marks significant impact in the field of multiferroic [24, 28, 29, 30]. The FE behavior also depends on the selection of foreign elements according to their availability states. For example, Gd^{3+}, La^{3+}, Y^{3+}, Sc^{3+} ions available only in +3 states, while Mn (+2, +3, +4, etc. states), Ti (+2, +3, +4) are available in various oxidation states. These states helps to manipulate the Fe^{3+} and Fe^{2+} ratio, which in turns suppressing the oxygen vacancies (O_{vs}). The histogram representing the FE properties of few multiferroic based BFO materials is shown in Fig.1.3.2. With Y-Sc co-doping, BFO (current thesis work) exhibit enhanced FE properties in comparison to some of the existence

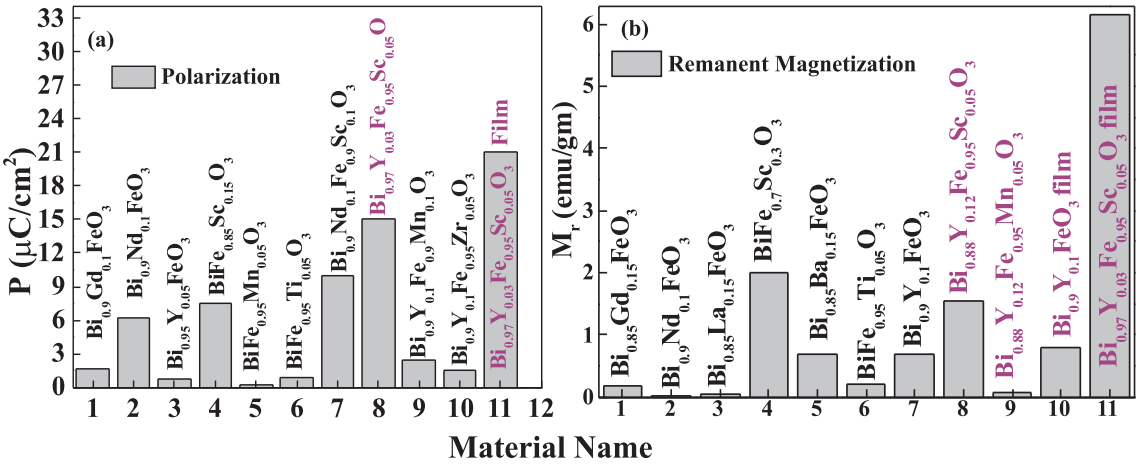

Figure 1.3.2: Comparative analysis of (a) ferroelectric and (b) ferromagnetic properties for some of the well-controlled multiferroic $BiFeO_3$ system.

multiferroic system. The detail of ferroelectricity in non-magnetic modified BFO system is explained in *Chapter-3 and -5*.

Ferromagnetism

If $\triangle M_{(s)i}$ in Eq.[1.1] is finite atleast one pair of domains (for any i), i.e. the two domains differ in their spontaneous magnetization, then the crystal system is termed as ferromagnetic (FM). The ferrimagnetic and weak FM also includes this particular class. The long-range magnetic ordering in materials comes in form of AFM. The magnetic properties are dominated by various interactions like *direct exchange, indirect exchange (superexchange), double exchange*, etc. The term direct exchange refers to the partial exchange of electron orbitals of neighboring magnetic ions. But in many systems this interaction is negligible due to large separation between the ions. There is instead an indirect exchange interaction, also called superexchange interaction, where the magnetic ions mediate through a non-magnetic ion (e.g. O^{2-}). Basically the superexchange interaction relies on the change in bond-distance, bond-angle of the crystal structure. Hence, the structural distortion influence the magnetic structure and vice versa. This interaction between magnetic and structural order is essential for multiferroics as it provides a mechanism that can couple the magnetic structure to other ferroic properties.

The bulk BFO is considered as an AFM system near to $T_N \sim 643\ K$ due to its linear magnetization-field (M-H) hysteresis curve [31]. The spins of Fe^{3+} are coupled ferromagnetically within the $(001)_h$ planes, while the AFM behavior is obtained due to the spin of Fe^{3+} ion propagating along the [1 0 1] direction [32]. The presence of the Dzyaloshinskii-Moriya (D-M) interaction suggests a weak FM behavior, which arises due to the SSMS of order 62 nm [Fig. 1.3.3]. The cycloid spin arrangement nullified the net magnetization, which leads to disturbs the ME effects [33]. There were several argument reported on SSMS by using X-ray photoelectron spectroscopy (XPS), Neutron diffraction, Mossabauer spectroscopy, etc. techniques.

Many reports clasims the elementary substitution effect, BFO in thin film form exhibit low field saturation at RT. Inserting with forign element helps to unlock the SSMS in BFO, which leads to improving the magnetic properties of BFO. Magnetic metal rare-earth (Gd/Nd/La) and transition

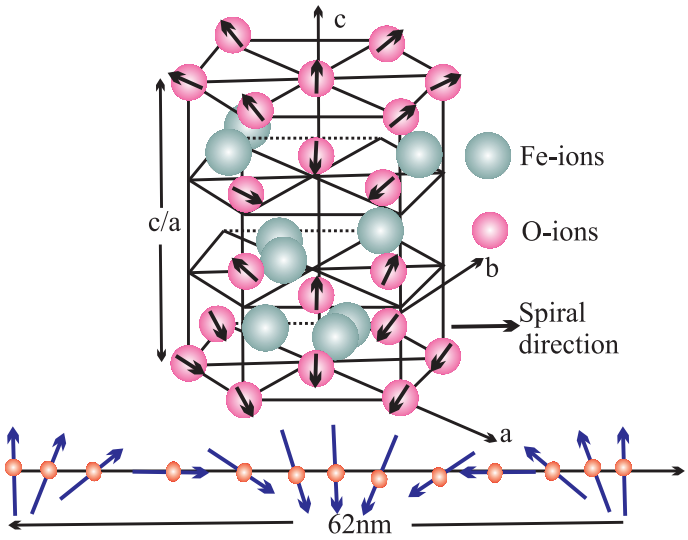

Figure 1.3.3: Schematic representation of spiral spin arrangement of spins in multiferroic $BiFeO_3$.

metal compounds (Sc/Mn/Ti) improves the magnetization of BFO due to superexchange interaction, distortion of oxygen octahedra (FeO_6 in BFO), and appearance of other magnetic interaction form the foreign elements [24, 25, 34, 35, 36, 37, 38]. Divalent compound modified BFO shows significant magnetization due to superexchange, double exchange interaction with other intrinsic effects [39, 40]. Hence, it is clear that the ferromagnetic behavior of multiferroic BFO is controlled by magnetic interaction and controll FeO_6 octahedra. The sol-gel coated and epitaxially grown BFO films successfully saturated at very low coercive field [41, 42]. The histogram for variation in the magnetization of BFO based materials is represented in Fig. 1.3.2 (b). From the Fig. 1.3.2 (b), the non-magnetic Y-Sc (present studied material) have a significant impact on the magnetic properties of BFO, which will explain briefly in *Chapter-3 and 5.*

Ferroelasticity

If at least two domains of a crystal differ in their spontaneous strain ($\triangle\epsilon_{(s)ij}$ in Equation [1.1] is finite), the crystal system is termed as ferroelastic. As the ferroelasticity is controlled by two domains variables, i, j in Equation [1.1], so a small displacement can hamper the crystal structure. Although the evidence for the existence of proper ferroelastic is least and the maximum available ferroelastics are improper [43]. Hence, the possibity of $\triangle\epsilon_{(s)ij}$ may be originated from some other primary defects. Mechanical stressstrain characteristics may verify the change in strain with respect to applied mechanical load only. There are very few reports available for the change in strain with respect to the applied stress in bulk BFO. Wefring *et. al.* observed the linear elastic response in BFO with weak remanent strain and minor strain-stress hysteresis that can be improved by quenching the materials above T_c in the air atmosphere [44]. The ferroelasticity can be induced by modulating either magnetic or electric order through piezoelectric or magnetostriction, respectively. In BFO thin-films, rhombohedral FE polarization is oriented in 71^0, 109^0, and 180^0 direction, while the ferroelastic switching only prefer in 71^0 and 109^0 direction [45].

1.3.2 Secondary ferroic orders in $BiFeO_3$

The resultant order of correlation between any two ferroic orders is termed as *secondary ferroic orders*. The many-body effects such as magnetoelectricity, piezoelectricity, magnetostriction, etc. include in this particular class of ferroic orders. Materials for which the finite terms in Equation [1.1] that are *quadratic* in the external applied fields (E_i, H_i, and σ_{ij}). In contrast to their primary counterparts, these exhibit no difference between domains in their spontaneous magnetization, polarization or strain. They instead differ in their induced magnetization, polarization or strain, when an external field is applied. By applying an appropriate combination of external fields, E_i, H_i, and σ_{ij}, it is then possible to switch between secondary ferroic domains. From a practical perspective, secondary and higher-order ferroics are of significant interest because they often exhibit coupling between properties that would otherwise behave independently. Let's discuss the existence of important secondary ferroic orders in multiferroic BFO system.

Magnetoelectric (ME) Effects

The ME materials possess finite $\triangle\alpha_{ij}$ for no less than single pair of orientation states. In magnetoelectricty, the polarization can be induced either by the application of electric or magnetic field and vise versa [46]; such an effect is termed as linear ME effects. The first multiferroic study perused by Rontgen in 1888, where the multiferroicity or magnetodielectric was neglected [47]. After a few years in 1894, Madam Pierre Currie observed the first-ever possible ME effect in the crystal system under symmetry consideration [48]. The practical ME effect was first predicted by Dzyaloshinskii in 1959 [49] and evident in Cr_2O_3 [50]. A very few reports on the ME effect appeared till the 19^{th} century until the so-called "Revival of the magnetoelectric effect" came into the attention yearly 2000s [51]. The demand for this novel phenomenon is much for the modern scientific community due to its unique properties. Figure 1.3.4 (a) displays the schematic representation of the origin of the ME effect from the charge and spin ordering.

Several ME composites are available that shown a significant ME effect at RT. However, the existence of such an effect in multiferroic materials is still challenging and have a wide scope for research. Till now, BFO is the most prototype multiferroic which possesses properties well above RT. But the weak magnetoelectric coupling (MEC) restricts the possible application, which motivates the researchers to search for new RT multiferroic with high MEC. The manipulation of BFO under the elemental substitutional effect marks lots of attention in the current scenario due to the unavailability of good RT multiferroic. Arya *et. al.* explained the role of In-dopant and its respective size effect enhances the MEC up to 4.92 $mV/cmOe$ [52]. Kolte *et. al.* reported, co-doping with La-Mn improved the magnetic ordering, which leads to enhanced the MEC in BFO under microwave synthesis [$\alpha_{ME:BFO}$: 3.37 mV/cm and La-Mn co-doped $\alpha_{ME:BLFMO}$: 10.11 mV/cm] [53]. Roy *et. al.* obtained longitudinal MEC coefficient (α) for BFO nano-particle is 20.935 [54] and obtained linear ME effects for Co-doped $BiFe_{0.98}Co_{0.02}O_3$, which is well enough for memory, sensor, actuator applications. A statistics of a few available ME multiferroic BFO is represented schematically in Fig. 1.3.4 (b). In the present thesis, we obtained moticiable magnetoelectric coupling (MEC) in Y-Mn/Sc tuned BFO system, which explained in *Chapter-1.* However, BFO exhibits good ME effect either in composite form or under the precise specific conditions [55, 56].

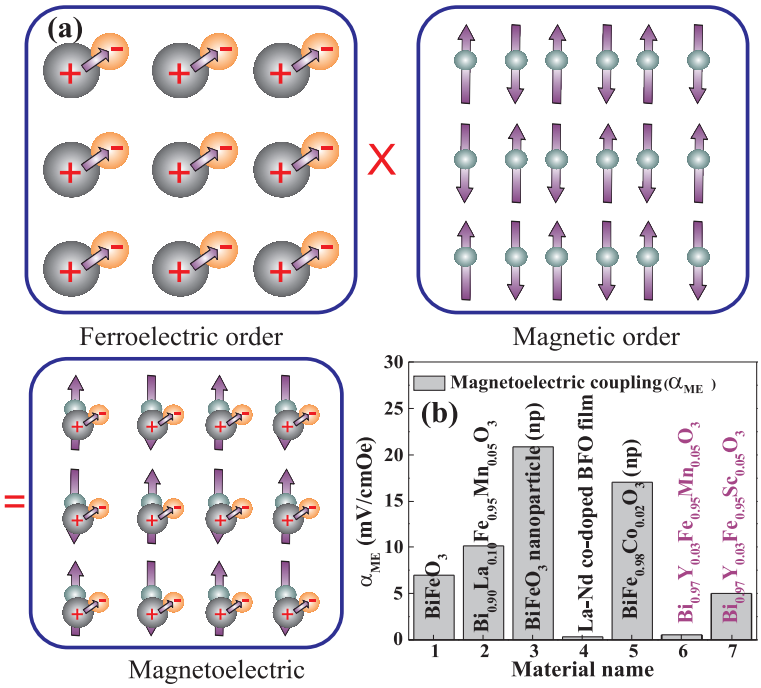

Figure 1.3.4: Schematic representation of interplay between polarization (P) and magnetization (M) leads to magnetoelectric effects, (b) statistical comparison of few ME effect multiferroic BFO.

Piezoelectric (PE) Effects

The variation of induced spontaneous strain under the application of external electric field or bias voltage in material referred as *piezoelectricity*. Materials displays these properties have finite $\triangle d_{ijk}$ in Equation [1.1], i.e. the elements of PE tensors varies between the piezodomains. Thin film materials show appreciable polarization switching as comparison to bulk. The ferroelectric domain switching and its domain evolution play an important role in ferroelectric or piezoelectric materials. For a prototypical ferroelectric, the polarization switching in 180^0 is not favorable due to high-activation energy. Hence, the polarization switching of 180^0 mediates through either 71^0 or 109^0 type ferroelastic switching, which leads to change in the direction of polarization and direction of lattice distortion at 71^0 or 109^0 domain walls [57]. In multiferroics, there is an easy magnetization plane that is always perpendicular to the FE polarization, and the switching of anyone (71^0 or 109^0) changes the orientation of magnetization plane [57]. For example, polycrystalline BFO exhibit 8 possible FE polarization [Fig.1.3.5 (a)] switching angles [71^0, 109^0, and 180^0 (Figs.6.3.7 (b)-(c))] and for ME effect, rhombohedral R3c BFO requires 71^0 or 109^0 type ferroelastic switching rather than FE 180^0 domain switching [58]. The evidence for such phenomena in BFO promises for multistate memory application [59]. Hence, the transient MEC exists during 180^0 domain switching, which is composed of 71^0 and 109^0 switching.

In the bulk BFO system, the existence of PE effect is minimal. Elementary substitution effect and controlling the film thickness helps to improve the PE properties of BFO. Chen *et. al.* explained in his report, the complete F polarization switching is observed in epitaxial BFO thin-film, when the film is thin down to 70 nm [60]. PE properties were improved in Ca-doped by due to structural effect and charge defects of BFO after doping. Simoes *et. al.* reports, Nd-coping induced 71^0 and

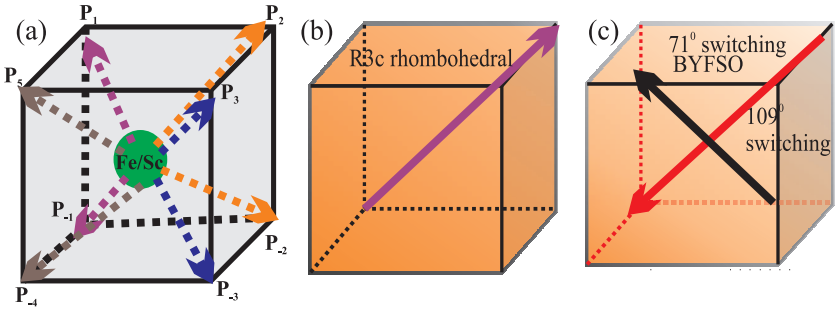

Figure 1.3.5: Schematic representation of interplay between polarization (P) and magnetization (M) leads to magnetoelectric effects.

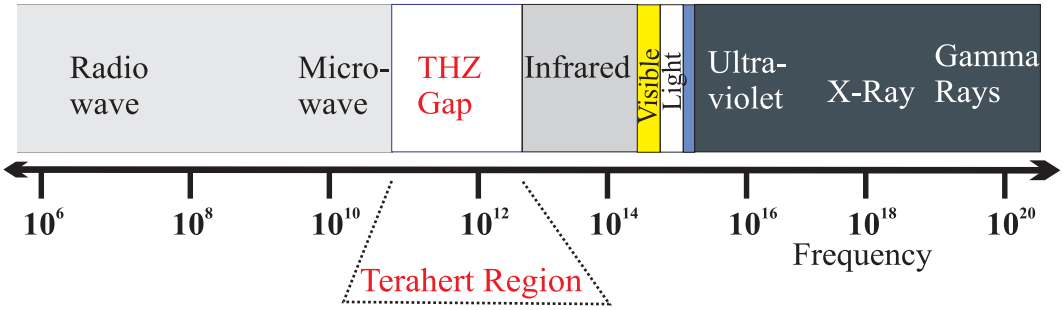

Figure 1.4.1: Schematic representation of terahertz gap in the frequency range.

109^0 domain reversal along with striped-domain patterns oriented along 45^0 [61]. The nano-scale domain patterns were identified in BFO films when grown of (0 0 1) $LaSrAlO_4$ substrate due to the large compressive strains created at the interface between the film and substrate [62]. Seidel *et. al.* reported that the electrical conduction is possible through 71^0, 109^0 ferroelastic domain walls in (1 1 0) BFO thin-film ensures the correlation between the conduction process at domain wall and the strain effects created due to application of voltage [63]. $Co-Pr$ co-doping suppresses 180^0 at the expense of 71^0 and 109^0 type polarization switching, which is useful for memory applications [64]. The non-magnetic $Y-Sc$ co-doping (current thesis work) switched all domains in BFO along 71^0 and 109^0 direction [42]. Another possible way for complete polarization switching under poling with opposite applied voltage biasing [65]. In the present thesis, the piezoelectric effects are studied in detail and explain in *Chapter-5*.

However, to achieve the practical application in BFO, defects like secondary phases, high-leakage current, SSMS, etc. need to overcome. The above discussion suggests, elemental substitution modification and thin-film BFO successfully overcome these defects. Some other possible way to suppress the leakage current and SSMS is thermal quenching, rapid thermal annealing, the materials in thin-film form, etc [66, 67]. In *Chapter-5*, we will explains the creation and manipulation of structural and physical properties in un-doped and do-doped BFO films.

1.4 Field of Terahertz (THz) Spectroscopy

Terahertz (THz) region is the gap between 1 Gigahertz (GHz) to 1 Terahrtz (THz) [Fig. 1.4.1]; 3 mm to 30 μm and required about 4.1 meV energy. The major spectroscopic measurements are carried out

at VIS, UV and NIR range by considering the absorption of light. However, the evidence for major optical phenoemena for materials have not explored due to lack of suitable sources between the THz gap. The available table top sources didn't have the clear resolution and difficulty in optimization. The eigen modes of biomolecules and to study the large mass at single site of molecular study need the THz sources [68]. THz spectroscopy promises to unveil some of the most interesting physics rich phenomena in the solid-state materials. For high-temperature superconducting material, the origin of attractive interaction between the electron is still not clear. The superconductive gap corresponds to the cooper pairs have the width of few meV, i.e. few GHz. Heavy fermion compounds (partially filled f-orbitals) analogous with the conduction band of rare-earth. Due to conduction band, the effective mass of electron is larger than 1000 higher the mass of free electrons [69]. The width of the Drude peak in Heavy fermion compounds lies in range GHz to THz [70]. In multiferroic materials, the magnons carries the electric-dipolemoment i.e. polarization, referred novel phenomenon *electromagnon*. The excitation energy of electromagnon lies in the THz region. The existence of electromagnetic coupling in multiferroics, THz study is utilization.

There is a broad spectrum of applications such detection and quantification of pollution, security, drugs or explosive identification, biomedical, etc. can be achieved under THz. The major problem in THz field is the unavailability of THz sources. Backward-wave oscillators, gun-diodes, quantum cascade laser, free electron laser are successfully achieved THz, but at certain condition [71, 72, 73, 74]. However, the major breakthrough was achieved by laser based THz. The time-dependent (TDS) THz spectroscopy generate upto 10 THz, which is successfully utilize to identify the phase formation, high signal to noise ratio. The continuous wave terahertz spectroscopy (CW-THz) is one of the most youngest and promising technique to study the material systems.

In present thesis, the THz studies performed on un-doped BFO and Y-Mn/Sc co-doped BFO bulk ceramics. The behavior of THz signal in time-domain and frequency domains have been explored at various temperature. Moreover, the calculated complex optical properties of the material provides intrinsic dielectric and conductivity of the materials. The detail information is presented in *Chapter-3*.

1.4.1 Dynamic Magnetoelectric Coupling

The static magnetoelectric coupling (MEC) is briefly explained in the section [1.3.2]. Now lets understand the behavior of MEC away from the static region. The microscopic origin of the MEC is similar for both static and dynamic region explained earlier. But in this system, the order parameters of polarization and magnetization are *oscillatory*. In this section, the concept of *dynamic magnetoelectric coupling* (DMEC) is briefly discussed. The role of *electromagnons* as "carriers" in DMEC is the complex task to explored. Since we are dealing with dynamic effects, it is convenient to prefer the *frequency-domain* [75, 76, 77]. The behavior of order parameters of DMEC can be starts from the static state.

The systems with the absence of MEC, the relation involving polarization (P) and magnetization (M) under the application of electric field (E) and magnetic field (H), respectively are:

$$P = \chi^e E \; and \; M = \chi^m H \tag{1.2}$$

where, χ^e and χ^m are the dielectric and magnetic susceptibilities, respectively. The current density

equation relating to P and H are expressed as: $J_m = \triangle_r \times M$ and $J_e = \partial_t P$, where r and t refers to the space-inversion and time-reversal derivatives, respectively. Two coupling coefficient can be obtained by breaking both r and t, simultaneously [78] and expressed as:

$$P \sim M \times (\nabla_r \times M) \longleftrightarrow M \sim P \times \partial_t P \tag{1.3}$$

Here, the interplay coupled parameters P and M are the spatial divergence and time-dependent of magnetic moments ($\triangle_r \times M$) and polarization ($\partial_t P$). The DMEC expression can be expressed by following the linear MEC in equations 1.1 and 1.2 with some additional perturbations appears at the P and M:

$$P_i^{\omega} = \chi_{ii}^{e}(\omega) E_i^{\omega} + \alpha_{ij}^{\omega} H_j^{\omega} \; and \tag{1.4}$$

$$M_j^{\omega} = \chi_{jj}^{m}(\omega) H_j^{\omega} + \alpha_{ji}^{\omega} E_i^{\omega} \tag{1.5}$$

where i, j are the spatial co-ordinates, and α_{ij}^{ω} is the dynamic magnetoelectric coefficient. P_i^{ω} and M_j^{ω} are the oscillating polarization and magnetization induces by oscillating electric (E_i^{ω}) and magnetic field (H_j^{ω}), respectively.

Electromagnons

The word electromagnons (electro-active magnons) signifies, "the lattice and spin excitation couples the magnetic and dielectric properties" [79]. Basic information regarding spin and lattice excitation has been presented. The possibility of existence of such type coupling first proposed by Baryakhtar and Chupis in 1960 and termed it as "seignette-magnons" [80, 81]. In 1982, they further reported on the excitation of magnons and referred them as "ferroelectromagnon". The first experimental evidence of DMEC observed in $RMnO_3$ by Pimenov in 2006 [79]. They observed the coupling via terahertz transmittance measurements. Theoretical and experimental analysis of $Eu_{0.75}Y_{0.25}MnO_3$ revealing, the spectral wave transfer from low frequency phonon to terahertz magnons [82]. The polarization induced from spin-orbit coupling under helical magnet, which coupled the lattice and spin excitations, hence termed as electromagnons. However, the magnon phonon study can possible on terahertz region. Lets discuss in brief about the field of Terahertz spectroscopy.

1.4.2 Optical properties of solids

Refractive Index ($\tilde{n}$)

Refractive index ($\tilde{n}$) is one of the most important properties of the materials, and expressed in terms of both magnetic and dielectric susceptibility as:

$$N_i, j^{\pm} = \sqrt{\epsilon_{ii}(\omega)\mu_{jj} \pm \frac{1}{2}\{\chi_{ji}^{me}(\omega) + \chi_{ij}^{em}(\omega)\}} \tag{1.6}$$

where the symbols have their usual meaning. When an electromagnetic wave propagate on the refractive index medium, some part of it reflected, some absorbed and rest of it transmitted through the material. The Schematic representation of electromagnetic wave falls on the material is illustrated in Fig 1.4.2. The complex transmittance spectrum T (ω) expressed as:

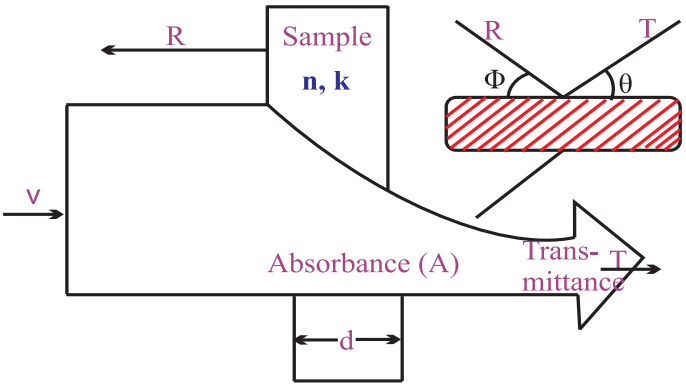

Figure 1.4.2: Electromagnetic wave propagation through the medium for optical properties.

$$T\ (\omega) = \frac{E_{sam}\ (\omega)}{E_{ref}\ (\omega)} = \rho\ (\omega) exp[-i\phi(\omega)] \tag{1.7}$$

where E_{sam} and E_{ref} are the frequency domain signals for reference and samples. $\rho\ (\omega)$ and $\phi(\omega)$ are the amplitude ratio and phase difference, respectively, which can be calculated from the real and imaginary part of $T\ (\omega)$.

For normal incidence, $T\ (\omega)$ can be obtained using transfer function approach [83, 84, 85]:

$$T\ (\omega) = \frac{4\tilde{n}\ (\omega)}{[\tilde{n}\ (\omega) + 1]^2} exp\left(-i[\tilde{n}\ (\omega) - 1]\frac{\omega d}{c}\right) \tag{1.8}$$

where $\tilde{n}\ (\omega) = n\ (\omega) + ik\ (\omega)$ is the complex refractive index (attenuated part of electromagnetic wave), which is the unique property of the material. $n\ (\omega)$ is the refractive index (real part), which indicates the phase velocity. $k\ (\omega)$ is the extinction coefficient, which indicates the amount of attenuation when the electromagnetic wave propagate through the medium. c and d are the velocity of light in vacuum and thickness of the sample, respectively. The detail derivation is presented in somewhereelse [86].

Dielectric Properties

The dielectric properties in the material are responsible due to the several polarization effects (i) interfacial, (ii) dipolar, (iii) ionic, and (iv) electronic polarization. The interfacial and dipolar polarization dominates at extremely low frequency region, while ionic and electronic dominates the dielectric properties at very high frequency region. The complex dielectric constant of the material can be directly measured by using THz spectroscopy. By comparing Equations [1.7]-[1.8] and after some simplification, $n\ (\omega)$ and $k\ (\omega)$ can be expressed in form of $\rho\ (\omega)$ and $\phi\ (\omega)$ as [85]:

$$n\ (\omega) = \frac{\phi\ (\omega) c}{\omega d} + 1 \tag{1.9}$$

$$k\ (\omega) = \frac{ln\left(\rho\ (\omega) \frac{[n\ (\omega)+1]^2}{4n\ (\omega)}\right) c}{\omega d} \tag{1.10}$$

$n\ (\omega)$ and $k\ (\omega)$ helps to determine the velocity of light passed through the medium and absorption coefficient ($\alpha\ (\omega)$), respectively. The relationship between $\alpha\ (\omega)$ and $k\ (\omega)$, is obtained by

propagating the plane electromagnetic waves through the medium as:

$$\alpha\ (\omega) = \frac{2\omega k\ (\omega)}{c} \tag{1.11}$$

The complex dielectric constant can be expressed with the relation $\epsilon\ (\omega)^* = \epsilon'\ (\omega) + i\epsilon''\ (\omega)$, where $\epsilon'\ (\omega)$ is the real part and $\epsilon''\ (\omega)$ is the imaginary part of the complex dielectric constant. The polarization vector $(\overrightarrow{P})$ can be expressed as $\overrightarrow{P} = \epsilon_0[\epsilon\ (\omega) - 1]\overrightarrow{E}$, where ϵ_0 is dielectric permittivity at free space. $\overrightarrow{E}$ is the direction of local electric field. The dielectric constant in term of $n\ (\omega)$ and $k\ (\omega)$ is expressed as: $\sqrt{\epsilon}\ (\omega) = n\ (\omega) + ik\ (\omega)$. After simplification, $\epsilon'\ (\omega)$ and $\epsilon''\ (\omega)$ obtained as:

$$\epsilon'\ (\omega) = n\ (\omega)^2 - k\ (\omega)^2 \tag{1.12}$$

$$\epsilon''\ (\omega) = 2n\ (\omega)k\ (\omega) \tag{1.13}$$

The terahertz measurements in high dielectric materials have significant applications in the field of biomedical, THz imaging, security, etc.

Optical conductivity

The relation involving complex conductivity $[\sigma\ (\omega)]$ and current density $[J\ (\omega)]$ under local electric field is expressed as:

$$\overrightarrow{J}\ (\omega) = \sigma\overrightarrow{E} \tag{1.14}$$

After simplification of Eqs.(1.12)-(1.14), the real part $\sigma'\ (\omega)$ and imaginary part $\sigma''\ (\omega)$ expressed as [85]

$$\sigma'\ (\omega) = \omega\epsilon_0\epsilon''\ (\omega) = 2\omega\epsilon_0 n\ (\omega)k\ (\omega) \tag{1.15}$$

$$\sigma''\ (\omega) = \omega\epsilon_0(1 - \epsilon'\ (\omega)) = \omega\epsilon_0(1 - n\ (\omega)^2 + k\ (\omega)^2) \tag{1.16}$$

The optical conductivity of the material in THz region odeys the empirical power law, MottDavis model, Drude model, or Drude-Smith model [87, 88, 89, 90].

1.5 Resistive Switching and its applications

Resistive switching (RS) refers to the physical phenomena whereby the change of resistance of the dielectric material was observed under the application of strong external electric field. It differs from the dielectric breakdown concept, where the device unable to restore to its original configuration due to the permanent reduction of resistance. The RS process is repeatable and reversible for large number of cycles. In this process, the resistance states maintained for a long-period after the withdrawal of external field. These effects occur in several insulating materials, oxides, chalcogenides, semiconductors, etc [91, 92, 93, 94]. In addition to this, the RS effect also widely studied in oxide materials. The multiferroic films shows effective RS behavior under applied bias electric field. The straightforward application of resistive switching is non-volatile memory (NVM), digital logic applications,

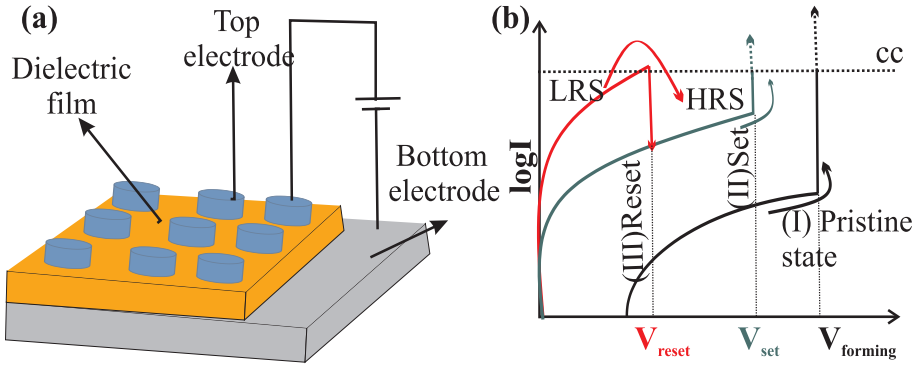

Figure 1.5.1: Schematic representation of (a) resistive memory configuration, (b) origin of pristine, low resistance, and high resistance states.

neuromorphic computing [95, 96, 97]. The $Ag/BFO/FTO$ heterostructure ans $BF/BFTO$ bilayer structure successfully tested for RRAM NVM and digital logic applications [98, 99]. Due to presence of many-order parameter in multiferroics, the RS effect results promises for future multifuctional activities.

1.5.1 Non-volatile memory

The Complementary Metal-Oxide Semiconductor (CMOS)-based memories like flash-memory, DRAM, SRAM, etc. are currently conventional memory technology to store permanent or temporary data in an information processing systems. The memory wall considerably affects the speed gap between the logic and memory [100]. In modern technique, the memory devices requires high-data density, varying speed, and low-cost to optimize the device performance. With CMOS memories are slowly approaching towards its fundamental scaling limit, some novel non-volatile memory (NVM) devices has been proposed to overcome the drawbacks. In last two decades the NVM marks a significant attention in the information technology [101]. Till date, few emerging NV memories are available with high-density, low-cost data storage and ultra-low power computing [102]. Also, additional perturbation like magnetic field, light, temperature provide extra degree of freedom for multifunctional activities in NVM [103, 104]. Flash memory, ferroelectric random access memory (FRAM), resistive random access memory (RRAM), magnetic random access memory (MRAM), phase change memory [105], etc. includes emerging NVM in modern technology. The RRAM devices operates according to the concept of resistive switching and is one of the prime work of the present thesis.

1.5.2 Operation of electric field-induced resistive switching and its classification

The RS effect can be studied by sandwiching a dielectric oxide material between two metal electrodes (capacitor-like configuration), as shown in Fig. 1.5.1 (a). The capacitor-like structure is more convenient due to response of large applied electric field [106] and ease of fabrication. This configuration successfully utilized to examined the practical RRAM applications. However, its difficult to investigate the change in internal structural of the film during RS. For example, in oxide based films the RS process induced in the film due to formation or rupture of oxygen vacancies migrated

conducting filaments between the two metal electrode [107]. Its is difficult to direct observation of the changes occur during the formation of conducting filaments in the films.

The basic operation of an RS device is illustrated in Fig. 1.5.1 (b) under the external bias voltage. In prototypical dielectric, the resistance is very high due to large separation of energy gap ($1 - 4 \sim \ eV$) between conduction band and valence band and the thermal energy at room temperature ($\sim 22\ meV$). Therefore, the pristine state of the device exhibit large resistance i.e. high resistance state (HRS). However, under high applied voltage, the device switch to low resistance state (LRS). The resultant process termed as '*electroforming*', indicate in Fig. 1.5.1 (b) and the voltage require to switch the state is termed as 'forming voltage ($V_{forming}$)'. The limit of flow of current during forming should choose carefully to avoid the dielectric breakdown in the films. To avoid such damage in the films, the maximum value of current need to fixed, which referred as compliance current (cc) [108]. Following forming process, the device back and forth between LRS and a HRS by modulating the external field. During LRS, with increase the external voltage, the device evident a sharp in leakage current at certain voltage and the process is called *'RESET process'* [red line in Fig. 1.5.1 (b)]. The voltage requires to switch the device from LRS to HRS is called RESET voltage 'V_{RESET}'. Similarly, with increase in applied voltage, the resistance of the device switch to HRS to LRS, the process is called '*SET process*' [blue line in Fig. 1.5.1 (b)] and the voltage is referred as 'V_{SET}'. The HRS of the device is typical non-metallic $I - V$ characteristics. The switching between two states is repeatable for several cycles. The change in resistance between HRS and LRS is fluctuating for higher repeated cycles in these memories.

In practical memory operation, the $I - V$ characteristics of the device is more important. HRS and LRS of the device referred '0 or OFF state' and '1 or ON state', respectively, and analogous to the binary state of memory. Depending on the relative polarity (V_{SET}, V_{RESET}), the RS is divided int three category (i) unipolar, (ii) bipolar, and (iii) threshold resistive switching.

Unipolar resistive switching

When the switching operation from HRS to LRS does not depends on the polarity of the bias voltage, such a polarity is called as unipolar resistive switching (UPR), as shown in the Fig. 1.5.2 (a). The switching operation is depend on the choice of insulating material and its interfacial properties and the metal electrodes [109]. Oxide based $Pt/NiO/Pt$, $Pt/TiO_2/TiN$, $Pt/ZrO_2/Pt$, $Ni/HfO_2/TiN$ [110, 111, 112, 113], etc. devices exhibit effective URS behavior. For example, during application of positive bias the device switch to LRS following forming process. Further the device evident a sharp decrease in current at V_{RESET} during reducing the bias voltage, which switch the device LRS to HRS. Typically, the V_{SET} is larger than the V_{RESET}. Note, for URS, the $I - V$ characteristics are symmetric to the external bias voltage. Similarly, during negative applied voltage the SET and RESET process also observed.

Multiferroic based $Pt/BiFeO_3/Pt$ and $BiFeO_3/Pt/Ti/SiO_2/Si$ [114, 115] shows URS behavior for larger number of multiple cycles. However, the later requires higher SET voltage to switch the device.

Bipolar resistive switching

The switching effect is termed bipolar resistive switching (BRS), when the SET process to LRS occurs at one voltage polarity and the RESET process to the HRS at the opposite voltage polarity,

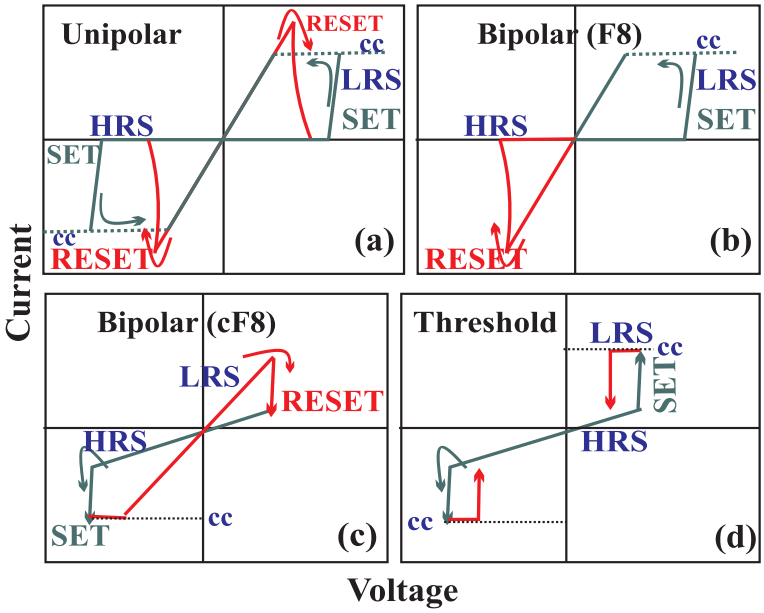

Figure 1.5.2: Schematic representation of (a) unipolar resistive switching (URS), (b) bipolar-resistive switching (BRS) (F8), (c) bipolar-resistive switching (BRS) (cF8), and (d) threshold resistive switching effect in resistive memory.

as shown in Figs. 1.5.2 (c)-(d). If the SET and RESET process observed during positive (+ve) and negative (-ve) bias voltage, such type of BRS referred as '*figure-of-eight (F8)*' bipolar switching. However, the opposite trend is referred as '*counter-figure-of-eight (cF8)*' bipolar switching. WO_x, Al_2O_3, $Sr_Ti_{1-x}Nb_xO_3$ single crystal, $SrTi_{0.99}Nb0.01O_3$ single crystal, $Sm_{0.7}Ca_{0.3}MnO_3$, $Pr_{0.7}Ca_{0.3}MnO_3$, Cr-doped $SrZrO_3$, Pt-dispersed SiO_2 [116, 117, 118, 119, 120, 121, 122, **?**] materials shows BRS behavior. However, WO_x, Nd-doped $SrTiO_3$ [116, 117] based devices exhibit both F8 and cF8 type BRS. The existence of both type of BRS is complected and its physical origin related to its microscopic properties.

Multiferroic based $Ag/BiFeO_3/FTO$ RRAM device shows effective BRS effect with good reproducibility [98]. Wu *et. al.* explained the element insertion reverse the switching direction in BFO after Sr-doping and Ca-Co co-doping [124] i.e. tuning of both F8 and cF8 BRS via elementary substitution effect. Vagadia *et. al.* reports, the switching performance damaged with increase in film thickness of $Bi_{0.8}Ba0.2FeO_3$ [125]. But, increase in Ba-concentration for low-thickness BFO film improves the switching performance significantly. BFO evident both URS and BRS simultaneously after manganese (Mn) doping [126]. In the present thesis, we modulate the switching phenomena of BFO under elemental substitution effect, which may modify the oxygen vacancy stoicheometry.

Threshold resistive switching

Threshold resistive switching refers to the RS phenomena for which, the device exhibit single stable state without any external bias [91]. The schematic representation of such type switching is illustrated in Fig 1.5.2 (d) in form of $I-V$ curve. At SET voltage, the device switches from the HRS to LRS. The LRS is stable over for a certain range of applied biases, and when the applied bias decreases below this range, the device restores to the HRS. Many applications such as electrical

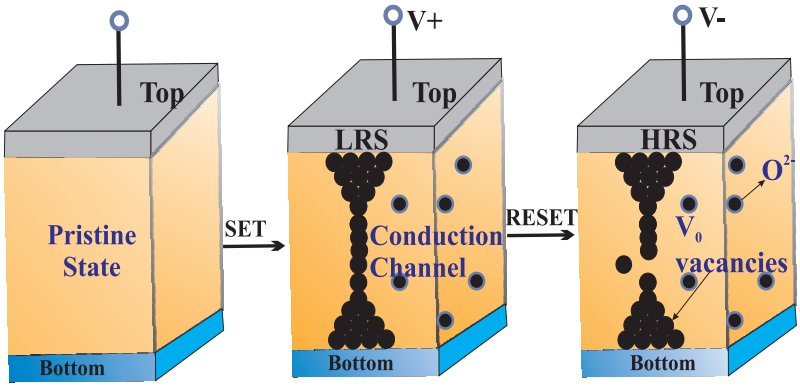

Figure 1.5.3: Oxygen vacancy migrated pristine state, low resistance states (formation of conducting filaments), and high resistance states (rupture of conducting filament).

switches, terahertz naonantennas, memory metamaterial, etc. has been proposed using threshold switching [127, 128, 129].

As the BRS is useful for RRAM NVM application, this thesis have more focus on BRS in multiferroic based resistive memory devices.

1.5.3 Microscopic origin of bipolar resistive switching

Oxygen vacancy migrated conducting filament

As per discussion in the above section, the BRS is polarity dependent i.e. if the SET (RESET) process observed in positive (+ve) bias voltage, the RESET (SET) process must evident in the negative (-ve) region. Extensive study revealed, two charge species oxygen vacancies (O_{vs}) and electrons are plays an important role during switching. The O_{vs} are the point defect under certain thermal equilibrium i.e. the oxides contain O_{vs} upto a certain finite temperature due to the entropic disorder. In various oxide films, the O_{vs} created during electroforming process. Alternatively, elemental insertion method is an effective approach i.e. Gd-doped CeO_2, Y-doped ZrO_2, and Ca-doped BFO creates O_{vs} in films [130, 131]. The O_{vs} are positively charges defects. During the application of +ve sweeping voltage (V_+) to the top electrode (Fig.1.5.3) to the device configuration, the O_{vs} moves towards the cathode and the oxygen ions (O^{2-}) moves towards the anode. The resultant ionic motion which is parallel to the applied electric field forms a conducting filament channel between the top and bottom electrode, which switch the device to LRS or ON state. Similarly, during -ve sweeping voltage (V_-), the O^{2-} combines with the electrons, which leads to rupture the conducting filament and device restores to HRS. The schematic representation of formation and rupture in oxide based RRAM devices is displayed in Fig. 1.5.3. Disorder interfaces and grain boundaries effect have prominent effect during oxygen migration.

Trap/detrap of electrons during switching operation

The electron transport in RRAM devices dominated by trapping and detrapping of electrons due to defects. The transport mechanism under these process is usually described by three conduction models: space-charge limited current (SCLC), PooleFrenkel emission (P-F emission), and trap-assisted tunneling. Theses models shortly summarize as follows:

(1) The P-F emission conduction model deals with the thermally assisted trapped electrons. The thermal fluctuation provides sufficient energy to the trapped electron to knockout from the localized state to conduction band [132]. The trapped electron move freely in the crystal until trapped by the other localized states. The $I-V$ characteristics follows the relation $I \sim Vexp(V^{1/2})$. For $ITO/LaAlO_3/SrTiO_3$ and Cr_2O_3 films, the P-F emission dominate the conduction mechanism [133].
(2) The SCLC model is considered when the injected charge carriers are dominated over the free charge carriers present in the oxide films. At low voltage region, the thermally generated charge carrier concentration is larger than the injected charge carrier concentration and evident linear $I-V$ curve. However, with increase in voltage the injected charge carrier concentration dominates the thermally generated charge carrier concentration [134]. The $I-V$ characteristics has a non-linear relationship as $I \sim (V^n)$, $n > 1$. With further increase in voltage, the electrons starts to be trapped in the defects and when all the traps are filled in defects, the injected charge carriers moves through the entire film. Ca-doped $LaMnO_3$ and TiO_2 films exhibit trap controlled SCLC conduction process [135, 136].
(3) In trap-assisted-tunneling model, the electrons are tunneled between successive traps via hoping [137]. The $I-V$ characteristics follows the relation $ln(I/V^2) \sim I/V)$. The RS effect in $TiN/HfO_x/Pt$ device is controlled by trap-assisted tunneling model [138].

In some RRAM devices, the electrical transport is dominated by '*Schottky barrier emission*' conduction models. The Schottky barrier is created at metal-oxide interface due to difference in work-function, which causes a current rectification. The barrier is conducting during forward biasing, while behaves insulating during reverse bias. Due to the thermionic emission between the dielectric layer and an electrode, the electrons are unable to cross the barrier. Hence, to continue the conduction process, the electrons requires sufficient energy to cross the barrier. The $I-V$ characteristics follows the relation $ln(I) \sim V^{1/2})$. The above models utilize to simulate the experimental results obtained from the device. The detail mechanism of all models is explained in some other review articles and books [139, 140].

However, for multiferroic BFO films the conduction process varies with foreign elemental substitution. The Ce-Mn co-doped BFO, Mn-doped BFO, Ba-doped BFO films exhibit SCLC process are reported [126, 125]. $Nb-STO/BFO/SRO$ nanocapacitors modeled as p-n junction diode [142]. The conduction process in Y-doped BFO device controlled by both SCLC and Schottky emission model [**?**].

1.5.4 Effects of additional perturbation on resistive switching

Most RRAM devices controlled by the electric or voltage response. However, with the development of technology, the requirement of multifunctional device is the desire for the modern community. Disciplines like multiferroic (MF), spintronics, etc. deals with both electrical and magnetic phenomena. Application of extra perturbation such as magnetic field, light, temperature etc. provides additional degree of freedom for achieving the multifunction [**?**, **?**]. The resistance states of TiO_2 and Si-based RRAM devices successfully tuned under the influence of external magnetic field [**?**, 104]. The appreciable modulation of resistance states can be achieved under the light in $Pt/CeO_2/Nb:SrTiO_3$ based resistive device [**?**].

As multiferroic materials exhibit many coupling parameters such as MEC, PE effects etc., which

helps the RRAM device for multifuction activities under external perturbation. The RS effect in multiferroic films under magnetic field not explored much, hence this thesis will introduce some of the important aspects, which is still not explored in multiferroic based RRAM devices.

1.6 Motivation

Multiferroic $BiFeO_3$ (BFO) [rhombohedral: R3c] is well studied system for last three to four decades. Still the synthesis of single phase BFO bulk system is challenging. The single phase BFO achieved under several conditions like ambient temperature, thermal quenching, pressure control etc. The d-shell ions are responsible for ferroelectricity and ferromagnetism. Elementary insertion method i.e. doping or co-doping by rare-earth or transition elements helps to achieve single-phase structure along with improved ferroelectric and ferromagnetic properties of BFO. We manipulate the BFO under various d-shell ions, to achieve multifunctional behavior of the multiferroic material. The existence of many-body effects such as magnetoelectric effect, piezoelectric effect, magnetostriction, etc. is not only useful to understand the underlying physics behind it but also promises for potential applications (non-volatile memory, solar cell, etc.) for modern community. The existence for magnetoelectric coupling evident in some of doped BFO. However, the role of electromagnon in ME effect, whose excitation lies in THz range, is not explored much and have many space for research. In rhombohedral ferroelectric, the 180^0 polarization switching is mediated through 71^0 and 109^0 ferroelastic type switching. The stable polarization switching through different stages will be useful for multilevel memory applications, which promises for future neuromorphic applications. The modern technology demand for multifunctional applications and to fulfill such a requirement, the availability of stable multifunctional is desired.

Summary

The thesis is organized as follows:
In *Chapter 2*, the experimental techniques used for sample preparation and the characterization technique used to investigate the properties is briefly introduced.
In *Chapter 3*, a brief discussion on synthesis process, structural, magnetic properties of un-doped and non-magnetic Y-Sc/Mn modified BFO ceramic is presented. A detail explanation of role of magnon at extremely low frequency region and terahertz region is presented.
In *Chapter 4*, the variation of dipolar polarization in multiferroic Y-Sc/Mn modified BFO ceramics discussed in detail by frequency dependent dielectric study at various temperature.
In *Chapter 5*, a brief discussion on synthesis process, structural, magnetic properties of Y-Sc modified BFO films is presented. The effect of elemental substitution on ferroelectric polarization briefly introduced.
In *Chapter 6*, the role of elemental substitution effect and applied external magnetic field on resistive switching of BFO based RRAM device briefly explained.
In *Chapter 7*, the overall conclusions are summarized and various suggestions proposed for the future work.

Chapter 2

Experimental Techniques

2.1 Introduction

In this chapter, we discuss the various experimental techniques that we used to prepare un-doped and co-doped $BiFeO_3$ (BFO) materials and to characterization them. The bulk ceramics were synthesized by the conventional solid-state reaction route, while sol-gel spin coating techniques were used to grow thin-films. The structural characterizations of bulk ceramic and thin-film materials, the powder X-ray diffraction (XRD), and Grazing Incidence X-ray Diffraction (GIXRD), respectively, were used. Field-effect scanning electron microscope (FESEM), atomic force microscope, magnetic force microscopy (MFM), piezoforce microscopy (PFM) were used to characterize the inherent microstructural properties. Optical properties have been explored using Raman, UV-Vis-NIR, terahertz, X-ray photoelectron spectroscopy (XPS), photoluminescence (PL) techniques. The magnetic measurements performed under the vibrating sample magnetometer (VSM) and superconducting quantum interference device (SQUID). Dielectric properties and electrical properties were carried out using LCR-meter and P-E loop tracer, respectively. The C-V measurements were carried out using an ultra-precision capacitor bridge. The experimental techniques used for bulk and thin-film characterization are summarized in Fig. 2.1.1. The multiferroic based RRAM devices were fabricated in thin-film materials. The resistive switching behavior of the device was studied under the magnetic field (electromagnet unit) by using 2400 and 4200 Keithley source meters.

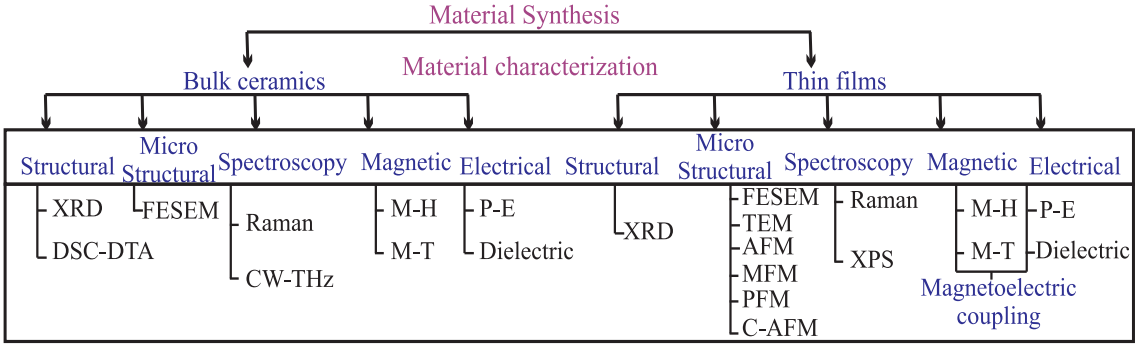

Figure 2.1.1: Characterization techniques used to explore the properties of bulk ceramics and thin film materials.

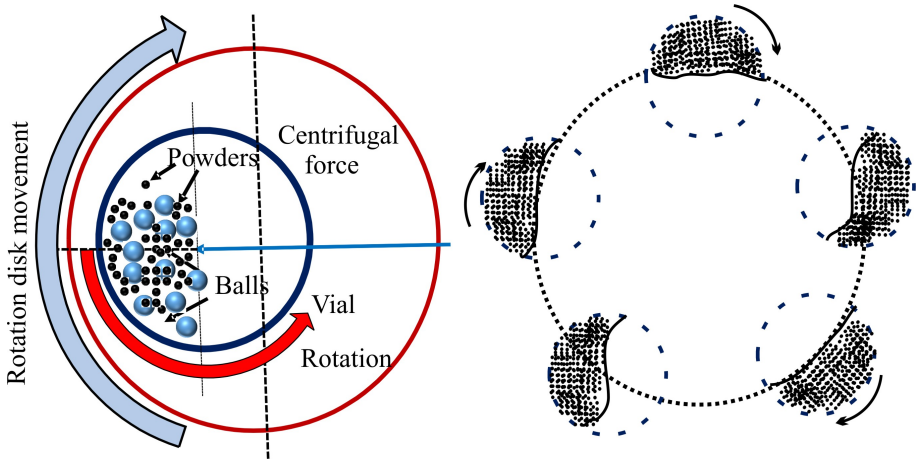

Figure 2.2.1: Schematic representation of working principle of high-energy ball milling technique.

2.2 Material synthesis

2.2.1 Solid-state reaction route

The solid-state route is one of the most widely used methods to synthesize the complex polycrystalline oxides using starting precursor raw powders in stoichiometry amount [143]. The raw precursor powders don't react together at normal room temperature (RT) over standard time scales and only formed the amorphous phases at low temperatures. Hence, for the proper phase formation, high synthesis temperature in the range of $900 - 1500^0$ C is required. At high temperatures, the ions of the starting precursor diffuse with appropriate molecular interaction, which leads to desired phase formation. The physical diffusion between the precursor powders depends on the atmospheric condition, structural properties of the reactants, area of contact between reacting solids, reactivity, and the change in thermodynamic free energy accompanied by the reaction. For manual mixing of starting reactants, usually, agate mortar and pestle are utilized while for mechanical mixing, the high-energy ball milling technique can be useful. The mixed powders were pressed into circular pellets to produce high-density ceramics after heat treatment (calcination and sintering).

For controlling the particle size, density, proper molecular level mixing, composition with minimum man-power, we adopted the high-energy ball milling technique over the mortar, and pestle grinding. The solid-state route is one of the low-cost material synthesis techniques.

High-energy ball milling technique

The ball-milling technique is one of the simplest methods to prepare the samples from the metals and alloys in the form the powders. This method is quite easier and versatile than the traditional grinding method for high-temperature synthesis bulk ceramics and nano-particles. The milling method was carried out with different apparatus e.g., attritor, planetary mill, or a horizontal ball mill. In contrast, planetary ball milling is a most frequently used due to small amount sample requirement. The laboratory used a planetary ball milling system consists of a vial, tungsten or zirconium ball and one turn disk. For milling, the powders or mixed powders are placed in a vial and are subjected to high-energy collision from the balls. The size of the vial depends on the quantity

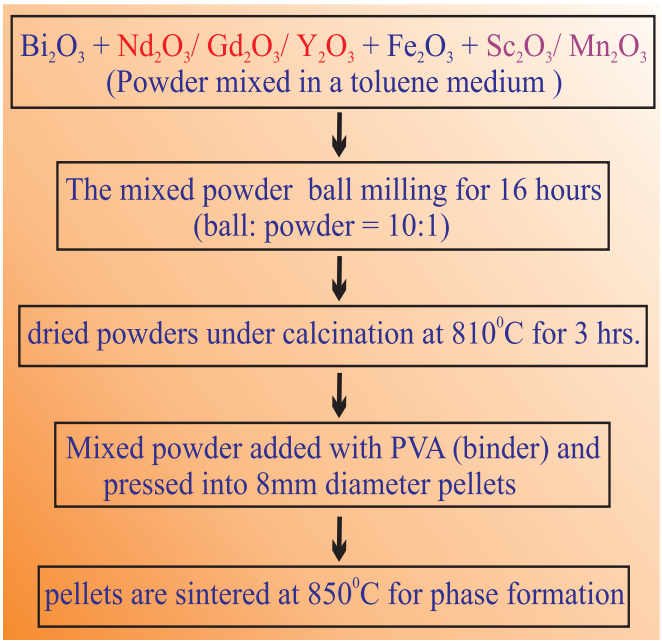

Figure 2.2.2: Flowchart for ceramic sample preparation through high-energy ball milling technique.

of interest. The effective of milling is reduced if the vial is more than half-filled. The vial needs to be closed with the tight lid. Sometimes, the vial is filled with air or inert gas to avoid impurities. The hardened tungsten carbide balls are put in the vial along with the powders in a proper ball to powder ratio (10:1). The 6 mm balls were used to restrict the particle size in the micrometer range. The low-temperature cooling system sometimes used to avoid dissipate heat energy during high rpm rotation. However, in our synthesis method, we use 250 rpm, which didn't require any cooling system. The vial is rotated in hundreds of rpm around its own axis and adds to some central axis, hence called 'planetary ball milling'. The turning disk and the vial is rotating in the opposite direction, which causes centrifugal forces around the vial axis shown in Fig. 2.2.1. These centrifugal forces are applied to the powder mixture and milling balls, which crushes the particles up to the nanometer scale. Figure 2.2.1 represents the motions of the milling ball and the powder. The energy of milling balls exhibits 40 times higher than the energy due to the gravitational acceleration, which can be used for high-energy milling. The material synthesis process is performed through (a) initial stage, (b) intermediate stage, (c) final stage, and (d) completion stage [144]. The flowchart for all substituted BFO ceramics sample preparation is given in Fig. 2.2.2.

2.2.2 Thin-film fabrication using sol-gel spin coating

Spin coating is one of the most common and low-cost uniforms thin-film fabrication method. Last few decades, it has considerable interest in both scientific and industrial sectors due to its several advantages over the other existing techniques. The sol-gel process is a low-temperature process, which leads to less energy consumption during synthesis. The molecular level mixing between the precursor ions is well controlled in comparison to the conventional solid-state route. By taking the sol-gel, it is possible to obtain the powders in the nanometer scale or even thin films. This route best synthesizes the oxide-based materials. We used low-cost with higher purity (99%) nitrate

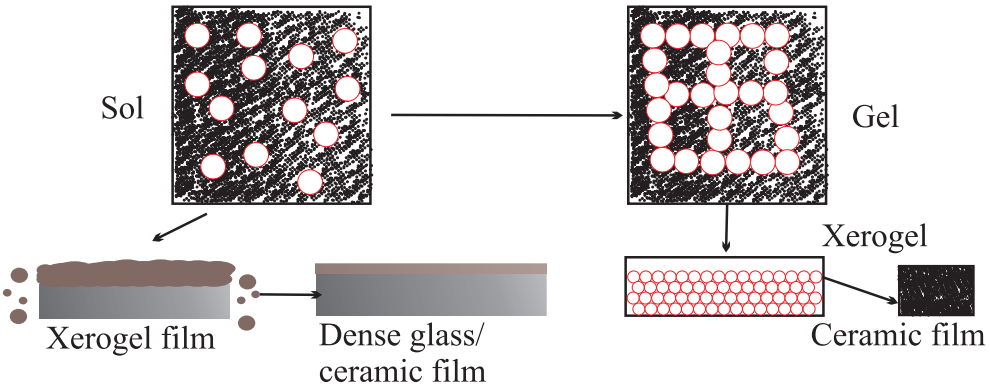

Figure 2.2.3: Processes for thin film fabrication using spin-coating technique.

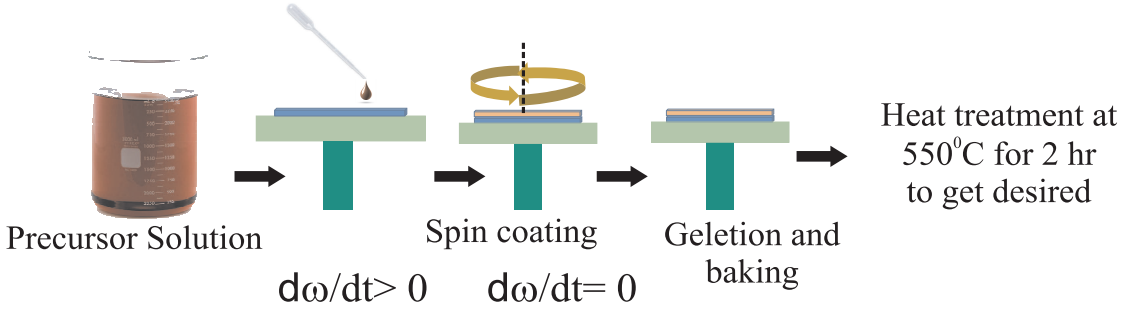

Figure 2.2.4: Processes for thin film fabrication using spin-coating technique.

compounds as starting precursors for this process. In spin-coating, the solution is spread evenly over a substrate using the centripetal force. The substrate accelerates to final radial velocity. The film coating depends on the velocity at which the wafer is spinning and the viscosity of the fluid. The spin-coated film baked for a few minutes to get the desired film. The schematic representation of thin-film deposition using the spin-coating technique is shown in Fig. 2.2.3 [145]. This method has extensive use in nanotechnology and microelectronics for effective device fabrication [146]. Our studied sol-gel coated grown films effectively utilized for RRAM device and solar cell applications.

In present work, the $BiFeO_3$, Y-doped $Bi_{0.90}Y_{0.10}FeO_3$, Y-Sc co-doped $Bi_{0.97}Y_{0.03}Fe_{0.95}Sc_{0.05}O_3$ films were deposited on either glass or Fluorine doped Tin Oxide (FTO) coated glass substrates. The sol-gel was prepared by using the chemical route. The detail synthesis process for film fabrication is illustrated schematically in Fig. 2.2.4.

2.3 X-Ray diffraction

X-ray diffraction (XRD) technique extensively used to study the crystallographic phase and structure of the materials. It is a non-destructive technique and also provides information about even an unknown compound [147]. In the present thesis, we used regular incident XRD (RIXRD) to analyze bulk ceramics while the GIXRD technique used for thin-film materials. The working principle of XRD is illustrated in Fig. 2.3.1 (a) [148]. In RIXRD [Fig. 2.3.1 (b)], the [source, sample plane] and [sample plane, detector] simultaneously swept. However, in GIXRD [Fig. 2.3.1 (c)], the angle between the [source, sample plane] is fixed at 1^0 with varying the angle between [sample plane,

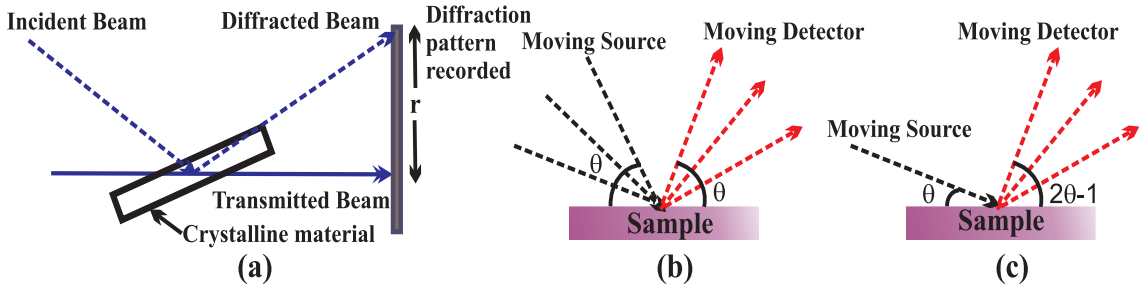

Figure 2.3.1: (a) XRD, (b) regular incidence XRD, (c) Grazing incidence XRD.

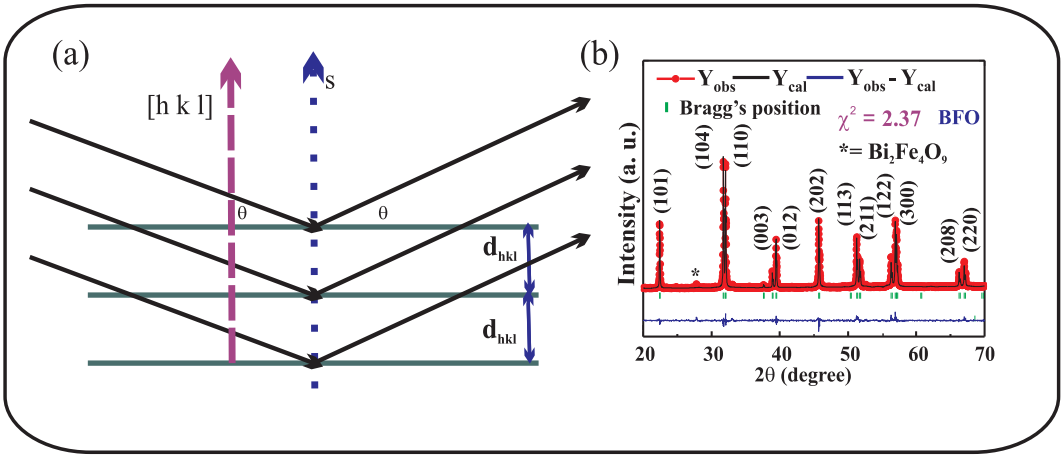

Figure 2.3.2: (a) Schematic representation for origin crystal planes from various Bragg's angle during X-ray diffraction measurement and (b) Rietveld refinement for $BiFeO_3$ ceramic.

detector]. But the total angle between source and detector in both systems is 2θ.

The powder XRD manifests the principle of Bragg's law, as displayed in Fig. 2.3.2 (a). The interaction between the incident ray and the sample with a parallel plane produces a constructive interference pattern only when the path difference is an integral multiple of the wavelength (λ). The expression relates λ, and the lattice spacing (d) of the compound is:

$$n\lambda = 2d_{hkl}sin\theta,\ n \geq 0 \tag{2.1}$$

where n is an integer. For the RIXRD, one condition need to satisfy: n=*1*. However, for GIXRD two criteria: (i) $n = 1$, (ii) the angle between the (hkl) plane and wafer surface plane= $(\theta - 1)$ are important. The diffraction peaks corresponding to the various d_{hkl} planner spacing were obtained by using $\theta - 2\theta$ scanning mode.

In the present work, the $10 - 90^0$ Bragg's angle was used and scanned for one hour. In this mode, the X-ray source was fixed, whereas the material was rotated about an axis that was perpendicular to the plane containing the source and detector. In general, from the diffraction pattern, the crystal structure, and the symmetry of the contributing phase can be determined. The detail working principle and other information for the XRD technique is explained somewhere else [147].

Reitveld refinement of experimental XRD results

Rietveld refinement is a theoretical simulation approach to verify the experimental XRD diffraction patterns. This method is widely used due to the computational method, uses the complete spectrum, provides information about impurities, fast calculation, and quantitative phase analysis. Rietveld refinement technique helps to understand the structural confirmation and phase purity of a compound. The refinement is based on the least square method [149]:

$$M_{in} = \sum_{i=0}^{n=1} [W_i (Y_{obs\ i} - Y_{calc\ i})^2] \tag{2.2}$$

where the symbols have their usual meaning. $Y_{calc\ i}$ can be expressed as:

$$Y_{calc\ i} = \sum_{ph=1}^{phases} [S_{ph} \Sigma (K_{hkl} \left| F_{hkl}^2 \right| \phi_{hkl} (2\theta_i - 2\theta_{hkl}] \tag{2.3}$$

Before start the refinement, the Wykoff positions of the individual atoms, lattice parameters, crystallographic angle, peak shape, and the structural model need to be known. The various stages of rietveld refinement are (i) initial known structure, (ii) background point correction, (iii) unit-cell dimensions refinement, (iv) zero point correction, (v) refine peak shape, (vi) atomic coordinates and (vii) thermal parameters. The background correction needs to refinement after each stages. Finally, the goodness of fitting (χ^2) provides the closeness of fitting [149]. The fitting criteria for the refinement are depends on the factors:

Profile factor:

$$R_p = 100 \times \left[\frac{\sum_{i=1,n} |y_i - y_{c,i}|}{\sum_{i=1,n} y_i} \right] \tag{2.4}$$

where y_i, $y_{c,i}$ are the observed and calculated points, respectively. 'n' represents the number of data points. The Weight profile factor:

$$R_{wp} = 1000 \times \left[\frac{\sum_{i=1,n} \omega_i |y_i - y_{c,i}|}{\sum_{i=1,n} \omega_i y_i^2} \right]^{\frac{1}{2}} \tag{2.5}$$

where $\omega_i = \frac{1}{\sigma_i^2}$, σ_i^2 is the observation variance of y_i. The Expected weight factor:

$$R_{wp} = 1000 \times \left[\frac{n-p}{\sum_{i=1,n} \omega_i y_i^2} \right]^{\frac{1}{2}} \tag{2.6}$$

where n and p are the total number of experimental and refined data points, respectively. The difference between (n-p) represents the number of degree of freedom. Finally, the reduced chi-square factor:

$$\chi^2 = \left[\frac{R_{wp}}{R_{ex}} \right]^2 \tag{2.7}$$

In the present thesis, we have refined the powder XRD patterns of all synthesized ceramics using

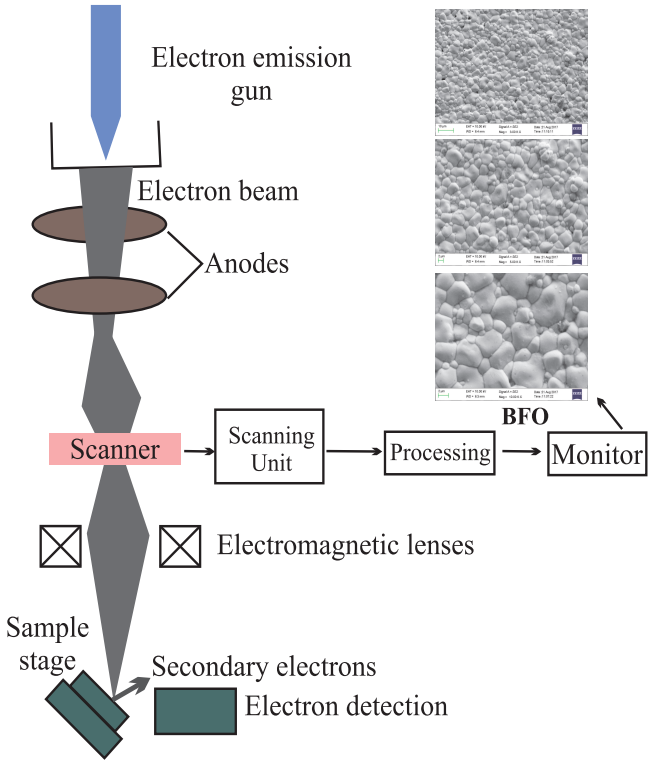

Figure 2.4.1: Schematic diagram of FESEM technique and the scanned topography images of BFO ceramics at 3X, 5X and 10X.

Fullprof software. The PCR file was created by using Wykoff positions, crystallographic angles, lattice parameters, background points, etc. to perform the refinement. The Pseudo-Voigt function is used to perform refinement for all samples. The model overall line broadening is expressed as:

$$FWHM^2 = U\tan^{\theta} + V\tan\theta + w \tag{2.8}$$

where the symbols are their usual meaning. During the refinement, the global parameters like lattice parameters, half-width parameters, scaling factors, and the coefficients of background polynomial were mainly adjusted. In addition to this, the atomic coordinates, occupancy, thermal parameters (B_{iso}) also changed during refinement. The chemical occupancy for oxygen (O) was taken as 1 during the refinement. For example, we presented a refined XRD spectra of $BiFeO_3$ ceramics in Fig. 2.3.2 (b). The line (black), line-symbol (red), represents the calculated and observed spectra. The blue line represents the difference between the observed and calculated spectra, which leads to perfect fitting. With such good advantages, this method has some common problems such as (i) background not well fitted, (ii) missed peaks, (iii) peak shape displays the poor description, etc.

2.4 Microscopy Techniques

2.4.1 Field-emission scanning electron microscope (FESEM)

Field-effect scanning electron microscope (FESEM) is a useful technique to investigate the topographical and elemental information of the materials at higher magnification. Compared to conventional SEM, FESEM produces high-quality images, large focus-depth, high-resolution (HR), and easy sample preparation. The working principle of FESEM illustrated schematically in Fig. 2.4.1 [150]. The electrons emitted from the electron emission gun penetrate the surface of the sample and generates numbers of low energy secondary electrons (SE). The intensity of the SE is governed by surface topography. The surface micrograph image is developed by optimizing the SE intensity as a function position of the primary electron beam. For example, the FESEM micrograph of BFO ceramics is presented in Fig. 2.4.1 with various depth resolution. The atomic and molecular weight percentage of present elements also can be extracted.

In addition to this, it is also used for back-scattered electrons (BSE) imaging and Energy Dispersive X-ray (EDX)analysis for chemical analysis of the elements present in the sample. The intensity of BSEs collision can identify the atomic number of the element within the selected volume, and a qualitative elemental distribution can be revealed.

In the present thesis, FESEM measurements are carried out on gold (Au) coated ceramics and thin films (due to dielectric behavior of the materials) with various resolutions. In addition to this, EDX analysis also performed on all present studied materials.

2.4.2 Transmission Electron Microscope (TEM)

Transmission Electron Microscope (TEM) is ideally used for investigative the materials in nanoscale at very HR, which is more significant than 0.5 nm. TEM is more convenient than the conventional optical microscope, where the resolution and magnification are much higher. As the name suggests, a beam of the electron is transmitted through the ultra-thin sample. The electrons of very high energy are used to pass through the number of electromagnetic lenses. The various components and their basic working principle are illustrated in Fig. 2.4.2. The electrons generated from the electron guns are interacting with the matter of the specimen, results in a magnified and focused image are produced at the imaging device, such as the fluorescent screen. The developed high-quality image is detected by a sensor called the CCD camera. The sample preparation for thin-film material is tedious than a nanoparticle.

In addition to this, TEM has the advantage that one can identify the structural analysis and chemical composition of the specimen by using diffraction patterns. The variation of lattice parameters and defects of the sample can be obtained from the observed fringes of high-resolution TEM (HRTEM). The SAED pattern of TEM is used to identify the existing planes in the sample and degree of crystallinity. During the TEM measurement of nano-powder and thin-film multilayer heterostructure, the sample preparation is essential [145]. For example, the TEM image of BFO, the lattice fringes obtained from HRTEM, and the diffraction pattern of the SAED pattern is present in Fig. 2.4.2.

In the present thesis, the TEM images of un-doped BFO and its associate doped/co-doped films were studied using TEM (Jiol TEM 2100). HRTEM and SAED pattern imaging were performed

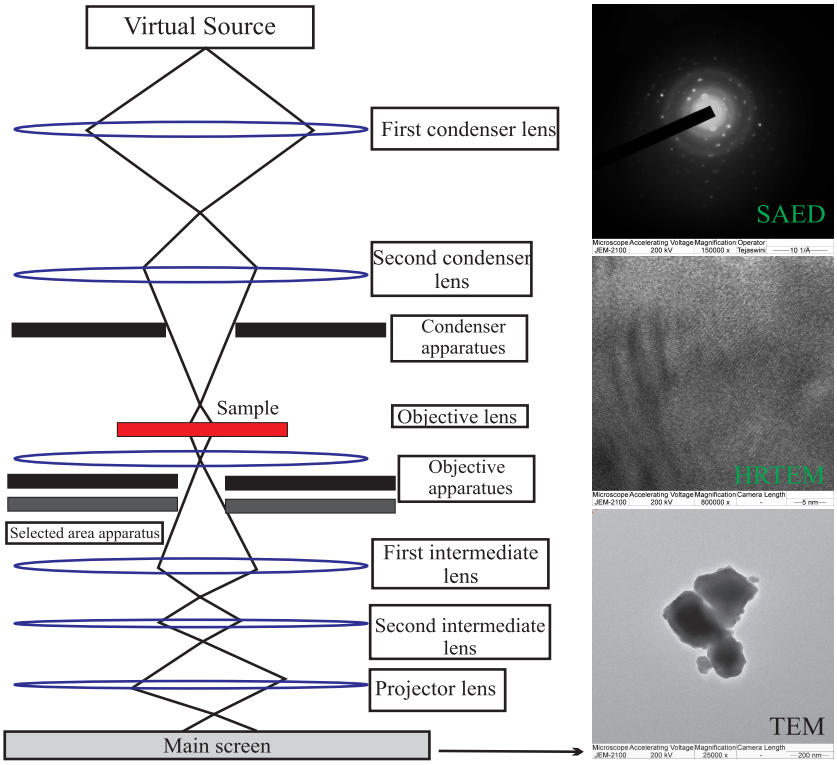

Figure 2.4.2: Schematic representation of working principle of TEM technique and the scanned images (TEM, HRTEM,and SAED) of BFO film.

on materials. Due to the micrometer size, the bulk ceramics were not considered for the TEM measurement in this thesis.

2.4.3 Atomic Force Microscope

Atomic Force Microscope is a very high-resolution microscopy tool use for the nanoscale probe to over a surface. As the name suggests, it measures the forces acting between the cantilever tip and the sample. The force between the two atoms at a very close distance is:

$$F(R) = \frac{A}{R^x}\hat{r} + \frac{B}{R^y}\hat{r} \tag{2.9}$$

F is the resultant force, A, B, x, and Y are constant, and R is the distance between two atoms. $\hat{r}$ is the unit vector. The first term of the equation is the repulsive force between the two atoms, which is more prominent at a very short distance and varied rapidly with R due to the Pauli exclusion principle. The second term is termed as an attractive force. Due to high-depth resolution, this technique gathers the intrinsic topographic information. The combination of force measurement and spatial resolution makes the atomic force microscope a versatile microscopy technique. The schematic representation of an atomic force microscope system with its various components is shown in Fig. 2.4.3 (a). It measures the sample topography by monitoring the deflection of the cantilever in Z-direction. Photo-detector will send the signal as an image and constructed at the monitor screen. The main advantages of the atomic force microscope over scanning tunneling microscope (STM) is

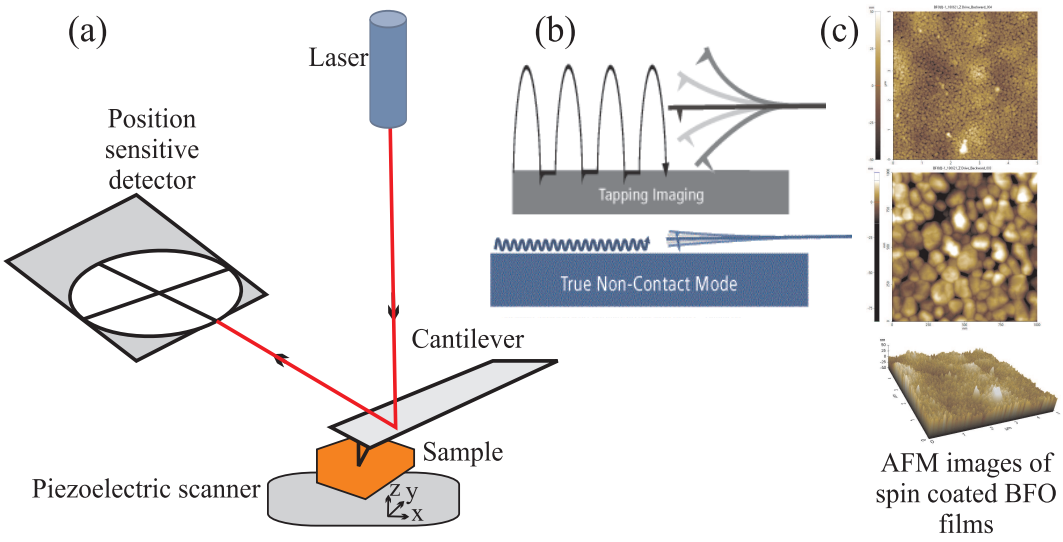

Figure 2.4.3: (a) Schematic representation of working principle of AFM technique, (b) tapping and non-contact mode in AFM, and (c) scanned AFM images of spin coated BFO film.

the former can only demonstrate for non-conducting samples [151, 152]. The surface roughness and root mean square roughness of films can be recorded.

The AFM can operate in three modes such as (i) contact mode, (ii) tapping-mode, (iii) non-contact mode (NCM) [Fig. 2.4.3 (b)]. The present studied films were investigated by using the PARK NX10AFM system in NCM operation. The recorded atomic force microscope images (both in 2D and 3D) of $BiFeO_3$ film at various scanned area is displayed in Fig. 2.4.3 (c).

2.4.4 Magnetic Force Microscope (MFM)

Magnetic Force Microscope (MFM) is a sensitive technique that images the spatial variation of magnetic forces on the material surface. MFM is widely used for studying the surface magnetic properties of the magnetic materials and operate in NCM. This technique is quite similar to the atomic force microscope, only for the tip of the former coated with the ferromagnetic layer to detect the magnetic properties. The schematic diagram of the MFM technique is shown in Fig. 2.4.4 (a) [153].

In the present thesis, MFM measurement has been performed on sol-gel coated $BiFeO_3$ films and its associate doped/co-doped films to track the surface magnetic properties. The lift height between sample and tip during measurements was used 50 nm. The low moment sensitivity magnetic probe LM-MFMR was used during measurements. The scan MFM image of spin-coated BFO films presented in Fig. 2.4.4 (b). The scanned signal evident in-plane magnetization in all studied films.

2.4.5 Piezo Force Microscope (PFM)

Piezo Force Microscope (PFM) is a type of atomic force microscope that allows scanning and manipulation of piezoelectric (PE) or ferroelectric (FE) domains. The FE domain modification can be achieved by bringing a sharp conductive tip into contact with an FE surface and applying an ac bias signal to the tip to excite the deformation of the material through converse piezoelectricity. The resulting deflection of the tip cantilever is detected at the photodiode detector and again de-

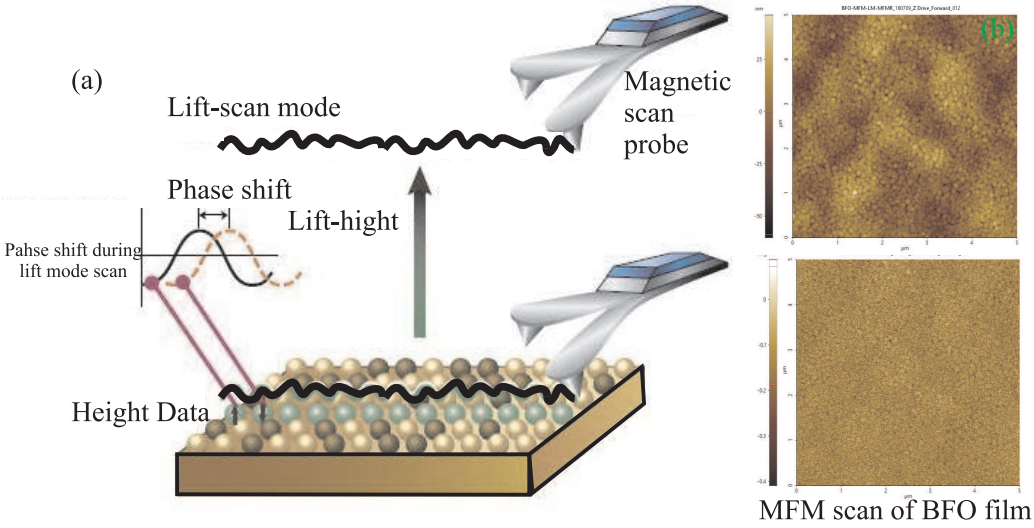

Figure 2.4.4: (a) Schematic representation of working principle of MFM technique in NCM, (b) scanned MFM images of spin coated BFO film.

modulated by using a lock-in-amplifier. In this process, PFM generates topography and FE domain up to an high-resolution simultaneously. The working principle is quite similar to the conventional atomic force microscope. The PFM imaging is possible in both in-plane (IP) and out-of-plane (OP) mode simultaneously and represented schematically in Fig. 2.4.5 (a)-(b) [154]. This technique has an advantage in measurements of phase-voltage and amplitude-voltage "butterfly-like" curves. The generated strain (d_{33}) with the response to the voltage signal can be demonstrated.

In the present thesis, the PFM imaging in both IP and OP-mode was performed for un-doped BFO and doped/co-doped BFO film by using NX10 AFM (Park) and Bruker system. The amplitude-voltage or phase-voltage measurements also investigated. The domain switching behavior for the Y-Sc co-doped BFO film was studied with the poling effect by applying the opposite bias voltage. The scanned images of PFM is presented in Fig. 2.4.5.

Besides these microstructural analysis, conducting atomic force microscope (CAFM) was carried to understand the conductivity of the films. During CAFM measurements, current mapping and its $I-V$ characteristics were recorded simultaneously.

2.5 Spectroscopy techniques

2.5.1 Raman spectroscopy

Raman spectroscopy is regarded as the figure-print of the materials and is used to observe the vibration, rotational, and low-frequency phonon modes in the material. When a monochromatic light probe on a material, it may reflect, absorbed, or transmitted. Raman spectroscopy based on the scattering technique and provides the structural and chemical information of the molecule. A coherent laser source is used to irradiate the sample. The maximum radiation scattered elastically, called Rayleigh scattering. A minimum portion scattered inelastically, composed of Stoke and anti-Stoke. The inelastic anti-Stoke portion particularly provides the information in which we are

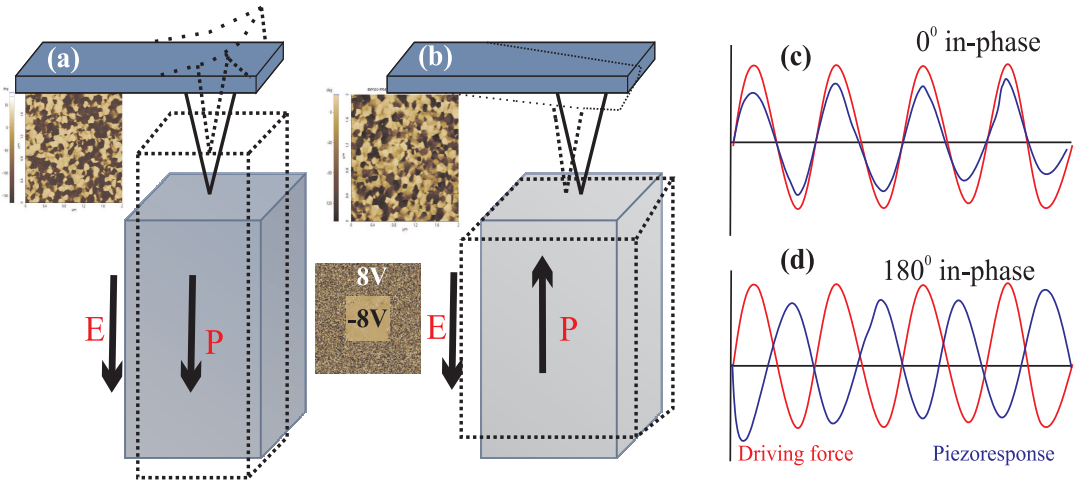

Figure 2.4.5: Schematic representation of cantilever movement during (a) in-phase, (b) out-of-phase piezoresponse with respect to driving voltage, and its respective signal (c) in-phase, and (d) out-of-phase.

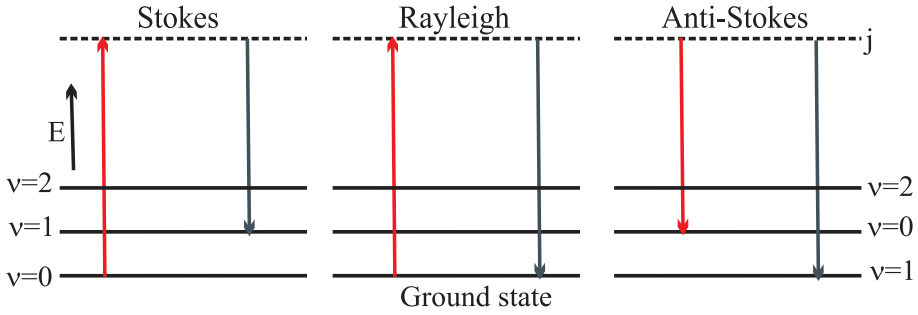

Figure 2.5.1: Schematic representation of energy-level diagram of the Raman scattering.

interested [155].

During the experiment, the monochromatic light knocked out the molecule from the lower energy level to a higher energy level and returned to the initial state by releasing a photon with three various frequencies. (i) Rayleigh scattering: $\nu_{emmitted\ photon} = \nu_{incident\ radiation}$, (ii) Stoke scattering: $\nu_{emmitted\ photon} < \nu_{incident\ radiation}$, and (iii) anti-Stoke scattering: $\nu_{emmitted\ photon} > \nu_{incident\ radiation}$. The energy-level diagram of the Raman scattering is presented schematically in Fig. 2.5.1. Essentially, these frequencies lie in the ranges associated with rotational, vibrational, and electronic level transitions of the molecular system. The scattered radiation usually consists of polarization characteristics different from those of the incident radiation. The scattering occurs overall directions, and both the intensity and polarization of the scattered radiation depend on the direction of observation. Through Raman spectroscopy, one can obtain structural information such as bond vibrations or various modes that would arise due to structural distortion in the compound.

In the present thesis, Raman spectra of both bulk ceramic and spin-coated thin films were recorded at RT using a Laser Micro Raman spectrometer (Bruker, Senterra, $\lambda = 532\ nm$, power= 10 mW). The technique was useful to understand the structural distortion in BFO after doping/co-doping.

2.5.2 Terahertz (THz) spectroscopy

Terahertz spectroscopy is one of the most trending research areas in current science and technology. This technique rapidly involving medical imaging, security, communication, and the manufacturing industry. Non-availability of THz generator, detector, and stable femtosecond (fs) laser source restricts the application of THz. However, the researchers trying to overcome these problems and can utilize it in a full-fledged manner in the next ten years. The THz spectroscopy is considered as another technique for material characterization by using optics technique. The continuous-wave terahertz (CW-THz) is the new and youngest field in the THz field. It is based on the photo mixing technique, and have greater resolution than THz time-domain spectroscopy, where the material properties are probed with short pulses of THz radiation [156, 157, 158]. The CW-THz consists of two NIR fs lasers which employed to generate heat signals. The generate heat converted to THz radiation inside the photo mixer. This leads to phase formation and allows to the determination of both real and imaginary part of the complex optical function, according to the expression:

$$I_{ph} \propto E_{THz} \tag{2.10}$$

where I_{ph} and E_{THz} are the photo-current and THz energy of laser radiation. The advantages of CW-THz are the broad, accessible frequency range, frequency selectivity, and much higher resolution over conventional THz sources and on the way to becoming a powerful spectrometer. The working principle of CW-THz is representing schematically in Fig. 2.5.2 (a).

THz spectroscopy is a versatile technique to understand the magnon and phonon behavior of multiferroic (MF) materials. The distribution of properties under various frequencies is displayed in Fig. 2.5.2 (b). In MF, the magnon carries the electric dipolemoment, and this excitation is called electromagnon, whose excitation energy lies in the THz range. The coherent magnons and acoustic phonons of MF are excited and probed at RT using fs laser. The excitation creates a magnon oscillation at 15 GHz, which supports the presence of DzyaloshinskiiMoriya (D-M) interaction, which has energy 0.31 MeV. The existence of magnetoelectric coupling in MF materials can be studied by THz radiation. Their are limited reports exist on THz study of MF $BiFeO_3$ materials [159, 160].

In the present thesis, we performed CW-THz spectroscopy to understand the complex optical properties of un-doped and non-magnetic Y-Sc co-doped $BiFeO_3$ compounds on 0.8 mm thick pellets. The air is taken as a reference during measurements. The THz amplitude curve as a function of frequency for BFO, BYFMO, and BYFSO ceramics is shown in Fig. 2.5.2 (c).

2.5.3 X-ray photo-electron spectroscopy (XPS)

X-ray photoelectron spectroscopy (XPS) is popularly known as the Electron Spectroscopy for Chemical analysis (ESCA) and based on the photoelectric effect. This technique widely used to investigate the chemical composition of the materials. Other properties such as chemical shift, valence band, Auger peas, satellites, plasmon loss, multiplet splitting, spin-orbit splitting of the materials can be understood by using XPS. The detail working principle of XPS technique is explained else were [145, 161]. The information about the binding energies can be recorded, which further useful for chemical information.

In the present thesis, the XPS is used for thin-film materials to understand the role of oxygen vacancies and variation in elemental composition and the ions of $BiFeO_3$ film after foreign ion

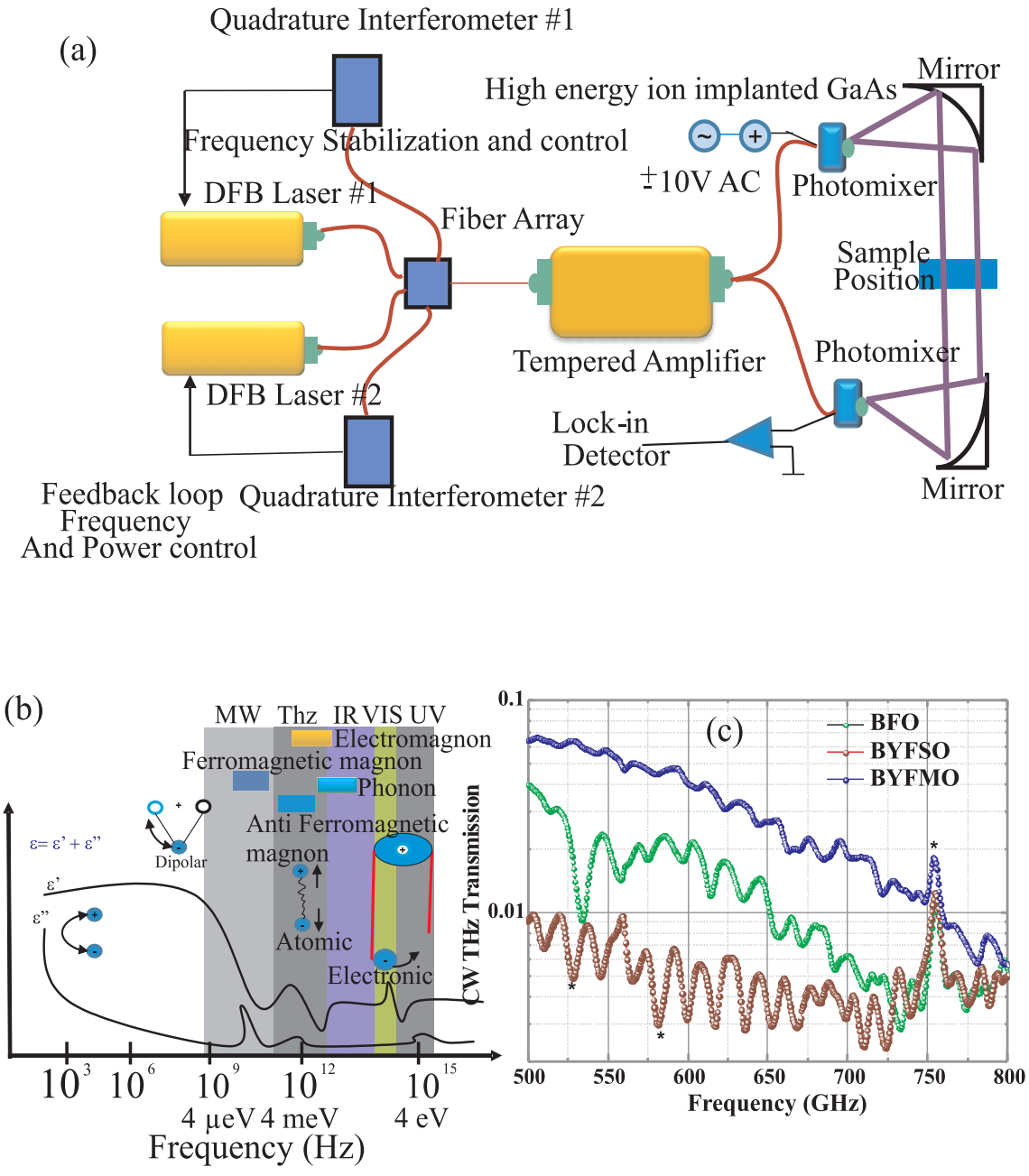

Figure 2.5.2: Schematic representation of (a) CW-THz spectrometer technique (b) material behavior at various frequency range.

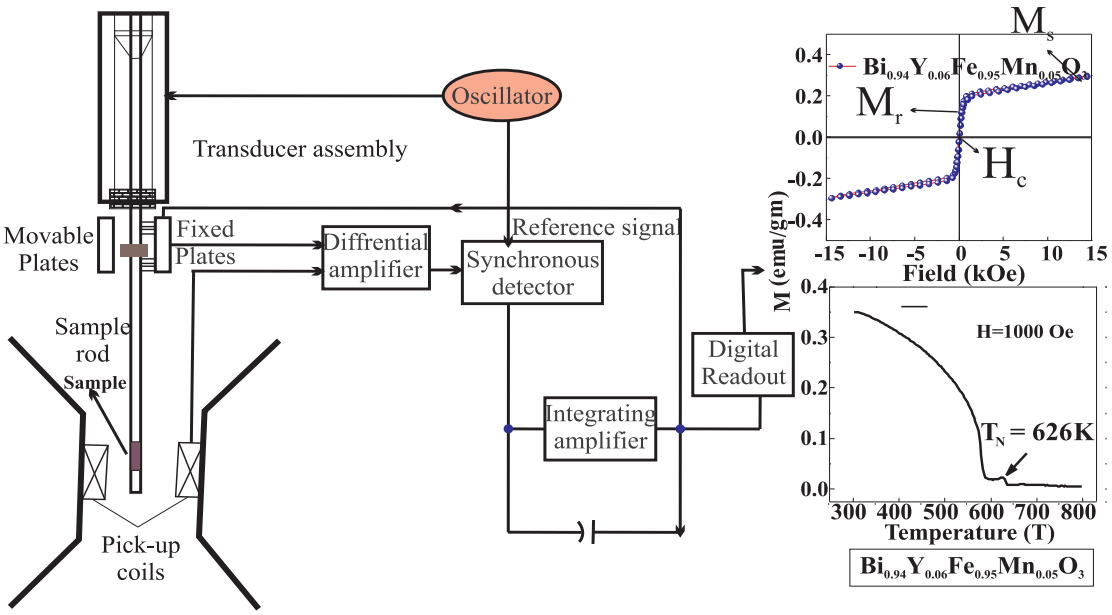

Figure 2.6.1: Schematic diagram of VSM and magnetization measurement of $Bi_{0.94}Y_{0.06}Fe_{0.95}Mn_{0.05}O_3$ ceramic.

insertion.

2.6 Magnetic measurement techniques

The magnetic measurements of present studied ceramic and thin-film materials were investigated under the vibrating scanning magnetometer (VSM) and superconducting quantum interference device (SQUID).

2.6.1 Vibrating scanning magnetometer (VSM)

Vibrating scanning magnetometer (VSM) is a versatile and sensitive technique to measure the magnetic moment of the magnetic materials at very high precision. This technique is based on the principle that an oscillatory magnetic field (H) can be created by vibrating the magnetic materials (Faraday's laws of magnetic induction). The magnetization (M) of the sample can count by applying a uniform H. The induced manipulation in the H is detected by the pick-up coils. The applied H is quite high, but being constant is not searched by the coils. Notably, the uniform magnetic field is not constant but modulate smoothly so that induced M in the material as a function of various fields can be recorded. The schematic representation of VSM is displayed in Fig. 2.6.1. In standard VSM, a large electromagnet with 0 to 1.5 T is used. This method widely uses for detecting the magnetization of powder, single-crystal, or thin films. VSM also allows measuring the magnetization as a function of temperature, crystallographic orientation, and magnetic field strength precisely. The complete mechanism of the working principle of VSM is found elsewhere [162]. The disadvantages of this technique are self-demagnetization, size, indispensable, and limited field.

In this thesis, the VSM (ADE Technologies USA, EV7 VSM) was used to determine the magnetization as a function of field (M-H hysteresis) and temperature (M-T) of modified BFO bulk and

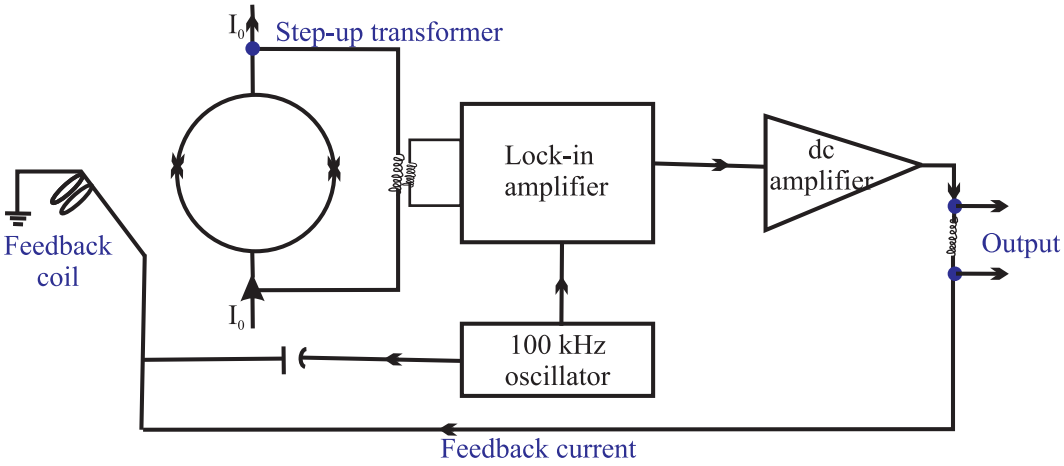

Figure 2.6.2: Schematic representation of SQUID magnetometer [163].

thin film with maximum applied field 1.5 T. For example, the M-H and M-T curve for bulk Y-Mn cod-oped $Bi_{0.94}Y_{0.06}Fe_{0.95}Mn_{0.05}O_3$ ceramic is shown in Fig. 2.6.1. The magnetic properties of all compounds extensively studied in detail in chapter 3, chapter 4, and chapter 5 of the present thesis.

2.6.2 Superconducting quantum interference device (SQUID)

SQUID magnetometer is used to precisely count the extremely small magnetic field changes and based on the theoretical concepts of the Josephson effect. It measures magnetic flux induced from the magnetic moment and output voltage signal, which is a periodic function of a flux holing a superconducting loop in which one or two weak links are inserted. The single-junction SQUIDs are called RF-SQUIDs, while double junction SQUIDs coined as DC-SQUIDs. For our samples, we used the DC-SQUID magnetometer technique. The DC-SQUID applies current slightly larger than the critical current, and voltage drop can be monitor across the device [163, 164]. The working mechanism for DC-SQUID is represented schematically in Fig. 2.6.2.

In the current thesis, the magnetization measurements for thin films fabricated in the spin-coating technique as a function of magnetic field and temperature by using SQUID. M-H hysteresis loop for Y-doped BFO films was carried out precisely at a maximum applied field of 1 T. Field-cooling (FC) and zero-field cooling (ZFC) measurements were performed in the temperature range of 10-300 K at 100 Oe.

2.7 Electrical measurement techniques

2.7.1 Ferrolectric Polarization

The ferroelectric properties (P-E hysteresis loop) of bulk ceramics and thin-films were studying using a P-E loop tracer. For P-E measurement, the pellets were coated with silver paint on both sides to make a capacitor like structure. The measurements were carried out under a dielectric medium (Si-oil) to avoid the break-down of the pellets in the high applied field. The schematic of P-E measurement is displayed in Fig. 2.7.1 (a). The P-E loop of bulk ceramics was investigated

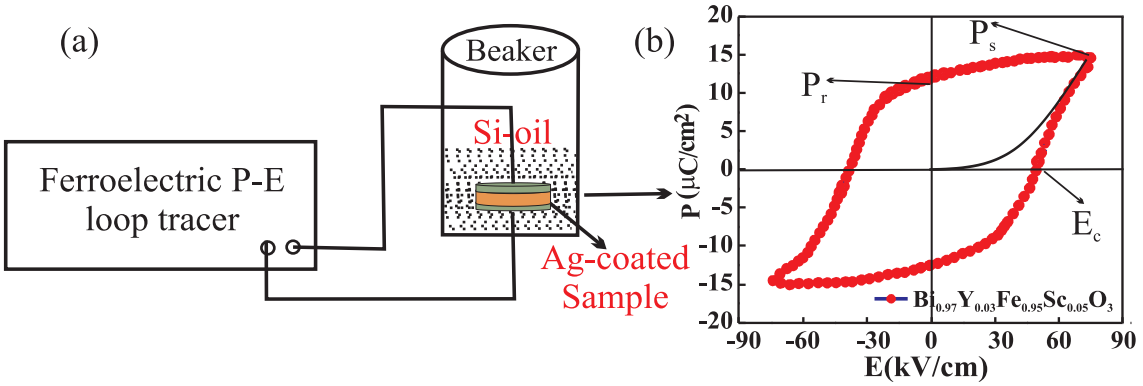

Figure 2.7.1: (a) Schematic representation of P-E measurement set-up and the obtained (b) P-E hysteresis loop for $Bi_{0.97}Y_{0.03}Fe_{0.95}Sc_{0.05}O_3$ ceramics.

with an applied electric field of 85 kV/cm at 50 Hz. However, for thin-film material, the applied field and frequency are 85 kV/cm at 30 Hz, respectively considered. The P-E hysteresis loop for $Bi_{0.97}Y_{0.03}Fe_{0.95}Sc_{0.05}O_3$ ceramic is shown in Fig. 2.7.1 (b). The details regarding ferroelectric properties are explained in the coming chapters.

2.7.2 Dielectric measurement

The dielectric measurements were carried out using an LCR Novo-control system. This system is used to measure the dielectric properties precisely as a function of frequency and temperature. The principle arrangement of dielectric compounds measurement is represented schematically in Fig. 2.7.2 (a). Like P-E, for dielectric measurement, the pellets of thickness 0.5 mm need to coat with the silver of either side. The material is placed between two circular plates to act as a capacitor structure display in Fig. 2.7.2 (b). A generator is used to apply a sinusoidal ac voltage $U(\omega)$ of frequency $\frac{\omega}{2\pi}$ to any of the plate and the current $(I(\omega))$ generated in the sample is determined at other plate [165]. The current vector measure both current amplitude (I_0) and phase shift (ϕ) of the current signal as a function of voltage. The calculations between voltage, material properties, and current leads to the calculation of capacitance, which further determine the dielectric constant (ϵ) by the expression:

$$\epsilon^* = \epsilon' - i\epsilon'' = \frac{C_s^*}{C_0} \tag{2.11}$$

where symbols have their usual meaning.

In the present thesis, the frequency modulation dielectric properties were studied at various temperatures ranging between $30 - 210^0$ C for all studied ceramic samples in a wide frequency range 1 Hz-1 MHz. For our studied samples, the diameter and thickness of the pellets were taken 8 mm and 0.5 mm, respectively. The high thickness may lead to small capacitance and is difficult to measure precisely. However, for thin-film materials, the room temperature frequency variation dielectric measurement was carried out. During dielectric measurements, the impedance, modulus, conductivity of the ceramics also investigated, which are explained in detail of *Chapter-4*. In addition to this, the empirical Cole-Cole, Nyquist plot fitting by EIS impedance analyzer, Jonscher's power law, was used to simulate the experimental results.

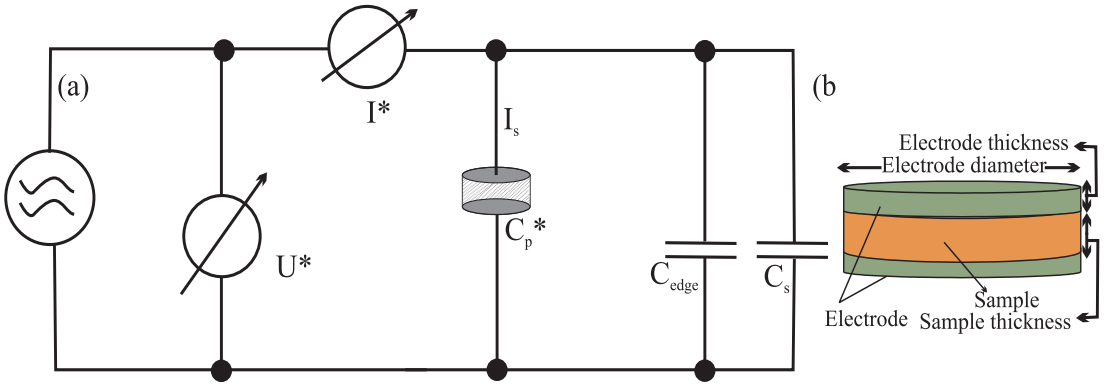

Figure 2.7.2: (a) Schematic representation principle arrangement for dielectric setup and (b) material sandwitched between the electrodes [165].

2.8 Magnetically Induced Magneto-Electric Coupling

Magnetoelectric coupling (MEC) in multiferroics is one of the modern phenomena, which is not only used to understand the enrich physics but also promises for multifunctional applications as per modern community demand. Magnetically induced MEC coefficient is described by the expression:

$$\alpha_{ij}^{H} = \left(\frac{\delta P_i}{\delta H_j}\right) \tag{2.12}$$

where H and P are the applied field and induced polarization, respectively. Alternatively, by the magnetically induced voltage MEC coefficient,

$$\alpha_{V}^{H} = \left(\frac{\delta E}{\delta H}\right) = \frac{1}{t}\left(\frac{\delta V}{\delta H}\right) \tag{2.13}$$

Since it is much easier to record a voltage medium than electric polarization, Equation [1.15] and the measurement of the voltage MEC coefficient are preferred. Integrating Equation [1.15] we obtain a relationship between the voltage induced on the electrodes of a multiferroic device and the amplitude of an externally applied magnetic field:

$$V = \alpha_{V}^{H}.H.T \tag{2.14}$$

where t is the thickness of the ferroelectric layer in the case of laminates, H is the amplitude of the externally applied magnetic field, and V is the measured voltage. According to Equation [1.16], the voltage response of a multiferroic varies linearly with the amplitude of the applied magnetic field. It is important to mention that this relation is valid to both single-phase and composite multiferroics. However, the H field, in this case, is in fact an AC magnetic field and, unless one has the ability to apply large-amplitude AC magnetic fields, the measurement requires the application of a DC magnetic field bias. The magnetic DC bias field couples with the AC magnetic field to produce a pseudo-piezo-magnetic linear response, which in turn modulates the electrical voltage response. The experimental set-up of voltage magnetically induced MEC coefficient is schematically illustrated in Fig 2.8.1 [166].

In this current thesis, the MEC measurements performed on silver coated bulk un-doped and

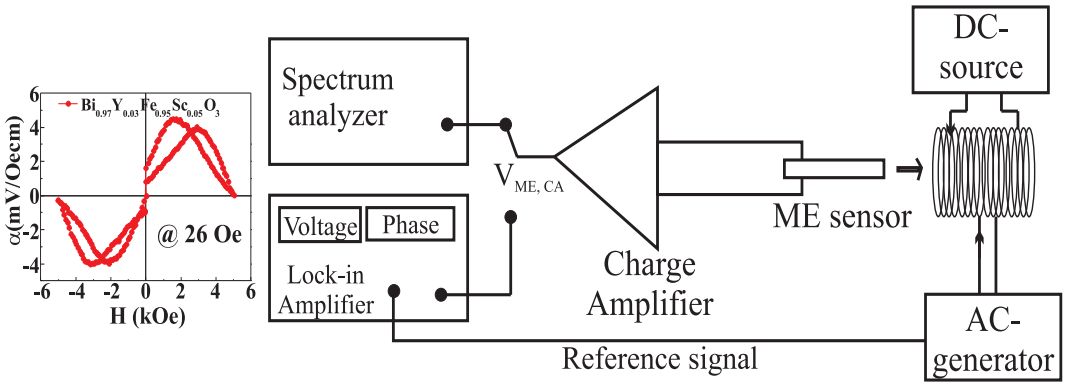

Figure 2.8.1: Schematic representation of magnetically induced magneto-electric coupling experimental set-up.

Y-Mn/Sc co-doped BFO ceramics at applied magnetic bias 26 Oe.

2.9 Summary

The multiferroic un-doped and co-doped $BiFeO_3$ (BFO) materials were synthesized using the solid-state route and sol-gel spin-coating techniques. For structural characterization, XRD and its theoretical simulations were performed to understand the distortion in doped/co-doped materials. Raman spectroscopy helps to verify the distortion evident from XRD analysis. The FESEM, TEM, AFM, MFM, PFM, etc. techniques are extensively used to investigate the intrinsic microstructural analysis. CW-THz spectroscopy helps to identify the complex optical properties of multiferroic ceramics. The optical properties, such as photoluminescence (PL) and XPS, are performed. The intrinsic magnetic properties are studied under VSM and SQUID as a function of field and temperature. The electrical properties are explained by dielectric, ferroelectric, $I-V$, $C-V$ characteristics. The resistive random access memory device characterization performed by 4200 and 2400 Keithley source meter in the presence of various perturbations.

Chapter 3

Optimization for stable multifunctional magnetoelectric $BiFeO_3$ ceramics under d-shell ion modification

This chapter describes the structural and microstructural effect on structural and multiferroic properties of various d-shell [Gd-Nd, Y-Mn, Y-Sc] ion co-doped $BiFeO_3$ ceramics. The major goal of this chapter is to achieve the multifunctional material, which will useful for possible applications. A perfect correlation between the structure, electronic, magnetic properties has been obtained.

3.1 Experimental Details

3.1.1 Sample preparation

Polycrystalline $BiFeO_3$ (BFO), partially filled d-shell Gd-Nd co-doped $Bi_{1-(x+y)}Nd_xGd_yO_3$, unfilled-partially filled Y-Mn co-doped $Bi_{1-x}Y_xFe_{1-y}Mn_yO_3$, and unfilled Y-Sc $Bi_{1-x}Y_xFe_{1-y}Sc_yO_3$ ceramics were prepared by conventional solid-state synthesis technique using. The value of x and y is presented in Table 3.1.1. For parent BFO, high purity Bi_2O_3 and Fe_2O_3 (Sigma Aldrich 99.99%) powders were used as starting materials. Similarly, for $Bi_{1-(x+y)}Nd_xGd_yO_3$ [Bi_2O_3, Fe_2O_3, Gd_2O_3 and Nd_2O_3], $Bi_{1-x}Y_xFe_{1-y}Mn_yO_3$ [Bi_2O_3, Y_2O_3, Fe_2O_3, and Mn_2O_3], and $Bi_{1-x}Y_xFe_{1-y}Sc_yO_3$ [Bi_2O_3, Y_2O_3, Fe_2O_3, and Sc_2O_3] were used. Stoichiometric proportion of powders were dissolved in toluene medium. The mixed solution was grinded for 16 hours by using high energy ball milling [Retsch] with the ball (6 mm) to powder ratio 10:1. The grinded powder was baked at 65^0 C for 20 minutes to evaporate the toluene. The dried powder was calcined at 810^0 C for 3 hours for initial phase formation. For high density, the calcined powder was mixed with Polyvinyl Alcohol (PVA) as a binder and pressed into 8 mm diameter pellets. Finally, the pellets were sintered at 850^0 C for 2 hours for the desired phase with higher density.

Table 3.1.1: Synthesized Gd-Nd, Y-Mn, and Y-Sc co-doped $BiFeO_3$ bulk samples at various concentration level.

Sample code	1		2		3	
	x	y	x	y	x	y
Nd-Gd	0.00	0.00	0.05	0.10	0.10	0.10
Y-Mn	0.03	0.05	0.06	0.05	0.12	0.05
Y-Sc	0.03	0.05	0.06	0.05	0.12	0.05

3.1.2 Material characterization

The structural and physical properties of all studied BFO were studied by using various techniques. The crystalline structure and phase purification of all samples were obtained from X-ray diffraction (XRD) [PanAnalytic Pro, Cu-K_α, $\lambda = 1.54\ A^0$]. Raman spectroscopy was performed to understand the phonon mode behavior after co-doping. FESEM analysis was carried out to check the microstructural properties. The magnetic properties were examined by using VSM (ADE Technologies USA, EV7 VSM) [1.5 T] and P-E ferroelectric loop tracer [85 kV/cm, 50 Hz]. The ME effects of un-doped and single-phase Y-Mn/Sc co-doped BFO ceramics were obtained from ME coupling at the applied field of 26 Oe.

3.2 Partially filled d-shell $Nd^{3+} - Gd^{3+}$ ions tuned $BiFeO_3$ ceramic systems

Perovskites $BiMeO_3$ (Me=metal cations) materials are always interesting due to its unique properties and easy synthesis process at ambient conditions [167]. Bulk ceramics like $BiScO_3$ and $BiMnO_3$ are successfully synthesized only at high pressure [168, 169], while room temperature (RT) multiferroic bismuth ferrite ($BiFeO_3 : BFO$) have their boundaries. The displacement of Bi ions in these materials is antipolar due to the centrosymmetric behavior and is associated with *tolerance factor (t)*. The tolerance factors, of $BiScO_3$ (t=*0.92*) and $BiMnO_3$ (t=*0.96*) has smaller to BFO (t=*0.96*). Theoretical postulates support as t reduces, antipolar order is more prominent than the polar order [170]. Hence, materials like gadolinium (Gd) [ionic radii:Gd^{3+} (0.93 $\mathring{A}$)], neodymium [ionic radii: Nd^{3+} (0.983 $\mathring{A}$)] has the ability to suppress t in BFO, which leads to increase the antipolar order than polar [171]. Moreover, Gd^{3+} ions have the largest number of the unpaired electron (seven) in the outer most d-shell with a high magnetic moment 7 μ_B. But, the appearance of secondary phases at higher concentration with weak magnetic and electronic properties in Gd-doped BFO makes it difficult to utilize for practical application. However, it is interesting, observing the combine effect of Nd^{3+} [3 unpaired electron and 3.8 μ_B] and Gd^{3+}, on physical properties of BFO. Also, Nd^{3+} can be increased antipolar order of BFO.

Figures 3.2.1 (a)-(b) shows the structural and microstructural properties of un-doped and Nd-Gd co-doped BFO ceramics, respectively. Pristine BFO exhibits rhombohedral. The phase purity and crystal structure analysis of simulation results (Reitveld refinement) reveal, all the ceramics in this group exhibit Rhombohedral (space group: R3c) structure (JCPDS no. 86-1518). From Fig. 3.2.1 (a), it is observed that the residual phases $Bi_2Fe_4O_9$ ($*$) and $Bi_{25}FeO_{40}$ (#) are appeared along with the parent. The extracted structural parameters from refinement are listed in Table 3.2.1.

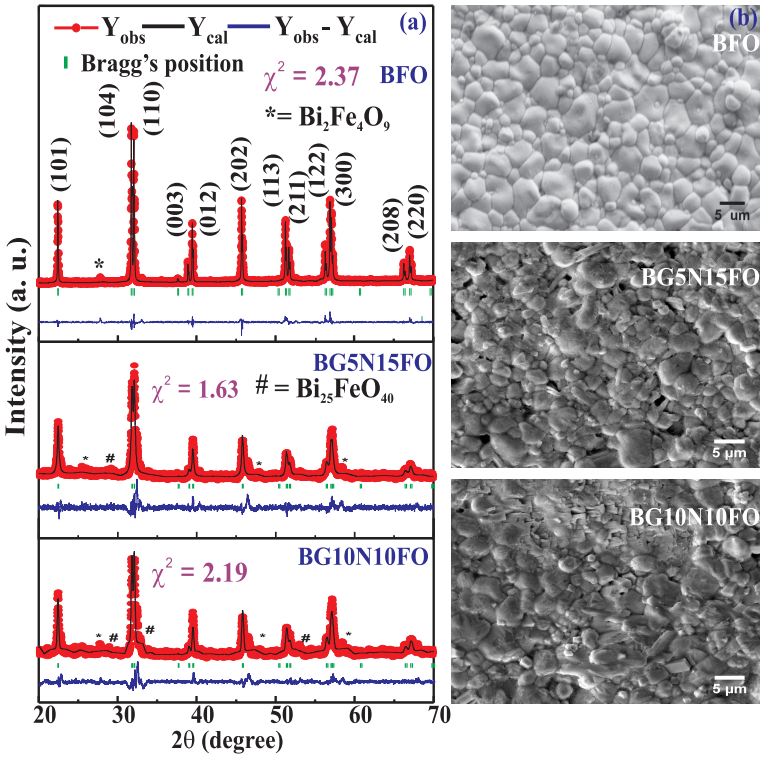

Figure 3.2.1: (a) X-ray rietveld refinement, and (b) FESEM micro-graph for un-doped and Gd-Nd co-doped BFO ceramics.

The change Bi-O, Fe-O bond-length and Fe-O-Fe bond-angles indicates, the octahedra distortion in co-doped ceramics. In grains in BFO are well distributed and separated by developed grain boundaries [Fig. 3.2.1 (a)]. However, co-doping affects the nucleation process during heat treatment, which reduces further grain growth in Gd-Nd co-doped BFO ceramics. The average grain size of studied BFO and BGNFO ceramic is given in Table 3.2.1. The reduction is grain size may change the oxygen vacancy O_{vs} stoichiometry.

Table 3.2.1: Structural and microstructural parameters extracted from the simulation results and FESEM micrograph images of un-doped and Nd-Gd co-doped BFO ceramics.

Sample Code	a=b ($\AA$)	c ($\AA$)	Bi-O ($\AA$)	Fe-O ($\AA$)	Fe-O-Fe ($\AA$)	V ($\AA^3$)	Grain size (μm)
BFO	5.5801 (4)	13.8727 (3)	2.346 (1)	2.56 (2)	153.50 (8)	374.1017	6
BG5N15FO	5.5758 (9)	13.8440 (2)	2.307 (7)	2.42 (4)	153.02 (11)	372.7406	–
BG10N10FO	5.5740 (4)	13.8400 (5)	2.240 (2)	2.39 (2)	152.93 (8)	372.3923	–

Reitveld refinement predicts the structural distortion in co-doped ceramics, which can be analyzed by considering the phonon modes obtained from the Raman spectroscopy, depicted in Fig. 3.2.2 (a). According to the group theory and from other experimental results, the Rhombohedral R3c BFO exhibit 13 possible phonon modes, assigned by the equation [172]:

$$\gamma = 4A1 + 9E \tag{3.1}$$

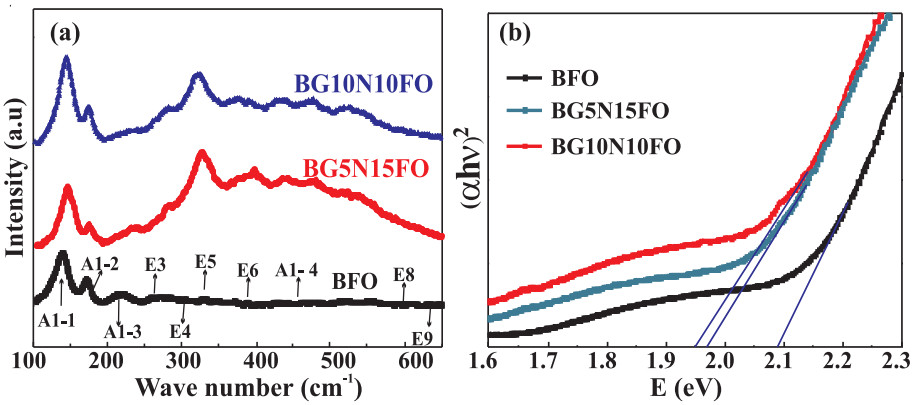

Figure 3.2.2: (a) Raman spectroscopy, (b) Tauc's plot for un-doped and Gd-Nd co-doped BFO ceramics.

Table 3.2.2: Modulation of phonon modes and energy band-gap (E_g) of magnetic Nd-Gd ion modified BFO ceramics.

Sample Code	A1-1	A1-2	A1-3	E3	E4	E5	E6	E7	A1-4	E8	E9	E_g (eV)
BFO	140	171	219	263	282	351	367	430	469	561	607	2.08
BG5N15FO	143	173	220	260	284	326	396	433	477	559	–	1.98
BG10N10FO	144	174	221	261	283	323	389	437	480	556	–	1.97

where A-Modes at the low-frequency region arrises from parallel polarization, and E-Modes at the high-frequency region arises from cross polarization [173]. The position of each peak corresponding to the wave-number is presented in Table 3.2.2. The shifting of phonon modes in co-doped ceramics indicates, the structural distortion at FeO_6 octahedra cage of BFO. The material features with the response to the UV-VIS light is explained through UV-VIS Tauc's plots, as shown in Fig. 3.2.2 (b). The energy band-gap (E_g) is calculated from Tauc's expression:

$$E = (\alpha h\nu)^2 \tag{3.2}$$

where α, h, and ν are the absorbance, Plank's constant, and frequency, respectively. The calculated E_g is given in Table 3.2.2 and are reduced drastically from the vicinity of BFO. The reduction in band-gap may possibly by due to the structural distortion and suppression of bond-length distance. Also, individual doping of either Gd or Nd also compresses the band-gap of BFO [174, 175]. The energy-gap of appeared secondary phases also much lower, which may affect the E_g [176].

RT magnetization hysteresis curve (M-H) for un-doped and Gd-Nd co-doped BFO ceramics are represented in Fig. 3.2.3 (a). The unsaturated linear M-H curve indicates the AFM ordering in all ceramics, which indicates for the larger field. The magnetic parameters such as remanent magnetization (M_r), magnetization at $H_{1.5\ T}$, and coercivity (H_c) extracted from the magnetization curve are listed in Table 3.2.3. The large opening in the M-H loop of Gd-Nd at (x,y)= (10, 10) indicates the presence of both ferromagnetic (FM) and antiferromagnetic (AFM) ordering. Moreover, the magnetic parameters of the Gd-Nd co-doped BFO system are found higher than individual Gd at low applied field [177, 24]. The magnetization enhancement in rare-earth ion modified BFO is explained on the basis of a few valid points:

(i) Co-doping causes FeO_6 octahedral distortion due to the change in Fe-O bond-length and Fe-O-Fe

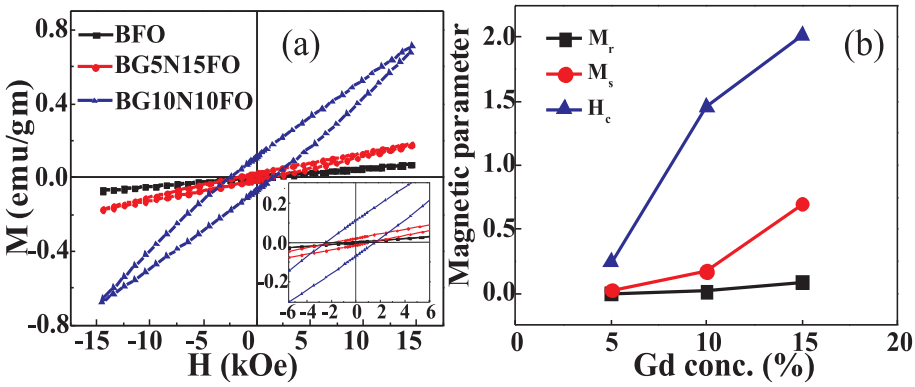

Figure 3.2.3: (a) M-H hysteresis loops at maximum applied magnetic field 15 kOe and (b) magnetic parameter of BFO at various Gd-concentration label.

Table 3.2.3: (a) Room temperature M-H hysteresis curve (b) variation of magnetic parameters at various Gd-concentration of BFO and BGNFO ceramics.

Sample Code	$M_{1.5\ kOe}\ (emu/gm)$	$M_r(emu/gm)$	$H_c(\ kOe)$
BFO	0.0020	0.0274	0.245
BG5N15FO	0.0175	0.1784	1.457
BG10N10FO	0.0914	0.7000	2.012

bond-angle, which leads to a magnetic modification.

(ii) Appearance of weak canted FM behavior is evident due to the suppression of SSMS and Dzyaloshinskii-Moriya (D-M) exchange interaction. The reduction of grain size may be another factor for magnetization enhancement [24].

(iii) Magnetic ions $Gd^{3+} - Nd^{3+}$ leads to suppress the formation Fe^{2+} ion which enhances the super-exchange interaction between $Fe^{3+} - O^{2-} - Fe^{3+}$.

(iv) Gd^{3+} have a maximum number of unpaired electron in their outermost d-shell and can provide additional magnetic interaction between Gd-Gd, Ge-Fe to the system.

(v) High concentration Gd-doping leads to an increase in coercivity (H_c) of BFO. Nd-doping helps to form the Nd-O-Bi chains in the expense of the Bi-O-Bi chain.

The magnetic properties in Gd-Nd co-doped BFO system is prominently controlled by Gd^{3+} and the coercivity is controlled by Nd^{3+}. The modulation of magnetic parameters concerning doping concentration is represented schematically in Fig. 3.2.3 (b).

In summary, the appearance of secondary phases may lead to weak electronic and magnetic properties diminish the existence of strong magnetoelectric coupling (MEC) Gd-Nd co-doped BFO ceramic system. Moreover, due to the appearance of secondary phases, the exact contribution from the parent phase in electrical properties is complicated. Necessarily, this MF system can be useful to study the intrinsic magnetic properties.

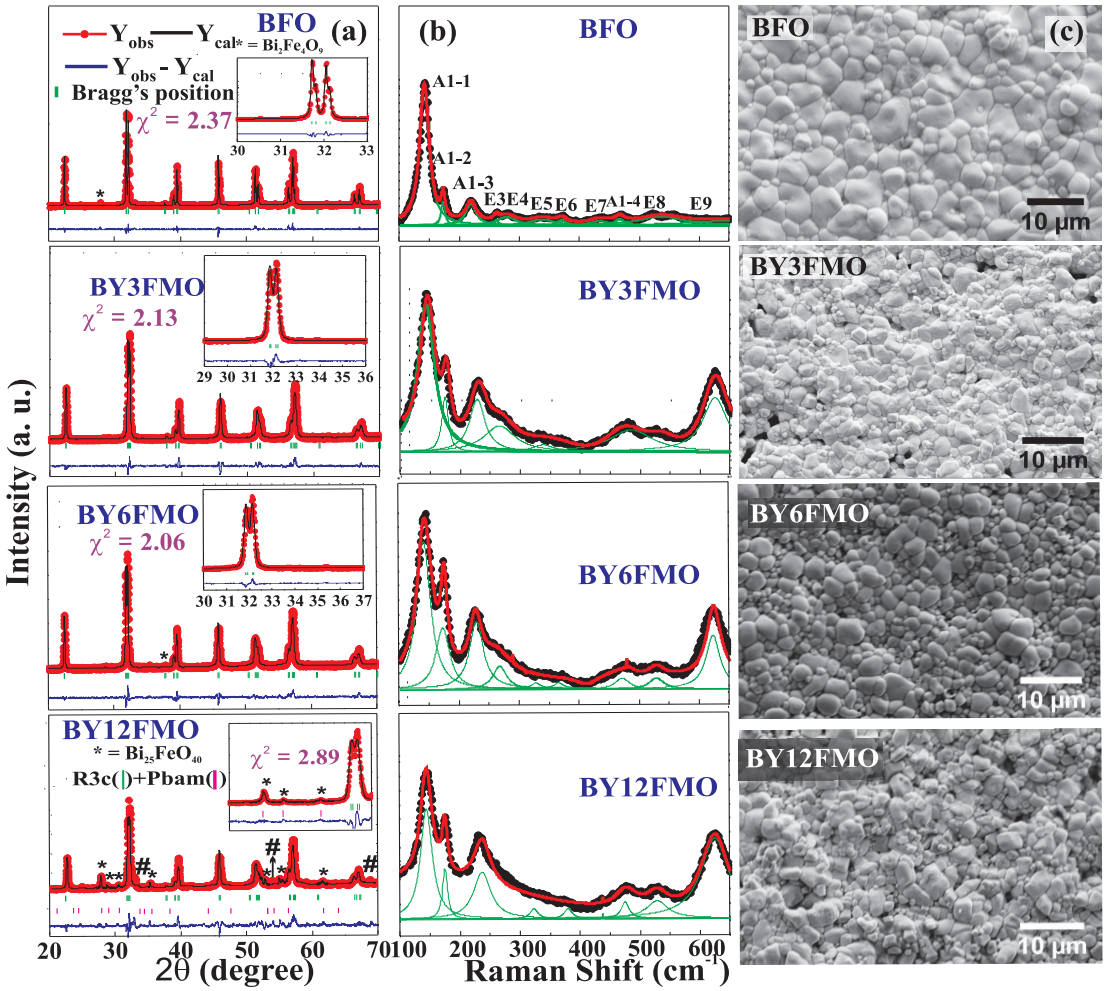

Figure 3.3.1: (a) XRD Reitveld refinement, (b) Lorentzian fitted Raman spectra, and (c) FESEM micrograph images for BFO, Y-Mn co-doped BFO ceramics.

3.3 Unfilled (Y)-Partially filled (Mn) d-shell ions tuned $BiFeO_3$ ceramic systems

Partially filled d-shell Gd-Nd co-doped BFO system didn't bring much attention due to the appearance of secondary phases, weak MF properties at RT. This surge for searching for new multiferroic materials with stable primary and secondary properties. This section will provide a perfect correlation between the structural and magnetic properties of Y-Mn co-doped BFO ceramic systems. Y^{3+} (1.07 $\AA$) has lower ionic radii as comparison to Bi^{3+} (1.07 $\AA$), while Mn-ions (+2, +3, +4) always in higher side from Fe^{3+} (0.654 $\AA$). Due to the minimal difference of ionic radii between parent and foreign ions, BFO may don't suffer large crystal structure variation.

Figure 3.3.1 elucidated the structural and microstructural properties of Y-Mn tuned Y-Mn co-doped $Bi_{1-x}Y_xFe_{1-y}Mn_yO_3$ [(x, y)=(0, 0), (0.03, 0.05):BY3FMO, (0.06, 0.05):BY6FMO, (0.12, 0.05):BY12FMO] ceramics. Figure 3.3.1 (a) depicts the simulation results of XRD spectra obtained from BFO and BYFMO powders through Reitveld refinement technique. The obtained results in-

dicate the unchanged crystal structure [Rhombohedral (R3c: space group)] after co-doping. Some traces of residual phase ($Bi_2Fe_4O_9(*)$) are appeared along with parent, which have been suppressed at low doping concentration of BY3FMO. The appearance of secondary phases is significant in BY12FMO. After rigorous fitting with various two-phase system, we obtained best fit with orthorhombic *Pbam* phase [R3c(86%)+Pbam(14%)]. The extracted structural parameters are given in Table 3.3.1. The Wykoff positions for oxygen atoms (Orthorhombic: Pbam phase) in BY12FMO ceramic are (x, y, z)= O1 (0.259, 0.169, 0), O2 (0.273, 0.077, 0.5), O3 (0.008, 0.242, 0.291), O4 (0, 5, 0.203), O5 (0, 0, 0.205). The modulation of structural parameters after co-doping evident from Table 3.3.1 and indicate the structural distortion.

Table 3.3.1: (a) Structural parameters of Y-Mn co-doped $Bi_{1-x}Y_xFe_{1-y}Mn_yO_3$ (x=y=0; x=0.03, 0.06, 0.12, y=0.05).

Sample code		BFO	BY3FMO	BY6FMO	BY12FMO	
					R3c (86%)	Pbam(14%)
a=b($\AA$)		5.5802(2)	5.5722(6)	5.5683(3)	5.5687(2)	a=5.6125(6), b=11.2436(3)
c($\AA$)		13.8727(7)	13.5254(4)	13.8171(2)	13.8201(9)	7.8120(9)
Volume($\AA^3$)		374.10(8)	371.75(3)	371.01(8)	371.16(7)	493.24(6)
Bi/Y	x	0	0	0	0	0.739 (11)
	y	0	0	0	0	0.1364 (5)
	z	0	0	0	0	0
Fe/Mn	x	0	0	0	0	0.2324
	y	0	0	0	0	0.1239
	z	0.2190	0.2218	0.2208	0.2226	0.2451
O	x	0.4540	0.4318	0.5378	0.454	
	y	0.0088	0.0125	0.0113	0.018	
	z	0.9575	0.9572	0.9638	0.9564	
Fe-O		1.951(7)	1.96(6)	1.97(3)	1.96(11)	1.93(3)
Bi-O1		2.57(11)	2.44(8)	2.65(5)	2.51(4)	1.98(4)
Bi-O2		2.346(9)	2.345(8)	2.336(4)	2.321(4)	2.117(4)
Fe-O-Fe		161.60(4)	163.76(4)	167.85(9)	158.6(8)	151.8(2)
χ^2		2.37	2.13	2.06	2.89	

For more details regarding structural distortion, the Raman spectra of all studied non-magnetic system is shown in Fig. 3.3.1. BFO with rhombohedral R3c structure exhibit 13 phonon modes. The position of each phonon mode of BFO and BYFMO ceramics is extracted from Lorentzian fitting results and listed in Table 3.3.2. The Y-Mn co-doped BFO system associated with 11 phonon-modes. The shifting of phonon modes with an increase in Y-concentration (Mn=5% constant) indicates the structural distortion evident from XRD analysis.

FESEM micrograph images for un-doped and Y-Mn co-doped BFO ceramics are displayed in Fig. 3.3.1(c). *ImageJ* tool was used to calculate the average grain size. Polycrystalline BFO possesses homogeneous grains in the range of $6\mu m$, connected through well-defined grain boundaries.

Table 3.3.2: Modulation of Raman phonon modes of BFO ceramics after Y-Mn co-doping.

Sample Code	A1-1	A1-2	A1-3	E3	E4	E5	E6	E7	A1-4	E8	E9
BY3FMO	143	174	226	263	309	–	371	437	476	571	619
BY6FMO	144	175	227	266	312	–	375	441	478	571	623
BY12FMO	145	176	229	–	323	–	376	447	481	576	625

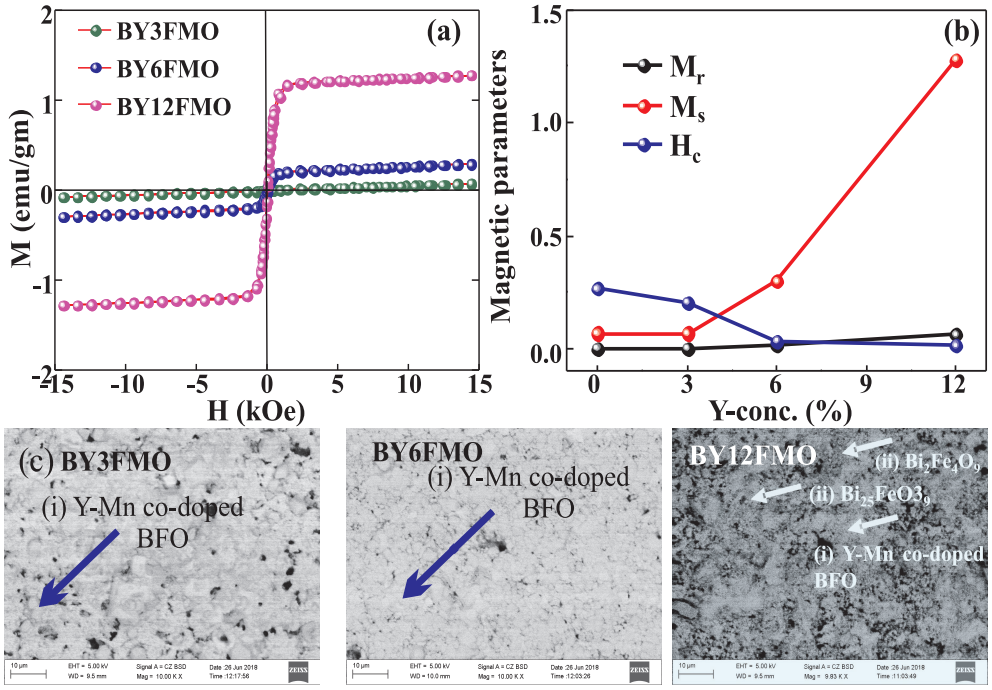

Figure 3.3.2: (a) Room temperature M-H hysteresis curve, (b) tuning of magnetization with Y-concentration, and (b) BSD images for BFO and BYFMO ceramics.

However, co-doped based ceramics have inhomogeneous grains with some voids created between loosely connected grains. The grain growth in co-doped ceramics suppressed during the nucleation process at high sintering temperature due to the low diffusivity rate of Y^{3+}. The average grain size of BY3FMO, BY6FMO and BY12FMO are 3.1 μm, 1.7 μm and 1.4 μm, respectively. The suppression of grain growth may be due to ionic radii difference between Bi and Y ions, the density of oxygen stoichiometry, and distortion. The larger bond dissociation energy (BDE) difference between Y-O (715 kJ/mol) and Bi-O (339 kJ/mol) plays a vital role in grain modification. The effect of Mn is minimal due to a very small BDE between Mn-O (409 kJ/mol) and Fe-O (402 kJ/mol). The observation of secondary phases (observed from XRD) may also appear in an agglomerate form.

RT M-H hysteresis curve for BFO and Y-Mn co-doped ceramics at maximum applied field 15 kOe is shown in Fig. 3.3.2 (a). BFO exhibit weak FM behavior due to D-M exchange interaction [Fig. 3.2.3]. A noticeable enhancement in magnetic properties of BFO with complete magnetic saturation obtained after Y-Mn co-doping. The extracted magnetic parameters of Y-Mn co-doped BFO ceramics are presented in Table 3.3.3. The parameters are well improved in comparison to parent and the Gd-Nd co-doped BFO. The enhanced magnetization in such a system can be explained as:

(i) Due to non-magnetic behavior of Y^{3+} ions, the magnetization improvement due to Y-dopant is discarded. But, the manganese (Mn) ions are magnetically active with larger magnetic moments (5.9 μ_B) than the Fe (5.1 μ_B) may improvise the magnetic properties of BYFMO. Moreover, the Mn can create additional magnetic interaction between Fe-Mn, Mn-Mn.

(ii) The magnetic enhancement due to impurities $Bi_2Fe_4O_9$ and $Bi_{25}FeO_39$ is ruled out due their paramagnetic behavior [178]. The presence of other magnetic phases in Y-Mn co-doped BFO is also

Table 3.3.3: Magnetic parameters extracted from the M-H magnetization curve and M-T curve of Y-Mn co-doped BFO ceramics.

Sample code	M_r (emu/gm)	M_s (emu/gm)	H_c (kOe)	T_N (K) From M-T	From DSC
BY3FMO	0.07	0.032	0.207	629	632
BY6FMO	0.30	0.0201	0.036	626	628
BY12FMO	1.28	0.0635	0.017	624	621

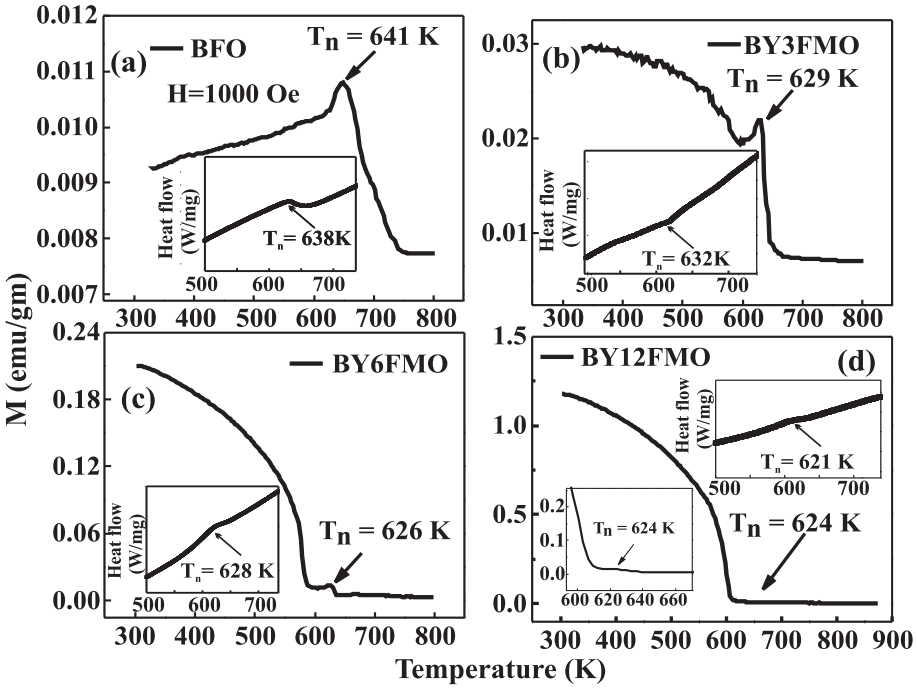

Figure 3.3.3: Magnetization-temperature (M-T) and [DSC: inset] plots for (a) BFO, (b) BY3FMO, (c) BY6FMO, and (d) BY12FMO at 1000 Oe .

ruled out from back-scattered diffraction (BSD) micrograph, as shown in Fig. 6.3.4 (c).

(iii) Y-Mn co-doping may suppress Fe^{2+}, which leads to strong super-exchange interaction between $Fe^{3+} - O^{2-} - Fe^{3+}/Mn^{3+}$. Since Mn_2O_3 was used as the starting material for sample preparation, there is minimal chance for presence of $Mn^{2+/4+}$ [179]. Hence any kind of double exchange magnetic interaction can be ruled out.

(iv) Moreover, substituting Mn to Fe-site affects the local environment of FeO_6 octahedral, due to change in Fe-O bond-distance and Fe-O-Fe bond angle. This may unlock the SSMS and or improve the canting angle of AFM ordered adjacent planes, resulting in improved ferromagnetism [180]. Rao *et. al.* explained the reduction in grain size could be enhances the magnetic proerties [24].

(v) The change in magnetocrystalline anisotropy energy affects the coercivity of BFO after Y-Mn co-doping.

The temperature-dependent magnetization (M-T) curve for BFO and Y-Mn co-doped BFO ceramics at 1000 kOe between the temperature $300 - 800$ K, as displayed in Figs. 3.3.3 (a-c). All compounds exhibit antiferromagnetic (AFM)-paramagnetic (PM) transition temperature (T_N) between 620-641 K, given in Table 3.3.3. The non-appearance of any other peaks ensure, the contribution of

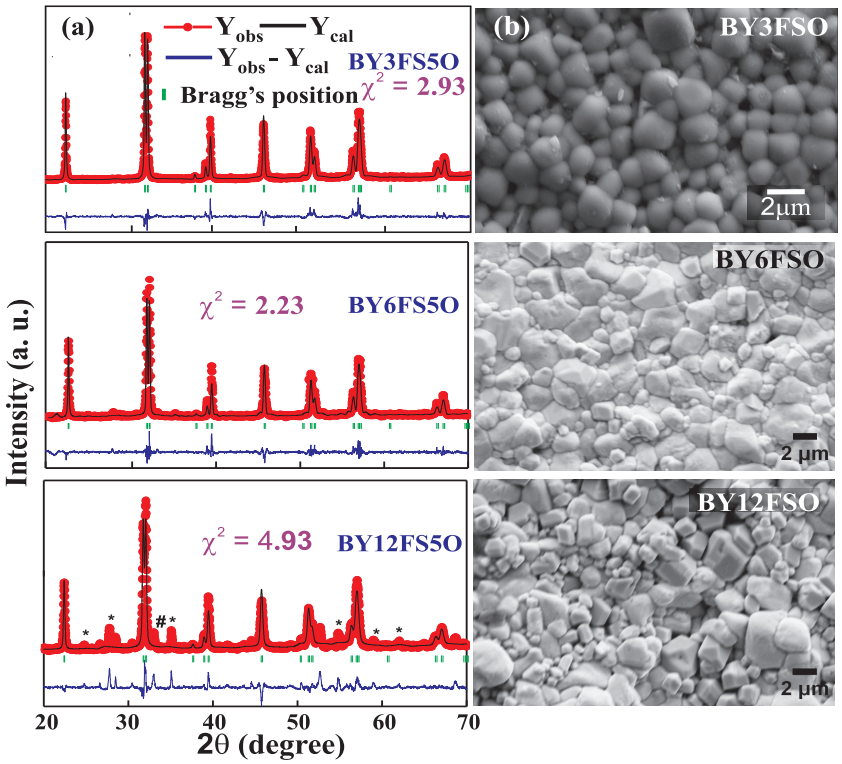

Figure 3.3.4: (a) Reitveld refinement of XRD spectra and (b) FESEM micrograph for BYFSO ceramics.

any magnetic phases. T_N shifts towards the lower temperature with an increase the Y-doping concentration due to the non-magnetic behavior of Y^{3+} and the decrease in magnetic interaction above room temperature. The DSC measurements [inset:Figs. 3.3.3 (a-c)] further examined to understand the AFM-FM transition and found analogous with the result obtained in M-T measurements.

The Y-Mn co-doped BFO shows structural stability and noticeable change in FM properties, which previously was suppressed in Gd-Nd co-doped based ceramic systems. From the above results, Y-Mn modified BFO system promises for future spin-ordering mediated applications.

3.3.1 Unfilled $Y^{3+} - Sc^{3+}$ d-shell ions tuned $BiFeO_3$ ceramic systems

Individual non-magnetic Y tuned BFO system is always exciting due to its magnetic enhancement at the low applied magnetic field. However, its poor electrical performance and structural instability at higher doping level minimize the many-body effects [181]. These drawbacks can be successfully withdrawn in BFO by substituting the similar types of elements (Sc^{3+}: non-magnetic and inert electronic configuration) at Fe-site.

The structural, microstructural, and magnetic properties were studied in Y-Sc co-doped BFO ceramic systems. Reitveld refinement of experimental XRD results presented in Fig. 3.3.4. The structural properties of BFO with the increase in Y concentration (Sc= 5% constant) behaves as similar to Y-Mn co-doped BYFMO based multiferroic system. However, its electronic and magnetic properties may appealing. Tuning with various concentrations, the novel single-phase MF material obtained at (Y, Sc)= (3%, 5%) and (3%, 10%: Appendix). Reitveld refinement analysis reveals Y-Sc

Table 3.3.4: Structural and microstructural parameters extracted from the simulation results and FESEM images of Y-Sc co-doped ceramics.

Sample Code	a=b ($\AA$)	c ($\AA$)	V ($\AA^3$)	Fe-O-Fe ($\AA^3$)	Grain size (μm)
BY3FSO	5.5808 (4)	13.9099 (3)	376.53	155 (8)	1.5
BY6FSO	5.5726 (9)	13.8753 (2)	374.27	157 (11)	1.72
BY12FSO	5.5822 (9)	13.8669 (2)	374.2146	158 (11)	1.42

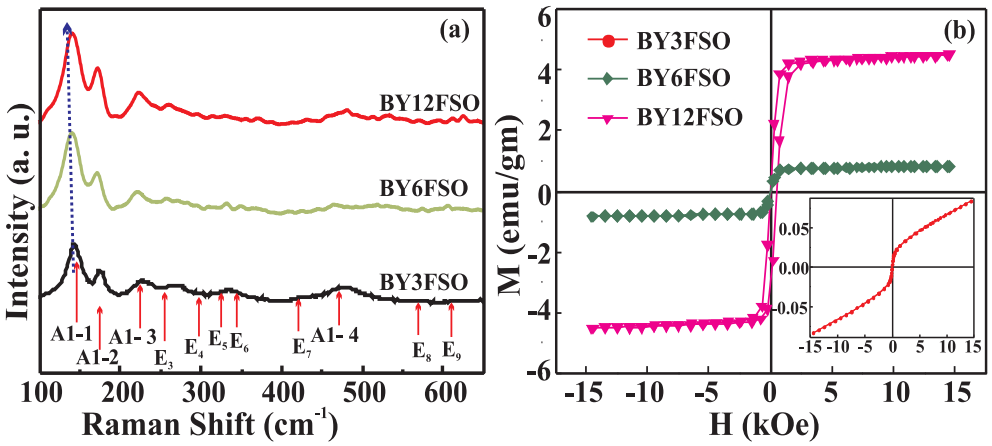

Figure 3.3.5: (a) Raman spectroscopy phonon modes and (b) M-H hysteresis curve obtained from Y-Sc co-doped BFO ceramics.

co-doped BFO ceramics exhibit Rhombohedral R3c structure without deviating from the parent. The structural parameters extracted from the simulation results are listed in Table 3.3.4. The modulation of structural parameters ensures structural distortion in co-doped ceramics. FESEM micrographs for un-doped and co-doped BFO ceramics are shown in Figs. 3.3.4 (b). The homogeneous grains with well-developed grain boundaries are obtained at lower Sc-concentration. The average grain sizes for BY3FSO, BY6FSO, and BY12FSO are 1.5 μm, 1.72 μm, and $0.5-3$ μm, respectively, obtained from *ImageJ* imaging tool. The stable electronic configuration of foreign ions may suppress the oxygen stoichiometry, which leads to grain modification in co-doped ceramics.

RT Raman scattering spectra for Y-Sc co-doped BFO ceramics is shown in Fig. 3.3.5 (a). Like Y-Mn, Y-Sc co-doping shifts the position of A- and E-modes, which indicates structural distortion, as the modes are associated with bond-length and bond-angle. The shifting of these modes after co-doping may be due to the minimal ionic radii difference between $Bi^{3+} - Y^{3+}$ and $Fe^{3+} - Sc^{3+}$. The decrease in intensity of A-modes co-doped ceramics may be due to the weakening of Bi-O covalent bond and low atomic weight of Y in comparison to Bi [182]. The E-modes are gradually hardened between frequency ranges 270300 $cm1$ due to Sc-insertion due to the FeO_6 octahedral distortion. Because doping with Sc3+ at Fe site may change the internal chemical pressure, which makes unstable Fe^{3+} ion resulting in FeO_6 octahedral tilts [183]. The modification of oxygen octahedra may affect the magnetic properties of BFO. The position of each phonon modes extracted from Lorentzian fitting of spectra, as illustrated in Table 3.3.5.

Figure 3.3.5 (b) shows the RT M-H hysteresis curve of Y-Sc co-doped BFO ceramics with the maximum applied field of 15 kOe. The extracted magnetic parameters M_r and M_s are listed in

Table 3.3.5: Modulation of Raman phonon modes of BFO ceramics after Y-Mn co-doping.

Sample Code	A1-1	A1-2	A1-3	E3	E4	E5	E6	E7	A1-4	E8	E9
BY3FSO	141	171	215	263	335	355	370	–	476	570	611
BY6FSO	142	172	224	261	316	355	371	447	480	570	612
BY12FSO	142	173	223	258	318	350	–	455	481	573	607

Table 3.3.6: Magnetic parameters extracted from the M-H magnetization curve of Y-Sc co-doped BFO ceramics.

Sample code	M_r (emu/gm)	M_s (emu/gm)	H_c (kOe)
BY3FSO	0.0015	0.30	0.036
BY6FMO	0.0201	0.30	0.036
BY12FMO	0.0635	1.28	0.017

Table 3.3.6. The magnetic properties enhance systematically with the increase in the Y-doping level and almost higher [BY12FSO] among all the studied ceramic systems in present work. The improved magnetization in non-magnetic ion modified BFO ceramics is explained as:
(i) The change in Fe-O bond-distance and Fe-O-Fe bond-angle in co-doped ceramics leads to distorts the Fe-O octahedra, which in turn modify the magnetization [183].
(ii) Due to non-magnetic behavior and stable electronic configuration of Y^{3+} and Sc^{3+} ions, the M enhancement due to the insertion of foreign dopant is discarded. Also, the paramagnetic behavior of secondary phases observed from XRD have minimal effect in magnetic modifications.
(iii) Banerjee *et. al.* reported, doping Ni^{3+} into Fe^{3+}, their is partial chance for formation of Fe^{2+}, which bring strong double-exchange interaction [184]. Both Y^{3+} and Sc^{3+} are available in +3 state, which can suppress the Fe^{2+} ions. This results, a strong super-exchange interaction between Fe-O-Fe, which improve the magnetization.
(iv) Inserting Sc into Fe, Sc^{3+} ions may distort the FeO_6 octahedral by partially overlapping with the neighbor Fe^{3+} ions, which results in a non-symmetrically AFM spin ordering [185].
(v) The intrinsic magnetic properties are depends on grain size i.e., decrease in grain size enhance magnetization, may be the possible reason for enhancing magnetization in YSc co-doped BFO by suppressing the SMSS.
The decrease in coercivity (H_c) in BYFMO and BYFSO compounds may be due to the decline in magneto-anisotropy energy. However, Neutron diffraction and Mossbauer spectroscopy analysis can provide dip information regarding magnetization improvement in co-doped ceramics.

After analyzing the various types of foreign ions, the low-field magnetic saturation of BFO ceramic is achieved by non-magnetic Y-Sc/Mn substitution. However, the ferroelectric (FE) properties have been carried out for un-doped BFO, Gd-Nd co-doped BFO, (BGNFO), single-phase Y-Mn co-doped BY3FMO (BYFMO), and Y-Sc co-doped BY3FSO (BYFSO).

3.4 Ferroelectric properties

Figure 3.4.1 displays the polarization-electric field (P-E) hysteresis curve for BFO, BGNFO, BYFMO, and BYFSO pellets with the maximum applied electric field (E) of 80 kV/cm at 50 Hz. The FE behavior in BFO ceramic is arising due to the hybridization of lone pair electron of $6s^2$ of Bi^{3+} with

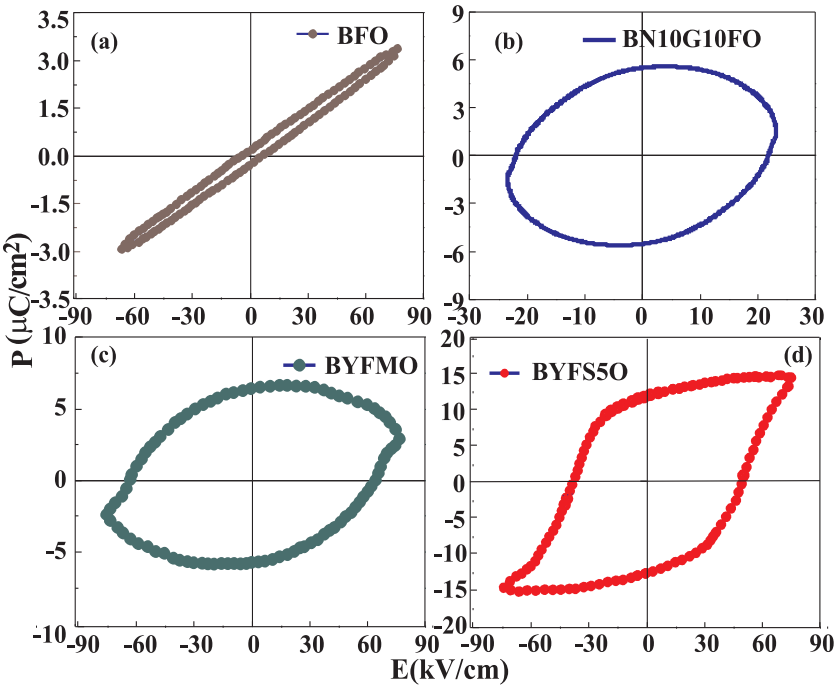

Figure 3.4.1: Ferroelectric polarization P-E curve for BFO, BG10N10FO, BYFMO, and BYFSO compounds.

$6p^0$ orbital of Bi^{3+}. The $2p^6$ orbitals of O^{2-} ion form Bi-O covalent bond, which causes the non-centrosymmetric distortion of the electron cloud and results in ferroelectricity [186]. From Fig. 3.4.1, the elliptical P-E curve of BFO shows weak FE behavior. The roundish BGNFO P-E curve indicates the presence of high leakage current, which is already predicted in Section **3.2**. With the presence of high leakage current, Gd-Nd based BFO system may lead to poor device performance. Y-Mn co-doping shows minimal improvement in FE properties of BFO, as shown in Fig. 3.4.1 (c). Also, both BG10F10FO and BYFMO ceramics are electrically broke down at higher E due to the presence of high leakage current ($I_{leakage}$). The factors like low crystallinity, lesser density, inhomogeneous grain growth, O_{vs}, etc. are responsible for $I_{leakage}$ [187]. The polarization parameters like remanent polarization (P_r), saturation polarization (P_s), and coercive field (E_c) are listed in Table 3.4.1 and found much higher in BYFSO ceramic. The calculated density for BFO, BG10N10FO, BYFMO, and BYFSO ceramics is 8.1 g/cm^3, 7.47 g/cm^3, 8.22 g/cm^3, and 8.39 g/cm^3 supports higher polarization behavior in BFO after Y-Sc co-doping. Y^{3+} and Sc^{3+} ions mark an abrupt modification in FE properties of BFO at RT and promising for future scientific applications. The improved polarization in BYFSO may be attributed from to d^0 shell of Y and Sc. In addition to this, Y-Mn/Sc substitution decreases Bi-O bond distance and strengthen the covalent Bi-O hybridizations in BFO, which induces the non-centrosymmetric distortion to drive the Bi^{3+} ions towards $[111]_c$ direction and enhance FE polarization [187]. The coercive field (E_c) increases in co-doped ceramics.

The Y-Mn/Sc co-doped BFO bulk ceramics show appreciable multiferroic properties in a single-phase. Hence, these compounds may show many-body complex phenomena such as magnetoelectric (ME) and piezoelectric (PE) effect.

Table 3.4.1: Ferrolectric polarization parameters extracted from P-E hysteresis curve of BFO, BGNFO, BYFMO, and BYFSO ceramics.

Sample code	P_r ($\mu m.cm^{-2}$)	P at 85 kV/cm ($\mu C.cm^{-2}$)	E_c (kV/cm)
BFO	0.007	2.5	15.52
BG10N10FO	5	1.25 at 23.15	21.78
BYFMO	6	3	62
BYFSO	13	15	50.35

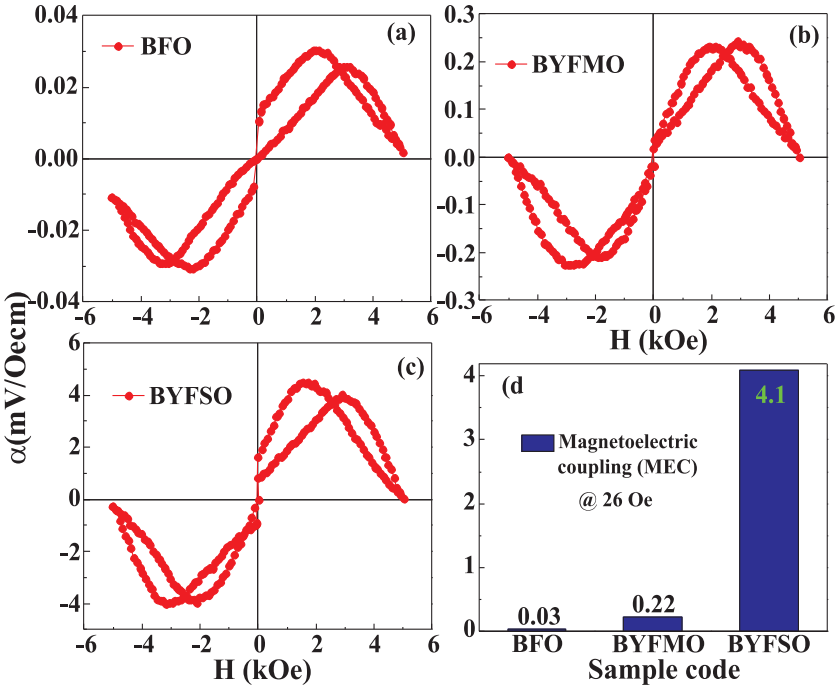

Figure 3.5.1: Magnetoelectric coupling plots obtained from BFO, BYFMO, and BYFSO compounds at 26 Oe.

3.5 Magnetoelectric Effect

Magnetoelectric coupling (MEC) measurements were carried out on un-doped BFO and single-phase Y-Mn/Sc co-doped BFO ceramics. Figure 3.5.1 shows the ME coefficients of synthesized BFO, BYFMO, and BYFSO bulk ceramics at RT, reflecting their hysteretic behavior. The coupling coefficients (α_{ME}) has been calculated using the following expression [188]:

$$\alpha_{ME} = \frac{\delta E}{\delta H} = \frac{V_{out}}{h_0 t} \tag{3.3}$$

where, E and H are the applied electric and magnetic fields, respectively. V_{out} is the ac ME voltages appearing across the sample surface (measured by the lock-in amplifier). t and h_0 are the thickness of the pellet and ac magnetic field amplitude, respectively. From Figs. 3.5.1 (a-c), it can be observed that α_{ME} increases rapidly with the rise in magnetic bias, and attain maximum value, $\alpha_{ME} = 0.032, 0.25, 4.1\ mV/Oe$, for BFO, BYFMO, and BYFSO ceramics. This shows the ME effect of BFO enhanced after Y-Mn/Sc co-doping. The observed values are smaller than some of the

values obtained in the BFO based nano-particle system due to large grain size and charge variation of Fe-ions, i.e. $Fe^{+2} - Fe^{3+}$. In bulk BFO, the long-range SSMS (62 nm) results in AFM ordering; this cancels the macroscopic magnetization and hampers the ME effect [189]. The observed ME in present ceramic, can be attributed to quantum confinement, spin-exchange constrictions, exchange-interactions, and magnetostriction effect [190]. The Y-Mn/Sc co-doped BFO ceramics get strain with applied magnetic field due to the coupling between FM and FE domains. The appeared strained induced stress in these materials and generates an electric field. The induced electric field orients the FE domains and leads to ME. The improved ME in Y-Sc/Mn co-doped BFO may be attributed to the increase in magnetization [Section:**3.3 and 3.4**], which strengthens the sub-lattice interactions [191]. From M-H analysis of BYFMO and BYFSO, the suppression of SSMS has been predicated, which may lead to enhance α_{ME}. The grain size of the as-synthesized co-doped ceramics reduces than the BFO; this leads to suppression of spiral cycloid, modifies the domain structure, and thereby results in MEC [189]. From XRD refinement, change in Fe-O bond-distance may affect the cycloid structure.

3.6 Summary

In summary, we have been explored the modulation of magnetic and electronic properties in various d-shell tuned multiferroic $BiFeO_3 : BFO$ ceramics. The partially filled d-shell with high magnetic moment Gd-Nd shows improved ferromagnetism in BFO. But, the presence of impurity phases and weak ferroelectric properties inhibits the possibility of a strong magnetoelectric effect. Y-Mn partially stabilizes the crystal structure of BFO and improved magnetization due to structural distortion. The ferroelectric studies unveil the weak ferroelectric properties after Y-Mn, which also indicates the presence of leakage current. The significant variation is observed in un-filled non-magnetic d-shell Y-Sc modified BFO ceramics; where both electrical and magnetic properties simultaneously improved in a single-phase. The nucleation of grain growth is homogeneous in BYFSO ceramics, which withdraws the pilling effects during electrical measurements. The magnetoelectric coefficient increases significantly for BYFSO, which is almost 100 times larger than the parent BFO in the present studies. The enhancement in the magnetoelectric coupling coefficient in co-doped ceramics may be attributed to the improved multiferroic properties of BFO after co-doping. The Y-Sc co-doped based BYFSO compound, with improved multiferroic and magnetoelectric, promises for potential applications in memory devices, sensors, transducer, etc.

Graphical Abstract

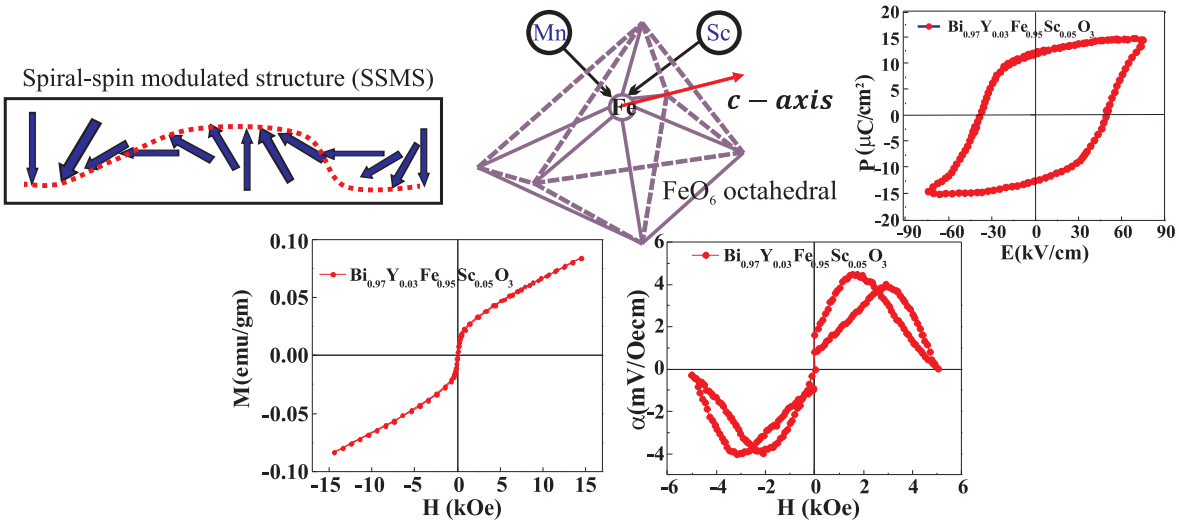

FeO_6 octahedral tuned primary and secondary ferroic orders

Chapter 4

Temperature dependent dielectric and terahertz spectroscopy studies of co-doped $BiFeO_3$ ceramics

4.1 Introduction

Electrical insulator materials which will prevent the flow of current in an electrical circuit are being used since from the beginning of the science and technology of electrical phenomena. Dielectrics are insulating materials that exhibit the property of electrical polarization; thereby they modify the dielectric function of the vacuum. *Chapter-1* provides brief information regarding the structural distortion induced multiferroic and magnetoelectric (ME) effect of Y-Mn/Sc co-doped BFO bulk ceramics. When a dielectric material placed inside an electric field, it induces the polarization. In a prototypical dielectric material, polarizations such as interfacial (also called space charge), dipolar, ionic, and electronic plays a significant role in carry out the process. However, at extremely low-frequency region (ELF) [e.g., 1 $Hz - 1$ MHz], the dipolar polarization provides major contribution. The schematic representation for dipolar polarization behavior and its distribution as a function of frequencies in the dielectric materials is elucidated in Fig. 4.1.1. There were many attempts to improve the dielectric properties of MF BFO ceramics [192, 193] and still have many grey areas which need to investigate. In *Chapter-1*, the physical properties improved under elemental (Y-Mn/Sc) substitution effect. However, the intrinsic electrical properties like conduction mechanism, relaxation behavior of un-doped, and Y-Mn/Sc co-doped BFO can be explored using dielectric studies. This chapter will provide an understanding for tuning of relaxation behavior and conduction mechanism after co-doping. To explore this, frequency and temperature-dependent dielectric properties were studied in a wide frequency range between 10 $Hz - 1$ MHz.

The static magnetoelectric coupling (MEC) behavior of the studied BFO system has been explored in the previous chapter. The scientific significance of strain mediated dynamical MEC, combined with the eminent implication of its technological applications, prompted the investigation of spin and lattice excitations of un-doped and Y-Mn/Sc co-doped BFO system excitations of multiferroic based materials. In the current chapter, the experimental findings of the complex optical

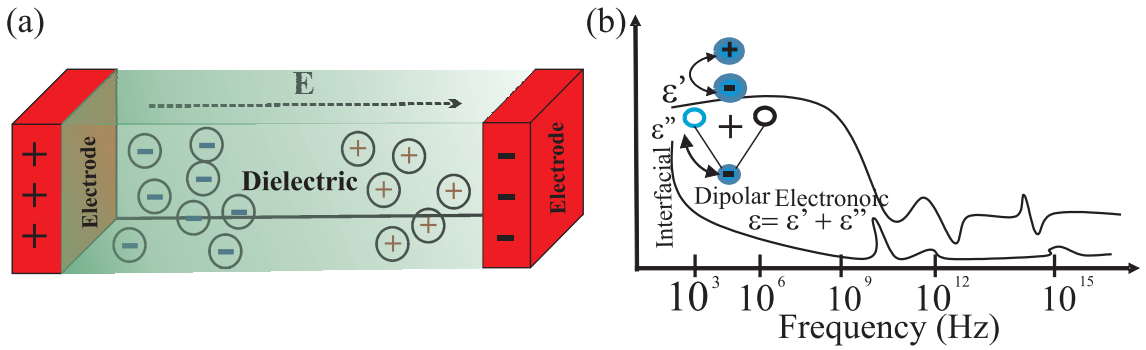

Figure 4.1.1: (a) Polarization mechanism in dielectric materials (b) polarization distribution with respect to the frequency.

properties of studied ceramics obtained from continuous-wave terahertz (CW-THz) spectroscopy will be presented. Hereby, the structure of the coming chapter will be briefed.

4.2 Experimental Details

The detail material synthesis process of $BiFeO_3$ (BFO), $Bi_{0.97}Y_{0.03}Fe_{0.95}M_{0.05}O_3$ [M= Mn:(BYFMO and Sc:(BYFSO)] is explained in the previous chapter. For dielectric studies, the 8 mm diameter pellets coated with silver paint on either side to make it capacitor like structure. The frequency-dependent dielectric measurements of BFO, BYFMO, and BYFSO ceramics were carried out at the various temperatures ranging between $30 - 210^0$ C using LCR meter [Novocontrol Technologies]. The THz spectroscopy measurements were carried out to explore the complex optical phenomena in un-doped BFO and its effects after Y-Mn/Sc co-doping. CW THz photomixing systems offer a low cost and compact solution to the conventional pulsed THz systems because of their use of semiconductor diode lasers. CW THz spectroscopy measurements were performed on un-doped and Y-Mn/Sc co-doped BFO system at the different temperatures ranging between 4-300 K. The low temperature is achieved by using a closed cycle refrigerator (CCR). Air is used as a reference during measurements for all materials.

4.3 Dielectric properties at extremely low frequency region (ELF)

4.3.1 Elemental substitution effect on the dipolar polarization of Y-Mn/Sc co-doped BFO ceramic

The relaxation process and conduction mechanism modulation of parent BFO and its co-doped (Y-Mn/Sc) compounds were studied by using frequency-dependent dielectric properties at various temperatures. The effects of co-doping on the dielectric properties of BFO have been explained with dielectric constant (ϵ_r) and tangent loss ($tan\delta$). However, the intrinsic electrical properties have been explored under impedance spectroscopy, complex electrical modulus, and conductivity techniques.

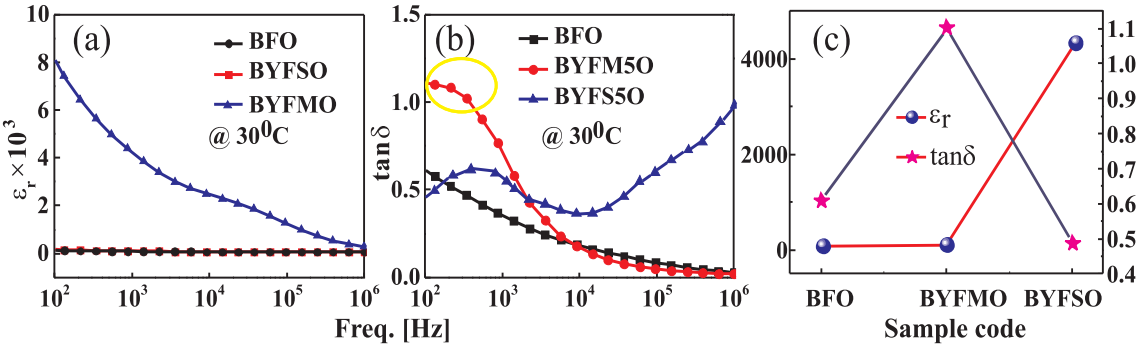

Figure 4.3.1: RT (a) dielectric constant (ϵ_r), (b) loss tangent ($tan\delta$), and their (c) comparative plots for BFO, BYFMO, and BYFSO ceramics.

Room temperature Frequency-modulation dielectric constant (ϵ_r) and tangent loss ($tan\delta$)

Figure 4.3.1 (a) shows the frequency-dependent ϵ_r for parent BFO and Y-Mn/Sc co-doped BFO ceramics at RT. ϵ_r decreases with the increase in frequency and found almost saturate at the high-frequency region due to the dielectric relaxation process and well supported by Koop's theory [194] and Maxwell-Wagner relaxation [195, 196]. The higher ϵ_r at the very low-frequency region is responsible due to the interfacial; however, with the increase in frequency, the dipolar polarization actively participates in the mechanism [197]. However, in the high-frequency region, the ionic and electronic polarization dominates the relaxation process, which causes the gradual drop-down of the ϵ_r. The increase in ϵ_r at 1 kHz for BYFMO [101 ϵ_r], BYFSO [4220 ϵ_r] from the vicinity of BFO [88 ϵ_r] indicate a systematic enhancement of dielectric properties of co-doped ceramics. The non-volatile nature of Bi^{3+} ions at the high sintering temperature and presence of O_{vs} leads to lower ϵ_r for BFO and BYFMO. However, the ϵ_r of BYFSO found almost 51 times than the BFO. Due to lower ionic radii of Y^{3+} than Bi^{3+}, it doesn't seem likely to create any larger vibration space in oxygen octahedral while may partially affect the FeO_6 octahedral cage. The increment in ϵ_r in co-doped ceramics due to the substitution of higher ionic radii Mn^{3+}/Sc^{3+} than Fe^{3+}, which causes FeO_6 octahedra distortion, as seen in our results. The distortion creates [change in Fe-O and Fe-O-Fe] FE strain, which is responsible for manipulating the dielectric constant. Also, the presence of space charge carriers may be another factor that influences the ϵ_r [198].

Figure 4.3.1 (b) displays the frequency-dependent $tan\delta$ plots for BFO, BYFMO, and BYFSO compounds. All loss tangent plots behave differently from each other, as observed from Fig. 4.3.1 (b). The loss value for parent BFO and BYFMO decreases with the increase in frequency. The behavior of the loss plot in BYFSO is quite strange, where it is found sharp increment at the low-frequency region may be due to the separation between the electrode and dielectric layer [42]. The appearance of relaxation peak in co-doped ceramics is attributed due to Debye relaxation [199]. The relaxation peak appears only when the frequency of hopping charge carriers matches the frequency of the applied electric field. The asymmetric broadening and shifting of relaxation peak towards the high-frequency region in BYFSO ceramic indicate the time distribution dielectric relaxation.

The variation of ϵ_r and $tan\delta$ at different doping elements are illustrated in Figure 4.3.1 (c). The excellent improvement in insulating properties at the low loss value, BYFSO promises for future

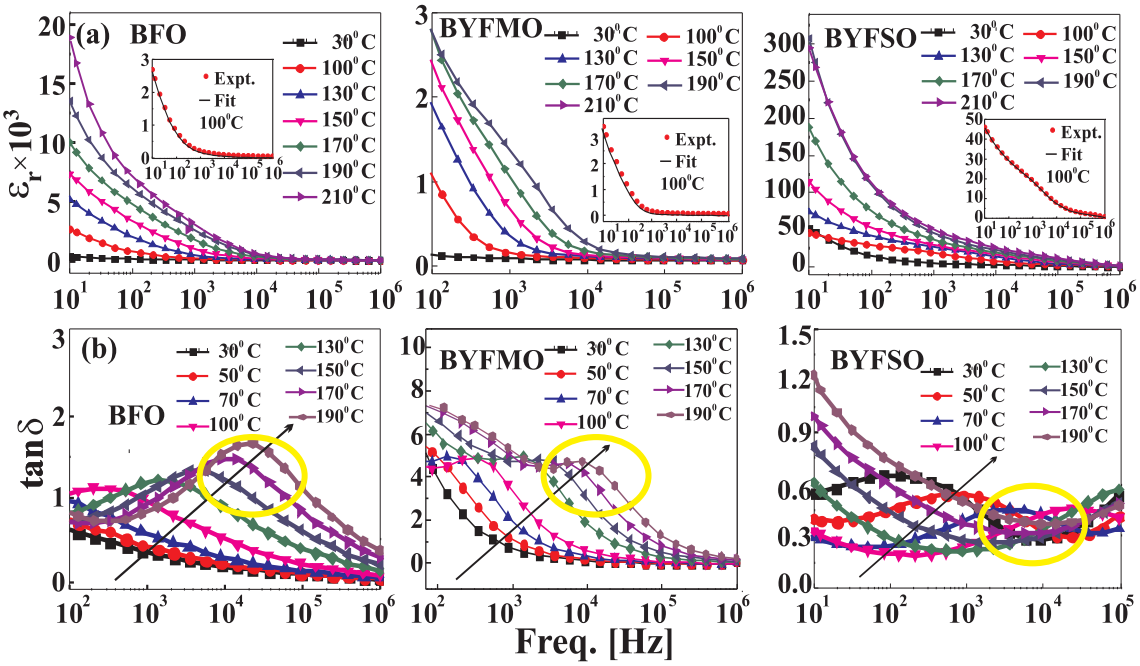

Figure 4.3.2: (a) Dielectric constant (ϵ_r), (b) loss tangent ($tan\delta$) at various temperature between $30^0 - 210^0$ C for BFO, BYFMO, and BYFSO ceramics.

scientific applications like memory, transformer, memristor devices.

Temperature-dependent frequency dependent dielectric constant (ϵ_r) and tangent loss ($tan\delta$)

Figure 4.3.2 (a) shows the frequency-modulated ϵ_r for BFO, BYFMO, and BYFSO ceramics at the various temperatures between $30^0 - 210^0$C measured in a wide frequency range between 10 Hz-1 MHz. The drop-down of ϵ_r with the increase in frequency is similar for all measured temperatures and is analogous to the dielectric behavior of the FE materials. Moreover, the magnitude of ϵ_r increases with the rise in temperature, confirming the dipoles are thermally activated. The interfacial and dipolar polarization improves the charge accumulation and easy orientation of dipoles at the higher temperature, which leads to enhancement in ϵ_r. The frequency variation of $tan\delta$ plots at various temperatures for BFO, BYFMO, and BYFSO ceramics are shown in Fig. 4.3.2 (b). For parent BFO, the loss peak seems to appear beyond 100^0 C when the hopping charge carrier resonates with the applied external field. However, the relaxation peaks start appearing near 70^0 and 30^0 for BYFMO and BYFSO, respectively confirming elemental substitution manipulating the relaxation process and shifted the peak towards the RT. For BYFSO, the relaxation peak is completely collapsed above 130^0 C. The loss peak shifts towards the higher frequency with the rise in temperature reinforces thermally assisted relaxation behavior. The loss values at higher temperature are above unity, which may be due to the increase in large O_{vs} concentration, results increase the conductivity [24]. The shifting of relaxation peak near RT motivates us to understand the enrich physics behind it and its possible applications.

The frequency dependent dielectric properties can be interpreted by empirical Cole-Cole relation [200]:

Table 4.3.1: Dielectric parameters extracted from Cole-Cole relation of BFO, BYFMO, and BYFSO ceramics at 100^0 C.

Sample code	ϵ_r at 10 kHz	$tan\delta$ at 10 kHz	ϵ_s	$\epsilon_\infty \times 10^{-4}$	τ (s)	α
BFO	157	0.51	2725	88	7.9	0.18 ± 0.002
BYFMO	233	0.84	3471	82	8.7	0.12 ± 0.004
BYFSO	19041	0.43	10152	15	19.2	0.09 ± 0.002

$$\epsilon^* = \epsilon'(\omega) - i\epsilon'' = \epsilon_\infty + \frac{\epsilon_s - \epsilon_\infty}{1 + (i\omega\tau)^{1-\alpha}} \tag{4.1}$$

The real (ϵ') and imaginary part (ϵ'') expressed as:

$$\epsilon' = \epsilon_\infty + \frac{(\epsilon_s - \epsilon_\infty)[1 + (\omega\tau)^{1-\alpha} Sin(\alpha\pi/2)]}{1 + 2(\omega\tau)^{1-\alpha} Sin(\alpha\pi/2) + (\omega\tau)^{2(1-\alpha)}}, \tag{4.2}$$

$$\epsilon'' = \epsilon_\infty + \frac{(\epsilon_s - \epsilon_\infty)(\omega\tau)^{1-\alpha} Cos(\alpha\pi/2)]}{1 + 2(\omega\tau)^{1-\alpha} Sin(\alpha\pi/2) + (\omega\tau)^{2(1-\alpha)}}, \tag{4.3}$$

where ϵ_∞ and ϵ_s are the high frequency and static dielectric constant, respectively. ω $(2\pi f)$ is the angular frequency, and τ is the most probable relaxation time. α is relaxation time distribution, which is varies between $\alpha \to 0$ *to* 1 and $\alpha > 0$ indicates relaxation has a relaxation times [200]. The extracted dielectric parameters at 100^0 C are listed in Table 4.3.1. For the present samples, the α values at 100^0 C are below one indicates the relaxation process deflected from the monodispersive Debye process ($\alpha = 1$).

4.3.2 Impedance Spectroscopy Analysis

The dielectric analysis only provides the physical sketch of the BFO and its immediate effect after co-doping. However, the true bulk effect can be understood by equivalent circuitry analysis related to grain and grain boundary. Impedance spectroscopy analysis ($Z'/Z''vs.frequency$) is a powerful approach to correlate the grain and grain boundary with the electrical parameters. The frequency and temperature dependence complex impedance can be expressed as [24]:

$$Z^* = Z_0(T) \int \frac{y(\tau, T)d(\tau)}{1 + j\omega\tau} \tag{4.4}$$

Z' and Z'' of complex impedance can be extracted from the above equation as:

$$Z' = Z_0(T) \int \frac{y(\tau, T)d(\tau)}{1 + \omega^2\tau^2} \tag{4.5}$$

$$Z'' = Z_0(T) \int \frac{(\omega\tau)^* y(\tau, T)d(\tau)}{1 + \omega^2\tau^2} \tag{4.6}$$

where ω, τ and $y(\omega, \tau)$ are the angular frequency, relaxation time and relaxation time distributions, respectively.

Frequency dependence real part of complex impedance for BFO, BYFMO, and BYFSO ceramics at various temperature are display in Fig. 4.3.3 (a). The low-frequency dispersive behavior of Z'

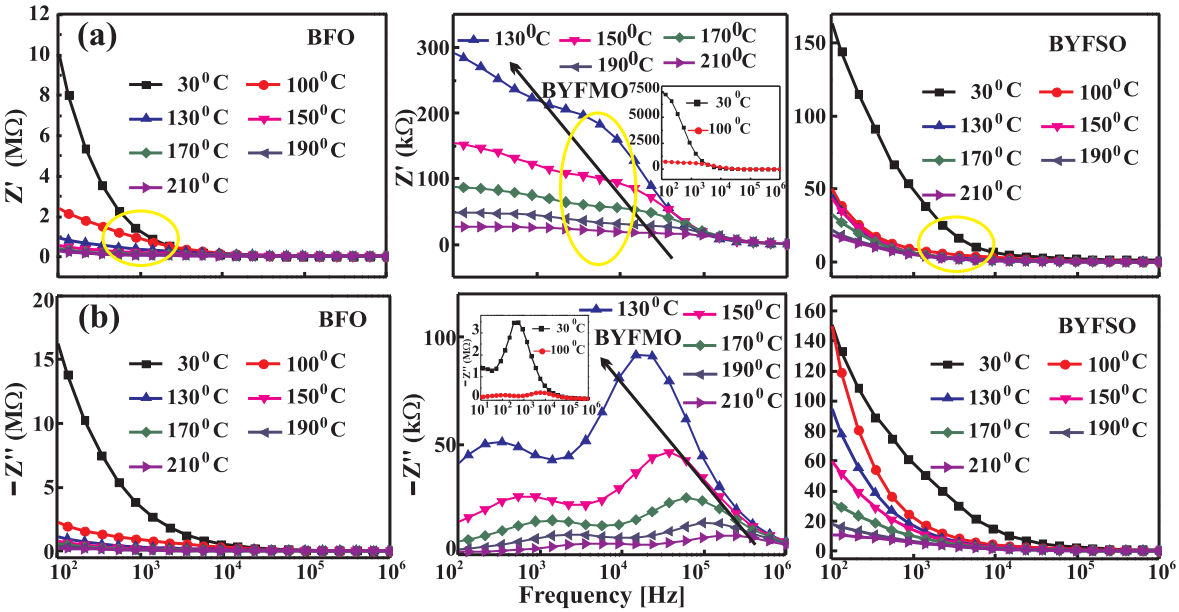

Figure 4.3.3: Frequency modulation (a) real part (Z') and (b) imaginary part (Z'') of complex impedance at various temperature for BFO, BYFMO, and BYFSO ceramics.

confirms the presence of dielectric relaxation in all studied materials. The Z' reduces with the rise in frequency for all temperature range due to the increase in hopping charge carrier, results in an enhancement in ac conductivity. All the studied samples behave as semiconducting material [band gap range $E_g = 2.08 - 2.18\ eV$], so the decrements in the magnitude of Z' with the increase in temperature can be expected due to negative temperature coefficient resistance (NTCR) effect. From the Fig. 4.3.3 (a), it is visualized that, for BFO and BYFSO, the Z' decreases systematically while BYFMO evident a relaxation peak in the mid-frequency range. The relaxation peaks appear only when the dipoles resonate with the frequency of the applied field. The fluctuation of the relaxation behavior of the elementary ion modified BFO system can be understood by the conduction mechanisms.

Figure 4.3.3 (b) depicts the frequency dependence Z'' at various temperatures of BFO, Y-Mn/Sc co-doped BFO ceramic system. The conduction mechanism of BFO, BYFSO, shows different characters from BYFMO. In the former, the Z'' shows dispersion behavior above $150^0\ C$, while for later, two broadened peaks are appeared at the various frequency range $10^2\ Hz - 10^3\ Hz$ and $10^4\ Hz - 10^5\ Hz$ confirms the manipulation of relaxation behavior. The low- and high-frequency relaxation peaks originated from the grain boundary and grain effect [172]. The origin of peaks may be due to unequal ionic radii of the parent [Bi^{3+}, Y^{3+}] and foreign ions [Fe^{3+}, Mn^{3+}], which may create defects like O_{vs} in addition to the charge carriers. The shifting of relaxation peak with the increase in temperature confirms extra thermal energy added to the applied field. Asymmetric broadening confirms the distribution of relaxation time [decrease in relaxation time period] [38].

The conduction mechanism in polycrystalline material can be explained with impedance spectroscopy Nyquist's plots ($Z' - Z''$). To explain the conduction mechanism, the bulk effects like grain and grain boundary effects due to the application of the electric field need to be understood. These effects with electric field response described in terms of successive semicircular arc obtained from

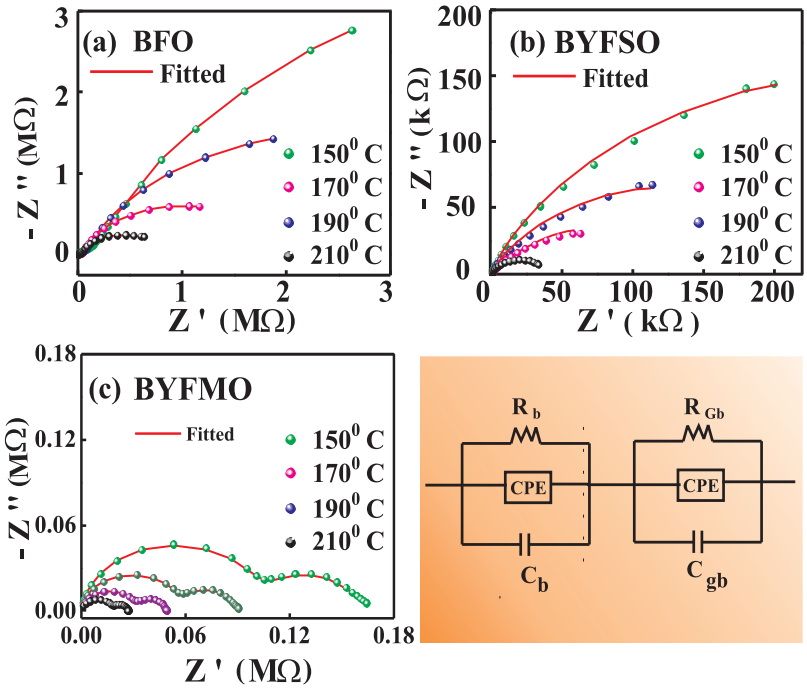

Figure 4.3.4: Nyquist's plots (a) BFO, (b) BYFMO, (c) BYFSO, and (d) equivalent electrical circuit to fit the Nyquist's plots.

the Nyquist's plots. The plots are explained with equivalent R-C circuits, where each semicircular arc is modeled as an equivalent electrical circuit. In polycrystalline material, the grain and grain boundaries are associated with semiconducting and insulating behavior, respectively. The appearance of the semicircular arc in the high-frequency region and the low-frequency region is due to grain and grain boundary effects, respectively. The impedance of equivalent R-C circuit cab be expressed as [201]:

$$Z^* = \frac{R_g}{1 + (j\omega R_g C_g)^{n_g}} + \frac{R_{gb}}{1 + (j\omega R_{gb} C_{gb})^{n_{gb}}} \tag{4.7}$$

where R_g, R_{gb}, C_g, and C_{gb} are the grain resistance, grain boundary resistance, grain capacitance, and grain boundary capacitance, respectively. n_g, n_{gb} represents the relaxation time variables of grain and grain boundaries respectively. Figures 4.3.4 (a-c) represents the Nyquist plots at different temperature for BFO, BYFSO, and BYFMO ceramics. The parent BFO exhibits two semicircular arc i.e., at higher frequency region due to the grain boundary effect and at the low-frequency region due to the grain effect. Y-Sc co-doping suppresses the diameters of semicircular arcs of BFO. However, Y-Mn co-doping marks a significant modification in the conduction process with the appearance of two complete semicircular arcs in BFO ceramics. The Nyquist's plots of all ceramics are well fitted with equivalent R-C or CPE (constant phase element) circuit with the EIS impedance modulus analyzer. The circuit comprises the parallel combination of the R-C circuit connected to another R-C circuit in series, as shown in Fig. 4.3.4 (d). The electrical parameters R_g, R_{gb}, C_g, and C_{gb} are extracted from fitting model are listed in Table 4.3.2. From the table, the $C_{gb} > C_g$ for all studied temperatures indicating the dominance of grain boundary effect in the conduction mechanism. The R_g and R_{gb} values are reduced with increasing temperature due to the NTCR

Table 4.3.2: Electrical parameters extracted from equivalent electrical R-C circuitry model of BFO, BYFMO, and BYFSO ceramics.

Sample	T (^{0}C)	R_g (MΩ)	R_{gb} (MΩ)	C_g (nF)	C_{gb} (nF)
BFO	150	0.55	0.4	0.08	0.74
	170	0.38	0.12	0.23	1.7
	190	0.1	0.04	2.18	6.4
	210	0.007	0.009	4.71	11
BYFMO	150	0.53	0.43	0.02	0.42
	170	0.21	0.15	0.18	2.06
	190	0.09	0.07	2.53	4.84
	210	0.04	0.043	2	6.23
BYFSO	150	1	0.52	0.02	6.59
	170	0.75	0.24	0.26	5.06
	190	0.13	0.11	3.53	6
	210	0.03	0.07	7	8.2

effect and increase in the density of O_{vs} [202]. The semicircular arc is depressed, with the rise in temperature towards the real $Z' - axis$ due to the thermal effect. The improved grain resistance in BYFSO ceramic indicates the improvement of barrier properties for the flow of charge [198].

4.3.3 Complex Modulus Analysis

The electrical modulus study is a powerful tool to investigate the microscopic behavior of the dielectric materials. The modulus behaves exactly in the opposite way to the dielectric constant (ϵ_r) i.e., the magnitude of modulus is saturated at the low-frequency and is maximum at the high-frequency region. In modulus calculation, the intensity of relaxation peaks is inversely proportional to the capacitance of the material. The impedance analysis [$C_{gb} > C_g$] ensures the grain boundary capacitance plays a critical role in the conduction process. The relation involving M^* and Z^* expressed as [203]:

$$M^* = M' + M'' = i\omega C_0 Z^* = i\omega C_0 (Z' - iZ'') = \omega C_0 Z'' + i\omega C_0 Z' \tag{4.8}$$

where ω is the frequency of applied electric field, and C_0 is the capacitance in the vacuum. Figure 4.3.5 (a) shows the frequency modulation of the real part (M') of the electrical modulus at various temperatures for un-doped BFO and Y-Mn/Sc co-doped BFO ceramics. At the low-frequency region, the value of M' is very weak, approximately close to zero due to the high capacitive nature of the material and showing dispersion behavior with an increase in frequency. The magnitude of M' is minimal from low- to high-frequency region, suggesting negligible electrode polarization phenomenon in the test materials [204]. The dispersion region of BFO and BYFMO ceramics shifts towards the high-frequency region with increasing the temperature indicate the polarization is thermally activated. However, for BYFSO, an asymmetric broadened peak was evident at mid-frequency range near RT and almost disappeared for higher-order temperature. The magnitude of M' decreases with increase in temperature due to an increase in capacitance which follows the relation:

$$C = \frac{\epsilon A}{d} \tag{4.9}$$

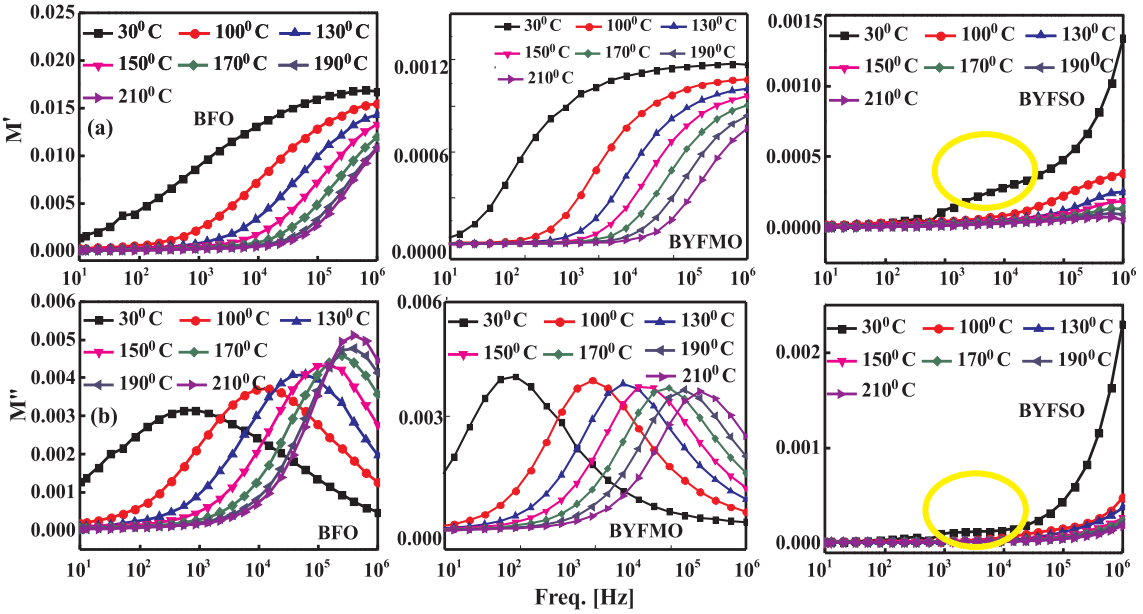

Figure 4.3.5: Frequency modulation (a) real part (M') and (b) imaginary part (M'') of complex electrical modulus at various temperature for BFO, BYFMO, and BYFSO ceramics.

where C is the capacitance, A is the area, and d is the thickness of the sample. Hence, the decrease in electrical modulus is expected.

Frequency dependence of the imaginary part (M'') of complex modulus at different temperatures of studied compounds is shown in Fig. 4.3.5 (b). M'' of BFO and BYFMO exhibit sharp non-Debye type relaxation peaks for all examined temperature range. The obtained relaxation peak shifts towards the higher frequency region with the increase in temperature confirms the relaxation being affected by thermal energy. M'' of BFO and BYFMO ceramics is minimal at the low-frequency region and increases to a maximum M''_{max} and again decreases with further increase in frequency. However, Y-Sc co-doping broadened the relaxation peak of BFO at RT and completely disappeared at a higher temperature. This confirms elemental substitution manipulate the relaxation behavior in BFO and promising for potential applications. The area below the maximum M'' is acting a potential well, where the transport of charge carriers occurs from one region to another region with long-range hopping. Whereas, the region outside the well hopping of charge carriers is short ranged [202, 205]. The frequency (ω_{max}) corresponds to the maximum imaginary complex modulus (M_{max}) gives the most probable relaxation time (τ_{max}) for the charge carriers. The Arrhenius equation, as a function of frequency and temperature, expressed as:

$$\omega_{max} = \omega_0 \exp(\frac{-E_a}{kT}) \tag{4.10}$$

where ω_0 and E_a are the exponential factor and activation energy (E_a), respectively. The Arrhenius plots between $ln\omega_{max}$ and $\frac{1000}{T}$ are shown in Fig. 4.3.6. The calculated activation energy for all compounds is given in Table 4.3.3. Generally, for a perovskite oxide material, the range of activation energy for singly ionized oxygen vacancy lies between 0.3-0.5 eV, whereas for doubly ionized oxygen vacancy, the range of activation energy lies between 0.6-1.2 eV [206]. Hence, the change in insulating behavior in the presently studied compounds can be believed due to the doubly ionized oxygen

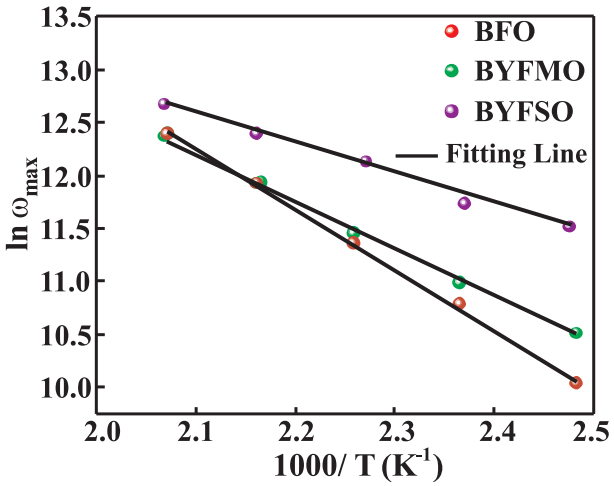

Figure 4.3.6: Arrhenius plots obtained from $ln\omega$ vs $\frac{1000}{T}$ of BFO, BYFMO, and BYFSO ceramics.

Table 4.3.3: Activation energy extracted from the Arrhenius plots of lnω vs $\frac{1000}{T}$ and $ln\sigma_{ac}$ vs $\frac{1000}{T}$ for BFO, BYFMO, and BYFSO samples.

Sample code	$ln\omega$ vs $\frac{1000}{T}$	From lnσ_{ac} vs $\frac{1000}{T}$			
		1 kHz	10 kHz	1000 kHz	1 MHz
BFO	0.69±0.02	0.86	0.37	0.19	0.08
BYFMO	0.75±0.04	1.76	0.36	0.13	0.10
BYFSO	0.89±0.04	1.20	0.91	0.86	0.64

vacancy.

4.3.4 Conductivity Studies:

Figure 4.3.6 manifests the ac conductivity behavior of un-doped and Y-Mn/Sc co-doped BFO ceramics with the response to the applied electric field. The conduction mechanism in dielectric materials depends on the movement of loosely bound charge carriers under the application of the applied electric field. The ac conductivity of dielectric materials follows the Jonscher's power rule [207]:

$$\sigma_\omega = \sigma_{dc} + A\omega^n \tag{4.11}$$

where σ_ω and σ_{dc} stands for net conductivity and dc conductivity of the material, respectively. *'A'* is the pre-exponential factor, and *'n'* value represents the degree of interaction between the mobile charge ions and the lattices [208]. Figure 4.3.7 (a) elucidate both the experimental and theoretical [Jonscher's power rule fitted] plots for the frequency-dependent ac conductivity spectrum at various temperatures. From the σ_ω vs frequency plots, it is evident that the conductivity spectrum consists of two main regions (i) I- the low-frequency region corresponds to grain boundary conduction and (ii) II- the high-frequency region corresponds to grain conduction. The magnitude of σ_{ac} increases with the increase for the temperature of $30^0 - 210^0$ C due to the creation of O_{vs} during the sintering process. The electrical parameters like σ_{dc}, *'n'* are calculated from the fitting results. The values of σ_{dc} at 100^0 C for BFO [region-I: 93×10^{-6} $(\Omega - m)^{-1}$, II: 71×10^{-6} $(\Omega - m)^{-1}$], BYFMO [region-I: 79×10^{-6} $(\Omega - m)^{-1}$, II: 54×10^{-6} $(\Omega - m)^{-1}$], and BYFSO [region-I: 56×10^{-6} $(\Omega -$

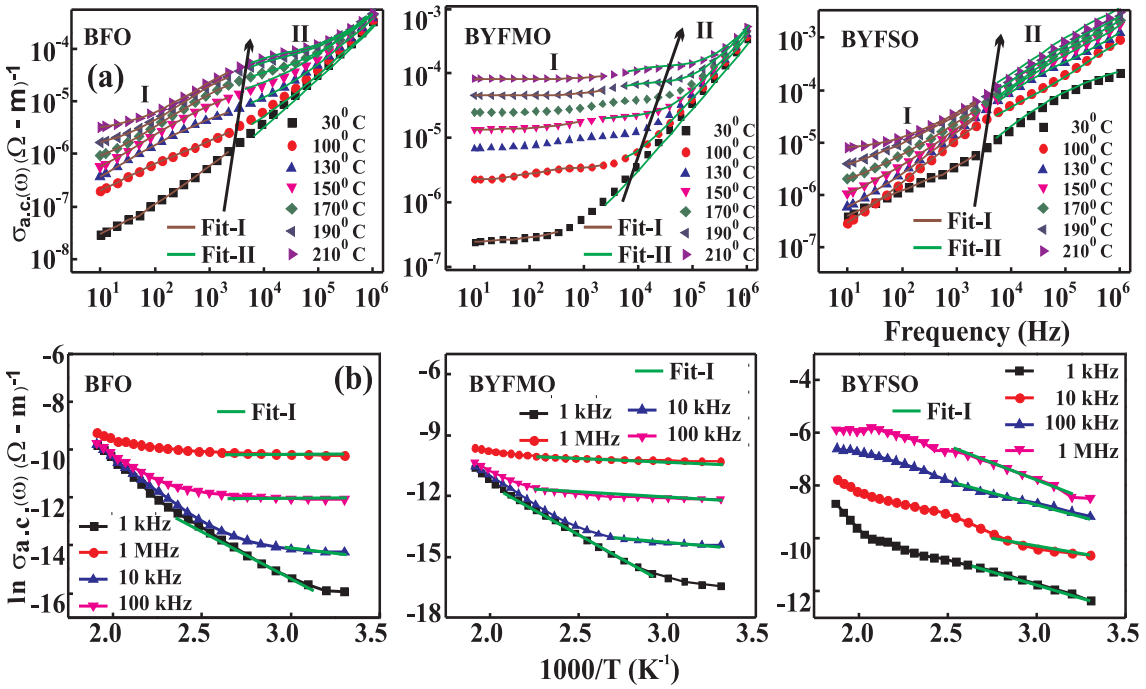

Figure 4.3.7: (a) Frequency dependent ac conductivity and (b) Arrhenius plots of $ln\sigma_{ac}$ vs $\frac{1000}{T}$ for BFO, BYFS5O, and BYFS10O ceramics.

$m)^{-1}$, II: 43×10^{-6} $(\Omega - m)^{-1}$] indicating the improved insulating properties of the co-doped ceramics. The variation of n with respect to temperature suggests the existence model, which explains the conduction mechanism of the ceramics. The different conduction models like quantum mechanical tunneling (QMT) [n is independent of temperature], correlated barrier hopping (CBH) [n decreases with increase in temperature], small polaron conduction (SPC) [n increases with increase in temperature], and overlapping large polaron tunneling (OLPT) [n reaches minimum followed by further increase in temperature] are explains the conduction process in dielectric ceramics [209, 210]. In the present ceramics, the *'n'* value for both the region-I and region-II decreases with the increase [Appendix-I] in temperature indicate the conduction mechanism follows the CBH model and are thermally assisted.

The activation energy (E_a) for BFO, BYFMO, and BYFSO calculated from temperature dependent Arrhenius plots are shown in Fig. 4.3.7 (b). The expression relating σ and E_a can be written as:

$$\sigma = \sigma_0 \exp(\frac{-E_a}{k_\beta T}) \tag{4.12}$$

The calculated E_a values for all compounds at different frequency is shown in Table 4.3.3. For parent and Y-Mn/Sc co-doped BFO, the activation energy decreases with the increase in frequency mainly due to long-range O_{vs}, which plays a significant role in the conduction mechanism.

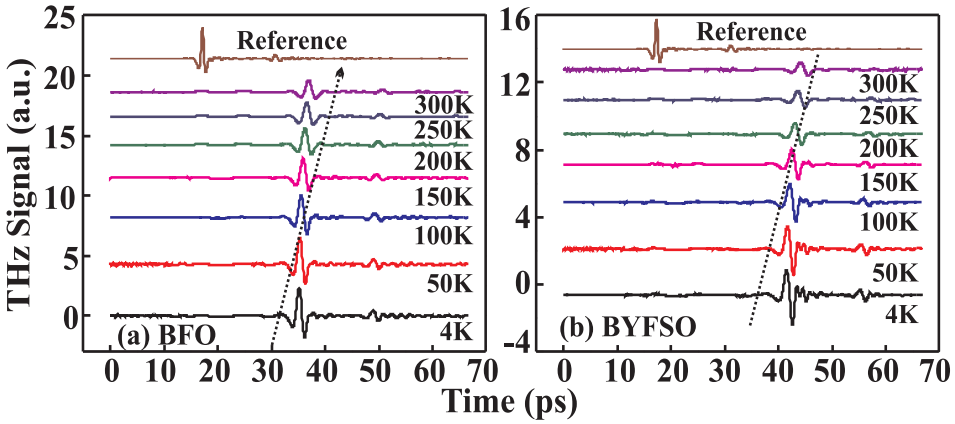

Figure 4.4.1: (a) Terahertz time-domain spectra obtained from BFO and BYFSO compounds.

4.4 Temperature-dependent continuous-wave terahertz (CW-THz) spectroscopy studies

The orthoferrites based semiconductor and insulators, have shown magnon softening near some various spin orinetation temepratures, colossal magnon-coupling, and symmetry exchnage coupling mechnaism [211]. Various theoretical models and analysis predict the existence of electromagnons (spin waves coupled to polar phonons) in multiferroic [212]. The existence of electromagnons in MF BFO single crystal was first evident in 2008 [213], while magnon-phonon coupling found in BFO thin-films [214]. The multiferroic BFO has two magnon branches, which are noted as u and k. The modulation of u and k magnon frequency with an external electric field was observed 30% and 15%, respectively, which suggest a very long time taken by the electric field to control the magnons [215]. Why was such a long time taken to show the electric control of BFO magnons? One answer lies in the difficulty to observe magnons at RT. The section will explained salient features of temperature-dependent THz signal generated from the non-magnetic Y-Sc co-doped BFO ceramics and its related optical properties.

Time-domain THz signal

The time-domain signal at various temperatures for un-doped and co-doped BFO compounds along with reference (air) signal is diaplayed in Fig. 4.4.1. The accuracy of time period measurement can be achieve 0.05 ps under the CW-THz system. Figure 4.4.1 (a) shows there are some oscillating signals (30-40 ps) are appeared before the original transmitted pulses (near to 50 ps) from the compounds, which evident to be generation of THz radiation signals. The THz signal is shifted towards the higher time period with rise in the temperature, which confirms the electromagnetic radiations are thermally activated. However, Y-Sc co-doping shifts both regular oscillating peaks (between 40-50 ps) and transmitted signals (near to 55 ps) of BFO towards the higher time-period. The shifting of the THz signal in co-doped compound may be due to the voids created by Sc^{3+} at Fe^{3+} [216] and defects. But both the MF ceramics shown well enough THz signal, which may useful for future potential applications.

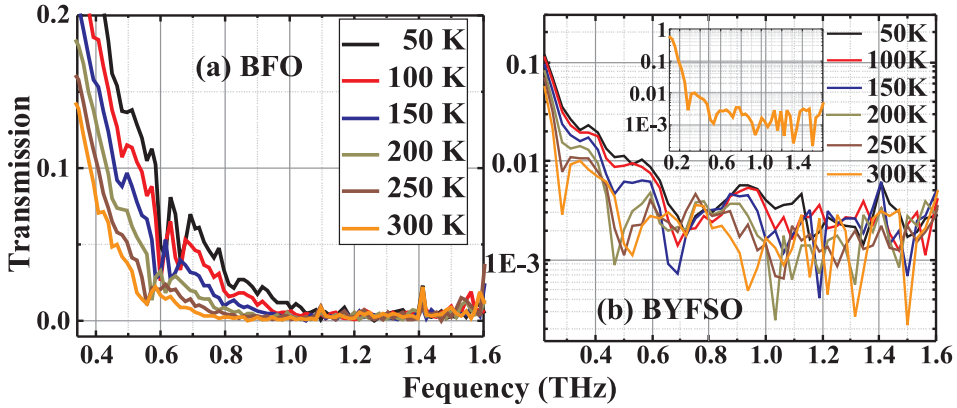

Figure 4.4.2: (a) Transmission spectra obtained from First Fourier Transform (FFT) of time-domain spectra of BFO and BYFSO ceramics.

Frequency-domain THz transmission signal

The Fast Fourier Transform (FFT) of time-domain spectra provides the amplitude and phase of the THz transmission spectrum from the BFO and BYFSO ceramics shown in the Fig. 4.4.2 studied in the temperature range 4-300 K. Only a partial spectrum is presented for better observable. Both the ceramics shows appreciable signal at THz region. The intensity of terahertz spectra gradually decreases with increase in THz frequency for all studied temperature indication of high carrier momentum relaxation time. The intensity of spectra further decreased with increase in temperature due to the decrease in mobility at higher temperature. For BFO, two weak kinks are found in transmitted spectum near the resonated frequencies at 0.25 THz and 0.55 THz and the later region may associated with AFM mode [159]. However, BYFSO exhibit high intense transmission peaks as compared to the parent, indicates the improved AFM order [216]. The resonate frequency of AFM mode is exhibit blue shifts as rise in temperature. The effect of temperature on the resonate frequencies more prominent below 200 K in BYFSO ceramic. Below 50 K, the frequency of AFM mode shifted from 0.55 THz to 0.62 THz. At ultra-lower temperature, the AFM modes becomes more harder at 0.72 THz and the resonant strength becomes weakening at higher thermal energy. The transmission spectrum evident for AFM order at RT, while the exact contribution of FM order due to D-M exchange interaction cannot be resolved properly.

Room temperature THz optical phenomena of non-magnetic tuned multiferroic $BiFeO_3$ compound

The THz spectra for un-doped and co-doped BFO system were successfully measured in the temperature range between 4-300 K. The complex refractive index can be determined by using the expression:

$$N(\omega) = n(\omega) + ik(\omega) \tag{4.13}$$

where N depends on the complex permittivity (ϵ^*) and permeability (μ^*) through $N = \epsilon^* \times \mu^*$ for magnetic systems. The THz optical constants refractive index (n) and extinction coefficient (k) extracted from the THz measurements. Since we are looking at the THz signal contributing to

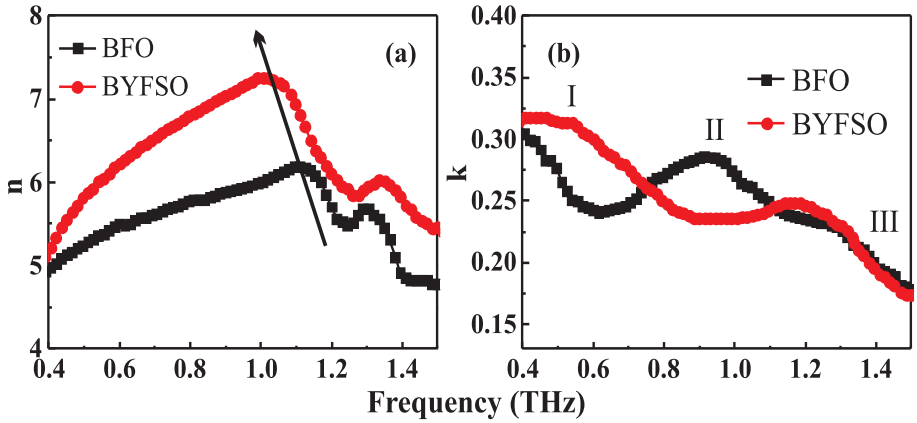

Figure 4.4.3: (a) Refractive Index (n) and (b) extinction coefficient (k) of BFO and BYFSO ceramics.

the magnons and phonons, the variation of n and k as a function of frequency only displayed in the Fig. 4.4.3. Figure 4.4.3 (a) shows the refractive indices of BFO and BYFSO with response to frequency in THz region. The obtained value of n for BFO and BYFSO are 4.2 and 5.5 at 0.5 THz indicating Y-Sc co-doping improved the refractive index of the material. The value of n found higher in co-doped ceramics in entire frequency region. However, the value of k at low frequency region only with 0.24 and 0.32 for BFO and BYFSO, respectively at 0.6 THz. The increase in optical constants after co-doping may be due to the softening of phonon mode and rise in phonon damping [217]. The sharp decreasing of n at low frequency region due to the suppression of free-electron gas behavior of the materials. From the Fig. 4.4.3, both n and k exhibit broadening peaks in the THz region. Co-doping shifts the peak of n towards high frequency region while behaves oppositely for the k spectra. The obtained values and appearance of peaks indicates the insulating behavior of the compounds.

The complex dielectric constant (ϵ^*) of BFO and BYFSO compounds is investigated both in extremely low frequency (ELF) and THz region. Figures 4.4.4 (a)-(b) depicts RT frequency modulated real (ϵ') and imaginary (ϵ'') part of ϵ^* for BFO and BYFSO, respectively. Both ϵ' and ϵ'' decreases with increase in frequency and attain saturation at high-frequency region due to Maxwell-Wagner relaxation. The interfacial and dipolar polarizations are dominate the dielectric properties in ELF region. The ϵ' of BYFSO (=3939.41) increases almost 51 times from the vicinity of BFO (=75.86) due to its single phase structure, oxygen octahedra distortion, and homogeneous grain distribution [218]. The non-magnetic ion modified BFO is a special class of MF system where the many-body effect found strong. ϵ' and ϵ'' can be extracted from the value of n and k from the expression [219]

$$\epsilon' = n(\omega)^2 - k(\omega)^2 \tag{4.14}$$

$$\epsilon'' = 2n(\omega)k(\omega) \tag{4.15}$$

ϵ' and ϵ'' at THz region behave in different way as compared to ELF. The real and imaginary dielectric constant exhibits a similar dispersion behavior to n and k, respectively. The ϵ' for both the ceramics exhibit similar behavior. The spectra can be observed in two region at the either side of 0.9 THz. ϵ' increases with increase in frequency and attains maximum at 0.9 THz and starts

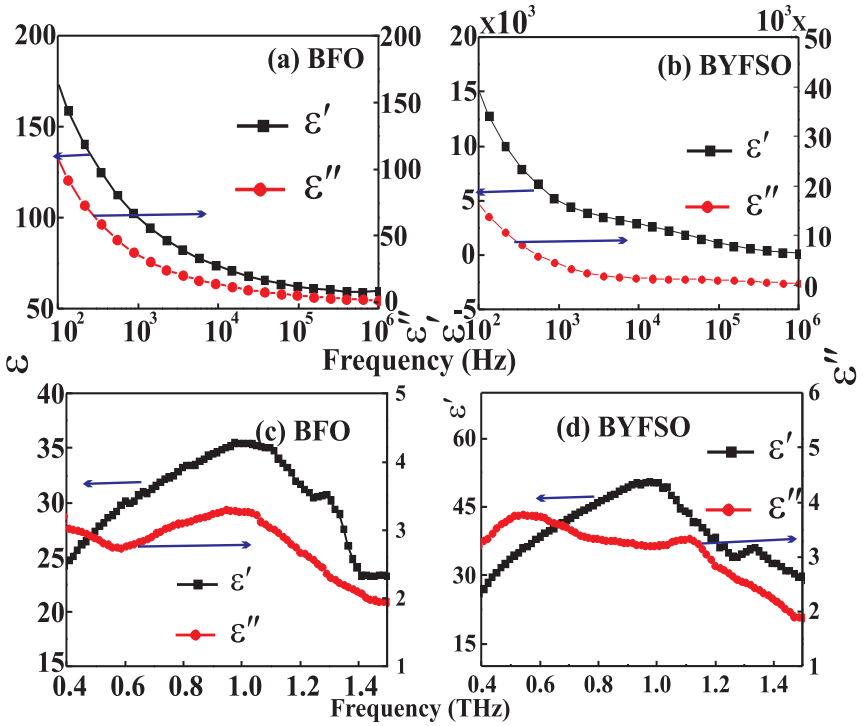

Figure 4.4.4: Extremely low frequency (a) ϵ', (b) ϵ'' and terahertz frequency (c) ϵ', (d) ϵ'' of BFO and BYFSO ceramics.

further decreasing with increase in frequency. The relaxation peak is appeared at higher frequency region of both the ceramics. The dispersive behavior of ϵ'' are varied with the frequencies. Below 0.57 THz, the value of BFO smoothly increase upto 0.4 THz, while follow opposite after co-doping. The behavior of ϵ'' follow similar trend for both ceramics. The appearance of dispersive nature may modulation of polarization relaxation at various frequencies or the scattering effects from THz EM waves [220]. However, the magnitude of ϵ' and ϵ'' found improved in comparison to parent, which also evident in ELF region.

The optical conductivity is an important property of the material. The conductivity can be extracted from the dielectric constant and only the real conductivity of the BFO and BYFSO is represent in Fig. 4.4.5. At low frequency region the conductivity of both ceramics found close, about 0.55 S/cm at 0.4 THz. The conductivity keeps increasing with rise in frequency and reaches 0.2 S/cm and 0.16 S/cm for BFO and BYFSO at 1.25 THz, respectively and indicate co-doping improves the insulating properties of BFO. To analogous this, the conductivity of both ceramics measured at ELF region between the frequency range 10 Hz-1 MHz at RT as shown in the inset of Fig. 4.4.5. Like THz, the conductivity is found minimum at the low-frequency, while maximum at the higher frequency region. The spectra also evident improved insulating properties after co-doping. The THz conductive spectra tried to fit with Drude, Lorentz, Drude-Smith, Drude-Loretz models, however the Drude-Smith model found the best fit to it. The Drude-Smith model is expressed as:

$$\sigma(\omega) = \frac{\frac{Ne^2\tau}{m^*}}{1 - i\omega\tau}[1 + \frac{c_1}{1 - i\omega\tau}] \tag{4.16}$$

c_1 represents the fraction of initial velocity of carriers which retained after a collision and can vary

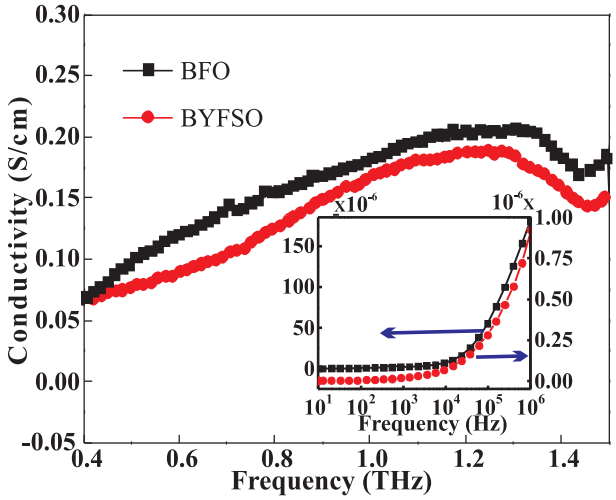

Figure 4.4.5: Frequency variation conductivity of BFO and BYFSO ceramics in THz region [inset: extremely low frequency region]s.

between 0 to -1 [$c_1 = 1$ Drude conductivity, $c_1 = -1$ complete carrier backscattering. e, τ, N, m^* are the charge, scattering time, charge carrier density, and effective mass. The Drude-Smith model effectively fitted to conductivity spectra of TiO_2 and ZnO nano-particles arrays [221, 222]. The extracted RT carrier density for BFO and BYFSO ceramics are $1.58 \times 10^1 6$ and $3 \times 10^1 6$. The scattering time for BFO reduces after Y-Sc co-doping ($32\ fs \rightarrow 25\ fs$) at RT. However, the charge carriers of both the conductivity spectra follows the correlated barrier hopping (CBH) model [223].

4.5 Summary

In summary, we have explored the modulation of dipolar polarization and relaxation behavior of multiferroic BFO with elementary substitution (Y-Mn/Sc) effect. A perfect correlational between the extremely low frequency and THz dielectric properties is obtained. The room temperature dielectric constant (ϵ_r) of BFO enhance 51 times after Y-Sc co-doping. The tangent loss peak slowly shifts towards the room temperature in the path $BYFMO$ [70^0 C] $\rightarrow$ $BYFSO$ [30^0 C], which was originally appeared above 100^0 C for the parent compound. The relaxation peak retains up to higher temperatures for BFO and BYFMO while wholly suppressed at a higher temperature for BYFSO. The grain resistance and grain boundary capacitance dominate the conduction mechanism for un-doped and co-doped BFO ceramic and are thermally assisted. The insulating behavior of co-doped ceramics modified due to the presence of doubly ionized oxygen vacancies. The conduction mechanism of all compounds follows the correlated barrier hopping (CBH) model and long-range oxygen vacancies when associated with thermal energy. The Y-Sc co-doped BFO compound produces intense THz signal in comparison to parent BFO, where the ϵ_r is nominal. The optical properties like complex refractive index, dielectric properties improved after Y-Sc co-doping. Weak conductivity in BYFSO indicates smaller leakage current. After analyzing the results obtained from *Chapter-1 and 2*, the BYFSO compound possesses improved multiferroic and magnetoelectric effect along with dielectric properties, which indicates multifunctional behavior. Currently, bulk BFO is not suitable for practical application; the physical properties of Y-Sc co-doped BFO need to discuss in thin-film

material, which will deeply explain in the *Chapter-5*.

Chapter 5

Electrically tuned stable ferroelectric switching in non-magnetic ion modified $BiFeO_3$ films

5.1 Introduction

In recent years, multiferroic (MF) materials having an enormous impact on the scientific community due to the possibility of tuning the magnetic ordering by an electric field and vice versa [224]. These materials possess the simultaneous coexistence of ferroelectric (FE), ferromagnetic (FM), ferroelastic, antiferromagnetic, etc. in a single phase. The presence of these parameters not only useful to understand the enrich physics but also provides depth information regarding many-body systems like magnetoelectric (ME) effect, piezoelectric (PE), magnetostrictions, etc. Recently, there has been much attention to the inherent properties associated with the FE or FM domain walls of perovskite systems [225]. Hence, the manipulation of room temperature (RT) MF properties of $BiFeO_3$ (BFO) thin films by domain wall engineering has tremendous prosperity to unveil the possible scientific phenomena for practical applications.

For rhombohedral FE materials, the non-180^0 polarization switching is most significant. It is known that 180^0 FE domain switching doesn't change the crystal structure, while non-180^0 FE domain switching may modify the elastic and magnetic properties of the rhombohedral system. Non-180^0 domain switching disturbed the switched domains, which may lead to losing the storage information in non-volatile system [45]. The magnetoelectric coupling (MEC) in the rhombohedral FE material is possible only when the non-180^0 domains switches under the applied electric field. Piezoresponse force microscopy (PFM) [226] has the advantage to study both FE and PE properties of the materials due to its high piezo-actuation sensitivity, spatial resolution, and ease of implementation [227]. Polycrystalline BFO based films exhibit different switching angles (71^0, 109^0, and 180^0), which may be useful for multistate memory device applications.

We obtained excellent MF properties in the single-phase non-magnetic (Y-Sc) modified BFO

ceramic system. The applications in bulk ceramic system restricted due to the presence of leakage current, SSMS, and some other defects in BFO. This motivates us to understand the physical origin of MF properties of Y-Sc co-doped BFO in thin-film material. In this chapter, we examine the physical properties of MF $BiFeO_3$ (BFO), Y-doped $Bi_{0.90}Y_{0.10}FeO_3$ (BYFO) and Y-Sc co-doped $Bi_{0.97}Y_{0.03}Fe_{0.95}Sc_{0.05}O_3$ (BYFSO) films. The change in the properties from $pristine \rightarrow doping \rightarrow co-doping$ was carefully examined. The structural, microstructural, magnetic, and electronic properties of Y-doped and Y-Sc co-doped BFO explained to understand the origin of MEC. This chapter explains the salient features regarding stable FE switching in non-magnetic modified BFO films. The electromechanical or PE properties of the films (BFO, BYFO, and BYFSO) deals for possible future memory storage applications.

5.2 Experimental details

BFO, BYFO, and BYFSO were deposited on glass or fluorine-doped tin oxide (FTO) coated glass substrate by using sol-gel spin coating technique. $Bi(NO_3)_3.5H_2O$ (BNH), $Y(NO_3)_3.5H_2O$ (YNH), $Fe(NO_3)_3.9H_2O$ (FNH), and $Sc(NO_3)_3.xH_2O$ (SNH) are used as starting raw materials. For 0.01-mole solution of BFO, BNH (5.0932 g) and FNH (4.0399 g) dissolved in 2-methoxy ethanol to make a complete solution. Similarly, for Y-doped BFO solution 4.5402 gm of BNH, 0.3449 gm of YNH, 3.8379 gm of FNH raw powders were taken. However, for the BYFSO solution, 4.9403 gm of BNH, 0.1149 gm of YNH, 3.8379 gm of FNH, and 0.1155 gm of SNH were used. The solution stirred for 20 minutes at 80^0 C to obtain a clear solution with the immediate addition of ethylene glycol and acetic acid to continue the chemical reaction for the next twenty minutes. Further, the solution was cooled down to RT and stirred for the next twelve hours to obtained the desired gel. The concentration of the final solution was maintained to 0.25 mol/L. The gel was spin-coated on the substrate for 40 s at 3000 rpm, and this process was repeated twice to obtained desired film thickness. The films were under heat treatment at 550^0 C for 2 hours to get the desired phase.

The crystallography structure and phase analysis were investigated with X-ray diffraction technology (PanAnalytic, $Cu\ K\alpha$, 1.54 A^0). The structural analysis further examined for all films with transmission electron microscope (JEOL). Field -effect scanning electron microscopy (Zeiss ultra 55 FESEM) and atomic force microscopic (NX10 AFM) imaging performed to understand the surface microstructure and roughness of the films with various resolutions (Zeiss). Magnetic measurements were performed by vibrating scanning magnetometer (ADE Technologies USA, EV7), superconducting quantum interference device (Cryogenic), and magnetic force microscope (MFM) technique. Electromechanical properties were performed on all film with various bias voltage under the piezo-force microscopy (NX10 & Bruker). Capacitance-voltage (C-V) measurement carried out for both films with Capacitance bridge AH2700A. Electric field controlled polarization for all films demonstrated by using P-E loop tracer at frequency 50 Hz. The FE domain switching was performed on BYFSO/STO(110) substrate under applied dc bias ± 10 V.

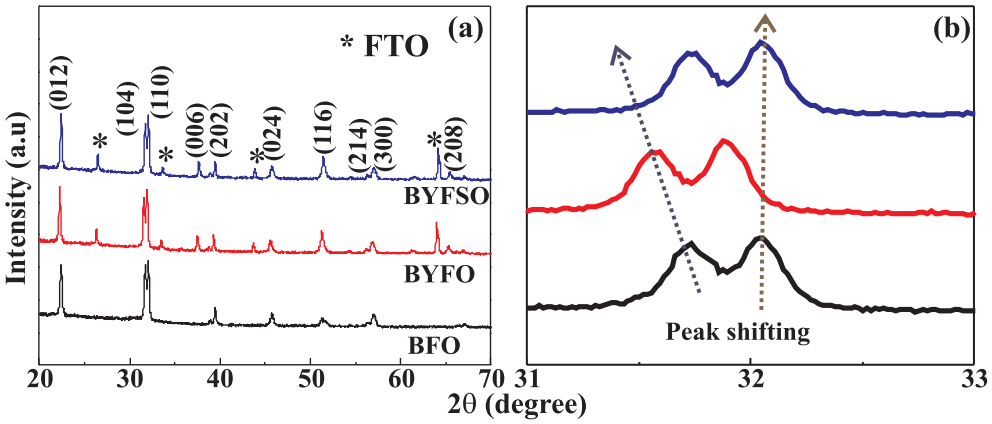

Figure 5.3.1: (a) X-ray diffraction pattern (b) shifting of primary peaks for un-doped BFO, doped BYFO, and co-doped BYFSO films.

5.3 Structural and Microstructural Analysis

Structural verification under X-ray diffraction pattern

Figure 5.3.1 shows the XRD patterns for BFO/glass, BYFO/FTO, and BYFSO/FTO systems. Doping or co-doping didn't induce any major structural transformation evident from the results. $*$ represents the FTO phases that appeared along with modified BFO films. All present films exhibit single-phase rhombohedral structure with space group R3c (JCPDA no.- 86-1518). The major rhombohedral peaks of BFO disturbed after the addition of Y-Sc, as shown in Fig. 6.1.1 (b), which was also noticed in bulk system. The shifting of these peaks evident due to the minimal ionic radii difference between Y^{3+} (1.04 $\AA$)-Bi^{3+} (1.17 $\AA$) and Sc^{3+} (0.754 $\AA$)-Fe^{3+} (0.654 $\AA$), which induce the structural distortion. The lattice parameters (*a, b, and c* and the volume (V) of the unit cell modified in BYFO and BYFSO film, which is given in Table 5.3.1.

The change in these parameters indicates the FeO_6 octahedral cage distortion, which will play a major role in multiferroic properties. The indirect evident for such type of distortion can be identified by using Goldschmidt tolerance factor (t) expressed as [228]:

$$t = \frac{[(1-x)r_{Bi^{3+}} + xr_{Y^{3+}} + r_{O^{2-}}]}{\sqrt{2}[(1-y)r_{Fe^{3+}} + yr_{Sc^{3+}} + r_{O^{2-}}]} \tag{5.1}$$

where $r_{Bi^{3+}}, r_{Y^{3+}}, r_{Fe^{3+}}, r_{Sc^{3+}}, and\ r_{O^{2-}}$ are corresponds to the ionic radii of Bi^{3+}, Y^{3+}, Fe^{3+}, Sc^{3+}, and O^{2-} ions, respectively. The calculated t for all film is found smaller than the ideal perovskite crystal structure, as shown in Table 5.3.1 (t=*1*) [229]. The values below unity recommend the presence of strain acting on bond-distance and bond angle. The strain developed in the films due to the insertion of foreign ions is neutralized by the distortion of FeO_6 octahedral. It can be seen Y-Sc reduces t, which further modify the $Fe/Sc - O$ and $Bi/Y - O$ bond-length, results in the FeO_6 rotation and alters the long-range FE order. t value for all films ($t < 0.964$) indicates the existence of both in-phase and anti-phase tilting of FeO_6 octahedral [230]. EDS confirms the elemental analysis and unchanged chemical composition stoichiometry after heat treatment.

Table 5.3.1: Structural and microstructural parameter obtained from the XRD pattern and various microscopy (FESEM, AFM, and TEM) techniques of BFO, BYFO and BYFSO film.

Sample code	Lattice parameters			**Grain size (nm)**			
	$a = b$ (Å)	c (Å)	V (Å^3)	t	FESEM	AFM	TEM
BFO	5.5784(4)	13.8704(6)	373.81	0.9162	87	75-90	171
BYFO	5.1325(3)	13.8457(5)	373.45	0.8802	61	59-70	120
BYFSO	5.5821(9)	13.9011(1)	375.13	0.8849	94	110-120	188

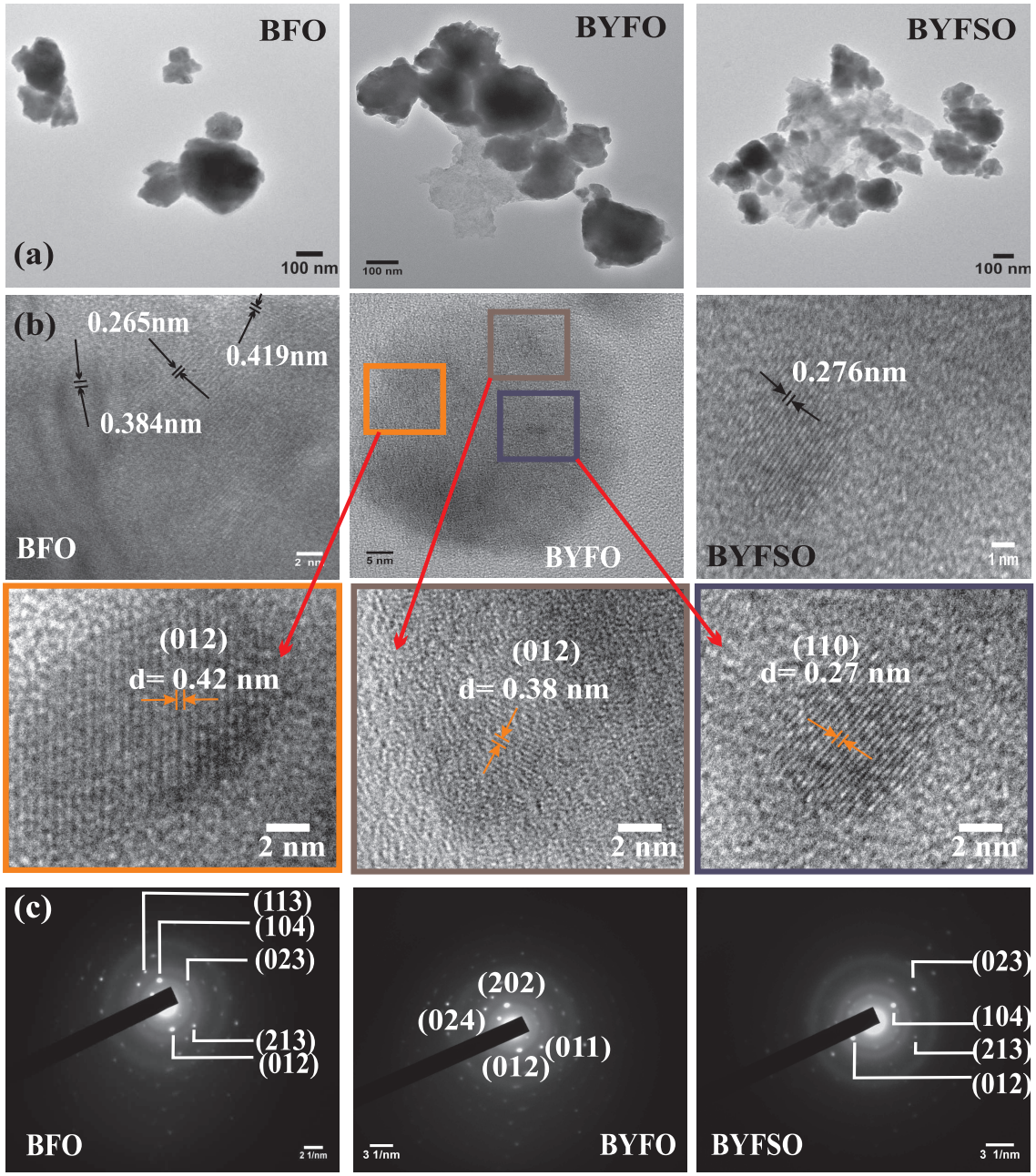

Figure 5.3.2: (a) Transmission electron microscope (TEM), (b) high resolution transmission electron microscope (HRTEM), (c) SAED patterns for BFO, BYFO, and BYFSO compounds.

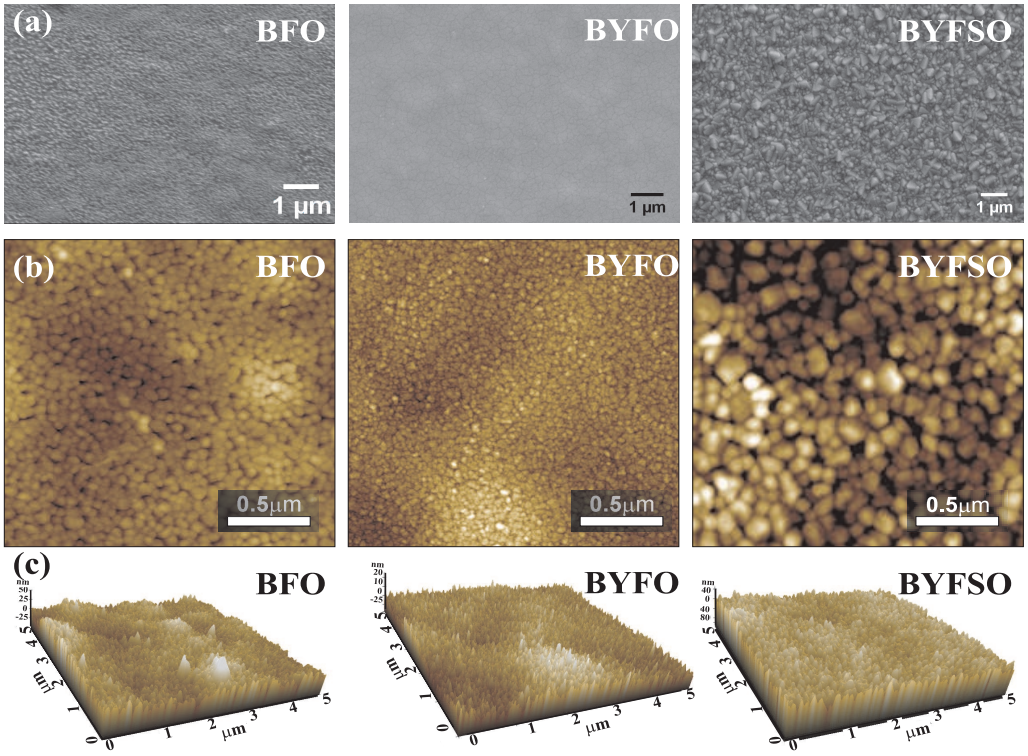

Figure 5.3.3: (a) FESEM micrograph, (b) 2D-AFM, and (c) 3D-AFM images of BFO, BYFO, and BYFSO film on 5×5 μm scanned region.

Structural verification under transmission electron microscope analysis

Figure 5.3.2 (a) depicts the TEM images of pristine BFO, doped BYFO, and co-doped BYFSO compounds. From the figure, it is evident that the particles are in perturbed spherical structure for all BFO systems. The average particle size was calculated by using *ImageJ* software and found around 171 nm, 120 nm, and 188 nm for BFO, BYFO, and BYFSO, respectively. Fig. 5.3.2(b) shows the lattice fringe patterns originated from HRTEM images. BFO exhibit three lattice fringes with interplanar spacing (d) 0.384 nm, 0.419 nm, and 0.265 nm, which are assigned to the crystal planes (0 1 2), (0 1 2), and (1 1 0), respectively. Y-doping didn't affect d (4.29 nm) of BFO, which leads to the minimal fluctuation of lattice parameters. However, Y-Sc co-doping marks an abrupt change in d, which leads to a larger variation of lattice parameters from the vicinity of BFO [Tab. 6.3.1]. Other fringes also identified at various locations and are corresponds to the BFO phase. The crystalline phases of BYFSO further verified with the SAED pattern, as shown in Fig. 5.3.2 (c). The obtained crystal planes assigned to the (1 1 3), (1 0 4), (0 2 3), (2 1 3), (0 1 2). These originated crystal planes are well-matched with JCPDS no. 86-1518, which confirming the retention of crystalline nature after non-magnetic modification.

Microstructural analysis

Figure 5.3.3 (a) shows the FESEM micrograph of the un-doped BFO and its associated films. All films exhibit dense microstructure without any grain diffusion at the grain boundaries, which avoids

the pilling effects during transport property measurements. The grain size for BFO, BYFO, and BYFSO are obtained 87 nm, 61 nm, and 64 nm, receptively. The variation of grain growth will modify the oxygen stoichiometry of BFO after doping/co-doping.

The AFM images [Fig. 5.3.3 (b)] are useful to investigate the surface morphology of the films. Pristine BFO comprises of mixed grains [$avarage\ grain\ size = 75 - 90\ nm$] with the surface roughness is approximately 8 nm. With Y-doping, the grain size ($59 - 70\ nm$) and surface roughness ($3\ nm$) found stable. However, for co-doped BYFSO film, both grain size ($110 - 120\ nm$) and surface roughness ($10\ nm$) posses significant change. The modification of grain size and roughness after doping/co-doping may be due to the variation of internal chemical pressure, defect complex, ionic radii mismatch [231]. The grain growth during the nucleation process may be modified in pristine BFO due to the void created at the center of the octahedra cage after Y-Sc co-doping. Fig. 5.3.3 (c) displays the 3D-AFM images for all films to understand the grain height distribution of the films. The 3D-AFM reveal BFO consists of inhomogeneous hills that are developed throughout the examined surface. However, non-magnetic ion insertion helps in nucleating smooth hills and found homogeneous for the BYFSO film. The improvement of hills due to the difference in electronegativity between *Bi-Y (2.02-1.22)* and *Fe-Sc (1.83-1.36)*, which provides stronger bond energy. The bond enthalpy of *Y-O* is stronger than *Bi-O*, which helps in the formation of stable structure in Y-Sc co-doped films. The film thickness was measured by optical profiler (Zeta) and found to be around 460 ± 5 nm for all films [Appendix].

Conductivity Analysis by Conducting AFM

Fig. 5.3.4 (a)-(b) shows the CAFM topography image and its current mapping with the application of bias voltage between ± 10 V. The current mapping explains the amount of current flow at various applied bias voltage, which affects the resistance of the materials. The detail explanation current mapping will be explained in the next chapter of the present thesis. The current of the corresponding topology profiles for all films also measure, as shown in Fig. 5.3.4 (c). By applying the positive voltage, the film conduct less as compare to opposite negative polarity, where the current flow is maximum i.e., the film exhibits low resistance. This behavior of the films indicates the existence of resistive switching phenomena in all films, which promises for future next-generation memory applications. The detailed study of switching phenomena is discussed in Chapter-6. The curves profile curve for all films, the $I_{leakage}$ value at 0 V of the CAFM mode, is in the current offset. The conductivity of BFO, BYFO, and BYFSO film are very weak *(pA range)* and found higher in Y-Sc co-doped BFO film, which supports effective resistive switching behavior.

5.4 Manipulation of ferromagnetic properties in non-magnetic ion modified BFO thin-film

The magnetic interaction was found weak in AFM bulk BFO ceramics, discussed in Chapter-3. However, the magnetization of BFO shows minimal growth after non-magnetic Y (3%: constant) and Sc (5%, 10%) modification [38]. Its a quite interesting to investigate the intrinsic magnetic properties of Y-Sc co-doped BFO in the form of thin films. Few reports suggest BFO film exhibits saturation magnetization under low magnetic field [232], which motivates to study the intrinsic

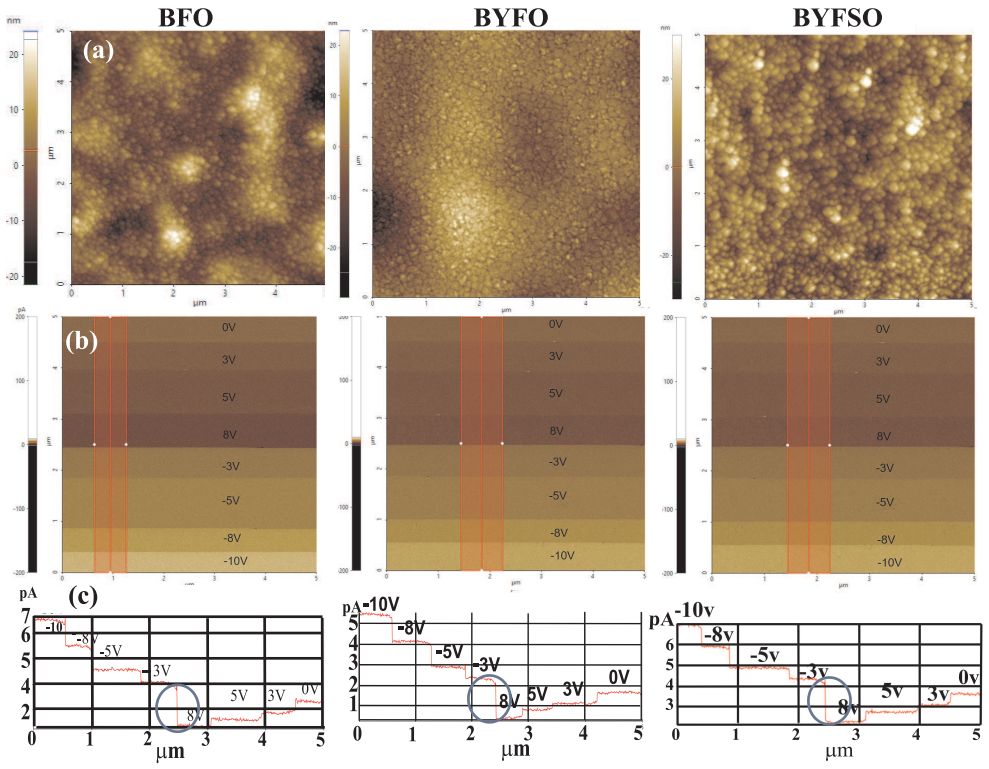

Figure 5.3.4: (a) C-AFM topography, (b) current mapping image, and (c) current profile of BFO, BYFO, and BYFSO film on $5 \times 5 \mu m$.

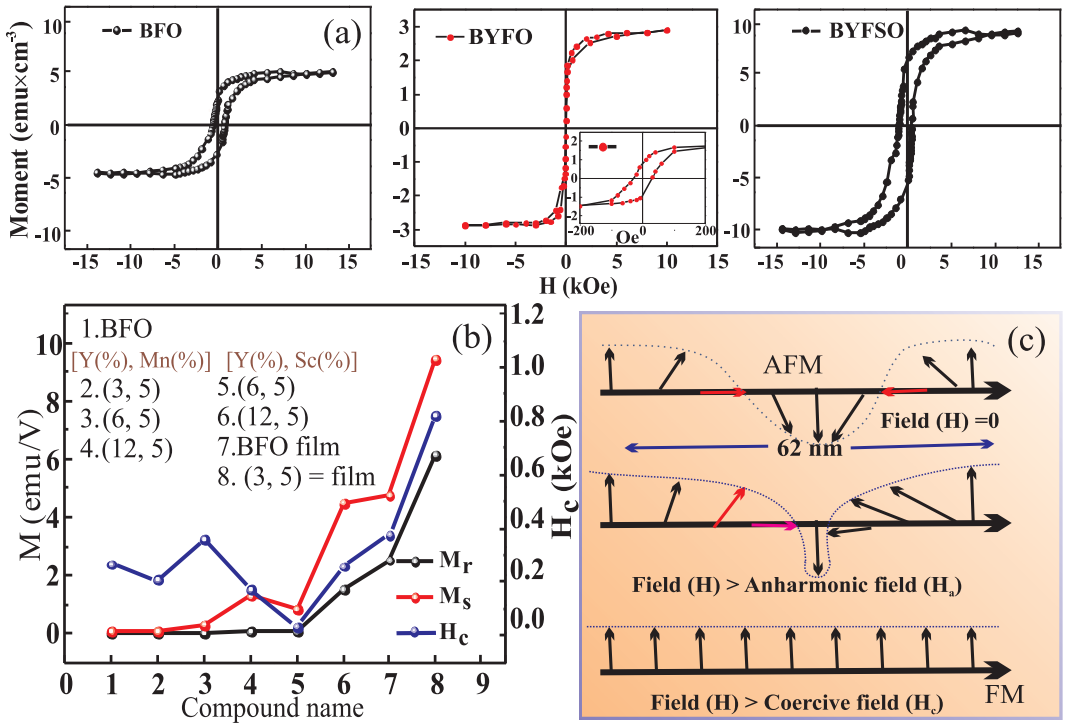

Figure 5.4.1: M-H hysteresis loop of BFO, BYFO, and BYFSO film at maximum applied field of 15 kOe. (b) comparison with various non-magnetic magnetization, and (c) spin-cycloid nature of multiferroic BFO.

Table 5.4.1: Magnetic parameters extracted from the M-H curve of BFO, BYFO and BYFSO film.

Sample code	M_r $(emu.cm^{-3})$	M_s $(emu.cm^{-3})$	H_c (Oe)
BFO	2.514	4.75 $(M_{1.5\ T})$	0.377
BYFO	0.79	2.87	0.266
BYFSO	6.154	9.45	0.822

magnetic behavior of non-magnetic modified BFO system. RT M-H hysteresis curve for all films with the maximum applied magnetic field of 15 kOe is displayed in Fig. 5.4.1 (a). Except for BFO, other films exhibit excellent saturation magnetization at the very low coercive field (H_c). The magnetic parameters extracted from the M-H curve are listed in Table 5.4.1. The parameters of BYFO are found lesser than BFO in the present system, while found much better properties in Y-doped BFO ceramics, and nano-fibers [25, 233]. Moreover, the BYFSO film exhibit very strong magnetization in comparison to the other studied films. In addition to this, the magnetization of thin film based materials found much stronger than the Y-Sc/Mn co-doped BFO bulk ceramics [216, 38]. The enhancement in magnetization in thin films may be due to reduced grain size of nm range [234], suppression of SSMS, and structural distortion created at the octahedral cage. The mechanism for improvement in doped/co-doped films isn't differed much from the bulk system, which is already explained in Chapter-1. We explained the enhance FM properties in non-magnetic modified BYFSO film based on the exchange interaction between the Fe-ions. Due to the non-magnetic behavior of foreign Y^{3+} and Sc^{3+} ions, the magnetic improvement due to Y and Sc insertion ruled out. The coercivity (H_c) of non-magnetic modified BFO systems fluctuated from the pristine due to a change in magnetocrystalline anisotropy. But all films exhibit low field saturation, which promises for future memory storage applications.

The observed saturated FM behavior may be referred to as ***"canted ferromagnetism"***, where the magnetic modification occurred due to change in the crystallographic angle and distance of the perovskite system. Figure 5.4.1 (c) shows the aspect of $AFM \rightarrow FM$ behavior in MF BFO in the presence of SSMS of order 62 nm. The magnetization only improved when the cycloid periodicity reduced below 62 nm. Application of a huge magnetic field will destroy the SSMS in transition through $anhormonic\ field\ (H_m) \rightarrow coercive\ field\ (H_c)$ and switch to FM system. In our system, the reduced particle size (nm range) and change in $Fe-O$ and $Fe-O-Fe$ (due to doping/co-doping) unlock the SSMS present at FeO_6 octahedra which result in an enhancement in magnetization. As MF BFO is a complicated system, the improvement of FM properties one can study deeply by using X-ray photoelectron spectroscopy (XPS), Neutron diffraction, Mossbauer spectroscopy, etc. We used the XPS technique to validate the magnetization results.

To identify the elements and its oxidation states, XPS measurements were carried out for all films. Figures 5.4.2 (a-b) and Figs 5.4.2 (c-d) elucidate the Gaussian-Lorentzian fitted XPS spectra for Bi4f and Fe2p regions, respectively. From the XPS spectrum of un-doped BFO, Bi4f spectrum consists of two different peaks that appeared at 158.1 eV and 164.3 eV, respectively. The appeared peaks are referred to $Bi4f_{7/2}$ and $Bi4f_{5/2}$, respectively, which assigned to Bi-O bond-distance [235]. However, the position of $Bi4f_{7/2}$ and $Bi4f_{5/2}$ is disturbed after elemental modification of BFO. The position of ($Bi4f_{7/2}$, $Bi4f_{5/2}$) for co-doped BYFO and double-doped BYFSO films extracted from the fitting results are (152.7 eV, 158 eV) and (152.7 eV, 158 eV), respectively. The gap between two Bi4f peaks is obtained approximately 5-5.5 eV, confirming the valence state of Bi is in +3

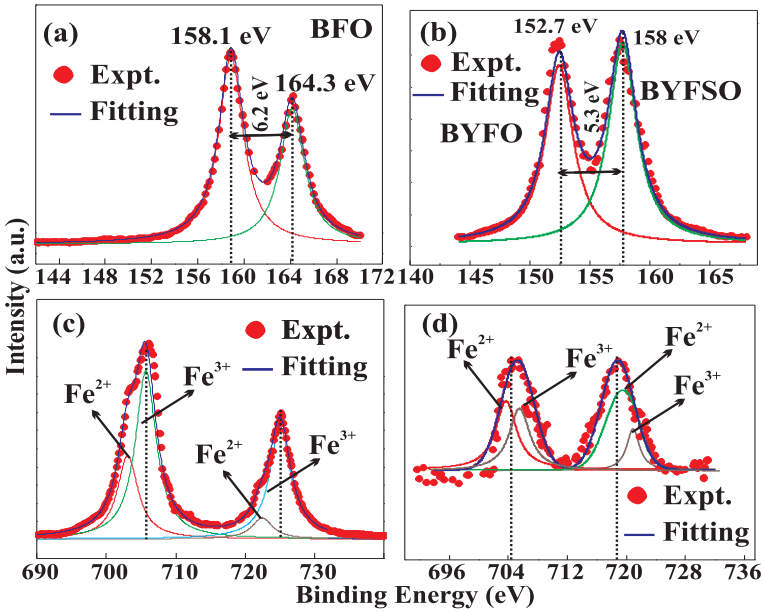

Figure 5.4.2: X-ray photoelectron spectrometer (XPS) spectra of Bi4f (a) BFO, (b) BYFSO; and Fe2p (c) BFO, (d)BYFSO films.

state in all studied films. From Fig. 5.4.2 (d), Fe2p is splits into two spectrum for $Fe2p_{1/2}$ and $Fe2p_{3/2}$ due to spin-orbit doublet components in all films. The Lorentzian fitting results suggest, the 707.6 eV, 725.8 eV belongs to Fe^{3+} ions, while 702.2 eV and 722.56 eV belong to Fe^{3+} originated from pristine BFO. Similarly, in BYFO film, the position of Fe2p didn't hamper much and found at similar location obtained for BFO. But after, Y-Sc co-doping the position of Fe region peak evident a shift and appeared at 702.2 eV and 722.56 eV. Moreover, all the studied films manifest both Fe^{3+} and Fe^{2+} ions observed from XPS results. Based on the fitting results, the ratio between Fe^{3+} : Fe^{2+} for BFO, BYFO, and BYFSO is calculated to be 1.27, 1.12, and 2.57, respectively, which confirm the increase in Fe^{3+} concentration after Y-Sc co-doping. In the present MF system, partially filled d orbital of Fe^{3+} in BFO plays a critical role in magnetic properties. As explained in bulk ceramics, the magnetization enhancement in non-magnetic Y-Sc co-doped BFO, patterning due to the increase in Fe^{3+} concentration, which makes stronger the Fe-O-Fe exchange interaction. In BYFO film, the decrease in Fe^{3+} : Fe^{2+} ratio indicates the weak super-exchange interaction, which results in lower magnetic properties. Similarly, the higher Fe^{3+} : Fe^{2+} ratio makes stronger Fe-O-Fe exchange interaction in BYFSO film, which improved the magnetization significantly, as evident from M-H curve.

Zero field cooling (ZFC) and field cooling (FC) are fundamental techniques to understand the intrinsic magnetic properties of polycrystalline materials. ZFC and FC magnetization curves (M-T) for BYFO [Inset: M-T of BFO] and BYFSO films within the temperature range $10-300\ K$ at applied field 100 Oe are shown in Figs. 5.4.3 (a)-(b), respectively. The contribution from the diamagnetic FTO substrate was subtracted from the magnetization data to obtain the exact contribution from the studied films. Sharma *et. al.* explained a broad gap between FC and ZFC curve is visible at 50 K of BFO film reveals the origin of spin-glass behavior [236]. The magnetization of the FC curve increases with reduction in temperature for all films. The gap is visible larger in both BYFO and

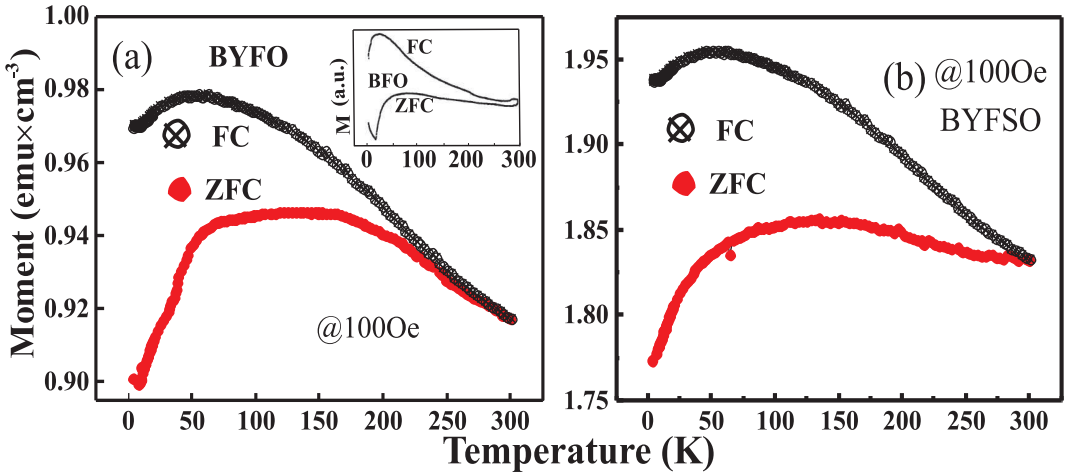

Figure 5.4.3: Field cooling (FC) and zero field cooling (ZFC) for (a) BYFO [Inset: BFO], and (b) BYFSO film between the temperature range 4-350 K at applied magnetic field of 100 Oe.

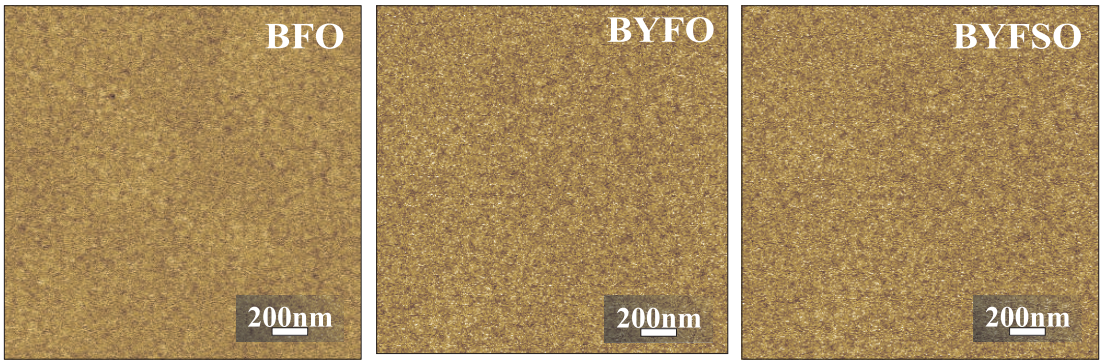

Figure 5.4.4: MFM images of un-doped BFO, Y-doped BYFO, and Y-Sc co-doped BYFSO films.

BYFSO film, which indicates the collapsing of the real AFM behavior due to spin frustration in SSMS. Thus, both RT and low-temperature magnetization results indicate, Y and Sc modify the original AFM of BFO, which leads to improving the magnetic properties.

The magnetic interactions in the sol-gel coated BFO, BYFO, and BYFSO films were identified by MFM techniques, as shown in Fig. 5.4.4. The M-H curve found saturation in in-plane (IP) mode and found weak when it was out-of-plane (OP). But some actions were present which may appear from the surface topography. It can be believed, as the M-H magnetization is strong during IP, the IP domains are persisting throughout the film surface. For MFM imaging, the film surface roughness must need to be smooth, and a pulse laser deposited (PLD) grown films may provide a better picture regarding magnetic information.

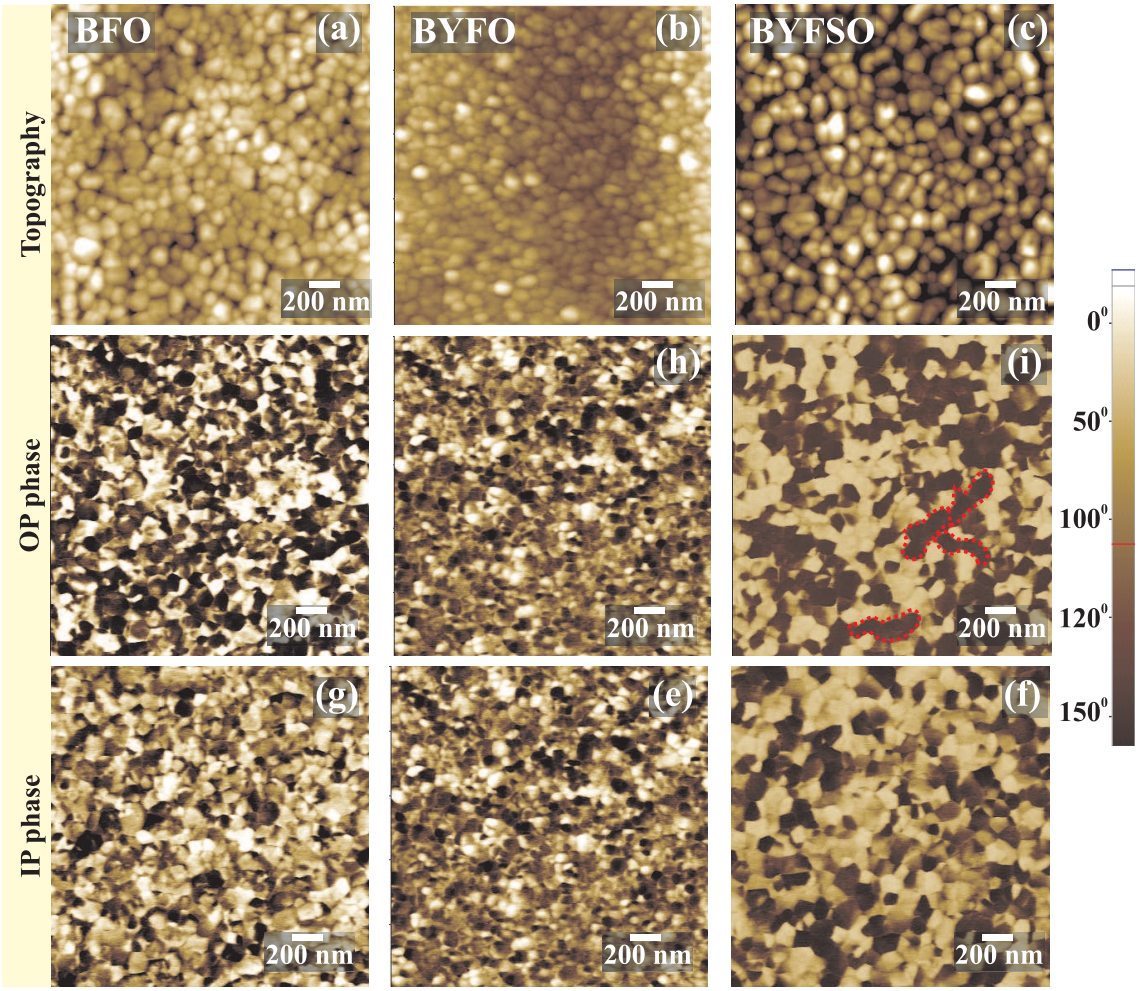

Figure 5.5.1: (a-c) Topography, (d-f) out-of-plane (OP), and (g-i) in-plane (IP) phase PFM images of BFO, BYFO, and BYFSO films.

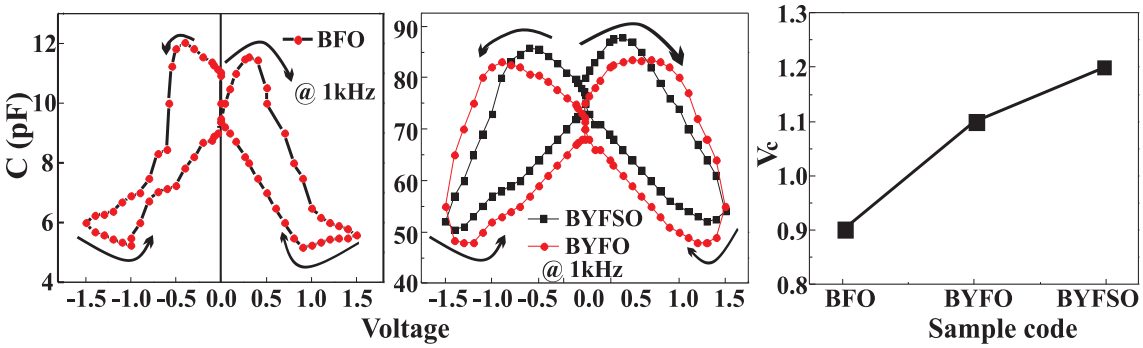

Figure 5.5.2: Capacitance-Voltage (C-V) measurements of BFO, BYFO, and BYFSO films.

5.5 Quantitative ferroelectric polarization switching in non-magnetic modified multiferroic films under voltage response

The piezoelectric (PE) or ferroelectric(FE) properties of BFO, BYFO, and BYFSO film investigated by using the piezoforce microscope (PFM) technique. The surface topography [Fig. 5.5.1 (a-c)] images reveal BYFSO posses higher domain size than other studied films, which is already demonstrated in Fig. 5.3.3 (b). Figures 5.5.1 (d-f) and Figs.6.3.7 (g-i) depicts the OP- and IP-phase PFM images respectively for all the films. From the images, it is evident that all sol-gel grown films exhibit strong OP and IP PFM signal. But the non-magnetic ion doping/co-doping marks a significant modification in FE domains of BFO film. The OP PFM image of pristine BFO consists of bright, dark, and mix contrasts, which represent the polarization direction either upward or downward or random, respectively. The mix phases indicate the FE domains are switched to the 71^0 and 109^0 type ferroelastic domains, which is analogous to the PE properties [65]. The IP PFM image of BFO has major differences as the majority of FE domains switched to the opposite polarization direction with suppressing the upward and downward FE domains. 180^0-type FE domain are suppressed with Y-doping, while completely lapse in BYFSO film, which indicates most of the FE domains 71^0 and 109^0 type domains. 180^0 type domain switching was completed through 71^0 and 109^0 with various states, which indicate the possible multistate memory application. From the above analysis, the strong IP and OP PFM signal confirm Y-Sc co-doing enhances the PE properties and can be useful for future potential applications. The FE switching behavior in prototypical FE materials directly affects the orientation of domains and domain walls [237].

PFM analysis reveals BFO and its associated films exhibit FE properties, and capacitance-voltage (C-V) measurement has a close association with it. Fig.5.5.2 (a) illustrates the RT C-V plots for parent BFO, Y-doped BYFO, and Y-Sc co-doped BYFSO films measured at 1 kHz between sweeping the voltage $0\ V \rightarrow 1.5\ V \rightarrow 0\ V \rightarrow 1.5\ V \rightarrow 0\ V$. The non-symmetric hysteresis C-V curve under +ve and -ve sweeping voltage indicates the presence of oxygen vacancies in BFO film, which leads to suppress the FE behavior of the film. However, for BYFO and BYFSO film symmetric hysteresis C-V curve with two sharp capacitance peak under +ve and -ve sweeping voltage indicates better FE behavior after non-magnetic modification. BFO exhibit lower coercive voltage ($V_c = 0.9\ V$) than BYFO ($V_c = 1.1\ V$) and BYFSO ($V_c = 1.2\ V$) indicate the presence of oxygen vacancies in doped

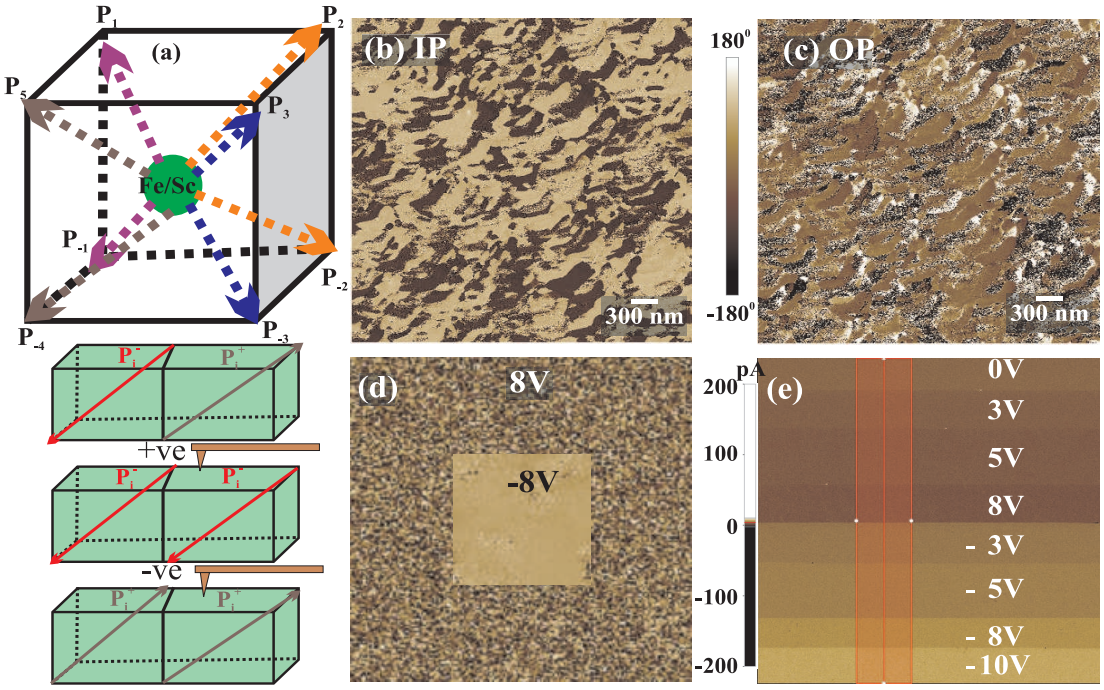

Figure 5.5.3: (a) Ferrolectric polarization orientation in BYFSO film and schematic representation of ferroelectric domain switching with opposite bias, (b) in-plane (IP) phase, (c) out-of-plane (OP) phase PFM images with applied bias of +2 V, (d) ferroelectric polarization switching under dc applied bias $\pm 8\ V$, (c) CP-AFM current profile image under various voltage ± 10 of BYFSO film.

and co-doped films. The C-V loop of Y and Sc modified films is more broadened from pristine BFO, which suggests the presence of high leakage current. In addition to this, the considerable variation in capacitance between parent BFO and non-magnetic modified films indicates the improvement in the degree of ferroelectricity in the Y-Sc co-doped BYFSO film.

Ferroelectric domains switching in BYFSO film under electrical influence

The electrical controlled FE domain switching of (1 1 0) grown BYFSO film on $SrTiO_3$ (STO) substrate is further examined with PFM techniques. The schematic representation of eight possible polarization orientations of BYFSO crystal cell are shown in Fig. 6.4.2 (a) [57]. The four upward polarizations (P_1, P_2, P_3, P_4) are approaching the surface and the other four downward polarizations (P_{-1}, P_{-2}, P_{-3}, P_{-4}) are towards the STO surface. Figures 6.4.2 (b-c) manifests the $5 \times 5\ \mu m$ region of IP- and OP-PFM images of as-grown BYFSO film polarized under bias 2 V. The tip was probe at 0^0 during scanning and found patchy irregular domains are evident from the PFM images. The polarization P_1 and P_2 appeared in yellow color, while P_3 and P_4 are brown observed from IP-PFM image.

Figure 5.5.3 (d) depicts the FE polarization switching of the BYFSO film by applying $\pm 8\ V$ dc tip bias. The upward (+ve) and downward (-ve) biases were probed on the square region of $3 \times 3\ \mu m$ (brown) and $2 \times 2\ \mu m$ (Yellow), respectively. The PFM images were taken of large square with immediate action of -ve bias the polarization switched suddenly to opposite direction. From Fig. 5.5.3 (d), the upward polarization of FE domains is dominating over the downward

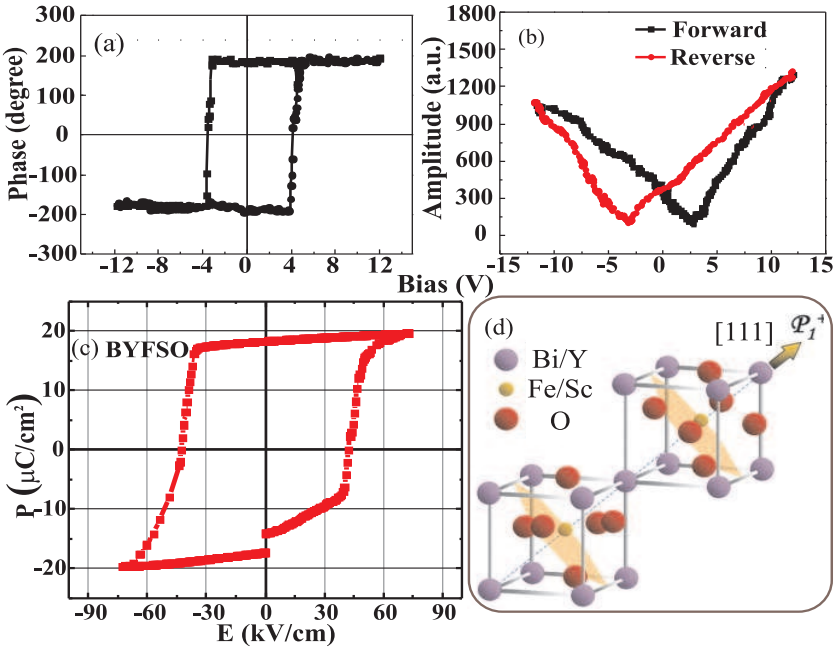

Figure 5.5.4: (a) phase vs. voltage, (b) amplitude vs. voltage obtained during PFM measurements, (c) Room temperature P-E hysteresis loop of Y-Sc co-doped BYFSO films, and (d) sketch to demonstrate FE polarization ordering along [111] direction.

polarization in BYFSO film. Maximum FE domains are switched to the downward direction (region-I: corresponds to brown color) when polarized with dc bias of +8 V during scanning. Oppositely, almost all the FE domains were reversed to upward polarization direction when the region-II is polarized with dc bias of -8 V, and become the yellow color domains. This confirms ± 8 V dc bias is sufficient to switch the upward and downward FE polarization domain completely in non-magnetic ion modified BFO films.

The CAFM image of the BYFSO film is presented in Fig. 5.5.3 (e) with various upward and downward voltages to examine the amount of flow of current. From the figure, it is observed that the region with downward polarization shows minimum current flow than the region with upward polarization (at ± 8), which may cause the FE polarization switching. Therefore the leakage current at certain voltage (V_c) can read out the information in a nondestructive way. These results discussed above implied a symmetric FE hysteresis characteristic possessed by our sample, which already verified with the C-V hysteresis loop (exhibit symmetry switching).

The local electrical properties were estudied through PE hysteresis loop measurement on BFO film. The electromechanical performance of the BFO film is explained by piezoresponse phase-voltage and the "butterfly-like" amplitude-voltage hysteresis loop displayed in Figs. 5.5.4 (a)-(b), respectively. The two symmetric coercive fields $V_+ = 4\ V$ and $V_- = -4\ V$ can be identified, which ensures the polarization reverse is symmetric, which is evident from FE domain switching. The amplitude is found higher in BFO film, which supports the higher PE constant (d_{33}) value. The presence of a maximum non-180^0 domain with high d_{33} value makes BFO promises for multistate memory device applications [65]. To verify the symmetry FE polarization switching, the RT P-E hysteresis loop of BYFSO film is represented in Fig. 5.5.4 (c). The P_r value is found 23 $\mu C/cm^2$, which is lower than the value (100 $\mu C/cm^2$) achieved in epitaxially BFO thin films [237] due to

the polycrystalline nature of the specimen prepared by sol-gel technique, line-defects from grain boundaries. But, the obtained electrical parameters (P_r & P_s) are higher than the value obtained in bulk-ceramics indicated the improved FE properties in thin-film materials and simultaneously useful for device applications. Y-Sc co-doping may suppress the BiO bond length and strengthens the covalent BiO hybridization in BYFSO film, which results in non-centrosymmetric distortion to drive the Bi^{3+} ions toward the $[111]_C$ direction and enhance long-range FE ordering, which explained schematically in Fig. 6.4.3 (d) [32, 186].

The above analysis suggests Y-Sc co-doping significantly affects the FE properties of BFO. With excellent FE polarization and complete domain switching, BYFSO film may be useful for non-volatile memory device applications, which has been explained in Chapter-5.

5.6 Summary

The single phase (Rhombohedral: R3c) un-doped BFO, and non-magnetic ion modified BYFO, BYFSO thin-films fabricated by using sol-gel spin coating technique. The grain and particle size manipulated due to Y/Y-Sc insertion. The conductivity of the BYFSO is found weak in comparison to BFO and Y-doped BFO film. The evidence for improved canted ferromagnetic properties and spin glass behavior for long range temperature obtained in BYFSO film. MFM analysis suggests in-plane magnetic domains are evident in all films. The ferroelectric domains switched completely to non-180^0 with a maximum of 71^0 and 109^0 type ferroelastic in Y-Sc co-doped BFO film. All upward and downward ferroelectric domains switched with the applied dc bias of ± 8 V, which is well supported with symmetry C-V, P-E, and amplitude-voltage hysteresis curves. With significant improvement in ferroelectric, ferromagnetic, and piezoelectric properties, the Y-Sc co-doped BFO system is useful for future non-volatile memory applications, which was predicted in the previous chapter.

Graphical Abstract:

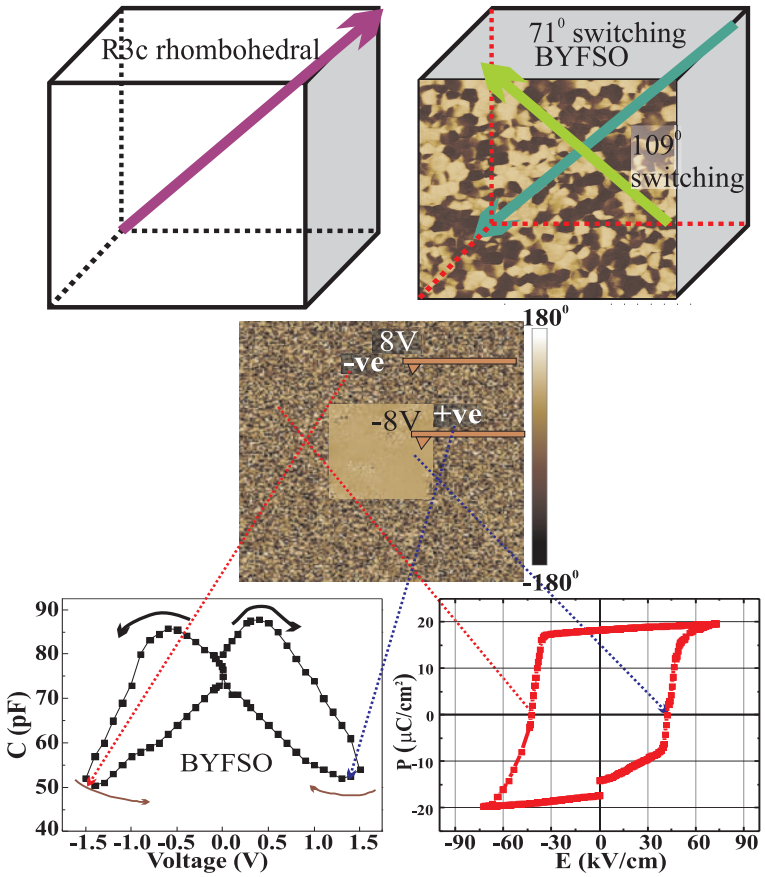

Chapter 6

Magneto-electric rectifying multilevel resistive switching in multiferroic based devices

6.1 Introduction

According to Moore's prediction, the semiconductor industry is fastly approaching its lowest possible scale limit [238]. This causes a surge in searching for new materials with more reliability and functionalities for future generation memory applications. Resistive random access memory (RRAM) can be considered as a potential candidate to cover up the shortcomings for the next-generation non-volatile memory (NVM) due to their high-caliber performance, ultra-fast switching, high storage data density, and low power consumption [239]. In RRAM, the data can be written and read by switching the resistance between lower resistance state (LRS) ["1"] and high resistance state (HRS) ["0"] [240, 241]. Novel MF BFO has a potential caliber for better switching performance due to its stable resistive switching (RS) effect at room temperature (RT), which promises for RRAM applications. However, the switching phenomena in MF material are quite completed due to the coexistence of many ferroic orders. The elementary substitution method is an effective approach to improve both the stability and performance of BFO based resistive memory. In the current thesis, we investigate the RS effect in highly improved dielectric Y and Sc modified films with improved magnetoelectric effects.

Considering the fact, most of the conventional RRAM operated under the application of applied electric field *(E)* or current *(I)*. However, with the development of technology, the requirement of a multifunctional device is the desire for the modern community. In the past few years, additional perturbations like magnetic field, light, and temperature are the new parameters are used to control the RS along with the applied E or I has been reported [242, 243, 244]. Systems like MF and spintronics deal with both electronic and magnetic phenomenon. Magnetic field H can provide an additional degree of freedom for achieving the multifunction [245]. The appreciable modulation of resistance states can be achieved under the light in $Pt/CeO_2/Nb:SrTiO_3$ based resistive device [246]. MF BFO response to both E and H, which promises for multifunctional activities. Material with good

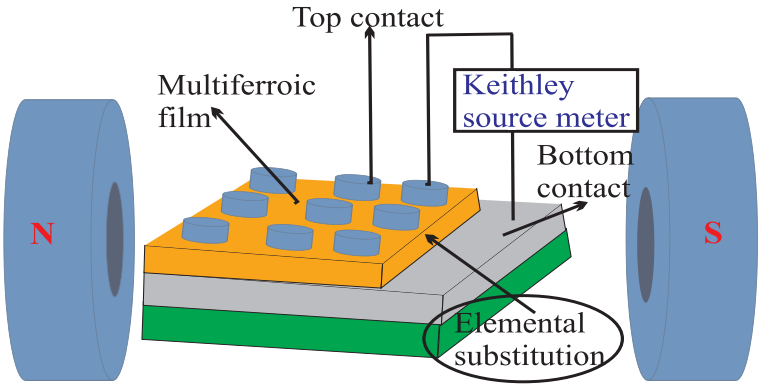

Figure 6.1.1: Multiferroic based $Ag/BFO/FTO$, $Ag/BYFO/FTO$, & $Ag/BYFSO/FTO$ resistive random access memory devices configuration and its effects under additional perturbation which provide extra degree of freedom to achieve multifunction.

ME effect and stable polarization switching useful to achieve the multistate memory application and BFO film have both ingradient [59]. Modulation of pulse-width (PW) and pulse-height (PH) useful for improving the switching performance along with the multilevel resistive state. Alamgir *et. al.* observed 14 various resistive states by tuning the PW of the device [247].

This chapter explains the salient features of the RS effect of BFO based RRAM device under the influence of elementary substitution effect and applied magnetic field [Fig. 6.1.1] as the additional perturbation. The effects of the magnetic field under the magnetic field not explored much. The study of such a novel system will use to achieve multifunction, which is the primary desire for modern technology.

6.2 Experimental Techniques

To fabricate $Ag/MF/FTO$ devices, high-density $BiFeO_3$ (BFO), Y-doped $Bi_{0.90}Y_{0.10}FeO_3$ (BYFO), and Y-Sc co-doped $Bi_{0.97}Y_{0.03}Fe_{0.95}Sc_{0.05}O_3$ (BYFSO) films need to grown on fluorine doped tin oxide (FTO) coated glass substrate (15 Ω). The film deposition process is already explained in the Chapter-5. For RRAM device configuration, the silver (Ag) contacts ($0.2\ mm$) were made on the all BFO based films due its favorable conduction and anti-oxidation properties. The distance between two consecutive Ag contact is maintained at $0.25\ cm$. The minimal work-function difference between MF films and FTO makes easier for electrons to overcome the barrier under a small applied potential. The device configuration of $Ag/BFO/FTO$, $Ag/BYFO/FTO$, and $Ag/BYFSO/FTO$ is illustrated in Fig. 6.4.26.1.1.

RRAM device characterization examined under Keithley 2400 and 4200. The RS effects were explained through conventional $I-V$ characteristics. The effect of the magnetic field on RS of MF based devices investigated by using an electro-magnetic unit (Walker Scientific), where the magnetic field is applied both perpendicular ($\perp$) or parallel ($\parallel$) to the applied electric field. PW modulated multilevel RS effect measurements were performed by keeping the SET voltage constant at +3 V and tune the PW from $30-60\ \mu s$ at fixed -3 V RESET voltage. However, pulse-height modulated multilevel resistive states measurements were carried by tuning the PH from -3 - -5 V (fix PW of 60 μs) at a constant SET voltage (+3 V). RT impedance spectroscopy was performed to understand

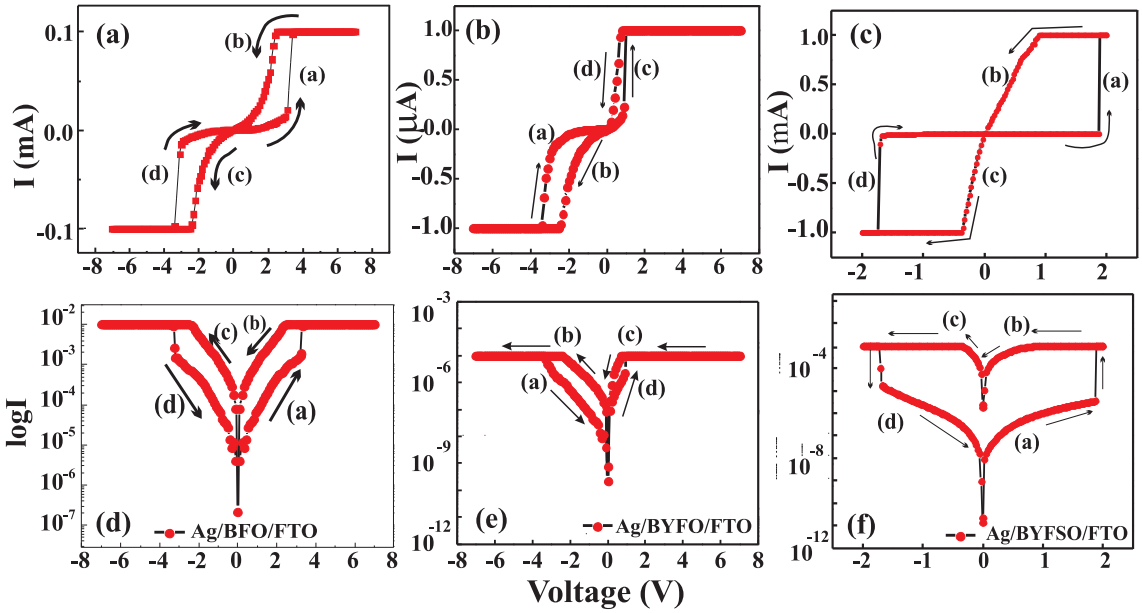

Figure 6.3.1: BRS $I-V$ characteristics for [(a) BFO, (b) BYFO, (c) BYFSO], and $logI-V$ curve for [(d) BFO, (c) BYFO, (c) BYFSO] based RRAM device.

the macroscopic origin of RS effect in MF based devices by using LCR meter (Novocontroller) in the presence of magnetic field (*0-3000 Oe*) in a wide frequency range between 1 $Hz-1$ MHz.

6.3 Effect of doping (Y) and co-doping (Y-Sc) on the resistive switching properties of multiferroic $BiFeO_3$

6.3.1 Electric field rectifying RS effect in un-doped and modified BFO system

Rhombohedral BFO, BYFO, and BYFSO films with improved MF properties and ME effect [explained in previous chapters] are promises for next-generation NVM technology. To examine the RRAM characteristics, the RS effect on 50×50 μm^2 $Ag/BFO/FTO$ (**A**), $Ag/BYFO/FTO$ (**B**), and $Ag/BYFSO/FTO$ (**C**) memory cells was studied under applied voltage. The RS effect in MF based devices is explained through conventional $I-V$ characteristics. Except for **A**, the other two devices (**B**, **C**) exhibit RS effect without any electroforming process, which is one of the novel characteristics of high-density data storage devices.

Figures 6.3.1 (a-c) & (d-f) displays the linear $I-V$ and semi-logarithmic ($logI-V$) "butterfly-like-curve" characteristics of **A**, **B**, and **C** devices obtained by sweeping the voltage between $0\ V\rightarrow7\ V\rightarrow0\ V\rightarrow-7\ V\rightarrow0\ V$ (**A** and **B**) and $0\ V\rightarrow2\ V\rightarrow0\ V\rightarrow-2\ V\rightarrow0\ V$ (**C**), respectively. (a)→(b)→(c)→(d) represents the direction of flow leakage current ($I_{leakage}$) for one complete cycle. For memory cell **A**, the electroforming process is obtained by applying a high positive voltage of 9 V on the Ag top electrode at the beginning with compliance current (cc) of *10 mA* to activate the RS properties of the memory cell. A compliance current (cc) of *10 mA* was applied to avoid the permanent dielectric breakdown for smooth operation. All the studied devices exhibit initial

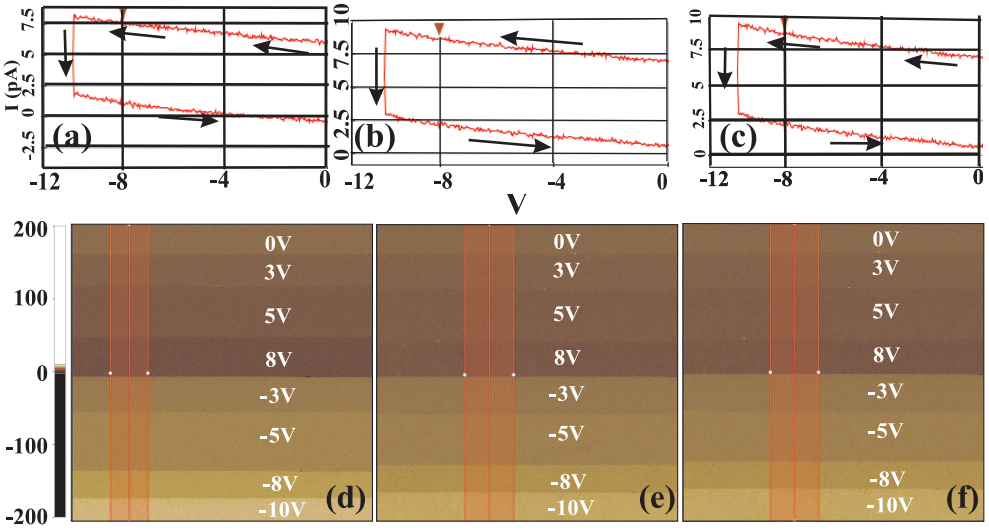

Figure 6.3.2: CAFM topography images for (a) BFO, (b) BYFO, (c) BYFSO, and their respective $I-V$ curves (d) BFO, (c) BYFO, (c) BYFSO films.

HRS due to the high dielectric behavior of MF films. When a positive (+ve) sweeping voltage is applied with respect to top electrode (Ag), $I_{leakage}$ evident a sharp jump at 3 V, called *'SET'* process (V_{SET} *or* $V_t = 3\ V$: *threshold voltage*) and switch to LRS. Similarly, during negative (-ve) sweeping voltage, the *'RESET'* process occurred at $V_{RESET} = -3\ V$, and the device restores to HRS. Similarly, for devices **B** and **C**, the (SET, RESET) process obtained at ($V_{SET} = 1\ V$, $V_{RESET} = -3.7\ V$) and ($V_{SET} = 1.8\ V$, $V_{RESET} = -1.8\ V$), respectively. Except for BYFO, other devices exhibit homogeneous symmetry BRS behavior ensures a better switching process. The modulation of threshold voltage (V_t) in Y-Sc modified BFO films may be due to the structural distortion, defects, and oxygen stoichiometry.

The evidence for the coexistence of RS phenomena is MF films is further examined through conducting atomic force microscopy on area $5 \times 5\mu m$. The $I-V$ characteristics [Figs. 6.3.2 (a-c)] obtained from CAFM measurements confirms the existence of the RS effect in all studied films, which is originally evident in device configuration [Figs. 6.3.1]. The conductivity is very weak, i.e. pA range for all films and found higher for Y-Sc co-doped BFO film due to larger $I_{leakage}$. The low conductive films also support the initial HRS state of the resistive device. The current mapping at the various voltage of BFO, BYFO, and BYFSO film is shown in Fig. 6.3.2 (d-f) under applied bias ± 10. The bright areas were written with -ve voltages, and the dark areas were erased with +ve bias voltages with overall mapped at 0.5 V read voltage. The uniform distribution of currents under -ve bias voltage indicates the coexistence of a large number of conducting filament which attributes the LRS, which is difficult to distinguish for a single filament on such a large scale.

6.3.2 Endurance characteristics or retention properties of $Ag/MF/FTO$ RRAM devices

The term 'endurance' refers to the reproducibility i.e., in RS, the maximum number of repeated cycles obtained from a single voltage operation. The endurance characteristics also termed retention properties. The endurance characteristics of A, B, and C devices obtained through sweeping the

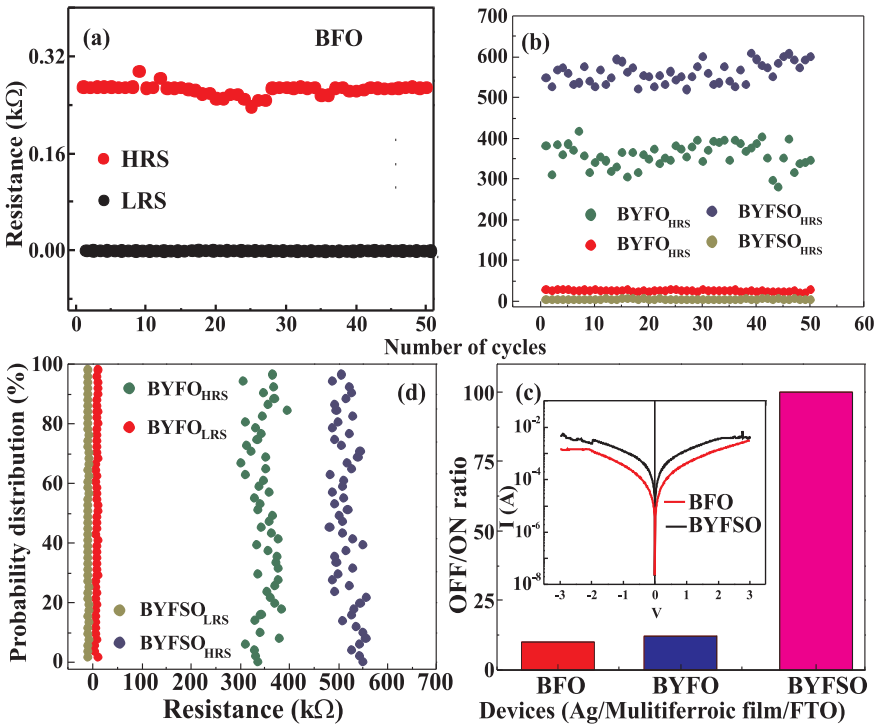

Figure 6.3.3: Endurance characteristics (a) BFO, (b) BYFO and BYFSO, (c) cumulative probability distribution, and (d) $R_{OFF}/R_{ON} = OFF/ON$ ratio for 50 complete testing cycles of BFO, BYFO, and BYFSO based device.

multiple $I-V$ hysteresis cycles. For the present devices, we performed 50 repeatable testing cycles, which is found stable without any large-degradation in the device performance. The non-degradation of the device ensure switching between HRS and LRS is reproducible, reversible, and controllable. The memory window ($R_{OFF}/R_{ON} = OFF/ON$) of device **A** for 50 repeated hysteresis cycles is obtained around 12, as shown in Fig. 6.3.3 (a). Both Y-doping and Y-Sc co-doping increase the resistance of HRS and LRS simultaneously. The OFF/ON ratio for **B** and **C** obtained around 12 and 100, respectively, observed from Fig. 6.3.3 (b). The systematic enhancement of resistance in BYFO and BYFSO films may be due to the increase in leakage current [inset: Fig. 6.3.3 (d)], which eventually increases the O_{vs} concentration. The change in O_{vs} stoichiometry in modified BFO system may be another possible reason for improved device stability and performance. The enhancement of switching ratio after foreign element substitution indicating the role of O_{vs} compensates for the charge neutrality. Figure 6.3.3 (c) displays the cumulative probability distribution of LRS and HRS for investigated A, B, and C device structure. The obtained plots ensure stable distribution of the LRS with the minimal unstable distribution of the HRS, which indicates the excellent switching performance of the devices.

Figures 6.3.4 (a-c) shows the XPS spectra of the O 1S core-level regions of BFO, BYFO, and BYFSO films. The spectrum for all films is fitted with the Lorentzian component. The position of two sub-peaks of BFO is located at 523.90 eV and 527.85 eV, which referred to as lattice (core spectrum of O 1S) and non-lattice oxygen (attributed to O_{vs}), respectively. Similarly, the positions of (lattice, non-lattice) oxygen after Y-doping and Y-Sc co-doping are (529 eV,532.4 eV) and 523.90 eV, 527.85 eV), respectively, obtained from the fitting results. Comparing the area ratio of BFO, BYFO,

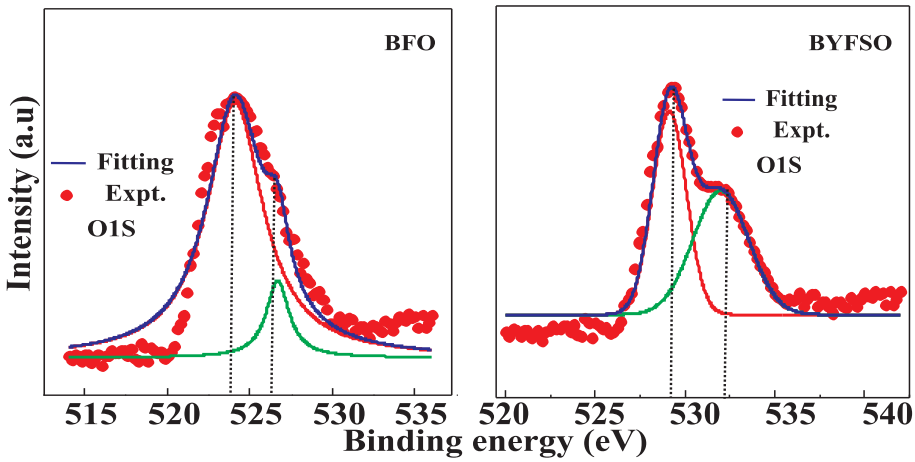

Figure 6.3.4: XPS spectroscopy for oxygen O1S core-level spectra of (a) BFO, (b) BYFO and BYFSO films.

and BYFSO, the ratio systematically decreases with doping and co-doping, indicating an increase in O_{vs}, supported by leakage current analysis. O_{vs} is maximum in BYFSO film, which leads to improving RS effect in the Y-Sc co-doped BFO film. The above results suggest, Y-Sc co-doping improves memory cell performance and storage capacity about ten times larger than the value obtained for BFO film, which promises for its implementation in future NVM devices.

6.3.3 Conduction mechanism of resistive switching behavior in multiferroic based devices

Charge transport at LRS and HRS:

To elucidate the BRS behavior in the fabricated devices, the current conduction mechanism should be properly understood. The RS effect in both single-phase and polycrystalline BFO thin films was reported earlier [248, 249]. We studied its effect on an improved MF system after non-magnetic ion modifications. The switching phenomena have been explained using various conduction models such as Ohmic conduction, space charge limited current (SCLC), Poole-Frenkel emission, Schottky barrier emission, etc [135, 133, 139]. The $I-V$ curves have been tried rigorously to simulate with the above-mentioned conduction models; however, it is found best fit with trap-controlled SCLC conduction process and Schottky emission model.

Figures 6.3.5 (a) and (d) displays the conduction process at LRS and HRS of $Ag/BFO/FTO$ device under opposite polarity (i.e., +ve and -ve sweeping voltage) by re-plotting the $I-V$ curve into the logarithmic scale. The memory cell is initially at HRS, and the conduction process in this state is assisted by trap-controlled SCLC. SCLC posses three various (i) Ohmic ($I \propto V$), (ii) Child's square law ($I \propto V^2$), and (iii) the sharp leakage current increase regions [250]. The Ohm's law and Child's law region are expressed with current density (J) [251]

$$J_{ohm} = qn_0\mu\frac{V}{d}\ and \tag{6.1}$$

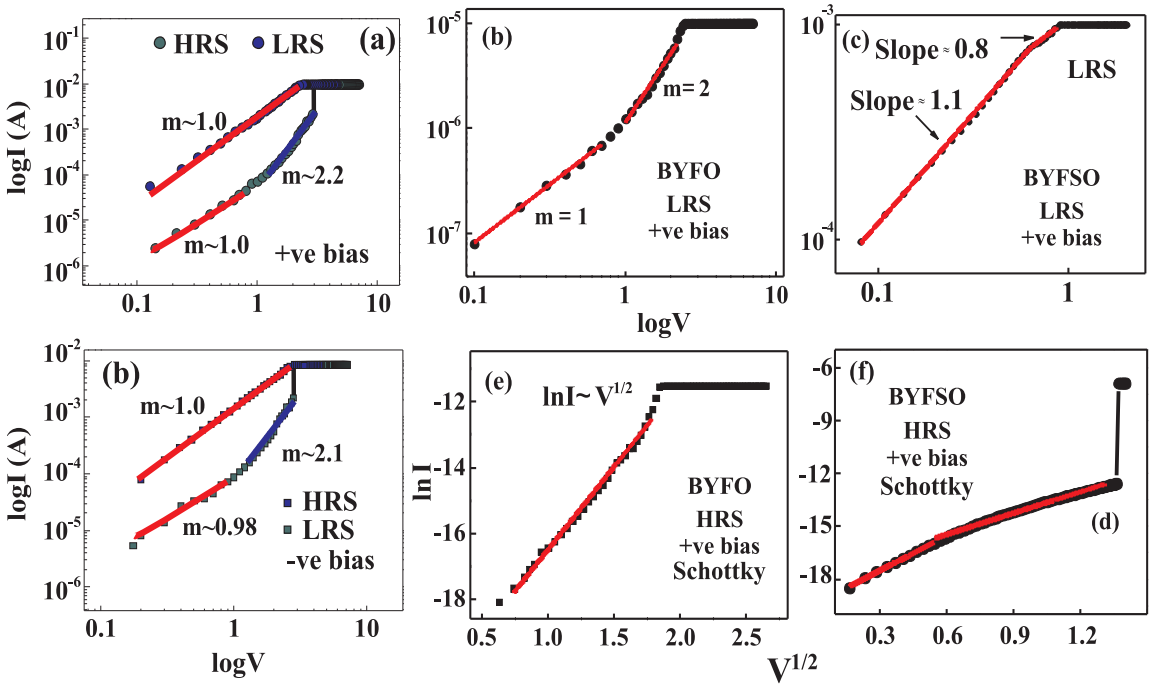

Figure 6.3.5: (a)LRS, (b) HRS Ohmic-SCLC conduction model for Ag/BFO/FTO; (c) LRS Ohmic-SCLC, (d) HRS Schottky barrier emission model for Ag/BYFO/FTO, (e) LRS Ohmic-SCLC, (f) HRS Schottky barrier emission model for Ag/BYFO/FTO.

$$J_{child} = \frac{9}{8}\mu\epsilon\frac{V^2}{d^3} \tag{6.2}$$

where, q, n_0, *and* μ are the elementary charge, free charge carriers density at thermal equilibrium, and mobility of electrons, respectively. V *and* d are the applied voltage and film thickness, respectively. According to the SCLC mechanism, the injected charge (n_i) carriers are lower than the thermally generated charge carriers (n_0), which depends on the electrical properties of the dielectric material and the applied electric field. n_0 exhibit higher relaxation time, which doesn't allow these carriers to transport through the entire film thickness, which causes the device to remain in HRS. With increase in voltage, the $n_i > n_0$, resulting in filling of available trap site present in the film and the Ohmic region transform to SCLC region. With further increase in voltage, all trap sites are filled, which allows n_i to move freely along the film, leading to the steep rise in current and device switch to LRS ($V_{set} = +3\ V$ *present device*). However, at LRS, the transport process is entirely dominated by Ohmic conduction with obtained slope $m \approx 1$. The different types of conduction mechanisms at HRS ($Ohmic \rightarrow SCLC$) and LRS (Ohmic) indicate that the ON state conductivity is due to the formation and rupturing of conductive filaments [248]. However, for -ve sweeping voltage, the conduction mechanism behaves similarly when the device evident switch from LRS to HRS [Fig. 6.3.5 (d)].

Like BFO, $Ag/BYFO/FTO$ and $Ag/BYFSO/FTO$ RRAM devices at LRS and HRS follow the similar conduction process under both +ve and -ve biasing voltage. We explain the results obtained from the **B** and **C** during +ve sweeping voltage as follows:

(i) Y-doping marks an abrupt change in the conduction process at LRS [Fig. 6.3.5 (b)], where the

State	LRS		HRS	
Sample code	+ve bias	-ve bias	+ve bias	-ve bias
BFO	Ohmic	Ohmic	SCLC	SCLC
BYFO	SCLC	SCLC	Schottky	Schottky
BYFSO	Ohmic	Ohmic	Schottky	Schottky

Table 6.3.1: Conduction models explaining the resistive switching effect at high resistance state (HRS) and low resistance state (LRS) by sweeping the positive and negative bias voltage for BFO, BYFO, and BYFSO based RRAM devices.

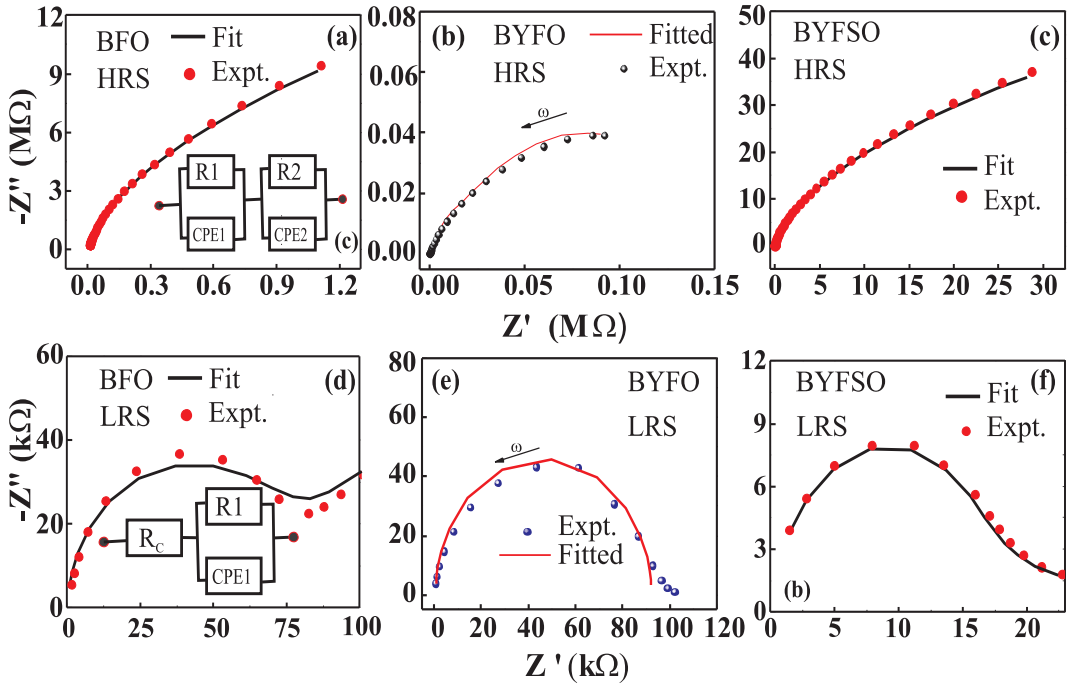

Figure 6.3.6: Impedance spectroscopy analysis explaining RS mechanism at HRS (a) BFO, (b) BYFO, and (c) BYFSO, and at LRS (d) BFO, (e) BYFO, and (f) BYFSO multiferroic based RRAM devices.

switching mechanism transfer from Ohmic-SCLC with obtained slope $m \approx 1$ at the low-voltage region and $m \approx 2$ obtained at the high-voltage region.

(ii) Addition of Sc to BYFO forth back the conduction process of LRS to its original state with obtained slope $m \approx 1$, as shown in Fig. 6.3.5 (c).

Doping and co-doping induce the charge transport mechanism at HRS with the response to the voltage signal. The HRS state for **B** and **C** devices has been explained through $ln(I) \propto V^{\frac{1}{2}}$ curve as shown in Figs. 6.3.5 (e)-(f). The curve is well fitted with the Schottky barrier emission conduction mechanism, which ensures that due to excess thermionic emission, the electrons are unable to jump the barrier height created between the interface of the switching layer and electrode, which results in a sudden drop-down in conductivity. The conduction models describing the RS effect at LRS and HRS during the +ve and -ve sweeping voltage for all studied device system is listed in Table 6.3.1.

Sample code	HRS				LRS		
	R1($M\Omega$)	R2($M\Omega$)	C1 (pF)	C2(pF)	R_c($k\Omega$)	R1 ($k\Omega$)	C1(pF)
BFO	17	54	18.4	21	114	7.8	15
BYFO	38	89	27	38	145	89	34
BYFSO	42	94	39	44.7	120	12	42

Table 6.3.2: The electrical parameters at HRS [grain/bulk resistance (R1), grain boundary resistance (R2), CPE1, and CPE2) and at LRS (contact resistance (R_c), R1, and CPE1) are extracted from the fitting model for BFO, BYFO, and BYFSO based memory device.

Impedance spectroscopy verification at LRS and HRS

The conduction mechanism has been further explored through the impedance spectroscopy analysis measurements carried out for the devices at HRS and LRS studied at a wide frequency range between 1 Hz-1 MHz. Figures 6.3.6 (a)-(c) displays Nyquist plots at HRS **A**, **B** and **C** devices, respectively, where the obtained impedance found in the range of $M\Omega$. After switching to LRS, a sudden drop-down of impedance ($k\Omega$) confirms the RS phenomenon driven by the formation of conducting O_{vs} channels through the MF films. The relaxation time due to the Debye relaxation process can be calculated by using the equation:

$$\omega\tau = 1 \tag{6.3}$$

ω and τ are the frequency and relaxation time, respectively. A substantial decrease in relaxation time (μs *to* s) during the RESET process explains the damping rate of hopping of charge carrier results in the HRS [252].

The Nyquist plots obtained from Impedance spectroscopy at HRS and LRS are simulated with equivalent electrical circuits shown in the inset of Fig. 6.3.6 (a) and (d). At HRS, he electrical circuit comprises of two parallel combinations of the R-C circuit connected in series. However, at LRS, the circuit consists of the parallel combination of a resistor (bulk resistance) and capacitor (bulk resistance) combined with a resistor (contact resistance) in series. The electrical parameters at HRS [grain/bulk resistance (R1), grain boundary resistance (R2), CPE1, and CPE2] and LRS [contact resistance (R_c), R1, and CPE1] are extracted from the fitting model listed in Table 6.3.2. The grain capacitance (C1) and grain boundary capacitance (C2) one can found by using the values of constant phase element CPE1 and CPE2, respectively.

From the above results, the grain boundary effect dominates the conduction process at HRS, while grain/bulk effect plays a vital role during the charge transport at LRS. The values of R1 from HRS to LRS asserting that the RS mechanism is driven by the large change in bulk resistance due to the creation of conducting O_{vs} channel inside the MF films [253]. There was no significant degradation in the capacitance (C) value during the transition from HRS to LRS of the devices. A negligible variation in C during the switching process suggests the construction of a large number of parallel conducting channels. The origin of the conducting channels analogous to the several capacitors is connected in parallel during the SET process.

Oxygen migration induced oxygen vacancies

The Ohmic-SCLC conduction mechanism and impedance analysis indicate the BRS behavior is attributed by the formation or rupturing of the conducting O_{vs} filament, as shown in Fig. 6.3.7. In

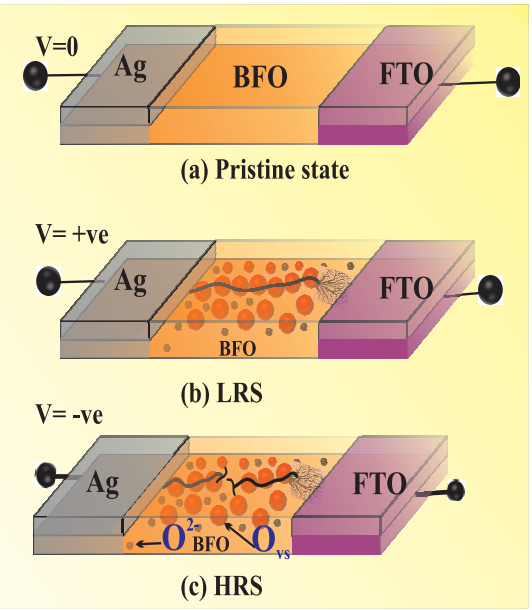

Figure 6.3.7: BRS mechanism with formation and rupturing conducting filament at (a) pristine state, (b) LRS, (c) HRS for Ag/BFO/FTO RRAM device.

MF BFO, O_{vs} is the primary driver for switching behavior. With the application of +ve voltage to Ag, the +vely charged O_{vs} moves towards the cathode, and O^{2-} ions move towards the anode. This resultant ionic motion build a conducting filament between Ag and FTO, which makes the device switch to LRS. However, during -ve voltage, the filament rupturing takes place and restores the device at HRS. The extensive electron diffraction spectroscopy (EDS) analysis confirmed there was no diffusion of Ag into the BFO film. In non-magnetically modified BFO devices, the volume cell modulation attributed the O_{vs} created towards the cathode, while the electrons knock out from O_{vs} drifts towards the opposite electrode.

6.4 Magnetic field modulated multilevel resistive switching behavior in $Ag/BiFeO_3/FTO$ device

The elemental substitution effect as an advantage to improve the RS behavior in MF BFO. In the above section, we explain the RS phenomena controlled under the action of current and voltage only. It is already discussed, BFO and its associated films exhibit multifunctional properties such as MEC, PE, magneto-striction, etc. due to the existence of many order parameters simultaneously in the single phase. ME effect phenomena not only useful to understand rich scientific phenomena but also promises for novel multifunctional application. Due to the MF nature of BFO, the charge carriers response under the application of the magnetic field in comparison to other non-magnetic compounds. The evidence for the existence of magnetoelectric coupling (MEC) in BFO is already explained in Chapter-3. However, there is a high chance for improving MEC in BFO thin films [254, 255]. A high ME effect material promises for multistate memory applications [256]. Hence, this motivates us to investigate the effect of the magnetic field on the RS effect of the device. Due to the application of an additional degree of freedom, the performance of the device can be improve for high-density data

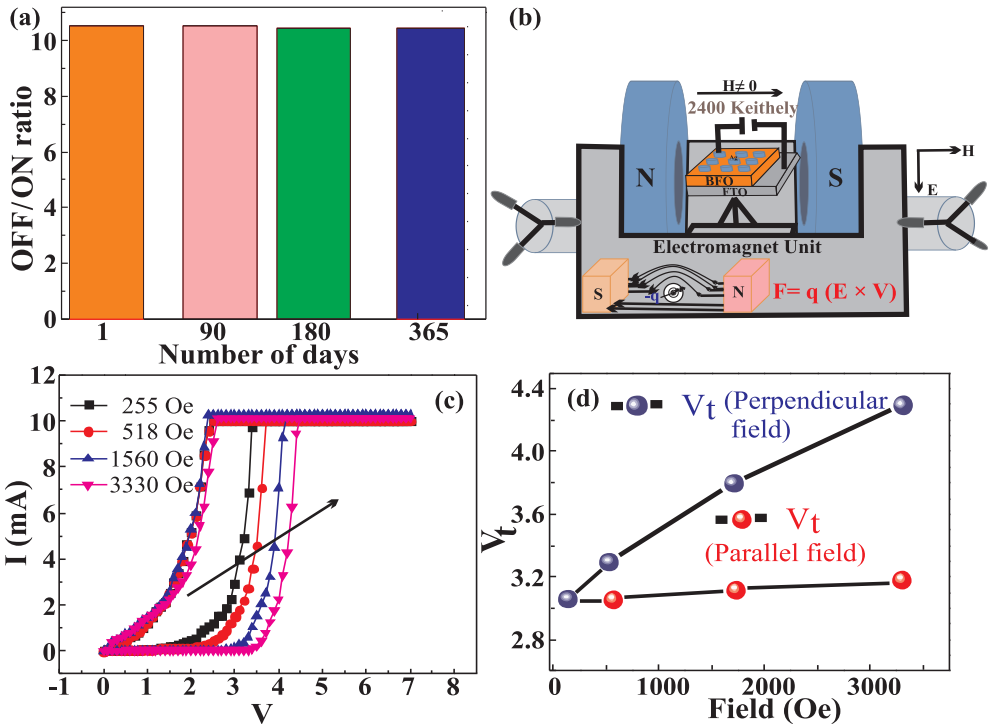

Figure 6.4.1: (a) Stability of the Ag/BFO/FTO device over a period of one year, (b) schematic representation of $I-V$ measurements set-up with the application of magnetic field, (c) typical $I-V$ characteristics in linear scale, and (d) shifting of V_t under the influence of various magnetic field.

storage capacity.

6.4.1 Effect of the magnetic field to the resistive switching behavior

The stability of the MF based Ag/BFO/FTO device observed for one year, which ensures the non-degradation of the device for a long time [Fig. 6.4.1 (a)]. Figure 6.4.1 (b) shows the schematic arrangement of device characteristics measurements under the application of the magnetic field (H) by using the electromagnet unit. We applied H perpendicular ($\perp$) to the flow of current (I), as shown in Fig. 6.3.7 (c). To observe the effect of the varying magnetic field to the resistance states of the device, we measure $I-V$ characteristics of the $Ag/BFO/FTO$ device at the various magnetic field displays in Fig. 6.4.1 (c). Originally, the device exhibit SET process at $V_t = 3\ V$ [Fig. 6.3.1 (a)] without any magnetic influence. However, the device evident a shift in V_t towards the higher voltage region with the rise in H, which indicates the magnetic influence delay the transition from HRS to LRS [257]. According to EM theory, the charge carrier experiences a Lorentz force, which is out of the plane of the paper ($\vec{E} \perp \vec{H}$) under the application of a transverse magnetic field. The expression for Lorentz force:

$$F = q(\vec{E} + v \times \mu_0 \vec{H}) \tag{6.4}$$

where q and E are the electron charge and the applied electric field, respectively. v is the drift velocity of the electron and μ_0 is the permeability in the vacuum. $\vec{H}$ the external applied magnetic field, which is perpendicular to the flow of current. The appearance of Lorentz force during $\vec{E} \perp \vec{H}$

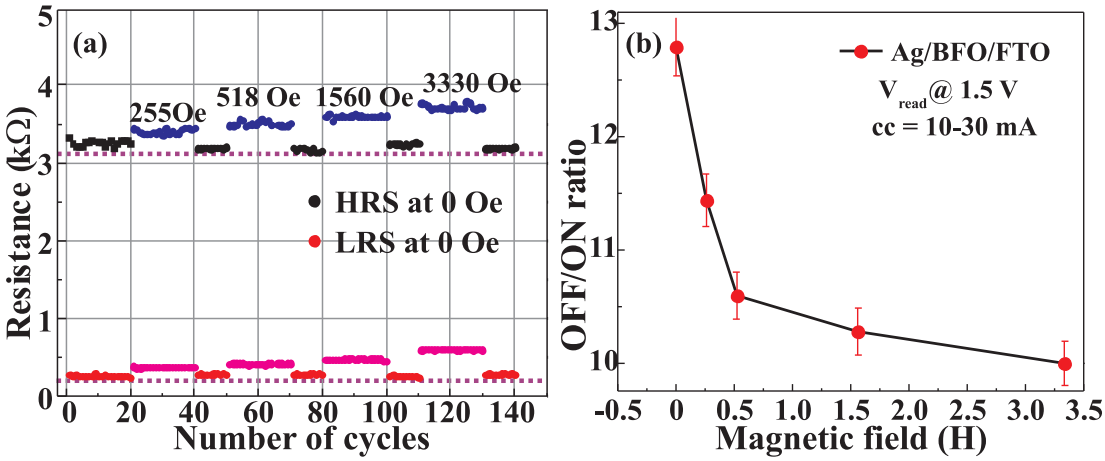

Figure 6.4.2: Enhance OFF/ON ratio with varying magnetic field applied externally to the device.

affect the device under the magnetic field. In TiO_2 based device, the residual Lorentz force was experienced, which carry forwards the transport mechanism [245], which cannot be ruled out in the present studied configuration. Essentially, in MF, the polarization (dipoles) are tuned by both electric (E) and magnetic field (H) and vise-versa. Hence, it is easy for the charge carrier to carry forward the process as compared to other magnetically controlled system. Also, the MEC in BFO plays a vital role to modulating the resistance when the voltage is applied in the presence of the magnetic field [45]. The device also tested while the magnetic field is parallel to the flow of current and found minimal effect. The modulation of the V_t under both condition is displayed in Fig. 6.4.1 (d).

The retention or the endurance characteristics of the $Ag/BFO/FTO$ device was investigated by performing 100 multiple testing cycles and found stable [Appendix]. The non-degradation of the device ensures the switching between HRS and LRS is reproducible, reversible, and controllable. The OFF/ON ratio already obtained [Fig. 6.3.3 (a)] was obtained 12 for the device. The endurance characteristics of the device further examined under the influence of the external magnetic field $[0 - 3330\ Oe]$ for 20 repetitive cycles ($cc \approx 10\ mA$ constant), as illustrated in Fig. 6.4.2 (a). The magnetic field was withdrawn intentionally at each state to verify the immediate effect after magnetic interaction for 10 cycles. However, the device restores to its original configuration once the magnetic field is removed. From Fig. 6.4.2 (a), the resistance of both LRS and HRS improved with increase in the magnetic bias from $0 - 3330\ Oe$. The increase in resistance may be due to the appearance of Lorentz force, which opposing the motion of oxygen vacancies to move freely inside the dielectric layer, resulting in weakening the conducting state and increase the resistance. Moreover, the switching between HRS and LRS is hampered, and OFF/ON ratio falls from 12 to 10 at 3330 Oe. The tuning of resistance confirms the magnetic field modulates the switching states of the device. Although the RS performance is not better than other conventional RRAM devices, our results indicate possible multifunctional applications in NVM industries.

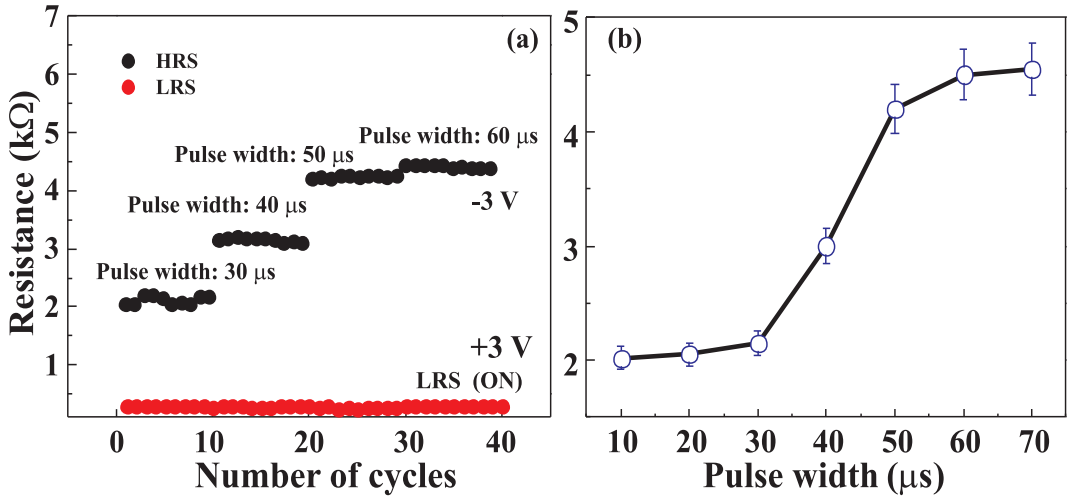

Figure 6.4.3: (a) The change of resistance state at pulse width 30 μs and 60 μs, (b) resistive switching of Ag/BFO/FTO device with varying pulse voltage and magnetic field.

6.4.2 Magnetic field controlled pulse-width (PW) and pulse-height (PH) modulated multilevel resistive switching behavior in $Ag/BFO/FTO$ device

RRAM devices categorized as one of the most leading emerging NVM technology and are the strong contender for replacing the existing present nonvolatile devices. Besides scaling down the cell area, the data density of the device can be increased in a multilevel cell (MLC) memory device. Presently in RRAM, the multilevel RS has been achieved by modulating the cc, RESET voltage, and voltage pulse amplitude [258, 259, 260]. However, many of these results have not shown sufficient switching ratio within these resistive states. Sometimes these states are overlapped during modulation of applied parameters, which can lead to create errors during data storage.

Pulse-width modulated multilevel resistive switching

The MF $Ag/BFO/FTO$ RRAM device can achieve multilevel resistive states by modulating the pulse-width (PW) to 50×50 μm^2 memory cell. For PW modulation, we applied a fixed SET voltage (+3 V) and pulse width (10 μs) to achieve the LRS of the device. A RESET voltage (-3 V) is applied to achieve the HRS state. The resistance of these states improved with a systematic increase in PW from $30 - 60$ μs ($cc \approx 10 - 30$ mA), as shown in Fig. 6.4.3 (a). From figure, the device achieved various resistive states by tuning the RESET PW. However, the saturation of resistance beyond 60 μs ensures no further available states. The OFF/ON for each RESET state ($30 - 60$ μs) is calculated for 10 repeated cycles, which suggests minimal growth during PW modulation. Alamgir *et. al.* reported thirteen discrete resistive states achieved in bi-layer TaO_x based RRAM device [247]. Moreover, the change in resistance is minimal in the present device in comparison to the Ta-based device. The variation of resistance of HRS as a function of PW is shown in Fig. 6.4.3 (b).

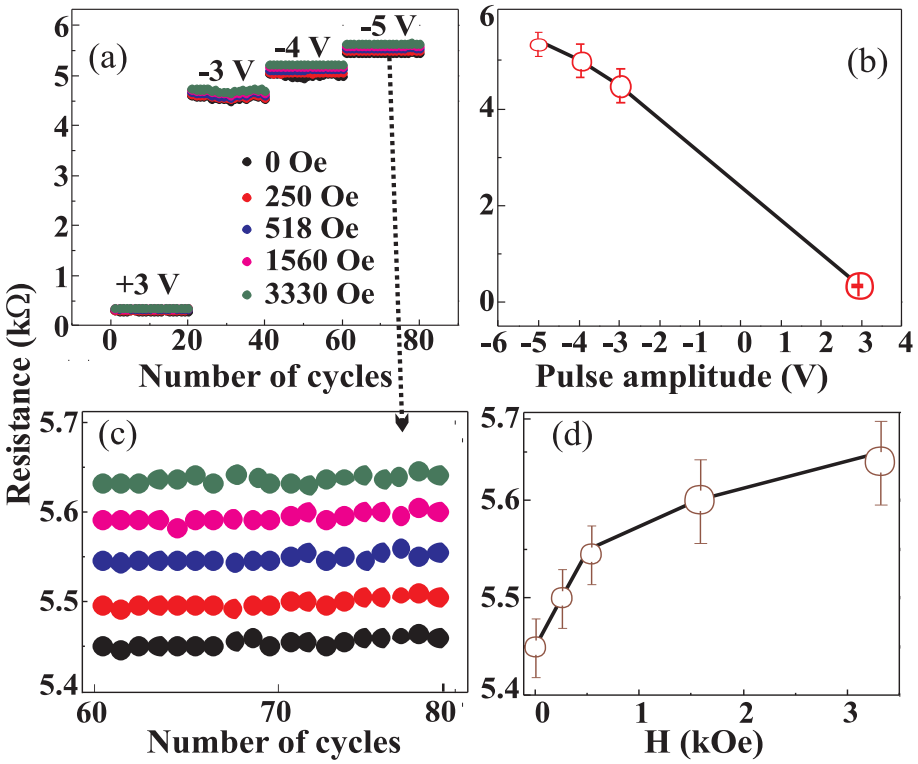

Figure 6.4.4: (a) The change of resistance state at pulse width 30 μs and 60 μs, (b) resistive switching of Ag/BFO/FTO device with varying pulse voltage and magnetic field.

Pulse-height modulated multilevel resistive switching:

Similarly, for pulse-height (PH) or pulse-amplitude modulated multilevel RS, we fixed the SET voltage at +3 V and PW of 60 μs. The device achieved discrete resistive states while changing the PH from -3 V to -5 V, as displayed in Fig. 6.4.4 (a). The OFF/ON ratio improved significantly, which is previously restricted during PW modulation. The variation of resistance with modulation of PH is displayed in Fig. 6.4.4 (b). We further examined the PH modulation under the various magnetic field between $0 - 3330$ Oe, as shown in Fig. 6.4.4 (a)-(c). The resistance of both SET and RESET states increases systematically with the rise in the magnetic field due to the appearance of Lorentz force and the existence of the ME effect in the MF BFO film. Shen *et. al.* achieved multilevel states in ME PMN-PT/Terfenol-D MF heterostructure due to ME effect [256]. The obtained resistive states with a magnetic field can be categorized into sub-multilevel resistive states and can be used for neuromorphic and future multi-bit data storage applications [261]. The variation of resistance under the magnetic field displays minimal growth, as shown in Fig. 6.4.4 (d). The studied results are reproducible and stable during measurements. The tuning of resistance states with various magnetic field precisely uses for future multilevel RRAM resistive memory device.

The above results suggest, achieving the discrete multilevel resistive states of $Ag/BFO/FTO$ by modulating the PW, PH, and magnetic field, indicating the tuning of RRAM device in a multifunction way, which can be operated in remote way.

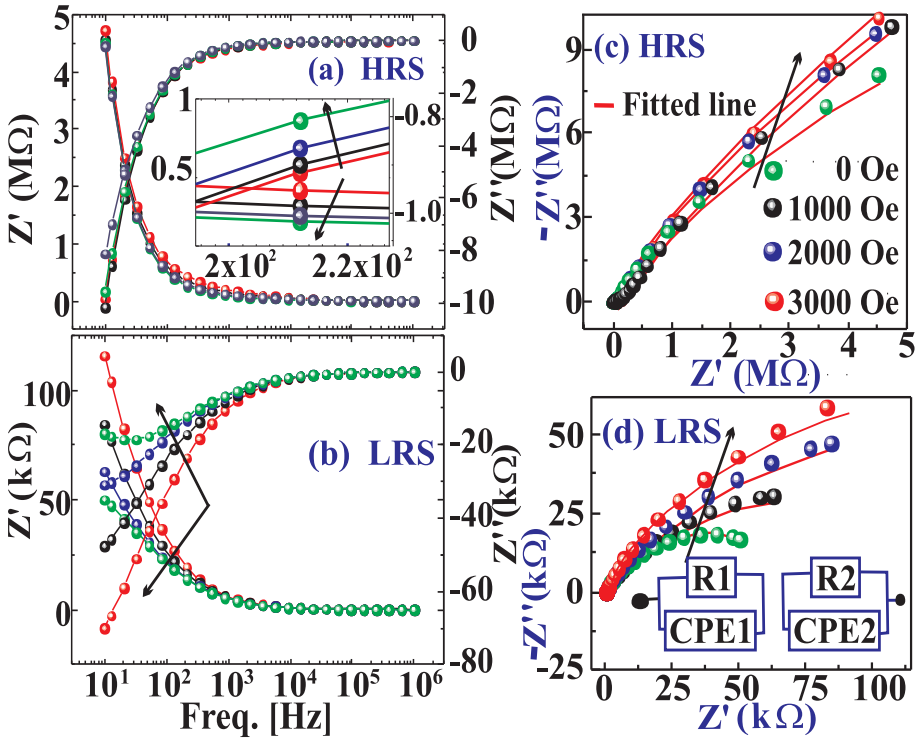

Figure 6.4.5: (a) Impedance spectroscopy at HRS and LRS, and (b) Nequist plots at HRS and LRS with varying magnetic field.

6.4.3 Magnetic field influence impedance spectroscopy analysis at HRS and LRS of $Ag/BFO/FTO$ device

To elucidated more discussion regarding the RS effect in $Ag/BFO/FTO$ device, the impedance spectroscopy has been performed under various magnetic fields (H) between $0 - 3000$ Oe. Figures 6.4.5 (a-b) shows the frequency, and the magnetic field modulated real (Z') and imaginary part (Z'') of complex impedance at both HRS and LRS, respectively. Z' and Z'' for both HRS and LRS increases with increase in H, which found analogous with the $I - V$ curves under the magnetic influence [Fig. 6.4.2 (a)]. Figures 6.4.5 (c)-(d) represent the Nyquist's plots under the magnetic field at both HRS and LRS, respectively. The appeared semicircular arcs are well fitted with the R-C equivalent circuit [inset: Fig. 6.4.5 (d)]. The extracted electrical parameters reveal, the grain resistances (R_1) increases with increase in H [for both states] confirms the control of impedance state with the magnetic field. Also, the diameter of semicircles for both switching states expanded with the rise in H supports the improved R_1. In addition to this, the sudden drop-down of resistance from HRS ($M\Omega$) to LRS ($k\Omega$) specifies the RS effect in MF based RRAM device. The change in impedance with the magnetic field looks promising for the future magneto-impedance based sensor in MF materials.

6.5 Conclusion

In summary, we have explored the effect of elemental substitution and magnetic field on the resistive switching behavior of the multiferroic based RRAM device. The performance of the device is improved significantly in the presence of additional parameters. The $I-V$ characteristics for $Ag/BFO/FTO$, $Ag/BYFO/FTO$, and $Ag/BYFSO/FTO$ devices are produced distinct hysteresis loop, which ensures the proper BRS behavior in the devices. The conduction models such as Ohmic, while trap-controlled SCLC, Schottky barrier emission dominates the conduction process. The memory window or switching ratio between the HRS and LRS improve significantly with doping/co-doping and found maximum for Y-Sc co-doped based device. The application of the magnetic field shifts the threshold voltage towards higher voltage due to the appearance of the Lorentz force when the magnetic field is perpendicular to the direction of the flow of current. Substantially, the resistance of the resistive states of Ag/BFO/FTO further increases systematically with the increase in the magnetic field. The modulation of resistance states under the application of magnetic field promises for high data-density and ultrafast multilevel RRAM devices. Discrete multilevel resistive states of $Ag/BFO/FTO$ by modulating the pulse width, pulse height, and magnetic field, indicating the MF based device behaves as a multifunctional memristor. The switching is reproducible, reversible, and controllable for all the devices, which can be utilized for future NVM and information technology.

Graphical Abstract

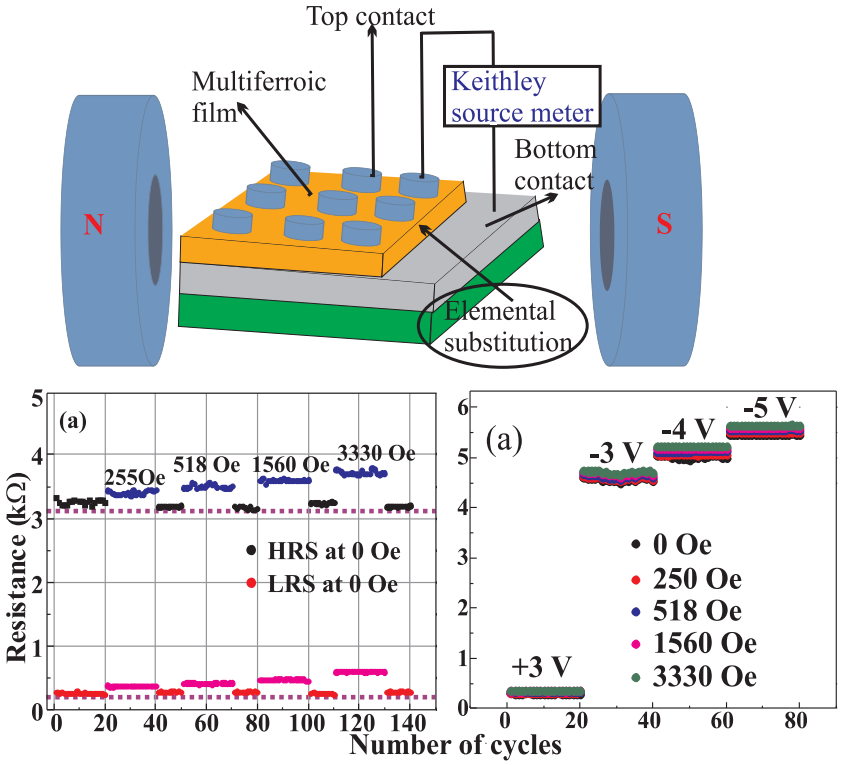

Chapter 7

Summary and scope for future work

In this thesis, we explored the existence of many-body effects such as magnetoelectric (ME) effects, piezoelectric effect, etc. and its possible applications in multiferroic Y-Sc/Mn co-doped $BiFeO_3$ compound. Based on the results that we presented in previous chapters, we summarize our results as follows:

7.1 Summary

7.1.1 Temperature-dependent terahertz signal from antiferromagnetic tuned $BiFeO_3$ ceramics

- Multiferroic bismuth ferrite system tuned under co-doping with combination of partially filled d-shell (Nd-Gd), unfilled (Y)-partially (Mn) filled d-shell, and unfilled d-shell (Y-Sc).
- Co-doping with partially filled d-shell Gd^{3+} and Nd^{3+} improved the ferromagnetic properties in rhombohedral R3c structure of BFO. However, the appearance of secondary phases and weak ferroelectric signals minimize the possibility for existence of any application.
- Y-Mn helps in stabilizing crystal structure with low field saturation of BFO. But, the poor ferroelectric and dielectric properties minimize the chances for good magnetoelectric material.
- Non-magnetic unfilled d-shell Y^{3+} and Sc^{3+} ions modified BFO ceramics marks much focus due to its stable crystalline structure with the noticeable improvement in multiferroic and magnetoelectric properties.
- Shifting of THz peaks with increasing the temperature indicates the delay in the signal, which leads to small modification in the refractive index observed from THz spectra of time-domain spectra. However, in frequency domain spectra for THz signal, the softening of magnon-modes are evident, which results in the shifting of the spectra with the rise in temperature.

- The THz spectroscopy analysis reveals the optical properties such as refractive index ($\tilde{n}$), dielectric constant (ϵ) increases in Y-Sc co-doped BFO ceramics. The optical conductivity follows the Drude-Smith model.

7.1.2 Elementary substitution effect on dipolar polarization modulation of multiferroic $BiFeO_3$ ceramics

- We have explored the modulation of dipolar polarization and relaxation behavior of multiferroic BFO with elementary substitution (Y-Mn/Sc) effect.
- A perfect correlational between the structural, multiferroic, and dielectric properties is obtained. The ferromagnetic and ferroelectric properties of co-doped BFO improved significantly due to the structural distortion [SSMS suppression] and reduction in leakage current density, respectively.
- The room temperature dielectric constant (ϵ_r) of BFO enhance 51 times after Y-Sc co-doping. The tangent loss peak slowly shifts towards the room temperature in the path $BYFMO$ [70^0 C]$-$ $BYFSO$ [30^0 C], which was appeared initially above 100^0 C for the parent BFO.
- The insulating behavior of co-doped ceramics modified due to the presence of doubly ionized oxygen vacancies (O_{vs}). The conduction mechanism of un-doped and co-doped Y-Mn/Sc co-doped follows the correlated barrier hopping (CBH) model and long-range oxygen vacancies when associated with thermal energy.
- From the above discussion, Y-Sc co-doped BFO found as an excellent multiferroic material with high insulating properties.

7.1.3 Electrically tuned stable ferroelectric switching in non-magnetic ion modified $BiFeO_3$ films

- The single-phase (Rhombohedral: R3c) un-doped BFO, and non-magnetic ion modified BYFO, BYFSO thin-films successfully synthesized by using sol-gel spin coating technique.
- The grain and particle size manipulated due to Y/Y-Sc insertion. The conductivity of the BYFSO is found weak in comparison to BFO and Y-doped BFO film.
- The evidence for improved canted ferromagnetic properties and spin-glass like behavior for long-range temperature obtained in BYFSO film. MFM analysis suggests weak in-plane magnetic domains are evident in BFO and Y-Sc modified BFO films.
- The 180^0 type domain switching mediates through 71^0 and 109^0 type ferroelastic switching. The presence of maximum non-180^0 domains indicates the improved piezoelectric response of BFO film after Y-Sc co-doping. All upward and downward polarization switching is evident under the applied dc bias of ± 8 V, which is well supported with symmetry C-V, P-E, and amplitude-voltage hysteresis curves.
- With significant improvement in ferroelectric, ferromagnetic, and piezoelectric properties, the Y-Sc co-doped BFO system is useful for future non-volatile memory applications.

7.1.4 Magneto-electric rectifying multilevel resistive switching in multiferroic based devices

- We have explored the effect of elemental substitution and magnetic field on the resistive switching behavior of the multiferroic based RRAM device.
- The performance of the device is improved significantly in the presence of additional parameters. The $I-V$ characteristics for $Ag/BFO/FTO$, $Ag/BYFO/FTO$, and $Ag/BYFSO/FTO$ devices are produced distinct hysteresis loop, which ensures the proper BRS behavior in the devices.
- The conduction models such as Ohmic, while trap-controlled SCLC, Schottky barrier emission dominates the conduction process. The memory window or switching ratio between the HRS and LRS improve significantly with doping/co-doping and found maximum for Y-Sc co-doped based device.
- The application of the magnetic field shifts the threshold voltage towards higher voltage due to the appearance of the Lorentz force when the magnetic field is perpendicular to the direction of the flow of current. Substantially, the resistance of the resistive states of Ag/BFO/FTO further increases systematically with the increase in the magnetic field.
- Discrete multilevel resistive states of $Ag/BFO/FTO$ by modulating the pulse width, pulse height, and magnetic field, indicating the multiferroic based device behaves as a multifunctional memristor. The switching is reproducible, reversible, and controllable for un-doped and co-doped BFO based RRAM devices.

7.2 Future outlook

Scientific interests always demand a sincere effort towards extending the present ideas and understanding to venture new avenues of discoveries. Similarly, a significant extension of this thesis work has been performed to unravel newer ways to create and control $BiFeO_3$ thin-films and its heterostructures. This section is going to provide a glimpse of the extended part of the thesis work, which will be continued in the near future to frame a complete scientific understanding.

7.2.1 Experimental evidence for the dynamic spin-charge ordering mediate through strain in $BiFeO_3$

The multiferroic (MF) and ME effect properties of BFO ceramic improved significantly after non-magnetic ion substitution, which is discussed in Chapter-3 and Chapter-4. BFO exhibit magneto-electric coupling (MEC) between the polarization and magnetization. Such a coupling is not only useful to understand the physics rich phenomena but also promises for designing novel applications. The MEC in multiferroic can be understood in two various approaches: (i) direct coupling between P and H and (ii) coupling mediate through strain (mixing of piezoelectricity and magnetostrictive). Both couplings are static property of the materials. But how strain affects the multiferroic properties *dynamically* is still have the grey area for investigation. The coexistence of magnetoelectric coefficient due to the strain effect in multiferroics is yet unclear. It is also legitimate to focus on the effect

of strain on the *electromagnon* (combination of magnon and phonon) or even on the identification of novel dynamical phenomena [213].

- To understand such a novel phenomenon one needs to perform THz spectroscopy on multiferroic Y-Sc co-doped BFO compound.
- Need to study the tuning of polarization (P) with respect to the magnetic field in both the time-domain and frequency domain. Similarly, the tuning of magnetization (M) under applied electric field, due to the origin of phonon mode of order few MeV, which lies in the THz range.
- Study of dynamic quadratic MEC in the frequency domain at (i) strain is relaxing and (ii) strain is frozen conditions.
- The strain-mediated MEC is of significant interest to design novel devices with the proper shape of the material for dynamic applications [262].
- The study of a new type of quasiparticle *electroacoustic magnon* have a large interest in multiferroic materials.

7.2.2 Tuning of magnetoelectric coupling in multiferroic based novel heterostructure for possible application

Multiferroic magnetoelectric nano-structures based heterostructure with coupled magnetization and electric polarization across their interfaces have stimulated intense research activities over the past few decades. Such interface-type MEC can be exploited to significantly improve the performance of broad novel applications in memories, microwaved devices, and sensors. In Chapter-5, the Y-Sc co-doped BFO film exhibit an improved ME effect with stable ferroelectric switching [263]. But, BYFSO based film promises for coexisting applications; however, the obtained MEC at room temperature is not sufficient for real practical applications to the modern community. Hence, a multilayer structure can be predicted by clamping a ferromagnetic layer with the ferroelectric BYFSO, which will may useful for the real application [263].

Development of magnetoelectric coupling in multiferroic based heterostructure

- The ME effect of multiferroic (MF) materials is not only useful to understand the enrich physics but also useful for novel potential applications.
- The MEC is found to be weak in single phase MF system and can be improved by clamping with ferromagnetic (FM) in the form of multilayer or heterostructure. We propose MF based bilayer systems with Ni, Fe, and Co alloys with the possibility of the existence of high MEC.

Electric field controlled magnetism

- The voltage (V) and magnetic (B) driven M is important to understand the fundamental interactions among electron, phonon, and spin due to its scalable limit, which prefer for applications in industrial sectors.

- The application of the electric field can be manipulated by the magnetic domains in heterostructure films. Careful control of growth conditions and unique substrate selection can lead to better magnetic signals under the applied electric field.
- The nano-structured system finds interest in exploring the role of 'V' controlled magnetism.

Magnetic relaxation dynamics under external perturbations

- The other possible way to manipulate the magnetism under the various external perturbations such as temperature, light, ion-beam irradiation.
- We want to probe the modified magnetic properties, which can be explained the relaxation dynamics over a millisecond (ms) the axenic of magnetic domain over an ms time-scale.

Ultrafast switching in nanostructure

- The dynamic behavior of electron, phonon, and spin in heterostructure can be understood in different length- and time-scale by probing with a femtosecond laser.
- We observed the magnetoelectric switching is difficult to probe in ultra-fast scale in single phase multiferroic due to weak MEC. However, it can be achieved in strong MEC *Ferromagnetic/Multiferroic* system, where the spins of FM are coupled to electromagnetic waves through both Zeeman coupling and MEC. The ultrafast and precise ME switching in nano-structural films find it more interesting.
- The manipulation of ME effect in heterostructure is not explored much in ultrafast scales. These scientific understanding can be implemented for possible applications in spintronic and storage devices.

References

[1] H. Schmid, Multi-ferroic magnetoelectrics, Ferroelectrics **162**, 317338 1994.

[2] R. Ramesh and N. Spaldin, Multiferroics: progress and prospects in thin films, Nature Materials **6**, 21-29 (2007).

[3] S. Dong, J. Cheng, J. F. Li, and D. Viehland, Enhanced magnetoelectric effects in laminate composites of $Terfenol - D/Pb(Zr, Ti)O_3$ under resonant drive, Appl. Phys. Lett. **83**, 4812 (2003).

[4] V. Garcia *et. al*, Ferroelectric Control of Spin Polarization, Science **327**, 1106 (2010).

[5] D. Khomskii, Trend: Classifying multiferroics: Mechanisms and effects, Physics **2**, 20 (2009).

[6] J. R. Teague, R. Gerson, and W. J. James, Dielectric hysteresis in single crystal $BiFeO_3$, Solid State Communications **8**,10731074, 1970.

[7] T. Kimura, T. Goto, H. Shintani, K. Ishizaka, T. Arima, Y. Tokura, Magnetic control of ferroelectric polarization, Nature **426** (6962), 5558, (2003).

[8] G. A. Smolensky, V. A. Isupov, N. N. Krainik, A. I. Agranovskaya, Isvest. Akad. Nauk SSSR, Ser. Fiz, 25 1333 (1961).

[9] N. A. Hill, J. Phys. Chem. B, 104 6694 (2000).

[10] A. M. dos Santos, S. Parashar, A. R. Raju, Y. S. Zhao, A. K. Cheetham and C. N. R. Rao, Solid State Comm., 122 29 (2002)

[11] Z. J. Huang, Y. Cao, Y. Y. Sun, Y. Y. Xue and C. W. Chu, Phys. Rev. B, 56 2623 (1997).

[12] P. Baettig, C. Ederer and N. A. Spaldin, Phys. Rev. B, 72 214105 (2005).

[13] I. Sosnowska, T. P. Neumaier and E. Steichele, J. Phys. C:Solid State Phys., **15** 4835 (1982)

[14] A. J. Jacobson and B. E. F. Fender, J. Phys. C: Solid State Phys., 8 844 (1975)

[15] F. Kubel and H. Schmid, Acta Cryst. B, 46 698 (1990).

[16] V. K. Wadhawan. Introduction to ferroic materials. CRC press, 2000.

[17] J Valasek. Piezo-electric and allied phenomena in Rochelle salt. Physical Review, 17: 475, 1921.

[18] G. Shirane, S. Hoshino, and K. Suzuki. X-ray study of the phase transition in lead titanate. Physical Review **80**, 1105 1950.

[19] G. H. Haertling, Ferroelectric ceramics: history and technology. Journal of the American Ceramic Society **82** 797818, 1999.

[20] S. Yuan, H. Z. Fei, M. Xing, W. C. Zhong, C. Gang, and F. H. Gang, Acta Phys. Sin. 58, 193 (2009).

[21] J. B. Neaton, C. Ederer, U. V. Waghmare, N. A. Spaldin, and K. M. Rabe, Phys. Rev. B, 71 014113 (2005)

[22] J. Li, J. Wang, M. Wuttig, R. Ramesh, N. Wang, B. Ruette, A. P. Pyatakov, A. K. Zvezdin and D. Viehland, Appl. Phys. Lett., 84 5261 (2004).

[23] S. Sharma, A. Mishra, P. Saravanan, O. P. Pandey, P. Sharma, Effect of Gd-substitution on the ferroelectric and magnetic properties of $BiFeO_3$ processed by high-energy ball milling, Journal of Magnetism and Magnetic Materials **418**, 188 (2016).

[24] T. Durga Rao and S. Asthana, Evidence of improved ferroelectric phase stabilization in Nd and Sc co-substituted $BiFeO_3$, J. of Appl. Phys. **116**, 164102 (2014).

[25] Wei *et. al.*, Crystal structure, leakage conduction mechanism evolution and enhanced multiferroic properties in Y-doped $BiFeO_3$ ceramics, Cer. Int. **42**, 13395 (2016).

[26] D. Lakshmi B. *et. al.*, Enhanced magnetic and magnetoelectric properties of Mn doped multiferroic ceramics, Cer. Int. **43**, 9272 (2017).

[27] T. Durga Rao, S. Asthana, and M. K. Niranjan, Observation of coexistence of ferroelectric and antiferroelectric phases in Sc substituted $BiFeO_3$, J. of Allo. and Comp. **642**, 192 (2015).

[28] A. K. Jena, J. Arout Chelvane, and J. Mohanty, Evidence for dielectric suppression in nonmagnetic modified multiferroic bismuth ferrite, J. of Appl. Phys. **126**, 184101 (2014).

[29] J. Xu *et. al.*, Enhanced dielectric and multiferroic properties of single-phase Y and Zr co-doped $BiFeO_3$ ceramics, J. of Appl. Phys. **114**, 184101 (2014).

[30] A. Mukherjee, M. Banerjee, S. Basu, N. T. K. Thanh, L. A. W. Green, M. Pal, Enhanced magnetic and electrical properties of Y and Mn co-doped $BiFeO_3$ nanoparticles, Phys. B: Cond. Matt. **448**, 199 (2014).

[31] G. A. Smolenskii, I. E. Chupis, Sov. Phys.- Usp., 25 475 (1982)

[32] K. F. Wang, J. M. Lin, and Z. F. Ren, Adv. Phys. 58, 321448 (2009).

[33] W. Eerenstein, N. D. Mathur and J. F Scott, Nature, 442 759 (2006).

[34] Ablat *et. al.*, Structural analysis and magnetic properties of Gd doped $BiFeO_3$ ceramics, Cer. Int. **40**, 14083 (2014).

[35] Y, H. Lin, Q. Jiang, Y. Wang, C.-W Nan, L. Chen, and J. Yu, Enhancement of ferromagnetic properties in $BiFeO_3$ polycrystalline ceramic by La doping, Appl. Phys. Lett. **90**, 172507 (2007).

[36] S. R. Shannigrahi, A. Huang, N. Chandrasekhar, D. Tripathy, and A. O. Adeyeye, Sc modified multiferroic $BiFeO_3$ thin films prepared through a sol-gel process, Appl. Phys. Lett. **90**, 022901 (2007).

[37] A. K. Jena, J Mohanty, Enhancing ferromagnetic properties in bismuth ferrites with nonmagnetic Y and Sc codoping, Journal of Material Science-Materials in Electronics **29**,5150-5156, (2017).

[38] A. K. Jena, S. Satapathy, and J. Mohanty, Journal of Applied Physics, **124**, 174103, (2018).

[39] R. Das, K. Mandal, Magnetic, ferroelectric and magnetoelectric properties of Ba-doped $BiFeO_3$, Journal of Magnetism and Magnetic Materials **324**, 1913 (2012).

[40] M. S. Bernardo *et. al.*, Intrinsic Compositional Inhomogeneities in Bulk Ti-Doped $BiFeO_3$: Microstructure Development and Multiferroic Properties, Chem. Mater. **25**, 1533 (2013).

[41] A. K. Jena, S. Satapathy, and J. Mohanty, Magnetic properties and oxygen migration-induced resistive switching effect in Y substituted multiferroic bismuth ferrite Phys. Chem. Chem. Phys. **21**, 15854-15860 (2019).

[42] A. K. Jena, J. Arout Chelvane, J. Mohanty, Simultaneous improvement of piezoelectric and magnetic properties in diamagnetic ion modified $BiFeO_3$ film, Journal of Alloys and Compounds **805**, 1168 (2019).

[43] J. C. Toledano and P. Toledano. Order parameter symmetries and free-energy expansions for purely ferroelastic transitions. Physical Review B, 21: 1139, 1980.

[44] E. T. Wefringa, F. H. Schader, K. G. Webber, M. Einarsruda, T. Grande, Electrical conductivity and ferroelastic properties of Ti-substituted solid solutions $(1x)BiFeO_3xBi_{0.5}K_{0.5}TiO_3$, J. of Euro. Cer. Soc. **36**, 497 (2016).

[45] S. H. Baek, *et al*, Ferroelastic switching for nanoscale non-volatile magnetoelectric devices, Nat. Mater. **9**, 309 (2010).

[46] M Fiebig. Revival of the magnetoelectric effect. Journal of Physics D: Applied Physics, 38: R123R152, 2005.

[47] W.C. Rontgen, Ann. Phys. 35, 264 (1888).

[48] P. Curie, J. Phys. Thorique Applique 3, 393 (1894).

[49] IE Dzyaloshinskii, On the magneto-electrical effect in antiferromagnets. Soviet Physics JETP-USSR, 10:628629, 1960.

[50] D. N. Astrov. The magnetoelectric effect in antiferromagnetics. Soviet Physics JETP-USSR, 11: 708709, 1960.

[51] N.A. Spaldin and M. Fiebig, Science 309, 391 (2005).

[52] G. S. Arya, R. K. Kotna, N. S. Negi, Enhanced magnetic and magnetoelectric properties of In and Co codoped BiFeO3 nanoparticles at room temperature, J. of Nano. Res. **16**, 2155 (2014)

[53] J. Kolte, A. S. Daryapurkar, M. Agarwal, D. D.Gulwade, P.Gopalana, Magnetoelectric properties of microwave sintered $BiFeO_3$ and $Bi_{0.90}La_{0.10}Fe_{0.95}Mn_{0.05}O_3$ nanoceramics, Mat. Chem. and Phys. **193**, 253 (2017).

[54] J. Ray, A. K. Biswal, P. D. Babu, V. Siruguri & P. N. Vishwakarma, Magnetoeletricity in $BiFeO_3$ and $Bi_Fe_{0.98}Co_{0.02}O_3$ nano particles, J. Alloys and Comp., 628, 32 (2015).

[55] T. H. Wang, C. S. Tu1, H. Y. Chen, Y. Ding, T. C. Lin, Y. D. Yao, V. H. Schmidt, and K. T. Wu1, Magnetoelectric coupling and phase transition in BiFeO3 and (BiFeO3)0.95(BaTiO3)0.05 ceramics, Journal of Applied Physics **109**, 044101 (2011).

[56] S. Yang, A. Kumar, V. Petkov, and S. Priya, Room-temperature magnetoelectric coupling in single-phase $BaTiO_3 - BiFeO_3$ system, Journal of Applied Physics 113, 144101 (2013).

[57] Chu, Y.-H. et al. Electric-field control of local ferromagnetism using a magnetoelectric multiferroic. Nat Mater **7**, 478482 (2008).

[58] Catalan, G., Noheda, B., McAneney, J., Sinnamon, L. J. and Gregg, J. M. Strain gradients in epitaxial ferroelectrics, Phys. Rev. B **72**, 020102 (2005).

[59] A. Hussain, X. Xu, G. Yuan, Y. Wang, Y. Yang, J. Yin, J. Liu, Z. Liu, The development of $BiFeO_3$-based ceramics, Chin. Sci. Bull. **59** (36), 51615169 (2014).

[60] L. Chen, Z. Cheng, W. Xu, X. Meng, G. Yuan, J. Liu and Z. Liu, Electrical and mechanical switching of ferroelectric polarization in the 70 nm $BiFeO_3$ film, Scientific Reports, **6**, 19092 (2016).

[61] A. Z. Simes, L.S. Cavalcante, F. Moura, E. Longo, J. A. Varela, Structure, ferroelectric/magnetoelectric properties and leakage current density of $(Bi_{0.85}Nd_{0.15})FeO_3$ thin films, J. of Allo. and Comp. **509**, 5326 (2011).

[62] Z. H. Chen, L. You, C. W. Huang, Y. J. Qi, J. L. Wang, T. Sritharan, L. Chen, Nanoscale domains in strained epitaxial $BiFeO_3$ thin films on $LaSrAlO_4$ substrate, Applied Physics Letters **96**, 252903 (2010).

[63] J. Seidel, L. W. Martin, Q. He, Q. Zhan, Y. H. Chu, A. Rother, M. E. Hawkridge, P. Maksymovych, P. Yu, M. Gajek, N. Balke, S. V. Kalinin, S. Gemming, F. Wang, G. Catalan, J. F. Scott, N. A. Spaldin, J. Orenstein, R. Ramesh, Conduction at domain walls in oxide multiferroics, Nature Materials **8**, 229 (2009).

[64] N. Panwar, I. Coondoo, A. Tomar, A. L. Kholkin, V. S. Puli, R. S. Katiyar, Nanoscale piezoresponse and magnetic studies of multiferroic Co and Pr co-substituted BFO thin films, Mat. Res. Bull. **47**, 4240 (2012) .

[65] Y. Jin, Y. *et al.* Studying the Polarization Switching in polycrystalline $BiFeO_3$ Films by 2D Piezoresponse Force Microscopy. *Scientific Reports* **5**, 12237 (2015).

[66] S. T. Zhang, M. H. Lu, D. Wu, Y. F. Chen, and N. B. Ming, Appl. Phys. Lett. **87**, 262907 (2005).

[67] B. Kundys, M. Viret, D. Colson, and D. O. Kundys, Nat. Mater. **9**, 803805 (2010).

[68] B. S. Kalanoor, M. Ronen, Z. Oren, D. Gerber, Y. R. Tischler, New Method to Study the Vibrational Modes of Biomolecules in the Terahertz Range Based on a Single-Stage Raman Spectrometer, ACS Omega **2**, 1232 (2017).

[69] A. Marouchkine, Room-Temperature Superconductivity, Cambridge International Science Publishing, (2004).

[70] G. Bosse *et. al.*, Low energy electrodynamics of the Kondo-lattice antiferromagnet $CeCu_2Ge_2$, Physical review. B, Condensed matter 85(15):155105 (2012).

[71] M. Y. WONG, G. D. SIMS & I. M. STEPHENSON, Operation of the Backward-Wave Oscillator, Nature volume 188, 803804 (1960).

[72] E. Alekseev, D. Pavlidis, GaN Gunn diodes for THz signal generation, 2000 IEEE MTT-S International Microwave Symposium Digest (Cat. No.00CH37017), (2000).

[73] X. L, K. Biermann, L. Schrottke, and H. T. Grahn, Terahertz quantum-cascade lasers for high-resolution spectroscopy of sharp absorption lines, Journal of Applied Physics 125, 151613 (2019).

[74] M. Ozerov *et. al.*, A THz spectrometer combining the free electron laser FLARE with 33T magnetic fields, Appl. Phys. Lett. 110, 094106 (2017)

[75] R. M. Hornreich and S. Shtrikman, Phys. Rev. 171, 1065 (1968).

[76] G. L. J. A. Rikken, C. Strohm, and P. Wyder, Phys. Rev. Lett. 89, 133005 (2002).

[77] M. Mochizuki, N. Furukawa, and N. Nagaosa, Phys. Rev. Lett. 104, 177206 (2010).

[78] D. M. Juraschek, M. Fechner, A. V. Balatsky, and N.A. Spaldin, Phys. Rev. Mater. 1, 14401 (2017).

[79] A. Pimenov, A.A. Mukhin, V.Y. Ivanov, V.D. Travkin, A.M. Balbashov, and A. Loidl, Nat Phys 2, 97 (2006).

[80] V.G. Baryakhtar and I.E. Chupis, Sov. Phys. Solid State 10, 2818 (1969).

[81] V.G. Baryakhtar and I.E. Chupis, Sov. Phys. Solid State 11, 26288 (1970).

[82] R. Valds Aguilar, A.B. Sushkov, C.L. Zhang, Y.J. Choi, S.-W. Cheong, and H.D. Drew, Phys. Rev. B 76, 60404 (2007).

[83] T. D. Dorney, R. G. Baraniuk, and D. M. Mittleman, Material parameter estimation with terahertz time-domain spectroscopy, J. Opt. Soc. Am. A 18(7), 15621571 (2001).

[84] L. Duvillaret, F. Garet, and J. L. Coutaz, A reliable method for extraction of material parameters in terahertz time-domain spectroscopy, IEEE J. Sel. Top Quantum Electron. 2(3), 739746 (1996).

[85] L. Duvillaret, F. Garet, and J.-L. Coutaz, Highly precise determination of optical constants and sample thickness in terahertz time-domain spectroscopy, Appl. Opt. 38(2), 409415 (1999).

[86] E. Mavrona, F. Appugliese, J. Andberger, J. Keller, M. Franckie, G. Scalari, and J. Faist, Terahertz refractive index matching solution, Optics Express **10**, 14536 (2019).

[87] Sibik, J.; Shalaev, E. Y.; Zeitler, J. A. Glassy Dynamics of Sorbitol Solutions at terahertz frequencies. Phys. Chem. Chem. Phys. 2013, 15, 1193111942.

[88] Tapia, A. K. G.; Tominaga, K. Conduction in Polyaniline Emeraldine Salt in the Terahertz Region: A Temperature Dependence Study. Chem. Phys. Lett. 2014, 598, 3942.

[89] Cooke, D. G.; MacDonald, A. N.; Hryciw, A.; Wang, J.; Li, Q.; Meldrum, A.; Hegmann, F. A. Transient Terahertz Conductivity in Photoexcited Silicon Nanocrystal Films. Phys. Rev. B: Condens. Matter Mater. Phys. 2006, 73, 193311.

[90] Smith, N. V. Classical Generalization of the Drude Formula for the Optical Conductivity. Phys. Rev. B: Condens. Matter Mater. Phys. 2001, 64, 155106.

[91] G. Dearnale, A. M. Stoneham, and D. V. Morgan, Reports on Progress in Physics 33, 1129 (1970).

[92] D. Panda, and T. Y. Tseng, Ferroelectrics 471, 23 (2014).

[93] A. L. Lacaita, and D. J. Wouters, Physica Status Solidi a-Applications and Materials Science 205, 2281 (2008).

[94] I. Valov, and M. N. Kozicki, Journal of Physics D-Applied Physics 46, 074005 (2013).

[95] D. B. Strukov, R. S. Williams. Four-dimensional address topology for circuits with stacked multilayer crossbar arrays. Proc. Natl. Acad. Sci. U.S.A., 106: 20155, 2009.

[96] E. Linn, R. Rosezin, C. Kgeler, R. Waser. Complementary resistive switches for passive nanocrossbar memories. Nat. Mater., 9: 403, 2010.

[97] D. Kuzum, S. Yu, H. P. Wong. Synaptic electronics: materials, devices and applications. Nanotechnology, 24: 382001, 2013.

[98] C. Kumari, I. Varun, S. P. Tiwari, A. Dixit, Super. and Micro. **120**, 67 (2018).

[99] Tiangui You, Xin Ou, Gang Niu, Florian Brwolf, Guodong Li, Nan Du, Danilo Brger, Ilona Skorupa, Qi Jia, Wenjie Yu, Xi Wang, Oliver G Schmidt, and Heidemarie Schmidt, Engineering interface-type resistive switching in $BiFeO_3$ thin film switches by Ti implantation of bottom electrodes, Scientific Reports, 2015, 5, 18623.

[100] W.A. Wulf, S.A. McKee, Hitting the memory wall: implications of the obvious, ACM SIGARCH Comp Arch News, 23 (March) (1995), pp. 20-24

[101] ITRS Emerging Research Devices Chapter, 2013.

[102] D. B. Strukov, G. S. Snider, D. R. Stewart, and R. S. Williams, Nature (London) **453**, 80 (2008).

[103] Chang Ming Lia, Retraction: Light-controlled resistive switching memory of multiferroic $BiMnO_3$ nanowire arrays, Phys. Chem. Chem. Phys., 19, 10699-10700, 2017.

[104] J. Wang, X. Zhang, H. G. Piao, Z. Luo, C. Xiong, X. Wang, and F. Yang, Appl. Phys. Lett. **104**, 243511 (2014).

[105] A. Chen, A review of emerging non-volatile memory (NVM) technologies and applications, Solid-State Electronics, 125 25-38, 2016.

[106] J. F. Verweij, and J. H. Klootwijk, Microelectronics Journal 27, 611 (1996).

[107] M. Janousch, G. I. Meijer, U. Staub, B. Delley, S. F. Karg, and B. P. Andreasson, Advanced materials 19, 2232 (2007).

[108] J. J. O'Dwyer, The theory of electrical conduction and breakdown in solid dielectrics. (Clarendon Press, 1973).

[109] K. M. Kim, D. S. Jeong, and C. S. Hwang. Nanofilamentary Resistive Switching in Binary Oxide System; a Review on the Present Status and Outlook. Nanotechnology, 22(25):254002, 2011.

[110] S. Seo, M. J. Lee, D. H. Seo, E. J. Jeoung, D.-S. Suh, Y. S. Joung, I. K. Yoo, I. R. Hwang, S. H. Kim, I. S. Byun, J.-S. Kim, J. S. Choi, and B. H. Park. Reproducible Resistance Switching in Polycrystalline NiO Films. Applied Physics Letters, 85(23):56555657, 2004.

[111] L. Goux, Y.-Y. Chen, L. Pantisano, X.-P. Wang, G. Groeseneken, M. Jurczak, and D. Wouters. On the Gradual Unipolar and Bipolar Resistive Switching of TiN/HfO2/Pt Memory Systems. Electrochemical and Solid-State Letters, 13(6):G54G56, 2010.

[112] D. Jeong, H. Schroeder, and R. Waser. Coexistence of Bipolar and Unipolar Resistive Switching Behaviors in a Pt/TiO2/Pt Stack. Electrochemical and Solid-State Letters, 10(8):G51G53, 2007.

[113] C.-Y. Lin, C.-Y. Wu, C.-Y. Wu, T.-C. Lee, F.-L. Yang, C. Hu, and T.-Y. Tseng. Effect of Top Electrode Material on Resistive Switching Properties of Film Memory Devices. IEEE Electron Device Letters, 28(5):366368, 2007.

[114] R. K. Katiyar *et. al.*, Unipolar resistive switching in planar $Pt/BiFeO_3/Pt$ structure, AIP Advances 5, 037109 (2015).

[115] S. W. Chen, J. M. Wu, Unipolar resistive switching behavior of $BiFeO_3$ thin films prepared by chemical solution deposition, Thin Solid Films 519, 499 (2010).

[116] G.-S. Park, Y. B. Kim, S. Y. Park, X. S. Li, S. Heo, M.-J. Lee, M. Chang, J. H. Kwon, M. Kim, U. I. Chung, R. Dittmann, R. Waser, and K. Kim, Nature communications 4, 2382 (2013).

[117] D. S. Jeong, B.-k. Cheong, and H. Kohlstedt, Solid-State Electronics 63, 1 (2011).

[118] T. Fujii, M. Kawasaki, A. Sawa, Y. Kawazoe, H. Akoh, and Y. Tokura, Physical Review B 75, 165101 (2007).

[119] T. Fujii, M. Kawasaki, A. Sawa, H. Akoh, Y. Kawazoe, and Y. Tokura, Applied Physics Letters 86, 012107 (2005).

[120] A. Sawa, T. Fujii, M. Kawasaki, and Y. Tokura, Applied Physics Letters 88, 232112 (2006).

[121] A. Sawa, T. Fujii, M. Kawasaki, and Y. Tokura, Applied Physics Letters 85, 4073 (2004).

[122] C. Rossel, G. I. Meijer, D. Bremaud, and D. Widmer, Journal of Applied Physics 90, 2892 (2001).

[123] S. C. Chen, T. C. Chang, S. Y. Chen, C. W. Chen, S. C. Chen, S. M. Sze, M. J. Tsai, M. J. Kao, and F. S. Y. Huang, Solid-State Electronics 62, 40 (2011).

[124] L. Wu, C. Jiang, and D. Xue, Resistive switching in doped $BiFeO_3$ films, Journal of Applied Physics 115, 17D716 (2014).

[125] M. Vagadia, A. Ravalia, P. Trivedi, S. Jethva, S. Katba, and D. G. Kuberkar, Resistive switching and magnetic behavior of $Bi_{0.8}Ba_{0.2}FeO_3/SrRuO_3/SrTiO_3$ films:role of thickness-dependent strain, J. Phys. D: Appl. Phys. 49, 185302 (2016).

[126] J. M. Luo, S. P. Lin, Yue Zheng, and B. Wang, Nonpolar resistive switching in Mn-doped $BiFeO_3$ thin films by chemical solution deposition, Appl. Phys. Lett. 101, 062902 (2012).

[127] S. H. Chang, S. B. Lee, D. Y. Jeon, S. J. Park, G. T. Kim, S. M. Yang, S. C. Chae, H. K. Yoo, B. S. Kang, M.-J. Lee, and T. W. Noh, Advanced materials 23, 4063 (2011).

[128] M. Seo, J. Kyoung, H. Park, S. Koo, H.-S. Kim, H. Bernien, B. J. Kim, J. H. Choe, Y. H. Ahn, H.-T. Kim, N. Park, Q. H. Park, K. Ahn, and D.-s. Kim, Nano Letters 10, 2064 (2010).

[129] T. Driscoll, H. T. Kim, B. G. Chae, B. J. Kim, Y. W. Lee, N. M. Jokerst, S. Palit, D. R. Smith, M. Di Ventra, and D. N. Basov, Science 325, 1518 (2009).

[130] E. D. Wachsman, and K. T. Lee, Science 334, 935 (2011).

[131] C. H. Yang, J. Seidel, S. Y. Kim, P. B. Rossen, P. Yu, M. Gajek, Y. H. Chu, L. W. Martin, M. B. Holcomb, Q. He, P. Maksymovych, N. Balke, S. V. Kalinin, A. P. Baddorf, S. R. Basu, M. L. Scullin, and R. Ramesh, Nature materials 8, 485 (2009).

[132] S. Wu, L. Ren, J. Qing, F. Yu, K. Yang, M. Yang, Y. Wang, M. Meng, W. Zhou, X. Zhou, and S. Li, Acs Applied Materials & Interfaces 6, 8575 (2014).

[133] S.-C. Chen, T.-C. Chang, S.-Y. Chen, H.-W. Li, Y.-T. Tsai, C.-W. Chen, S. M. Sze, F.-S. Yeh, and Y.-H. Tai, Electrochemical and Solid State Letters 14, H103 (2011).

[134] T. Harada, I. Ohkubo, K. Tsubouchi, H. Kumigashira, T. Ohnishi, M. Lippmaa, Y. Matsumoto, H. Koinuma, and M. Oshima, Applied Physics Letters 92, 222113 (2008).

[135] D. S. Shang, Q. Wang, L. D. Chen, R. Dong, X. M. Li, and W. Q. Zhang, Physical Review B 73, 245427 (2006).

[136] K. M. Kim, B. J. Choi, M. H. Lee, G. H. Kim, S. J. Song, J. Y. Seok, J. H. Yoon, S. Han, and C. S. Hwang, Nanotechnology 22, 254010 (2011).

[137] X. G. Chen, J. B. Fu, S. Q. Liu, Y. B. Yang, C. S. Wang, H. L. Du, G. C. Xiong, G. J. Lian, and J. B. Yang, Applied Physics Letters 101, 153509 (2012).

[138] S. Yu, X. Guan, and H. S. P. Wong, Applied Physics Letters 99, 063507 (2011).

[139] F.-C. Chiu, Advances in Materials Science and Engineering 2014, 578168 (2014).

[140] S. M. Sze, and K. K. Ng, Physics of Semiconductor Devices. (Wiley, 2006).

[141] Tang **et. al.**, Resistive switching properties of Ce and Mn co-doped $BiFeO_3$ thin films for nonvolatile memory application, AIP Advances 3, 122117 (2013).

[142] Lina **et. al.**, Current rectifying and resistive switching in high density $BiFeO_3$ nanocapacitor arrays on $Nb - SrTiO_3$ substrates, SCIENTIFIC REPORTS 5, 9680 (2015).

[143] A. R. West, Solid State Chemistry and its Applications, Wiley India, 2007.

[144] M. Sherif El-Eskandarany, Mechanical Alloying: Nanotechnology, Materials Science and Powder Metallurgy (Second Edition), Elsevier, 2015.

[145] S. K. Kulkarni, Nanotechnology: Principle and practices, Springer, (2007).

[146] D. H. Everett, Basic principles of Colloid Science, Royal Society of Chemistry, (1988).

[147] B. D. Cullity, Elements of X-ray diffraction, Addison-Wesley Publishing Company, Inc, 1956.

[148] M. A. Wahab, Solid State Physics, 2nd Edition, Narosa Publishing House, 2005.

[149] H. M. Rietveld, A profile refinement method for nuclear and magnetic structures, J. Appl. Cryst. **2**, (1969) 65.

[150] D. Semnani, Geometrical characterization of electrospun nanofibers, Elctrospun Nanofibers, Woodhead Publishing, (2017).

[151] G. Binnig, C. F. Quate, C. Gerber, Atomic Force Microscope, Phys. Rev. Lett. **56(9)**, 930-933 (1986).

[152] B. Cappella, G. Dietler, Force-distance curves by atomic force microscopy, Surf. Sci. Rep. **34(1-3)**, 1-104 (1999).

[153] G. Cordova, B. Lee and Z. Leonenko, Magnetic Force Microscopy for Nanoparticle Characterization, (2016)

[154] C. Z. Rosen, B. V. Hiremath, R. Newnham, Piezoelectricity, American Institute of Physics, Key Papers in Physics **5**, 227283 (1992)

[155] Ian R. Lewis and Howell G. M. Edwards, Hand Book of Raman Spectroscopy, Taylor and Fransis group, 2001.

[156] M. Suzuki and M. Tonouchi, Fe-implanted InGaAs terahertz emitters for 1.56m wavelength excitation, Appl. Phys. Lett. **86**, 051104 (2005).

[157] R.J.B. Dietz, B. Globisch, M. Gerhard, *et al.*, 64W pulsed terahertz emission from growth optimized InGaAs/InAlAs heterostructures with separated photoconductive and trapping regions, Appl. Phys. Lett. **103**, 061103 (2013).

[158] L. Duvillaret, F. Garet, J. F. Roux, J. L. Coutaz, Analytical modeling and optimization of terahertz time-domain spectroscopy experiments, using photoswitches as antennas, IEEE J. of Sel. Top. in Quan. Elect. **7(4)**, 615623 (2001).

[159] C. Caspers, V. P. Gandhi, A. Magrez, E. de Rijk, and J. P. Ansermet, Sub-terahertz spectroscopy of magnetic resonance in $BiFeO_3$ using a vector network analyzer, Appl. Phys. Lett. **108**, 241109 (2016).

[160] M. Bialek, T. Ito, H. Rnnow, and J. Ph. Ansermet Terahertz-optical properties of a bismuth ferrite single crystal, Phys. Rev. B **99**, 064429 (2019).

[161] K. Siegbahn et. al. Nova Acta Regiae Soc. Sci. IV, **20** (1967).

[162] A. Niazi, Pankaj Poddar, A. K. Rastogi, A precision, low-cost vibrating sample magnetometer, Current science **79**(1), 99-109 (2000).

[163] T. Van Duzer and C. W. Turner, Superconductive devices and Circuits Prentice Hall PTR, QC611.92V36 2nd ed., 1998.

[164] J. Clarke, A. I. Braginski, Fundamental and Technology of SQUIDs and SQUID Systems, WILEY-VCH Volume-I, (2004).

[165] G. Schaumburg and D. Wilmer, Improving the Accuracy of Dielectric Measurements, (2018) 1-5.

[166] M. M. Vopson, Y. K. Fetisov, G. Caruntu, and G. Srinivasan, Measurement Techniques of the Magneto-Electric Coupling in Multiferroics, Materials **10**, 963 (2017).

[167] S. A. Fedulov, P. B. Ladyzhinskii, I. L. Pyatigorskaya, and Y. N. Venevtsev, Sov. Phys. Solid State **6**, 375 (1964).

[168] T. Kimura, S. Kawamoto, I. Yamada, M. Azuma, M. Takano, and Y. Tokura, Phys. Rev. B **67**, 180401 (2003).

[169] A. A. Belik, S. Iikubo, K. Kodama, N. Igawa, S. Shamoto, M. Maie, Y. T. Nagai, Y. Matsui, S. Y. Stefanovich, B. I. Lazoryak, and E. TakayamaMuromachi, J. Am. Chem. Soc. **128**, 706 (2006).

[170] D. I. Woodward, J. Knudsen, and I. M. Reaney, Phys. Rev. B **72**, 104110 (2005).

[171] R. D. Shannon, Acta Crystallogr., Sect. A: Cryst. Phys., Diffr., Theor. Gen. Crystallogr. **32**, 751 (1976).

[172] M. K. Singh, H. M. Jang, S. Ryu, M. H. Jo, Appl. Phys. Lett. **88**, 042907, (2006)

[173] A. A. Porporati, K. Tsuji, M. Valant, A.-K. Axelssond, and G. Pezzotti, J. Raman Spectrosc. **41**, 8487 (2010).

[174] A. K. Vishwakarma, P. Tripathi, A. Srivastava, A. S. K. Sinha, O.N.Srivastava, Band gap engineering of Gd and Co doped $BiFeO_3$ and their application in hydrogen production through photoelectrochemical route, Int. J. of Hyd. Ener. **42**, 22677 (2017).

[175] X. Yuan, X. Li, Y. Liu, and C. Li, Fabrication and property of Nd-doped $BiFeO_3$ nanofibers by electrospinning, AIP Advances **7**, 075018 (2017).

[176] S. R. Mohapatra, B. Sahu, T. Badapanda, M. S. Pattanaik, S. D. Kaushik, A. K. Singh, Optical, dielectric relaxation and conduction study of $Bi_2Fe_4O_9$ ceramic, J. Mater. Sci: Mater Elect. **27**, 3645 (2016).

[177] M. A. Basith *et. al.*, The 10% Gd and Ti co-doped BiFeO3: A promising multiferroic material, J. of All. and Comp. **694**, 792 (2017).

[178] N. Shamir, E. Gurewitz, and H. Shaked, Acta Cryst. 34, 662666 (1978).

[179] X. Wen, Z. Chen, E. Liu , X. Lin , C. Chen, J. of All. and Comp. **678**, 511-517, (2016).

[180] R. Xiao, T. Hu, X. Yuan, J. Zhou, X. Ma and D. Fu, Studies of La and Pr-driven reverse distortion of FeO_6 octahedral structure, magnetic properties and hyperfine interaction of $BiFeO_3$ powder, RSC Advances **8**, 12060 (2018).

[181] A. Mukherjee, S. Basu, G. Chakraborty, and M. Pal, Effect of Y-doping on the electrical transport properties of nanocrystalline $BiFeO_3$, J. of Appl. Phys. **112**, 014321 (2012).

[182] Y. J. Wu, X.K. Chen, J. Zhang, X.J. Chen, J. Magn. Magn. Mater. 324, 13481352 (2012)

[183] J. Z. Huang, Y. Wang, Y. Lin, M. Li, C.W. Nan, Journal of Applied Physics **106**, 063911, (2009).

[184] P. Banerjee, A. Franco Jr., Mater. Lett. 184, 1720 (2016)

[185] C. A. Wang, H. Z. Pang, A. H. Zhang, X. B. Lu, X. S. Gao, M. Zeng, and J. M. Liu, Mater. Res. Bull. 70, 595 (2015).

[186] S. Yuan, H. Zu-Fei, M. Xing, W.C. Zhong, C. Gang, and F. H. Gang, Acta Physica Sinica **58**, 193 (2009).

[187] N. A. Spaldin, S. W. Cheong, R. Ramesh, Phys. Today **63**, 38 (2010).

[188] J.M. Caicedo, J.A. Zapata, M.E. Gmez, P. Prieto, Journal of Applied Physics, 103 (2008) 07E306 (2008).

[189] T. J. Park, G.C. Papaefthymiou, A.J. Viescas, A.R. Moodenbaugh, S. S. Wong Nano Letters, 7 (3), p. 766 (2007).

[190] C. Ederer, N.A. Spaldin, Physical Review B 71, p. 060401I (2005).

[191] G. S. Lotey, N.K. Verma, Journal of Nanoparticle Research 15, p. 1553 (2013).

[192] L. Curecheriu, F. Gheorghiu1, A. Ianculescu, and L. Mitoseriu, Applied Physics Letter, **99**, 172904, (2011).

[193] A. Ghosh, D. P. Trujillo, H. Choi, S. M. Nakhmanson, S. P. Alpay and J. X. Zhu, Scientific Reports **9**, 194 (2019).

[194] C. G. Koops, *On the dispersion of resistivity and dielectric constant of some semiconductors at audio frequencies.* Physical Review **83**, 121 (1951).

[195] Maxwell J C, Oxford:Chesea, 1873.

[196] Wagner, Ann. Phys. **40**, 817 (1913).

[197] N. M. Tallan, H. C. Hraham, Interfacial Polarization and Electrical Conductivity in Sapphire, Journal of American Ceramic Society **48**, 512 (1965).

[198] G. L. Song, H. X. Zhang , T. X. Wang, H. G Yang , F. G. Chang, Effect of Sm, Co codoping on the dielectric and magnetoelectric properties of $BiFeO_3$ polycrystalline ceramics, Journal of Magnetism and Magnetic Materials **324** (2012) 2121.

[199] F. Azough, R. Freer, M. Thrall, R.Cernik, F. Tuna, D.Collison, Microstructure and properties of Co-, Ni-, Zn-, Nb- and W-modified multiferroic $BiFeO_3$ ceramics, J. Euro. Ceram. Soc **30**(2010) 727-736.

[200] R. S. Cole and R. H. Cole, J. Chem. Phys. **9**, 341 (1941).

[201] J. Liu, C. G. Duan, W. G. Yin, W. N. Mei, R. W. Smith and J. R. Hardy, Phys. Rev. B **70**, 144106 (2004).

[202] S. F. Shao, J. L. Zhang, P. Zheng, W. L. Zhong and C.L. Wang, J. Appl. Phys. **99**, 084106 (2006).

[203] P. B. Macedo, C. T. Moynihan, and R. Bose. The role of ionic diffusion in polarization in vitreous ionic conductors. Phys. Chem. Glasses **13**, 171 (1972).

[204] M. Sural and A. Ghosh, J. Phys.: Condes. Matter., **10**, 10577, (1998)

[205] P. Pandit, S. Satapathy, and P. K. Gupta, Physica B, **406**, 2669, (2011)

[206] S. Sarangi, T. Badapanda, B. Behera, and S. Anwar, Journal of Material Science-Materials in Electronics, **24**, 4033, (2013).

[207] A. K. Jonscher, Nature **267**, 673 (1977).

[208] Z. Lu, J.P. Bonnet, J. Ravez, P. Hagenmuller, Solid State Ion. **57** (1992) 235244.

[209] K. Funke, Progress. Solid State Chem. **22**, 111-195 (1993).

[210] A. P. -Barranco, M. P. G. -Amador, A. Huanosta, R. Valenzuela, Appl. Phys. Lett. **73**, 2039 (1998).

[211] N. Koshizuka and S. Ushioda, Phys. Rev. B 22, 5394 (1980).

[212] P. A. Fleury and R. Loudon, Phys. Rev. 166, 514 (1986).

[213] M. Cazayous, Y. Gallais, A. Sacuto, R. de. Sousa, D. Lebeugle, and D. Colson, Phys. Rev. Lett. 101, 037601 (2008).

[214] M. K. Singh, R. S. Katiyar, and J. F. Scott, J. Phys. Condens. Matter 20, 252203 (2008).

[215] P. Rovillain *et. al.*, Nature Mater. **9**, 975 (2010).

[216] A. K. Jena, J. Arout Chelvane, J. Mohanty, Journ. of Appl. Phys. **128**, (2019).

[217] J. Wesselinowa, S. Kovachev, Hardening and softening of soft phonon modes in ferroelectric thin films, Phys. Rev. B, Condensed matter **75**, 045411 (2007).

[218] M. Nadeem, Wasi Khan, S. Khan, S. Husain, and A. Ansari, Tailoring dielectric properties and multiferroic behavior of nanocrystalline $BiFeO_3$ via Ni doping, J. of Appl. Phys. **124**, 164105 (2018).

[219] X. Yan, L. Zhu, Y. Zhou, E. Y. L. Wang, and X. Xu, Dielectric property of MoS_2 crystal in terahertz and visible regions, Appl. Opt. **54**, 6732 (2015).

[220] A. Li, C. Yu, Y. Zhou, Z. Yao, X. Yan, X. Xu, and Z. Ren, Terahertz dielectric response of silica-encapsulated FePt core-shell colloid film, Appl. Phys. A **118**, 837843 (2015).

[221] E. Hendry, F. Wang, J. Shan, T. F. Heinz, and M. Bonn, Electron transport in TiO_2 probed by THz time-domain spectroscopy, Phys. Rev. B **69**, 081101 (2004).

[222] J. Yu, X. Chen, Y. Wang, H. Zhou, M. Xue, Y. Xu, Z. Li, C. Ye, J. Zhang, and P. A. Van Aken, A high-performance self-powered broadband photodetector based on a $CH_3NH_3PbI_3$ perovskite/ZnO nanorod array heterostructure, J. Mater. Chem. C **4**, 73027308 (2016).

[223] G. E. Pike, Phys. Rev. B **6**, 1572 (1972).

[224] T. Zhao *et al.*, Electrical control of antiferromagnetic domains in multiferroic $BiFeO_3$ films at room temperature. Nat Mater **5**, 823829 (2006).

[225] H. W. Jang *et al.*, Domain engineering for enhanced ferroelectric properties of epitaxial (0 0 1) $BiFeO_3$ thin films, Advanced Materials **21**, 817 (2009).

[226] O. Auciello, A. Gruverman, H. Tokumoto, S. A. Prakash, S. Aggarwal, and R. Ramesh, MRS Bull. **23** (1998) 37.

[227] R. Nath, Y. H. Chu, N. A. Polomoff, R. Ramesh, and B. D. Huey, Appl. Phys. Lett. **93** (2008) 072905.

[228] V. M. Goldschmidt, Naturwissenschaften **14** (1926) 477.

[229] R. E. Eitel, C.A. Randall, T.R. Shrout, P.W. Rehrig, W. Hackenbeger, S.E. Park, Jpn. J. Appl. Phys. **40** (part 1) (2001) 5999.

[230] I. M. Reaney, E.L Colla, N. Setter, Jpn. J. Appl. Phys. Part 1 **33** (1994) 3984.

[231] T. Kawae, Y. Terauchi, H. Tsuda, M. Kumeda, A. Morimoto, Appl. Phys. Lett. **94** (2009) 112904.

[232] F. Huang, Z. Wang, X. Lu, J. Zhang, K. Min, W.i Lin, R. Ti, T.g Xu, J. He, C. Yue and J. Zhu, Sci. Rep. **3**, 2907 (2013).

[233] F. Lu, K. Yin, K. Fu, Y. Wang, J. Ren, Q. Xie, *Cer. Inter.*, 2017, **43**, 16101-16106.

[234] Y. Zhang, J. Qi, Y. Wang, Y. Tian, J. Zhang, T. Hua, M. Wei,Y. Liu, J. Yang, Cer. Inter. **44** (2018) 6054.

[235] M. R. Islam, M. S. Islam, M. A. Zubair, H. M. Usama, M. S. Azam, A. Sharif, Evidence of superparamagnetism and improved electrical properties in Ba and Ta co-doped $BiFeO_3$ ceramics. J. of Alloys Compd. 2018, 735, 25842596.

[236] S. Sharma, P. Saravanan, O.P. Pandey, V. T. P.Vinod, M. Cernk, and P. Sharma, Journal of Magnetism and Magnetic Materials **401** 180 (2016).

[237] G. Catalan and J. F. Scott, Adv. Mater. **21** 2463 (2009).

[238] G. E. Moore, Cramming More Components onto Integrated Circuits, Electronics **38**, 114 (1965).

[239] D. B. Strukov, G. S. Snider, D. R. Stewart, R. S. Williams, The missing memristor found, Nature (London) **453**, 80 (2008).

[240] R. Waser, R. Dittmann, G. Staikov, K. Szot, Redox Based Resistive Switching MemoriesNanoionic Mechanisms, Prospects, and Challenges, Adv. Mat. **21**, 2632 (2009).

[241] J. S. Lee, S. Lee, T. W. Noh, Resistive switching phenomena: A review of statistical physics approaches, Appl. Phys. Rev. **2**, 031303 (2015).

[242] B. Sun, Y. Liu, W. Zhaoab, P. Chen, Magnetic-field and white-light controlled resistive switching behaviors in $Ag/[BiFeO_3/\gamma-Fe_2O_3]/FTO$ device, RSC Adv. **5**, 13513 (2015).

[243] M. Ungureanu, R. Zazpe, F. Golmar, P. Stoliar, R. Llopis, F. Casanova, L. E. Hueso, A LightControlled Resistive Switching Memory, Adv. Mater. **24**, 2496 (2012).

[244] J. Park, S. Lee, J. Lee, K. Yong, A Light Incident Angle Switchable ZnO Nanorod Memristor: Reversible Switching Behavior Between Two NonVolatile Memory Devices, Adv. Mater. **25**, 6423 (2013).

[245] D. P. Sahu, S. N. Jammalamadaka, Remote control of resistive switching in TiO_2 based resistive random access memory device, Sci. Rep. **7**, 17224 (2017).

[246] S. Xiea, L. Peib, M. Lia, Y. Zhuc, X. Chenga, H. Dinga, R. Xiong, Light-controlled resistive switching and voltage-controlled photoresponse characteristics in the $Pt/CeO_2/Nb:SrTiO_3$ heterostructure, J. of Allo. and Comp. **778** 414, (2019).

[247] Z. Alamgir, K. Beckmann, J. Holt, N. C. Cady, Pulse width and height modulation for multi-level resistance in bi-layer TaO_x based RRAM, Appl. Phys. Lett. **111**, 063111 (2017).

[248] C. Kumari, I. Varun, S. P. Tiwari, A. Dixit, Super. and Micro. **120**, 67 (2018).

[249] M. Vagadia, A. Ravalia, P. S. Solanki, R. J. Choudhary, D. M. Phase, Improvement in resistive switching of Ba-doped $BiFeO_3$ films, Appl. Phys. Lett. **103**, 033504 (2013).

[250] X. Chen, G. Wu, D. Bao, Appl. Phys. Lett. **93**, 2 (2008).

[251] G. R. Fox, S. B. Krupanidhi, Nonlinear electrical properties of lead lanthanum titanate thin films deposited by multi-ion-beam reactive sputtering, Journ. of Appl. Phys. **74**, 1949 (1993).

[252] E. Barsoukov, J. R. Macdonald, A Review of:Impedance Spectroscopy, Theory, Experiment, and Applications, Materials and Manufacturing Processes **21**, 425 (2005).

[253] A. Thakre , A. Kumar, Enhanced bipolar resistive switching behavior in polar Cr-doped barium titanate thin films without electro-forming process, AIP Advances **7**, 125115 (2017).

[254] E. T. Quickel, L. T. Schelhas, R. A. Farrell, N. Petkov, V. H. Le, and S. H. Tolbert, Mesoporous bismuth ferrite with amplified magnetoelectric coupling and electric field-induced ferrimagnetism, Nature Communication **6**, 6562 (2015).

[255] F. Yan, G. Chen, L. Lu, P. Finke, and J. E. Spanier, Local probing of magnetoelectric coupling and magneto-elastic control of switching in $BiFeO_3 - CoFe_2O_4$ thin-film nanocomposite, Appl. Phys. Lett. **103**, 042906 (2013).

[256] J. Shen, J. Cong, D. Shang, Y. Chai, S. Shen, K. Zhai, Y. Sun, Sci. Rep. **6**, 34473 (2016).

[257] J. Wang, X. Zhang, H. G. Piao, Z. Luo, C. Xiong, X. Wang, F. Yang, Magnetic field controllable nonvolatile resistive switching effect in silicon device, Appl. Phys. Lett. **104**, 243511 (2014).

[258] M. C. Wu, W. Y. Jang, C. H. Lin, T. Y. Tseng, A study on low-power, nanosecond operation and multilevel bipolar resistance switching in $Ti/ZrO_2/Pt$ nonvolatile memory with 1T1R architecture, Semicond. Sci. Technol. **27**, 065010 (2012).

[259] W. Kim, S. Menzel, D. Wouters, R. Waser, and V. Rana, IEEE Electron Device Lett. **37**, 564 (2016).

[260] L. Zhao, H. Y. Chen, S. C. Wu, Z. Jiang, S. Yu, T. H. Hou, H. S. P. Wong, Y. Nishi, Multi-level control of conductive nano-filament evolution in HfO_2 ReRAM by pulse-train operations Nanoscale **6**, 5698 (2014).

[261] Y. Wu, S. Yu, H. S. Wong, Y. S. Chen, H. Y. Lee, S. M. Wang, P. Y. Gu, F. Chen, M. J. Tsai, AlO_x-Based Resistive Switching Device with Gradual Resistance Modulation for Neuromorphic Device Application. *4th IEEE International Memory Workshop (IMW)*, 1-4 (2012).

[262] S. O. Sayedaghaee, B. Xu, S. Prosandeev, C. Paillard, and L. Bellaiche, Novel Dynamical Magnetoelectric Effects in Multiferroic $BiFeO_3$, Phys. Rev. Lett. **122**, 097601 (2019).

[263] J. J. Wang, J. M. Hu, T. N. Yang, M. Feng, J. X. Zhang, L. Q. Chen and C. W. Nan, Effect of strain on voltage-controlled magnetism in $BiFeO_3$-based heterostructures, Sci. Rep. **4**, 4553 (2014).

[264] J. J. Wang, J. M. Hu, R. -C. Peng, Y. Gao, Y. Shen, L. Q. Chen, and C. W. Nan, Magnetization Reversal by Out-of-plane Voltage in $BiFeO_3$-based Multiferroic Heterostructures, Sci. Rep. **5**, 10459 (2015).

Conference and School Participation

1. **Poster** Presentation at *"DAE-BRNS Symposium on Two Decades of Ion Beam Analysis, at 3 MV Tandetron"*, March 23-24, 2017 at NCCCM, BARC, Hyderabad, India.
2. A **School** on "*Nano-mission School on Nanoscience and Nanotechnology-Physical Sciences (Emerging Materials and Methods in Nanoscience and Nanotechnology)"* Oct 22 - Nov 3, 2017 at CeNS, Bangalore, India.
3. **Poster** Presentation at *International Conference on Condensed Matter and Applied Physics (ICC-2017)*, November 24-25, 2017 at Bikaner, India.
4. **Oral** Presentation at *Research Scholars Day 2018*, February 19, 2018 at IIT Hyderabad, India.
5. A **School** on "*International School on Electron accelerator, Free Electron Laser and Application of Electron beam/THz radiation"*, March 6-9, 2018 at IUAC Delhi, India.
6. **Oral** Presentation at *Physics Open Day 2018*, March 28, 2018 at IIT Hyderabad, India.
7. **Poster** Presentation at *"Analytical Sciences at NCCCM: A journey over 25 years, 30 Nov-1* Dec, 2018 at NCCCM, BARC, Hyderabad, India.
8. **Poster** Presentation at *"International conference on magnetic materials and application (ICMAGMA 2018)*", Dec 9-13, 2018 at NISER, Bhubaneswar, India.
9. **Poster** Presentation at *"Joint MMM-INTERMAG 2019 conference*, 14-18th January, 2019 at Washington DC, USA.
10. A **School** on *"Indo-Japan Accelerator School"*, 17th-22nd February 2019 at IIT Hyderabad, India.
11. **Poster and Oral** Presentation at *"IEEE Magnetic Society Summer School 2019"*, 2nd -7th June 2019 at Virginia commonwealth university (VCU), Richmond, USA.
12. A **Workshop** on *"2019 Park AFM Workshop India,"*, 17th June 2019, IIT, Hyderabad, India.
13. **IITH-Hokkaido University Joint Workshop** on *"Electron Transfer system in Artificial Photosynthesis"*, 1st August 2019, IIT Hyderabad, India.

Awards

1. **Research excellence award 2018** at IIT Hyderabad, India.
2. **Best poster award** at Analytical Sciences at NCCCM: A journey over 25 years, 30 Nov-1 December, 2018.
3. **Travel award** for Joint MMM-INTERMAG 2019 conference, 14th -18th January 2019, Washington, DC, USA.
4. **Research excellence award 2019** at IIT Hyderabad, India.
5. **Travel award** for IEEE Magnetic Society Summer School 2019, 2nd -7th June 2019, held at Virginia commonwealth university (VCU), Richmond, USA.